eman ta zabal zazu

Universidad del País Vasco
Euskal Herriko Unibertsitatea

DOKTORETZA TESIA – PhD THESIS

PNEUMATIKOETAKO KAUTXU BIRZIKLATUZ FABRIKATURIKO MATERIAL BATEN KARAKTERIZAZIOA KOLPEEN AURREAN

CHARACTERIZATION OF RECYCLED RUBBER COMING FROM USED TIRES UNDER IMPACT LOADINGS

Egilea / Author:

Irantzu Uriarte Gallastegi

Zuzendariak / Supervisors:

Iker Garitaonandia Areitio Dr.

Teresa Guraya Díez Dr.

Bilbao, 2017 Maiatza / May

Krisialdietan, irudimena soilik da ezagutza baino garrantzitsuagoa

Albert Einstein (1879-1955)

ESKER ONAK

Ezagutzen nauen orok daki niretzat zeinen zailak diren honako hitz hauek. Izan ere, horrenbeste dut eskertzeko, horrenbeste jenderi, beldurra ematen didala inor ahazteagatik minduta senti daitekeenaren pentsatze hutsak.

Nire eskerrak txikitatik unibertsitaterainoko bidean nire ikastola maitean jakin-mina, zirrara berezi hori sorrarazi zidaten guztiei. Baita unibertsitatean izan nituen irakasle itzel horiei ere. Mikel, Andoni, Javi eta Josu, zueri bere eskerrik asko bihotzez. Izandako lan desberdinetako kide eta gaur egungo lagun berezi horiei. Ibilbide horrek egin nau gaur naizen profesionala.

Nire tesi zuzendari biok ezin ahaztu, Iker eta Teresa.

Lanean ditudan kideei esker berezia. Esteban, Ziortza eta Iñakiri, zuokin ikasgaiak partekatzea plazer bat delako eta tesi honetan aritu naizen artean lagundu izan didazuen guztiarengatik, ez lan kontuetan soilik. Sarritan gogorrak egiten diren momentuetan euskarri izan zaretelako, Rober eta Mikelekin batera. Zer esan lan honetan gehien lagundu izan didan pertsona horri buruz, Ekaitz, zure moduko jendez beteta behar luke mundu honek; lagun itzela egin dut bidean, Ciceron. Berarekin batera Gasteizen zaitudan lagun miñ horri, behar zaitudan oro hor egoteagatik, milesker! Ta noski sailean eta unibertsitatean zaituztedan gainontzeko lagunoi ere (Juan, Aloña, Nekane, Amaia, Edorta), jada elkarrekin bizi izandako hainbeste gauzengatik. Maider, Pilar, Itzi, Antón,…ikusten?, zerrenda luzeegia; parkatu norbait ez bazaituztet aipatu.

Kuadrillako lagun guztioi, denbora guzti honetan ni jasan izanagatik, nire eskerrik beroenak. Azkenean badirudi *dottore dottore* abestu ahal izango dugula (Venecia-n ote?). Nire beste lagun *Ladies* horiei ere milesker hor egoteagatik! Bidean ezagutu eta horren berezietan bihurtu zaretenoi ere eskerrak, Yolanda, nire *Xelebreak*, Ibai, nire Death Star horren berezi horri.

Ta betiko moduan, ezin falta familia. Familiako guztioi bide honetan lagundu izanagatik. Batetik, aita-ama, Naia, amumi. Bestetik, Bego, Juan, Izas, izeko, osabak. Ta noski, Gari eta nire maitetxu biori, Izaro eta Laida, hor zaudetelako, beti.

Bidean joan zaidan persona garrantzitsuenari.

Amuma, zuretzat.

LABURPENA

Kautxuaren eskaria moteltze handia eta energia disipatzeko gaitasuna beharrezkoa den hainbat ingeniaritza arlotan modu zabalean ematen da. Erabilitako kautxuzko pneumatikoek material polimerikoen hondakin portzentai handi bat suposatzen dute, kontuan izanik automobil-industriak urterik urte pneumatikoen kopuru handiagoa eskatzen duela. Materiala birziklatzeko helburuarekin, motoziklisten babeserako diseinatzen diren babes-sistemen artean, errepideetako hesietan estaldura moduan erabiltzeko aplikazio potentziala eman zaio. Hortaz, tesi honek pneumatikoetako kautxuan oinarritutako materialaren karakterizazioa burutzeko egindako lana aurkezten du.

Hiru nahaste egin dira pneumatikoetako kautxu birziklatuarekin eta dentsitate txikiko polietileno linealarekin (LLDPE) itsasgarri moduan, material bakoitzaren proportzio desberdinekin eta koloratzailelez erabili den TiO_2-ren proportzio konstante batekin nahaste guztietan. Erabilera hau inpaktuen barne dago; hortaz, nahastearen karakterizazio mekanikoak abiadura altuko konpresiozko saiakuntzak barneratzen ditu.

Literaturan ondo ezagutzen den eredu osagarri hiper-biskoelastikoa aukeratu da materiala karakterizatzeko, hain zuzen ere Yang-en eredua. Zati hiperelastikoa minimo karratuen doiketa teknikaren bitartez doitu da. Zati biskoelastikoko parametroei dagokienez, Particle Swarm Optimization (PSO) algoritmoa aukeratu da parametro hauen balioak lortzeko.

Abiadurarik altuenean materialaren kurbek ondulazio bereizgarri batzuek aurkeztu dituzte, normalean “ringing” moduan ezagutzen direnak literatura espezializatuan. Datu esperimental hauek ezin dira jatorrizko eran erabili distortsionatuta daude eta. Hortaz, Analisi Modal Esperimentala (EMA) kontsideratu da makina serbo-hidraulikoaren ezaugarri dinamikoak xehetasunez ikasteko asmoz. Hortik askatasun gradu anitzeko eredu bat eraiki da EMAtik lortutako frekuentzia naturalen, moduen eta moteltze faktoreen bitartez. Modu honetan emaitza finalaren oszilazioak minimizatuta jada erabilgarria da.

Aurretiaz proposaturiko Yang-en eredua Ansys Elementu Einituetako software-an inplementatzeko metodologia aurkeztu da ondoren; analisi esplizituetarako LS Dyna erabiltzen duena. Ekuazio osagarri hau ez dago oraindik software honetan inplementaturik eta ondorioz, materialaren azpirrutina bat garatu da, lehendabizi Matlaben. Lan honetan materialaren azpirrutina inplementatzeko algoritmoa azaltzen da.

AURKIBIDEA

Irudien zerrenda

Taulen zerrenda

LABURDURAK ETA SINBOLOAK

a	non-dimensionalised modelling parameter
A_i	modelling parameters
$\boldsymbol{B}$	left Cauchy-Green deformation tensor
B_{ij}	components of $\boldsymbol{B}$
$\boldsymbol{C}$	right Cauchy-Green deformation tensor
$\dot{\boldsymbol{D}}$	non-dimensionalised strain rate
$\boldsymbol{E}$	Green-Lagrange strain tensor
$\dot{\boldsymbol{E}}$	strain rate tensor
$\boldsymbol{F}$	deformation gradient tensor
$\boldsymbol{I}$	unit tensor
I_i	invariants of $\boldsymbol{B}$
I'_i	invariants of $\boldsymbol{C}$
p	pressure
s	non-dimensionalised time
$\boldsymbol{S}$	non-dimensionalised stress tensor
t	time
W	strain energy potential
$\boldsymbol{x}$	position vector of a material particle at time t
$\boldsymbol{X}$	initial position vector of a material particle
β	integral variable of non-dimensionalised time
ε_{ij}	components of engineering strain
$\dot{\zeta}$	non-dimensionalised stretch rate
θ_i	relaxation time
λ	stretch
$\dot{\lambda}$	stretch rate
σ	Cauchy stress tensor
σ^0_{ij}	components of engineering stress
σ_{ij}	components of σ
τ	integral value of time
Ω	constitutive functional

1. SARRERA

1.1 AURREKARIAK

Kautxuaren eskaria moteltze handia eta energia disipatzeko gaitasuna beharrezkoa den hainbat ingeniaritza arlotan modu zabalean ematen da. Erabilitako kautxuzko pneumatikoek material polimerikoen hondakin portzentai handi bat suposatzen dute, kontuan izanik automobil-industriak urterik urte pneumatikoen kopuru handiagoa eskatzen duela. Kautxu bulkanizatuak hiru dimentsiotako sare-egitura du, modu naturalean degradatzea erraza ez delarik, eta beraz, interes handia dago kautxuaren birziklatzean[1-4]. Interes hau sustatu egin da hondakinen deuseztapenen kudeaketa mundu osoan zehar zabalduz doan joera izanik; produktuen bizitza amaierarako erabilpen alternatiboak ematen saiatzen ari da, ez bakarrik ingurumen-faktoreengatik, baizik eta arrazoi ekonomikoengatik ere.

Kautxuen ingeniaritza-aplikazioak zabalak dira eta bizkor hazten doaz: Eztanda-babeserako armada-ibilgailuetako errodamendu estrukturalak[5,6], edo eraikinak eta zubiak lurrikaretatik babesteko[7], pneumatikoak, ehun biologikoak[8], ibilgailu-esekiak, bibrazio-isolatzaileak[9], junturak, juntura malguak eta kolpeak jasateko motelgailuak. Soberakina den kautxuaren birziklatzea dentsitate txikiko polietileno linealarekin nahastatuz azken aplikazio honentzat soluzio interesgarria da. Inpaktuetan zehar energia xurgatzeko kautxuaren ahalmenak oso propietate erabilgarri bat hornitzen du errepideeetako motoziklistak babesteko hesietan estalduren diseinurako, bi gurpildun ibilgailuen erabiltzaileek[10] koherenteki erabilerrazago eta ziurragoak diren errepideetako hesiak eskatzen dituzte. Bide-azpiegituretarako sistema babesleen artean, hesi metalikoekin eraikitakoak motorziklistentzat bereziki kaltegarriak kontsideratuak daude, beraien kontrako inpaktu batek lesio larriak eragin ditzakeelako.

Aurretiaz aipaturiko eskaerak betetzeko helburuarekin, bi gurpildun ibilgailutarako egokitutako sistema babesle kantitate garrantzitsuak diseinatu dira, orokorrean Motoziklistentzat Babes Sistemak deituak (MPS). Birziklatutako kautxua errepideetako hesi metalikoetan kolpeak absorbatzeko motelgailulez erabiltzearen onurek motibatuta, tesi honek erabilitako pneumatikoetan oinarritutako material baten karakterizazioan oinarritutako lana aurkezten du. Lan hau EHU-ko ikerkuntza proiektu baten markoan kokatzen da; proiektuaren helburu nagusia erabilitako pneumatikoetako kautxua birziklatzeko / leheneratzeko aukerak aztertzean datza. Birziklatze-prozedura desberdinei buruz, bulkanizatutako kautxutik birrindutako partikulen tamainei buruz, kautxu partikula hauek beste osagai batzuekin nahastatuz osatu daitezkeen konposatu soluzio posibleetan, nahaste hauen proportzioetan eta abarretan xehetasunetan sartzen da.

Garrantzitsua da materialaren portaera mekanikoa ulertzea eta espezifikoki nahasteen abiadurarekiko dependentzia, karakterizazio egoki baten ezagutza jasotzeko asmoz; hortaz, hainbat konpresiozko saiakuntza egin dira. Saiakuntzetarako makina baten edo beste baten aukeraketa deformazio abiaduraren aplikazio eremuaren menpe dago; ez da existitzen deformazio abiaduren eremu guztia kontuan hartzen duen instalazio unibertsalik[11,12]. Normalean 1 s^{-1} - 100 s^{-1} tartean dagoen deformazio abiadurapean egiten diren saiakuntza esperimentaletarako deformazio-abiadura handiko saiakuntza makina serbo-hidraulikoak erabili ohi dira[13]. Halere, 10-60 s^{-1} tartean arazo bat ematen da makina hauekin; izan ere, bibrazio batzuk ematen dira tentsio-deformazio erantzun esperimentala distortsionatzen dutenak, datu hauek alferrekoetan bihurtuz. Bibrazio hauek "system ringing" edo "erresonantzia-sistemak" moduan ezagunak dira literatura espezializatuan eta saiakuntzako makinaren modu nagusien eszitazioek sortuak dira eta frekuentzia natural batean edo gehiagotan oszilazioak sortzen dituzte[14], datu esperimentalak kaltetuz.

Normalean, ikertzaileek bibrazio hauen ikasketa kuantitatiboa egin dute saiakuntza makina askatasun gradu bakarreko sistema moduan kontsideratuz nagusiki, zeinek prozesuan nahasitako aldagaien ulermen orokor batera eraman duen. Hala ere, iragarpen analitikoen eta behaketa esperimentalen arteko desadostasunak detektatu dituzte askatasun gradu bakarreko hurbilketarekin, eta beraz, makinaren ezaugarri dinamikoen ikasketa zehatzagoaren beharra jakinarazi da. Hemen aurkeztutako lanak betebehar honi heltzen dio MTS 819.10 abiadura handiko saiakuntza makinaren portaera dinamikoaren karakterizazio zehatz baten bitartez.

1.2 TESIAREN HELBURUA

Tesi honen helburu nagusia birziklaturiko kautxuarekin eta dentsitate txikiko polietileno linealarekin osaturiko nahastearen kolpeen aurreko karakterizazio mekanikoan datza, errepideetako hesietako estaldura bere aplikazio potentzial modura aztertzeko asmoz. Nahastearen osagaien proportzio egokiak lortzea espero da betebeharrak betetzeko. Helburu honekin abiadura handiko makina serbo-hidrauliko batean deformazio abiadura altuko konpresiozko saiakuntzak egin dira. Hortaz, tesiaren helburu espezifikoak ondokoak dira:

- Hiru nahaste prestatu dira kautxu birziklatuarekin eta dentsitate txikiko polietileno linealarekin, osagai bakoitzaren proportzio desberdinekin eta lau dentsitate desberdinekin. Makinaren lau abiadura desberdinetan egin dira saiakuntzak. Abiadura altuenean indar-denbora seinalean ondulazioak agertu dira, "system ringing" edo "erresonantzia-sistemak" moduan ezagutuak. Oszilazio hauek datu esperimentalak alferreko bihurtzen dituzte. Hortaz, saiakuntza makinaren, hots, MTS 819.10 makinaren, Analisi Modal Esperimentala egitea beharrezkoa da ondulazio hauen jatorria analizatzeko asmoarekin. Frekuentzia naturalak, moduak eta moteltze faktoreak aterako dira eta parametro modal hauetatik prozesuaren eredu matematikoa garatzea itxaroten da. Eredu matematiko hau "system ringing" horretan eraginik handiena duten moduak detektatzeko erabiliko da kautxuarengan abiadura altuetan saioak egiten direnean eta kuantitatiboki iragartzeko prozesuan sorturiko bibrazioen anplitudeak. Modu honetan materialaren kurbak zuzentzea itxaroten da.
- Literaturatik eredu material bat aukeratu eta bere parametroak Particle Swarm Optimization (PSO) algoritmoaren bitartez doituko dira. Algoritmo hau hautatu izanaren arrazoiak, bere erraztasuna, sendotasuna eta konbergentzia azkarra dira. PSO algoritmoa optimizazio metodo moldaerraz bat da, minimo lokaletatik urruntzeko gai dena eta ondorioz, minimo globalera irits daitekeena, optimizatu nahi den funtzioa os ez-lineala izanda ere. Doitu beharreko parametroek bilatze-espazioan zehar, minimo globalera iritsi arte, mugitzen diren partikulen posizioak definitzen dituzte.
- Hurrengo helburua eredu hau LS Dyna programan inplementatzeko metodologia ezartzean datza, bai Matlaben, baita LS Dynan ere. Programaren liburutegian ez denez oraindik eredu hau esistitzen, materialaren azpirrutina bat sortuz egingo da

hau. Beraz, probeten deformazio abiadura altuko konpresiozko saiakuntzen analisi esplizitua egitea itxaroten da, hau da, saiakuntza esperimentalen simulazioak. Hurrengo urratsa, tesi honen helburuetatik at daudenak, errepide hesien simulazioak maniki batekin egitea litzateke, eta azkenik, simulazio hobereneko konfigurazioarekin saiakuntza errealak egitea.

1.3 TESIAREN EDUKIAK ETA EGITURA

Tesi hau zazpi kapitulutan zatitu da. Tesiaren ikuspegi orokor bate matearen helburuarekin jarraian kapitulu bakoitzaren deskribapen labur bat egiten da.

2. kapituluak kautxu birziklatuan eta polietilenoan oinarrituta dauden existitzen diren materialak aurkezten ditu. Ondoren, existitzen diren eredu hiperelastiko eta biskoelastiko nagusiak laburbiltzen dira, Yang-en ereduaren hautaketarekin, zein lan honetan erabiliko den.

Hurrengo kapituluan, 3. ean, deformazio abiadura altuko konpresiozko saiakuntzak erakusten dira. Saiakuntza hauetan erabilitako materialaren probetak osagaien hiru proportzio desberdinekin egin dira, hau da, 60/40, 75/25 eta 90/10, eta lau dentsitate desberdinekin, 0.7, 0.8, 0.9 eta 1 g/cm^3.

Deformazio abiadura altueneko emaitza esperimentalak filtratzeko metodo bat garatu da 4. kapituluan. Nahi ez diren ondulazioak erakusten dituzten hondaturiko material kurbak zuzenduak izan dira; honetarako, jatorrizko neurketei iragarritako ondulazioak kenduz, kurba leunduak lortuz. Leundutako kurba hauek deformazio abiadura altuetan modu egokian isladatzen dute benetako naterialaren portaera. Modu honetan, deformazio abiadura altuenei dagozkien tentsio-luzapen kurbak prozesatuak dira eta posible egiten da berauek erabili ahal izatea ondorengo kapituluan egiten diren analisietan.

Yang-en materialaren ekuazio konstitutibo edo osagarria 5. kapituluan azaltzen da. Eredu honen hiru parametro hiperelastikoak minimo karratuen bitartez doituak dira, Particle Swarm Optimization algoritmoa zati biskoelastikoari aplikatzen zaiolarik hiru parametro biskoelastikoak doitzeko asmoarekin. Jarraian makinaren abiadura altuenei dagozkien kurbak Yang-en ereduarekin lortutakoekin konparatzen dira, azken honen parametroen balioetan aurretik doitutako balioak erabiltzen direlarik.

6. kapituluan LS Dyna programan inplementatua izango den materialaren azpirrutina deskribatzen da, ekuazio osagarri honekin konpresiozko saiakuntza esperimentalen simulazioak egiteko. Ondoren, maniki baten errepide hesi baten kontrako kolpearen simulazioak egin nahi dira (tesiaren helburuetatik kanpo), nahaste hoberena erabiliko delarik estaldura gisa.

Eta azkenik, 7. Kapituluan lan honetatik eratorritako ondorio nagusiak eta etorkizuneko ikerketa-lerroak laburbiltzen dira.

2.
ARTEAREN EGOERA

2.1 SARRERA

Urtero, pneumatikoen industriak 3 milioi tona pneumatiko erabili baino gehiago sortzen ditu[15,16]. Kautxua erretikulatua dagoenez bulkanizazioaren eraginez, hari emandako irtenbideak hiru arlo nagusitara mugatzen dira: balorizazio energetikoa errekuntza/pirolisi prozesuaren bitartez (pneumatiko erabilien % 40 gutxi gorabehera), zabortegiak (% 25) eta birziklapen prozesua (% 35). Azken aukera hori litzateke estrategiarik onena bere balioa berreskuratzeko[17], bai arrazoi ekonomikoengatik bai ingurumen arloko arrazoiengatik, produktu horiei balio erantsirik handiena ematen baitie.

Material horretarako soluzio bat izan daiteke pneumatiko erabilietatik eratorritako kautxu birziklatua errepideetako hesien estaldura gisa erabiltzea. Hala, motoziklistek jasandako inpaktuen energia xurgatu eta motoziklistak zauri larrietatik babestuko lituzke. Dentsitate txikiko polietilenoak (LDPE) itsasgarri gisa funtzionatzen du kautxuaren partikulak elkarri lotzeko. Etileno binil azetatoarekin (EVA) eta polietileno desberdinekin hainbat proba egin ondoren, azkenean, dentsitate txikiko polietileno lineala aukeratu zen, material horrek % 90erainoko kautxu birziklatua duen nahasketa egitea ahalbidetzen duelako. Izan ere, ahalik eta kautxu birziklatu gehien erabiltzea lehenetsi zen proiektuan.

Nahasketa horretatik eratorritako material konposatua merkea da. Estrusioaren bidez transformatu daiteke sekzio luze eta konstanteko produktuak lortzeko, eta propietate elastikoak gorde ditzake 60 °C-tik gorako tenperaturetan, bere aplikazioa kontuan hartuta.

Atal honen helburu nagusia eredu konstitutibo mekaniko egokia aukeratzea da, kautxu birziklatuarekin eta dentsitate txikiko polietileno linealarekin (LLDPE) egindako nahasketarako. Horretarako, lehenik eta behin, existitzen diren mota horretako materialen berrikuspena aurkeztu da eta, ondoren, propietate hiperelastikoak eta biskoelastikoak dituzten ereduen berrikuspena egingo da.

2.2 KAUTXU BIRZIKLATUAN ETA POLIETILENOAN OINARRITUTAKO MATERIALAK

Proiektu hau gauzatzeko ideiak hemen du jatorria: aplikazio industrialak bilatzea osagai nagusitzat kautxu birziklatua duen horri. Kautxua birziklapen plantetatik ateratzen da, eta 3 eta 5 mm arteko partikulak edo handiagoak ditu. Era horretara lortutako osagaia hauts bihurtutakoa baino merkeagoa da eta maneiatzeko errazagoa. Birrindutako pneumatiko erabilietatik lortutako partikulei pneumatikoen kautxu birrindu (GTR) ere esaten zaie. Oso garrantzitsua da partikulen neurria eta morfologia kontrolatzea[18,19]. Ondoren, GTR hori termoplastikoekin nahasten da, dentsitate txikiko polietilenoa (LDPE)[20-22], dentsitate handiko polietilenoa (HDPE)[18,23-25] eta polipropilenoa (PP)[26] izanik horien artean garrantzitsuenak, elastomero termoplastikoak (TPE)[27] lortzeko.

Hauts bihurtutako kautxua hartu du aintzat polietilenoarekin eta kautxu birziklatuarekin egindako nahasketei buruzko literatura gehienak[20,27-29]. Elastomero termoplastikoaren (TPE) fabrikazioarekin, polietilenoaren gogortasuna hobetzea izan da lan horien helburua. Literaturaren arabera, honako hauek dira GTR daukan TPEak ekoizteko baldintzak, nahasketaren osagaien arteko atxikitze interfasea hobetu dadin[24,29,30]: elastomero (fresko) gehiago erabiltzea, konpatibilizadoreak erabiltzea edo behinik behin GTR partzialki desbulkanizatzea[20].

Besteak beste, aplikazio ohikoenetan[31] GTR duten nahasketak erabili dira kirol eta aisialdi guneak estaltzeko, errepideetako elementuekin nahasteko (kautxu birziklatuaren tamaina handiagoa denean zoladuretan erabiltzen da), pneumatikoetarako, edo kautxoari edo termoplastikoari eransteko kantitate txikietan. Lan honetan, errepideetako hesiak estaltzeko erabili da TPE materiala, LLDPErekin batera.

2-1 Irudia. Kautxu birziklatuarekin eta dentsitate txikiko polietileno linealarekin egindako nahasketaren laginak, segurtasun hesi eta zutabe itxurakoak.

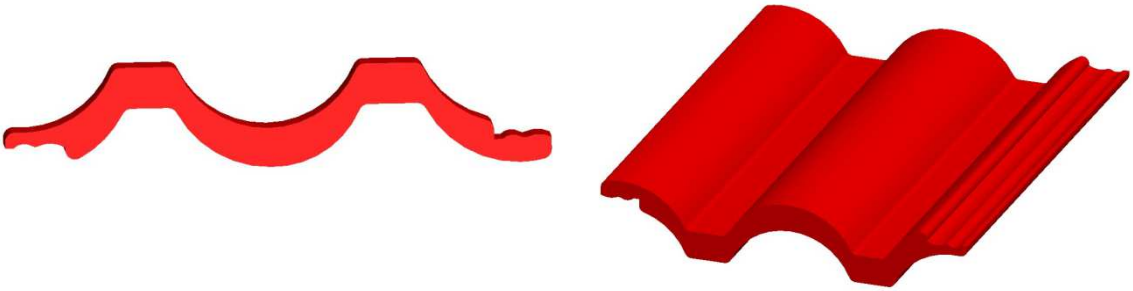

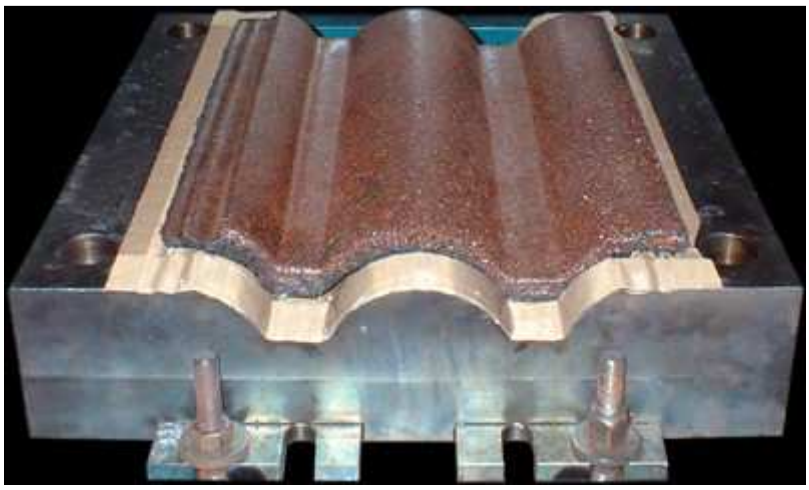

2-2 Irudia. Teilak

Hainbat hurbilketa egin izan dituzte ikertzaile desberdinek TPE hauen portaera mekanikoaren eredu bat ezartzen saiatuz. Ikerketa hauetatik abiatuz, kautxuaren

propietate hiperelastikoarekin batera, nahaste honek erakusten duen biskoelastikotasun ez-lineala ere kontuan hartu behar da. Mota horretako materialen propietate mekanikoak zehazteko hiru modu daude, hainbat ikertzailek idatzitako literaturaren arabera[32]. Lehenengoa, hurbilketa molekularra, kate sarea deskribatzen duena[33]. Bigarrena, metodo mikromekanikoa edo homogeneizazio metodoa, askotan material metalikoen alorrean erabilia, baita polimeroen alorrean ere[26,32,34]. Bigarren hurbilketa horretan, nahasketaren osagai bakoitzaren portaera hartzen da kontuan. Eta azkenik, hurbilketa fenomenologikoan oinarritutako ereduen garapena.

2-3 Irudia. Kautxu birziklatuarekin eta dentsitate txikiko polietileno linealarekin egindako nahasketa errepideko hesi batean jartzeko simulazioa

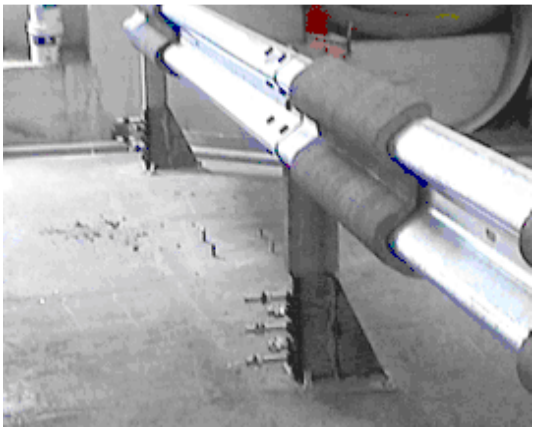

2-4 Irudia. Adibide erreala, nahasketa errepideko hesi batean kokatua. Abantailarik handienetakoa da, jartzen erraza eta merkea izateaz gain, malgua dela itxura desberdineko hesietara egokitzeko.

Propietate horiek sakonago azalduta daude hurrengo azpiatalean.

2.3 EXISTITZEN DIREN MATERIALEN EREDU KONSTITUTIBOAK

Ekuazio konstitutibo batek adierazten du zein den tentsioaren eta deformazioaren eta tenperaturaren arteko erlazioa; hau da, material baten benetako portaera erakusten du. Tesi honetan hizpide dugun material konposatuaren ezaugarriak direla-eta, hiperelastikotasunari erreparatu behar zaio lehenik eta behin, kautxua baita haren osagai nagusia. Denboraren eta kautxuaren deformazio abiaduraren efektuak nabarmenak direnean, kontuan hartzekoa da portaera biskoelastikoa.

Horrela bada, jarraian, existitzen diren ereduak aztertzeari ekingo diogu. Izan ere, beharrezkoa da ekuazio konstitutiboaren parametro kopurua ahalik eta txikiena izatearen garrantziaz ohartzea eta materialaren portaera ahalik eta ondoen zehaztea, hau da, parametro kopuruaren eta materialaren portaera zehatz azaltzearen artean dagoen erlazioa optimizatzea.

Kautxu bulkanizatuaren –betegarriak dituen kautxua barne– propietate mekanikoetako bat konprimagarritasun eza[9] da. Idealizazio bat da, kontuan hartuta presio hidrostatikoak eragindako bolumen aldaketak txikiak direla konpresiozko indarrek eragindakoen aldean. Lan honetan, material konposatua ia, baina ez guztiz, konprimaezintzat[9,35-39] hartu da, zenbakizko arazoak saihesteko eredua FE softwarean sartzean.

2.3.1 Eredu hiperelastikoak

Kautxuak deformazio handiak jasaten ditu karga baten menpe dagoenean, eta ia guztiz berreskuratzen du hasierako forma karga kentzean. Kautxu birziklatua beteta dago, eta horrek portaera guztiz ez-lineala eragiten du. Hori dela eta, oso zaila da tentsioa deformazioarekin erlazionatzeko matrize elastiko baliagarria zehaztea, matrize horretako osagaiak deformazioaren menpe daudelako eta ez direlako konstanteak. Irtenbidea da material elastiko guztiek daukaten deformazio energiaren funtzioa erabiltzea. Literaturan zenbait deformazio energia daude zehaztuta; esate baterako, Petiteauk[40] zenbait adibide erakusten ditu.

Atal honen helburu nagusia ekuazio konstitutibo hiperelastiko ezagunenak erakustea da. Horretarako, lehenengo ingurune jarraien mekanikari buruzko oinarrizko kontzeptu batzuk gogoraraziko dira; izan ere, aztertzen ari den materialak guztiz betetzen du okupaturiko espazioa eta, beraz, ingurune jarrai[41] gisa jokatzen du.

Gorputz deformagarri bati kanpoko indar bat aplikatzen zaionean, gorputzak desplazamendua jasaten du. Desplazamendu hau gorputz zurrun baten desplazamenduaren eta deformazioaren batuketan bana daiteke. Deformazioaren dimentsioaren arabera, bi teoriaren bitartez azter daiteke: batetik, deformazio infinitesimalen teoria deformazio txikietarako eta, bestetik, deformazio finituen teoria deformazio handietarako, elastomeroen kasurako alegia. Biskoelastikotasuna ere kontuan hartzekoa da eta hori da, hain zuzen ere, tesiaren ardatza.

Deformazioak bi ikuspegitatik azter daitezke: Lagrangeren eta Eulerren deskripzioak. Lehenengoan, behatzailea konfigurazio erreferentzialean dago eta denboran zehar partikulen posizio aldaketak behatzen ditu. Bigarrenean, behatzailea uneko konfigurazioan dago, mugimenduan dagoen koordenatu sistema batean. Lagrangeren deskripzioa gailentzen denez solido deformagarrien mekanikan –Eulerren deskripzioa fluidoen mekanikan erabiltzen da–, hori erabiliko dugu aurrerantzean.

Horrenbestez, **x** uneko konfigurazioan –hots, sistema deformatuan– partikula/puntu material baten posizio bektorea bada eta **X** erreferentziazko konfigurazioan –sistema deformatu gabean– haren posizio bektorea bada, euren arteko erlazioa h mapaketa funtzioaren bitartez adierazten da:

$$x = h(X,t) \tag{2.1}$$

Partikulen desplazamenduak ingurune jarraien mekanika ez-linealean funtsezkoa den matrize baten bitartez lortzen dira. Matrize horri[42] deformazio gradientearen matrizea (**F**) deritzo:

$$F_{ij} = \partial x_i / \partial X_i \tag{2.2}$$

Matrize horrek guztiz zehazten du puntu baten inguruan dagoen mugimendua. Erlazio horrek deskribatzen du nola aldatzen den material elementu lineal baten luzeera eta norabidea deformazioaren eraginez.

F_{ij} gorputz zurrunen biraketen menpe dagoenez gero, ez da egokia deformazioa neurtzeko. Honela deskonposa daiteke: F=RU (edo F=VR); U eta V matrize definitu positiboak eta simetrikoak dira eta R, aldiz, matrize ortogonala, deskonposaketa polarraren teoreman erakutsi bezala. Deformazioa neurtzeko aproposak dira U eta V, ez dakartelako gorputz zurrunen biraketarik. Hala ere, zehazten zailak dira praktikan.

Hauek dira Cauchy eta Green-en ezkerreko (**B**) eta eskuineko (**C**) deformazio tentsoreak:

$$B = FF^T \tag{2.3}$$

$$C = F^T F \tag{2.4}$$

Tentsore horiek deformazioa neurtzeko erabil daitezke, gorputz zurrunen mugimenduak ez baitie eragiten. I_1, I_2, I_3 deformazio inbariante berberak dituzte:

$$I_1(C) = tr(C) \tag{2.5}$$

$$I_2(C) = \frac{1}{2}\left[\left(tr(C)\right)^2 - tr(C^2) \right] \tag{2.6}$$

$$I_3(C) = \det(C) \tag{2.7}$$

Luzapen indizeak C-ren (edo B-ren) balio propioen erro karratuak dira eta λ_i^2 deritze. Inbariante nagusiak honela adieraz daitezke:

$$I_1 = \lambda_1^2 + \lambda_2^2 + \lambda_3^2 \tag{2.8}$$

$$I_2 = \lambda_1^2\lambda_2^2 + \lambda_2^2\lambda_3^2 + \lambda_3^2\lambda_1^2 \tag{2.9}$$

$$I_3 = \lambda_1^2 \lambda_2^2 \lambda_3^2 \tag{2.10}$$

Hiperelastikotasunak ezartzen du deformazio energiaren funtzioaren existentzia eta hortik eratortzen dela tentsioa. Material elastikoa den heinean, material hiperelastikoa gai da deformatzeko eta hasierako forma berreskuratzeko esfortzua kendu ostean, energia barreiatu edo disipatu gabe. Deformazio handiak/finituak jasaten ditu, eta $\boldsymbol{\psi}$ Helmholtz-en energia askearen funtzio bat du:

$$P = \frac{\partial \psi(F)}{\partial F} \tag{2.11}$$

Orokorrean, deformazio energiaren edo metatutako energiaren funtzio esaten zaio $\boldsymbol{\psi}$-ri, eta energiaren funtzio eskalarra da –material hiperelastikoak izaera kontserbakorra du–. F lehen definitutako deformazio gradientea da eta P, berriz, Piola-Kirchhoff-en lehen tentsio tentsorea.

Normalean, deformazio handietarako, P Piola-Kirchhoff-en lehen tentsio tentsorea edo tentsio nominalaren tentsorea eta σ Cauchy-ren tentsio tentsorea edo benetako tentsioaren tentsorea erabiltzen dira. Piola-Kirchhoff-en lehen tentsio tentsoreak uneko konfigurazioan dauden indarren eta erreferentziazko edo hasierako konfigurazioan dauden azaleren arteko erlazioa ezartzen du. Cauchy-ren tentsio tentsoreak, bestalde, uneko konfigurazioan dauden indarren eta azaleren arteko erlazioa ezartzen du. Hauxe da Cauchy-ren tentsio tentsorearen eta Piola-Kirchhoff-en lehen tentsorearen arteko erlazioa:

$$\boldsymbol{\sigma} = J^{-1} P = J^{-1} \frac{\partial \psi(F)}{\partial F} F^T \tag{2.12}$$

Non J bolumen indizea den.

Bi hurbilketa nagusi hauetan oinarritzen dira literaturan deformazio energia askea deskribatzeko agertzen diren adierazpenak:

1- Teoria estatistikoa edo zinetikoa. Polimeroaren kate sarearen edo egituraren propietate fisikoak hartzen ditu kontuan. Teoriaren oinarriei jarraituz, kautxuaren indar elastikoa batez ere entropiaren murrizketaren ondorioz gertatzen da, aplikatutako luzapena areagotzen denean presio konstantearen edo bolumen konstantearen eraginpean.

2- Teoria fenomenologikoa. Ekuazioak datu esperimentaletara doitzeko prozedura matematikoa du ardatz. Ez du problema fisikaren ikuspegitik aztertzen eta ez du kontuan hartzen materialen mikroegitura. Ingurune jarraien mekanikarren gaineko marko matematikoan oinarritzen da.

Eredu estatistikoei dagokienez, Treloar-en eredua –eredu neo-hookearra ere esaten zaio, Treloar-ek[43] garatua 1943an– edo Arruda-Boyce-ren[44] eredua (1993) aipa daitezke. Eredu horien abantaila nagusia da kautxuaren ezaugarriei buruzko azalpen fisikoa eskaintzen dutela, eredu molekular espezifiko batean oinarritzen direlako. Alabaina, zehaztasuna falta zaie, emaitza esperimentalekin alderatuz gero.

Hurbilketa fenomenologikoari dagokionez, teoria horren barruan sartu zen lehen eredu garrantzitsua Mooney-k[45] proposatu zuen 1940an, soilik oinarri fenomenologikoak ardatz hartuta. Ondoren, Rivlin-ek[46] aldaketa batzuk txertatu zituen eta Mooney-Rivlin eredua sortu zen, gaur egun erabiltzen den eredu ezegunenetako bat. Rivlin-en ereduari jarraituz, N=1 denean Mooney-Rivlin eredua ((2.14) ekuazioa) lortzen da, eta C_{01}=0 denean, berriz, eredu neo-hookearra. Autore batzuek, adibidez Yeoh-k[47], proposatu zuten soilik I_1-en menpe dagoen deformazio energia bat; izan ere, haien ustetan badirudi I_2-k ez duela eraginik deformazio energian kautxu betearen portaera kontuan hartzerakoan. Gent-ek[48] eredu propioa garatu zuen; bertan, berezitasun modura, I_1-k balio maximoa (I_m) du.

Eredu fenomenologikoen arazo nagusia ereduaren egonkortasuna bermatzea da, horrek normalean mugak edo murriztapenak eskatzen baititu. Aurreikuspen ez-fisikoak ematen dituzten parametroak lortzeko aukera dagoenez, konstante horiek kontu handiz aukeratu behar dira, errealitate fisikoa errespetatuz. Konstante horiek Drucker-en egonkortasun printzipioari jarraitu behar diote. Beste arazoetako bat da eredu horiek ez direla gai beste deformazio modu batzuk aurreikusteko, konstanteetara egokitzeko erabilitakoaz gain.

2-1 taulan, literaturan azaldutako teoria fenomenologiko nagusiak daude laburbilduta, aukeraturiko eredua eredu horren barruan sartzen baita. Informazio gehiago eskuratzeko, honako hauek egindako azterketetara jo daiteke: Marckmann eta beste[49], Steinmann eta beste[50], Gil-Negrete[9], Holzapfel[42] edo Verron[51].

2-1 Taula. Eredu fenomenologiko nagusiak

Eredu fenomenologikoa	Deformazio energia (ψ)	
Mooney[45] (1940)	$\psi = C_1(I_1-3)+C_2(I_2-3)$	(2.13)
Rivlin's form[46] (1948)	$\psi = \sum_{i+j=1}^{N} C_{ij}(I_1-3)^i (I_2-3)^j$	(2.14)
Rivlin and Saunders[52] (1951)	$\psi = C(I_1-3)+f(I_2-3)$	(2.15)
Gent and Thomas[53,54] (1958)	$\psi = C_1(I_1-3)+C_2\ln\left(\frac{I_2}{3}\right)$	(2.16)
Biderman[50] (1958)	$\psi = C_{10}(I_1-3)+C_{01}(I_2-3)+$ $C_{20}(I_1-3)^2+C_{30}(I_1-3)^3$	(2.17)
Carmichael and Holdaway[55] (1961)	$\psi = \sum_{i=1}^{3}\left[\phi(\lambda_i^2)-\phi(1)\right]$ *where* $\frac{d\phi(u)}{du}=\frac{1}{4u}\left[Ae^{\beta\left(\sqrt{u}-\sqrt{u^{-1}}\right)}-2B(u+u^{-1}-2)\right]$	(2.18)
Hart-Smith[49] (1966)	$\frac{\partial\psi}{\partial I_1}=Ge^{k_1(I_1-3)^2}$ *and* $\frac{\partial\psi}{\partial I_2}=G\frac{k_2}{I_2}$	(2.19)
Valanis and Landel[56] (1967)	$\psi=\psi(\lambda_1)+\psi(\lambda_2)+\psi(\lambda_3)$ *and* $\frac{d\psi}{d\lambda}=2\mu\ln(\lambda)$	(2.20)

Alexander	$\psi = \frac{\mu}{2}\left\{ \begin{array}{l} C_1 \int e^{k(I_1-3)^2} dI_1 + C_2 \ln\left(\frac{(I_2-3)+\gamma}{\gamma}\right) \\ +C_3(I_2-3) \end{array} \right\}$	(2.21)
Ogden[57] (1972)	$\psi = \sum_{n=1}^{N} \frac{\mu_n}{\alpha_n}(\lambda_1^{\alpha_n} + \lambda_2^{\alpha_n} + \lambda_3^{\alpha_n} - 3)$	(2.22)
Blatz, Sharda and Tschoegl[58] (1974)	$\psi = \frac{2G}{\alpha} I_{E_\alpha} + B {I_{E_\alpha}}^{\beta}$	(2.23)
Haines-Wilson[49] (1975)	$\psi = C_{10}(I_1-3) + C_{01}(I_2-3) + C_{11}(I_1-3)(I_2-3) + +C_{02}(I_2-3)^2 + C_{20}(I_1-3)^2 + C_{30}(I_1-3)^3$	(2.24)
Yeoh[47] (1990)	$\psi = C_{10}(I_1-3) + C_{20}(I_1-3)^2 + C_{30}(I_1-3)^3$	(2.25)
Arruda-Boyce[44] (1993)	$\psi = \mu \sum_{i=1}^{5} \frac{C_i}{\lambda_m^{2i-2}}(I_1^i - 3)$	(2.26)
Gent[48] (1996)	$\psi = -\frac{E}{6}(I_m - 3) ln\left[1 - \frac{I_1-3}{I_m-3}\right]$	(2.27)
Yeoh and Fleming[59] (1997)	$\psi = \frac{A}{B}[1 - e^{(-B(I_1-3))}] - C_{10}(I_m-3) ln(1 - \frac{I_1-3}{I_m-3})$	(2.28)

Shariff[60] (2000)	$\sigma = \lambda_i \frac{\partial \psi}{\partial \lambda_i} - p = E\sum_{i=0}^{n} \alpha_i \phi_i(\lambda)$ $\phi_0(\lambda) = \frac{2\ln(\lambda)}{3}$ $\phi_1(\lambda) = e^{(1-\lambda)} + \lambda - 2$ $\phi_2(\lambda) = e^{(\lambda-1)} - \lambda$ $\phi_3(\lambda) = \frac{(\lambda-1)^3}{\lambda^{3.6}}$ $\phi_j(\lambda) = (\lambda-1)^{j-1}, j = 4,5,\ldots n$	(2.29)
Beda (2005)	$\psi = \frac{K_0}{\beta}(I_2-3)^{\beta} + \frac{C_1}{\alpha}(I_1-3)^{\alpha} +$ $+C_2(I_1-3) + \frac{C_3}{\varsigma}(I_1-3)^{\varsigma}$ $0 < \alpha < 1$ $0 < \beta < 1$ $1 < \varsigma$	(2.30)
Pucci and Saccomandi[61] (2015)	$\psi = \frac{\mu}{2}\left[(I_1-3) + \frac{\beta}{2}(I_1-3)^2\right]$	(2.31)

2.3.2 Eredu biskoelastikoak

Arestian aipatu bezala, kautxuaren propietate elastikoak ondo azal daitezke eredu hiperelastikoen bitartez, bai kasu kuasiestatikoetan, bai deformazio handiak gertatzen direneko deformazio abiadura handiko kasuetan[40,64]. Hala ere, deformazioak handiak direnean eta aplikatutako indarrek deformazio abiadura moderatua dutenean, 2-5 Irudian ikusten den bezala, deformazio handiko biskoelastikotasuna aplikatu behar da[40], hots, portaera dinamikoa biskoelastikotasunaren menpe adierazi beharra dago. Material biskoelastikoek energia barreiatzen dute kalterik jasan gabe. Horrez gain, deformazioaren historia gordetzen dute; hau da, material horiek memoria daukate, memoria ahula.

Eredu biskoelastiko ez-linealen azterketak aurki daitezke hemen[65,66].

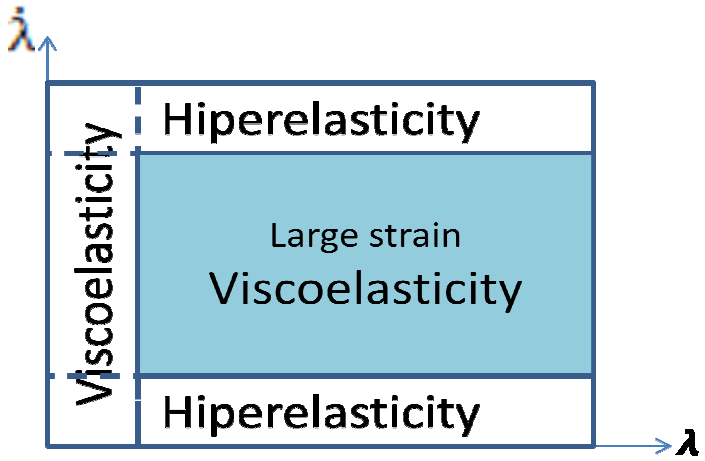

2-5 Irudia. Biskoelastikotasunaren aplikagarritasuna

2-5 irudiari jarraituz eta gogoan hartuta material hori errepideetako hesiak estaltzeko erabili nahi dela motoziklistek inpaktu txikiagoak jasan ditzaten, deformazio handiko biskoelastikotasuna hartu behar da kontuan aztergaian. Beraz, materialaren portaera dinamikoa modelatu behar da biskoelastikotasunaren bitartez.

Denbora eta deformazio abiadura aintzakotzat hartu behar dira. Hauek dira denborarekiko menpekotasunarekin lotuta dauden ohiko fenomenoak:

- Histeresia karga ziklikoetan; hots, kargen eta deskargen kurbek ez dira berdin mantentzen.
- Abiadurarekiko menpekotasuna, tentsioaren eta deformazioaren arteko erlazioan ikus daitekeena. Bestela esanda, deformazio balio bat hartuz gero, deformazio abiaduraren arabera tentsio balio desberdinak lortzen dira.
- Denborarekin tentsioa erlaxatzea, hau da, tentsioa denborarekin txikitu egingo da deformazio mailakatuko kargaren eraginez.
- Fluentzia geldoa, denborarekin deformazioa areagotu egiten da tentsio mailakatuko kargaren eraginez.

Erakutsi da deformazioaren arabera, biskoelastikotasuna deformazio txikiko biskoelastikotasun lineala edo deformazio finituko biskoelastikotasuna izan daitekeela. Lehehengoak modu linealean erantzuten du, hau da, tentsioa eta deformazioa erlazionatuta daude modulu elastikoaren bitartez. Biskoelastikotasun finituak, ordea, portaera elastiko ez-lineala ezartzen du tentsioaren eta deformazioaren artean deformazio

handietan. Teoria horren xedea da deformazio abiadurarekiko menpekotasuna aztertzea, deformazio handietan.

Deformazio handiko biskoelastikotasunaren oinarriak finkatzeko, komenigarria da BISKOELASTIKOTASUN LINEALA[67] berrikustea. Teoria horrek deformazio abiadurarekiko menpekotasuna aztertzen du deformazio txikietan.

Biskoelastikotasun lineala bi formulazioren bidez azter daiteke:

1- Boltzmann-en gainezarpen printzipioak proposatu zuen lehen aldiz tentsioaren eta deformazioaren arteko erlazioa. Asko erabiltzen da printzipioaren aplikazioa, konboluzioko integralaren edo integral hereditarioaren hurbilketa ere deitzen dena. Horren arabera, une jakin bateko deformazioak barik, deformazioren historia guztiak eragiten dio tentsioari. Hortaz, momentuko/uneko tentsioa lor daiteke, deformazio gehikuntza guztietarako tentsioen erantzunak gainezarriz gero. Deformazioaren historia kontuan hartzen da memoria ahularen funtzioen bitartez, Prony-ren serie deritzenak. Ikertzaile batzuek[68-71] biskoelastikotasun linealean oinaritutako BKZ integral fenomenologikoa erabiltzen dute. Hala, ereduaren erantzuna esfortzu guztiak gehituta lortuko da. Materiala isotropoa bada, Boltzmann-en gainezarpen integral[72] honen bitartez adieraz daiteke material biskoelastiko eta zaharkitu gabe baterako tentsio-deformazioaren ekuazio uniaxial eta isotermikoa:

$$\sigma(t) = \int_{-\infty}^{t} G(t-\tau)\frac{d\varepsilon(\tau)}{d\tau}d\tau \qquad (2.32)$$

Aplikatutako deformazioak $-\infty < t < 0$ tartean nuluak direnean, (2.32) ekuazioa honela idatz daiteke:

$$\sigma(t) = \varepsilon_0 G(t) + \int_{0^+}^{t} G(t-\tau)\frac{d\varepsilon(\tau)}{d\tau}d\tau \qquad (2.33)$$

t=0 izanik bat-bateko deformazioren balioa ε_0 denean, une horretako denbora t da eta lehenagoko denbora orokorra τ; non $\tau \in (0,t)$.

(2.33) ekuazioak memoriaren hipotesia, leuntasunaren hipotesia eta errepresentazio matematikoaren teorema (Christensen[73]) ditu oinarrian. Erreferentziazko egoera deformatu gabea eta tentsiorik gabea dela hartuko da

kontuan; beraz, integrala 0^+-tik hasita kalkulatuko da eta $\sigma(t)=0$ eta $\varepsilon(t)=0$ t<0 denean.

2- Bestalde, lehen ordenako eta ordena handiagoko denboraren deribatuak tentsioan eta deformazioan, malguki-motelgailuen ereduetan oinarrituta. Kasu uniaxialetan, malgukiz eta motelgailuz osatutako eredu erreologikoak erabili ohi dira. Tentsioa eta deformazioa erlazionatzeko ekuazio diferentzialak lortzen dira eredu horietatik. Ondoren, hiru dimentsioko kasuetan aplikatzen dira tentsore eran.

Deformazio txikietan, malgukietan eta motelgailuetan oinarritutako ereduak eta konboluzio integraletan oinarritutakoak antzekoak dira, emaitza berberak ematen dituztelarik.

Biskoelastikotasun linealaren aplikazio eremua deformazio txikietan baino ez da baliagarria. Drapaca-k eta bestek[66] adierazi bezala, lege konstitutibo ez-lineal batek baldintza hau bete behar du: eredu linealaren parera murriztea eredua, deformazioak txikiak direnean. DEFORMAZIO HANDIKO BISKOELASTIKOTASUNARI dagokionez, eredu biskoelastiko finituek deskribatzen dute materialaren portaera, deformazioak handiak direnean. Biskoelastikotasun finitua nagusiki bi hurbilketaren bitartez azaltzen da[74]:

1- Batetik, barne aldagaien ereduak daude; horien oinarria da **F** deformazio gradientearen tentsorea zati elastikoaren eta ez-elastikoaren[75] biderkaketa moduan deskonposatzea. Hurbilketa hori hasieran Green-ek eta Tobolsky-k formulatu zuten eta hainbat ikertzaile izan ziren haren jarraitzaile, hala nola Lubliner, Sidoroff, Bergström eta Boyce[76], Shim eta Mohr[77,78]. Oro har, eredu horiek modu esperimentalean balioztatu dituzte. Lan honetan, ez da hurbilketa hori aurkeztuko.

2- Bestetik, integral hereditarioen hurbilketa dago: eredu horiek memoria ahuleko funtzio polinomikoak erabiltzen dituzte, deformazioaren historiak momentuko tentsioan eragiten dituen ondorioak azaltzeko (Simo[79], Drozdov[80]). Boltzmann-en printzipioa deformazio handietara hedatu dute integralen ereduek. Jatorria autore hauen lanean aurki daiteke: Green eta Rivlin[81] eta Coleman and Noll[82] (Biskoelastikotasun Lineal Finitua). Yang-ek eta bestek[68] K-BKZ motako eredu fenomenologikoa erabili zuten. Pouriayevali-k[36,83] integral formako eredua erabili zuen deformazioren menpeko erlaxazio denborarekin batera.

Eredu horietako batzuk hurbilketa fenomenologikoan oinarritzen dira; beste batzuek, aldiz, mikromekanikan dute oinarria. Bigarren hurbilketa horretan sakontzeko, Drozdov eta Dorfmann[84], Bergström eta Boyce[85] eta bertan jasotako erreferentzietara jo dezakete ikertzaileek.

Tesi honek integral hereditarioen hurbilketa hartzen du ardatz. Horrenbestez, hurbilketa horretan garatutako eredu konstitutiboetan jarri da arreta.

Green eta Rivlin-en[81] teoriak aurreikusten duenez, t denboran tentsioa eta ondoko historia integralen batura berdinak dira, dimentsio bakarreko deformazio kasuetan:

$$\sigma(t)=\int_0^t G_1(t-\tau)\frac{d\varepsilon(\tau)}{d\tau}d\tau+\int_0^t\int_0^t G_1(t-\tau_1)G_2(t-\tau_2)\frac{d\varepsilon(\tau_1)}{d\tau_1}\frac{d\varepsilon(\tau_2)}{d\tau_2}d\tau_1 d\tau_2+\ldots \qquad (2.34)$$

Ekuazio horren bitartez, Cauchy-ren tentsioa eta deformazioaren historia erlazionatu zituzten. Green eta Rivlin-ek deformazioaren historiaren funtzional lineala erabili zuten (Frechet-Volterra-ren garapena), non G_1, G_2… egindako trunkatura ordenaren menpeko erlaxazio funtzioak diren.

Coleman-ek eta Noll-ek[82] proposatzen dute Biskoelastikotasun Lineal Finituaren teoria (FLV) erabiltzea. Teoria horrek hauxe baino ez du kontuan hartzen: tentsioak duen menpekotasuna iragan hurbileko deformazio gradientearekiko, puntu baten gertuko ingurunean gertatu dena. Tentsioa deskonposatu egiten da orekako tentsioan ematen den tentsio erantzunean, hau da, deformazio abiadura infinituki geldoan; eta biskositateak eragindako gaintentsioan ematen den tentsio erantzunean. Materialaren memoria neurtzeko erabiltzen da erlaxazio funtzioa. Material biskoelastikoetarako hastapeneko lege konstitutibo gehienak memoria ahularen teoriaren baitan garatu ziren. Hala, integral linealak tentsioa lortzeko deformazioaren historia zehazteko erabiltzen dira:

$$\sigma(t)=\sigma^{\infty}\{C(t)\}+F(t)\int_{-\infty}^{t} g\left(C(t),t-\tau\right)\frac{dE_t(\tau)}{d\tau}d\tau F^{T}(t) \qquad (2.35)$$

Solido biskoelastiko ez-linealen ekuazio konstitutiboetarako, ez dago oro har onartuta ondo zehazturiko eredurik, ez behintzat solido biskoelastiko linealetarako dagoen neurri berean. Erantzunaren funtzionalen hainbat errepresentazio espezifiko aurki daitezke literaturan, eta horiek laburtuta daude Lockett-en[86] liburuan, eta Wineman-en[65] zein Drapaca eta besteren[66] analisi artikulu berriagoan.

Bernstein, Kearsley eta Zapas-ek[87] eta Kaye-k[88] beste teoria bat proposatu zuten, K-BKZ teoria deritzona. Tanner-ek[89] ereduaren eta haren bertsioen loturak aztertzen ditu, ingurune jarraien mekanikarekin, teoria molekularrarekin eta saiakuntzekin. Solidoei zein fluidoei aplika dakieke K-BKZ eredua. Hauxe da material konprimaezinetan erabiltzen den adierazpen orokorrena:

$$\sigma(t) = -pI + 2\int_{-\infty}^{t}\left(\frac{\delta U}{\delta I_1}C_t^{-1}(\tau) - \frac{\delta U}{\delta I_2}C_t(\tau)\right)d\tau \qquad (2.36)$$

U potentziala da, eta denboraren eta I_1 eta I_2-ren menpe dago.

Bestalde, Chang-ek, Bloch-ek eta Tschoegl-ek[90] integral lineala duen eredu bat garatu zuten, CBT deritzona. Boltzmann-en gainezarpen integralean deformazio orokorra neurtzean oinarritzen da; deformazioaren efektuak eta denbora banatzen dituzte erlaxazio funtzioan.

$$\sigma(t) = -pI + \frac{1}{n}\int_{-\infty}^{t} G(t-\tau)\left[B^{n/2}(t)\frac{dC_t^{n/2}(\tau)}{d\tau} + \frac{dC_t^{n/2}(\tau)}{d\tau}B^{n/2}(t)\right]d\tau \qquad (2.37)$$

Parametro materialak dira n eta G(τ).

Christensen[73]:

$$\sigma(t) = -pI + F(t)\left[g_0 I + \int_0^t g_1(t-\tau)\frac{dE(\tau)}{d\tau}d\tau\right]F^T(t) \qquad (2.38)$$

Jarraian ageri den taulan laburbilduta daude arestian aurkeztutako teoria biskoelastiko ez-linealak:

2-2 Taula. Eredu biskoelastiko ez-lineal nagusiak

EREDU BISKOELASTIKO EZ-LINEAL NAGUSIAK		
Green and Rivlin[81] (1957)	$$\sigma(t)=\int_0^t G_1(t-\tau)\frac{d\varepsilon(\tau)}{d\tau}d\tau+\int_0^t\int_0^t G_1(t-\tau_1)G_2(t-\tau_2)\frac{d\varepsilon(\tau_1)}{d\tau_1}\frac{d\varepsilon(\tau_2)}{d\tau_2}d\tau_1 d\tau_2+\ldots$$	(2.34)
Coleman and Noll[82] (1961)	$$\sigma(t)=\sigma^{\infty}\{C(t)\}+F(t)\int_{-\infty}^t g\left(C(t),t-\tau\right)\frac{dE_t(\tau)}{d\tau}d\tau F^T(t)$$	(2.35)
Bernstein, Kearsley and Zapas[87] and Kaye[88] (1962)	$$\sigma(t)=-pI+2\int_{-\infty}^t\left(\frac{\delta U}{\delta I_1}C_t^{-1}(\tau)-\frac{\delta U}{\delta I_2}C_t(\tau)\right)d\tau$$	(2.36)
Chang, Bloch and Tschoegl[90] (1976)	$$\sigma(t)=-pI+\frac{1}{n}\int_{-\infty}^t G(t-\tau)\left[B^{n/2}(t)\frac{dC_t^{n/2}(\tau)}{d\tau}+\frac{dC_t^{n/2}(\tau)}{d\tau}B^{n/2}(t)\right]d\tau$$	(2.37)
Christensen[73] (1980)	$$\sigma(t)=-pI+F(t)\left[g_0 I+\int_0^t g_1(t-\tau)\frac{dE(\tau)}{d\tau}d\tau\right]F^T(t)$$	(2.38)
Fung[91] (1981)	$$\sigma(t)=-pI+F(t)\left\{K^{(e)}[C(t)]+\int_0^t K^{(e)}[C(s)]\frac{\partial G(t-s)}{\partial(t-s)}ds\right\}F(t)^T$$	(2.39)
Morman[92] (1988)	$$\sigma(t)=-pI+\frac{E(t)}{E_e}\left(\Gamma_1 B+\Gamma_{-1}B^{-1}\right)$$ $$\Gamma_1=2\frac{\partial\psi(I_1(t-s),I_2(t-s))}{\partial I_1(t-s)}$$ $$\Gamma_{-1}=-2\frac{\partial\psi(I_1(t-s),I_2(t-s))}{\partial I_2(t-s)}$$	(2.40)

2.4 AUKERATUTAKO EKUAZIO KONSTITUTIBOA

Tesian aztergai den material konposatuari buruzko informazioa mugatua da, haren mikroegiturari eta konposizioari dagokionez. Hori dela eta, lan honetan eredu fenomenologikoa hautatu da ereduaren zati hiperelastikoari dagokionez. Rivlin-en eredua hiru parametrorekin aukeratu da alor hiperelastiko hori deskribatzeko, kontuan hartuta gai dela erantzun zehatzak iragartzeko konpresio saiakuntzetan oinarrituta eta matematikoki kalkulatzeko erraza dela. EF kode guztietan ere ezarrita dago.

Aurkeztutako eredu biskolastikoei dagokienez, integral hereditarioen hurbilketa hautatu da, eta horren barruan K-BKZ eredua, Yang-ek eta bestek[68] txertatutako aldaketa batekin. Eredu hori sakonago aztertuko da 5. kapituluan.

Material homogeneo, isotropo eta konprimaezinetarako eredu biskoelastikoaren adierazpen orokorra[86] kontuan hartzen bada:

$$\sigma = -p + F(t) \cdot \Omega_{\tau=-\infty}^{t} \{C(\tau)\} \cdot F^{T} \tag{2.41}$$

Matrizearen funtzionala honela idatz daiteke:

$$\Omega_{\tau=-\infty}^{t} \{C(\tau)\} = \int_{-\infty}^{t} \phi(I_1, I_2) m(t-\tau) \dot{E}(\tau) d\tau \tag{2.42}$$

Yang-ek ereduari egiten dion ekarpena ϕ funtzioaren zehaztapen honetatik dator:

$$\phi(\tau) = C_2 + C_3 (I_2 - 3) \tag{2.43}$$

Erlaxazio denboraren gai bakarra aukeratu denez m(t-τ) erlaxazio funtzioan, ikus daitekeenez, parametro gutxi behar dira (hiru baino ez) portaera biskoelastikoa deskribatzeko.

Aukeratutako eredu hiper-biskoelastikoaren helburua materialaren portaera ahalik eta zehatzen azaltzea da, ahalik eta parametro gutxien erabilita.

3.
MATERIALAREN SAIAKUNTZA ESPERIMENTALA

3.1 SARRERA

Kapitulu honetan, bulkanizatutako kautxu birziklatuz, dentsitate txikiko polietileno linealez (LLDPE) eta titanio dioxidoz (TiO_2) osatutako material konposatuaren portaera mekanikoa aztertuko da. Material hori errepideetako hesien estaldura gisa erabili nahi da, talka batean sortutako energiaren zati bat xurga dezan.

Elastomeroek gaitasun handia dute deformazioak jasateko apurtu gabe, tentsioa areagotu ahala, materiala konprimatuz doalarik. Gainera, efektu biskoelastiko ez-lineala ere antzematen zaio barreiatze propietatek erakusten dituen kautxuari. LLDPEak energia xurgatzeko gaitasun handia dauka.

Material berezia denez, haren propietate mekanikoak ez dira modu sistematikoan deskribatu. Kontuan hartuta aplikazioan konposatuak talka bat jasango duela, materialak konpresio tentsioko egoerak nozituko ditu, denboran aldakorrak diren deformazio abiaduren arabera. Hori dela eta, beharrezkoa da baldintza jakin batzuetan saiakuntzak egitea. Batik bat konpresiozko talka saiakuntza eta pisu erorketaren saiakuntza erabiltzen dira konpresio baldintzen pean materialak duen kolpeak xurgatzeko edo moteltze gaitasuna neurtzeko. Pisu erorketaren saiakuntzaren bidez aurretik egindako azterketa batean lortu diren emaitzen arabera, deformazio abiadura handiko saiakuntzak egin dira hainbat karga egoeratan, konposatuaren propietateak ezagutze aldera, eta ikus daiteke,

deformazio handietan, material horrek deformazio abiadurarekiko duen menpekotasuna esanguratsua dela.

Oso zorrotzak dira "UNE 135900[93,94] Segurtasun hesietan eta petriletan motoziklistak babesteko sistemen portaera ebaluatzea. 2. zatia: portaera motak eta onarpen irizpideak" arauaren betekizunak. Arauari jarraiki, talka saiakuntzak egiteko, instrumentaturiko maniki baten buru eta lepo aldea jaurti behar da babes sistema baten kontra 60 km/h-ko abiaduran. Saiakuntzan parametro biomekaniko batzuk neurtzen dituzte, eta ezin dituzte zehazturiko balioak gainditu. Hori dela eta, homologaturiko babes sistema diseinatzeko jarraitu beharreko prozedura izango litzateke: dagozkion saiakuntzak egitea eskala errealeko prototipoekin eta egiaztatzea ea arauaren betekizunak betetzen diren edo ez. Saiakuntzaren emaitzak egokiak izanez gero, ez litzateke arazorik egongo. Bestela, beharrezko aldaketak txertatu beharko lirateke babes sisteman eta, ondoren, berriz ere saiakuntzak egin. Saiakuntza horiek oso garestiak direla aintzat hartuta, froga/akats bidezko prozedura ez da bideragarria ikuspuntu ekonomiko batetik. Ondorioz, proiektu honetan elementu finituen softwarean simulazioak egingo dira, babes sistemaren portaera zein den egiaztatzeko.

Kontuan hartu beharreko deformazio abiadura 10^{-3}-tik 10^{3} s^{-1}-ra bitartekoa da, UNE 135900-2:2008[94] arauan saiakuntzetarako ezarritako abiadurak barne. Efektu iragankorrak gero eta esanguratsuagoak direnez deformazio abiadura handitu ahala, oszilazio handiak ikus daitezke indar seinaleetan.

Saiakuntzak ez dira aldez aurretik baldintzatu, Mullins[95] efektua saihesteko. Hala ere, saiakuntza egitean ez zenez agertu barril itxurarik probetetan, gertakizun hori albo batera utz daiteke zehaztasuna galdu gabe.

Ondoren, material eredu bat proposatuko da eta bere parametroak emaitza esperimentalekin uztartuko dira. Jarraian, nahitaezkoa da saiakuntza prozedurak zehaztea materialaren portaera deskribatzeko. Kanpaina esperimentala sarritan garestia denez eta luze jotzen duenez, 6. kapituluan aurkeztuko den eredu analitiko/numeriko prediktiboa erabiltzea aukera egokia da kantitate hori kalkulatzeko.

Kapitulu hau era honetara dago antolatuta: lehenengo, probetak prestatuko dira kautxu birziklatuaren eta LLDPEaren proportzio desberdinetako 3.2. atalean. Deformazio abiadura handiko saiakuntzetarako metodologiak aurkeztuko dira 3.4**¡Error! No se encuentra el origen de la referencia.**. atalean. Ondoren, saiakuntza makina ere deskribatuko da.

Kapitulua ixteko nahasketen emaitza esperimentalak eta iruzkin batzuk aurkeztuko dira 3.5. atalean.

3.2 PROBETEN PRESTATZEA

Pneumatiko erabilietako kautxu birziklatuarekin eta dentsitate txikiko polietileno linealarekin egindako nahasketa erabili da. Kautxuaren partikulen neurria 0,8 – 3 mm artekoa da, eta LLDPEa trinkotzeko erabili da, itsasgarri gisa. Nahasketa hori da deskribatu beharreko materiala. Horrez gain, TiO_2 ere erabili da (3-3 irudian) probetak errepideetako hesien kolore antzekoena izan dezan, hori baita itxaroten den aplikazio potentziala.

Kautxua itsasgarri batekin nahastu eta trinkotzen denean, amaierako produktuak energia xurgatzeko duen gaitasuna honako hauen araberakoa da: itsasgarriaren izaera, material bien proportzioak, nahasketak amaieran duen dentsitatea eta materialaren lodiera. Kautxua izanik nahasketaren osagai nagusia, zaila da zehaztea talken aurrean materialak izango duen erantzuna. Izan ere, ezinezkoa da trakziopean materiala frogatzea, baldintza horietan oso erraz puskatzen delako. Ondorioz, beharrezkoa da frogak konpresiopean egitea.

Gero, simulazioen emaitzak alderatu dira saiakuntza esperimentalean lortutakoekin. Saiakuntzaren emaitzen eta simulazioen analisitik abiatuta, ondorio batzuetara heldu nahi da.

Kontuan hartu da saiakuntzaren errepikakortasuna, baita materialaren dentsitateak eta lodierak talkaren energia xurgatzeko gaitasunean duen eragina ere. Halaber, teknika esperimentalak eta zenbakizko teknikak uztartzeko aukerak ere ebaluatu dira, material mota horien karakterizazio egokia lortzeko asmoz. Modu horretara, materialen eredu konstitutibo hobeak aukera daitezke.

Lehengaia ez denez homogeneoa, asmoa da emaitzak uztartzea Roswand IFW5 makinan dentsitate eta lodiera askotako xafletan egindako pisu erorketaren saiakuntzetan lortu diren emaitzekin. Konpresiozko emaitza esperimentalak Ansys-LS Dyna FE programarako datu gisa erabili dira, konpresio saiakuntza horiek simulatzeko.

Kautxu birziklatuaren eta LLDPEaren hiru proportzio fabrikatu dira:

3-1 taula. Kautxu birziklatuaren eta LLDPEaren proportzioak nahasketa desberdinetan

	Kautxu birziklatua	LLDPE	TiO_2 (proportzio konstantea)
90/10	87%	10%	3%
75/25	72%	25%	3%
60/40	57%	40%	3%

Ikerketa honetan, onartutzat jo da kautxuak deformazio abiadura txikienean duen portaera funtsean bere erantzun estatikoaren berbera dela. Emaitza esperimentalek egiaztatu dute onarpen edo suposizio horrek ez duela errore esanguratsurik eragiten.

Kautxu birziklatua txikitu beharra dago, dagoeneko bulkanizatuta baitago, 3-1 irudian erakusten den moduan.

3-1 irudia. Birrindutako kautxu birziklatua

Giro tenperaturan LLDPEa solidoa da, 3-2 irudian ikus daitekeenez, baina estrusio makinan sartzean, tenperatura altuetan likidotu egiten da. Makinatik ateratzean, solido bihurtzen da berriz ere, kautxu zatiekin itsatsiz.

3-2 irudia. LLDPEa estrusionatu aurretik.

3-3 irudia. TiO_2 koloragarri gisa

Hiru osagaiak 3-4 irudian erakusten den nahasgailuan sartu eta zenbait minutuz birarazten dira, ahalik eta nahasketa homogeneoena lortzeko.

3-4 irudia. Nahasgailua

Estrusio lehorra egin da, 160°C-tan.

Nahasketa hori estrusio makinan sartu da (3-5 irudian), eta bertan LLDPEa urtu eta kautxuarekin nahasi da, estrusio makinaren biraketen eta barneko tenperaturaren eraginez.

3-5 irudia. Estrusio makina

Lortutako nahasketa erraza da maneiatzen. Eskuekin hartu eta moldean gogortu edo trinkotu da.

3-6 irudia. Nahasketa

Probetan lortu nahi den dentsitatearen arabera, 3-6 irudiko nahasketa gehiago edo gutxiago estutu behar da. Behin moldea bete ondoren, 24 orduz utzi da giro tenperaturan probeta hoztu dadin. Denbora hori igaro ostean, probeta eginda dago, saiakuntzetarako prest.

3.3 HIRU NAHASTE DESBERDINEN SORKETA

3.3.1 Lehen kasua 90/10

Fabrikatu den nahasketa honela osatu da: %87 kautxua, %10 LLDPE eta %3 TiO_2. 28 zilindroko sorta erabili da; 60 mm-ko diametro nominala eta 70 mm-ko lodiera/altuera dute eta probeta "handiak" deritze. Lau taldetan banatu dira dentsitatearen arabera: 0,7, 0,8, 0,9 eta 1 g/cm^3 (aztertutako dentsitate tartea 0,68-1,03 g/cm^3 izan da). 3-7 irudian, probeta horietako bat ikus daiteke. Saiakuntzak MTS 819.10 makina serbo-hidrauliko batean egin dira, lau abiaduratan: abiadura bat (0,004 m/s) analisi kuasiestatikorako, 0,057 s^{-1}-ko deformazio abiadura eraginez, eta hiru abiadura (0,04 m/s, 0,4 m/s eta 4 m/s) analisi dinamikorako, 0,57, 5,7 eta 57 s^{-1}-ko deformazio abiadurak eraginez hurrenez hurren. Horrek ahalbidetzen du materialaren portaera zehaztea deformazio abiadura ertain-txikietan, ingeniaritzan hainbat aplikazio izango dituena, nahiz eta ez dituen biltzen gerta daitezkeen talka guztietarako deformazio abiadurak. Abiadura bakoitzean dentsitate bakoitzeko bi probeta frogatu dira, abiadura handienean izan ezik, hor probeta bakarra frogatu baita.

Bestalde, 28 zilindroko beste sorta bat erabili da; 30 mm-ko diametro nominala eta 40 mm-ko lodiera dute probetek eta probeta "txikiak" deritze. Sorta hori ere talde berdinetan banatu da dentsitatearen arabera, eta saiakuntzak egiteko makinaren abiadurak berberak izan dira, deformazio abiadura hauek eraginez: analisi kuasiestatikorako 0,1 s^{-1} eta analisi dinamikorako 1, 10 eta 100 s^{-1} hurrenez hurren.

Eskuratutako datu fitxategiak honela izendatuta daude: probeta handietan, fitxategiaren izena G-rekin hasten da, *G_speed_densityA* deritzo hain zuzen ere (edo B-rekin amaitzen da dentsitate bereko bi probeta badaude; eta abiadura m/s-tan dago); eta lagin txikietan, izena antzekoa da, baina *p* letraz hasten da.

Hurrengo adibideetan, 0,7 g/cm^3-ko dentsitateko probeta handiei dagozkien fitxategi batzuen izenak azaltzen dira:

G_0.004_0.73B: probeta handia (G) + 0,004 m/s-ko makina abiadura + 0,73 g/cm^3-ko dentsitatea + B lagina

G_0.4_0.72A: probeta handia (G) + 0,4 m/s-ko makina abiadura + 0,72 g/cm^3-ko dentsitatea + A lagina

G_4_0.73A: probeta handia (G) + 4 m/s-ko makina abiadura + 0,73 g/cm^3-ko dentsitatea + A lagina

Jarraian, bi taula txertatu dira –bata probeta handietarako eta bestea txikietarako–, dentsitate eta abiadura guztiekin:

3-2 taula. Frogatutako probeta handien zerrenda, 90/10 proportzioan

(0,7 eta 1 g/cm^3 bitarteko dentsitateak eta 0,004 eta 4 m/s bitarteko abiadurak)

PROBETA HANDIAK												
d=0.7 g/cm^3			d= 0.8 g/cm^3			d=0.9 g/cm^3			d=1 g/cm^3		
0.004	m/s	0.73B	0.004	m/s	0.82A 0.83A	0.004	m/s	0.92A 0.93A	0.004	m/s	1.01A 1.03A
0.04	m/s	0.72A 0.72B	0.04	m/s	0.83A 0.83B	0.04	m/s	0.92A 0.92B	0.04	m/s	1A 1.01A
0.4	m/s	0.72A 0.73A	0.4	m/s	0.82A 0.83A	0.4	m/s	0.93A 0.93B	0.4	m/s	1.02A 1.03A
4	m/s	0.73A	4	m/s	0.83A	4	m/s	0.93A	4	m/s	1.02A

3-3 taula. Frogatutako probeta txikien zerrenda, 90/10 proportzioan

(0,7 eta 1 g/cm^3 bitarteko dentsitateak eta 0,004 eta 4 m/s bitarteko abiadurak)

PROBETA TXIKIAK												
d=0.7 g/cm^3			d= 0.8 g/cm^3			d=0.9 g/cm^3			d=1 g/cm^3		
0.004	m/s	0.68A 0.71A	0.004	m/s	0.77A	0.004	m/s	0.89A 0.91A	0.004	m/s	0.97A 0.99A
0.04	m/s	0.72A 0.72B	0.04	m/s	0.78A 0.79A	0.04	m/s	0.90A 0.91A	0.04	m/s	1A 1.03A
0.4	m/s	0.72A 0.72B	0.4	m/s	0.82A 0.82B	0.4	m/s	0.90A 0.91A	0.4	m/s	1.01A 1.02A
			4	m/s	0.82A	4	m/s	0.92A	4	m/s	0.99A

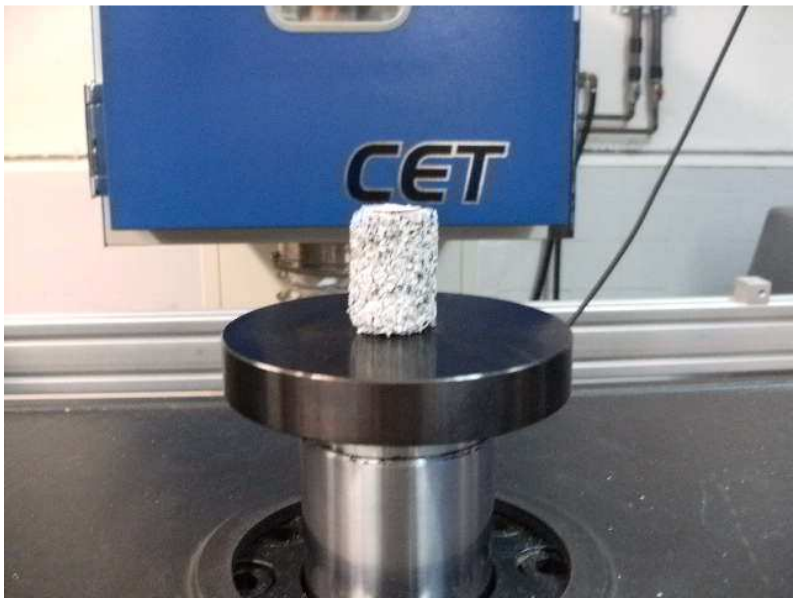

3-7 irudia. Kautxu birziklatuaren lagina

3.3.2 Bigarren kasua 75/25

Fabrikatu den nahasketa honela osatu da: % 72 kautxua, % 25 LLDPE eta % 3 TiO_2. Probeta handietarako, 11 zilindroko sorta erabili da, 60 mm-ko diametro nominala eta 70 mm-ko lodiera dituena. Probeta txikietarako, aldiz, 16 zilindroko sorta erabili da, 30 mm-ko diametro nominala eta 40 mm-ko lodiera dituena. Lau taldetan banatu dira dentsitatearen arabera: 0,7, 0,8, 0,9 eta 1 g/cm^3. Makina serbo-hidrauliko berean egin dira saiakuntzak, lau

abiaduratan: abiadura bat (0,004 m/s) analisi kuasiestatikorako eta hiru abiadura (0,04 m/s, 0,4 m/s eta 4 m/s) analisi dinamikorako.

3-4 taula. Frogatutako probeta handien zerrenda, 75/25 proportzioan

PROBETA HANDIAK								
d=0.7 g/cm^3			d= 0.8 g/cm^3			d=0.9 g/cm^3		
0.004	m/s	0.76	0.004	m/s	0.86	0.004	m/s	0.96
0.04	m/s	0.77	0.04	m/s	0.87	0.04	m/s	0.95
0.4	m/s	0.75	0.4	m/s	0.86	0.4	m/s	0.96
4	m/s	0.77	4	m/s	0.85			

3-5 taula. Frogatutako probeta txikien zerrenda, 75/25 proportzioan.

PROBETA TXIKIAK											
d=0.7 g/cm^3			d= 0.8 g/cm^3			d=0.9 g/cm^3			d=1 g/cm^3		
0.004	m/s	0.76	0.004	m/s	0.87	0.004	m/s	0.94	0.004	m/s	1.05
0.04	m/s	0.74	0.04	m/s	0.86	0.04	m/s	0.93	0.04	m/s	1.03
0.4	m/s	0.77	0.4	m/s	0.86	0.4	m/s	0.97	0.4	m/s	1.07
4	m/s	0.73	4	m/s	0.83	4	m/s	0.93	4	m/s	1.07

3.3.3 Hirugarren kasua 60/40

Fabrikatu den nahasketa honela osatu da: % 57 kautxua, % 40 LLDPE eta % 3 TiO_2. Probeta txikietarako, 16 zilindroko sorta erabili da, 30 mm-ko diametro nominala eta 40 mm-ko lodiera dituena. Lau taldetan banatu dira dentsitatearen arabera: 0,7, 0,8, 0,9 eta 1 g/cm^3. Makina serbo-hidrauliko berean egin dira saiakuntzak, lau abiaduratan: abiadura bat (0,004 m/s) analisi kuasiestatikorako eta hiru abiadura (0,04 m/s, 0.4 m/s eta 4 m/s) analisi dinamikorako.

3-6 taula. Frogatutako probeta txikien zerrenda, 60/40 proportzioan

PROBETA TXIKIAK											
d=0.7 g g/cm^3			d= 0.8 g/cm^3			d=0.9 g/cm^3			d=1 g/cm^3		
0.004	m/s	0.74	0.004	m/s	0.84	0.004	m/s	0.96	0.004	m/s	1.04
0.04	m/s	0.76	0.04	m/s	0.84	0.04	m/s	0.95	0.04	m/s	1.04
0.4	m/s	0.74	0.4	m/s	0.86	0.4	m/s	0.95	0.4	m/s	1.05
4	m/s	0.75	4	m/s	0.84	4	m/s	0.93	4	m/s	1.04

3.4 DEFORMAZIO ABIADURA HANDIKO KONPRESIO SAIAKUNTZETARAKO METODOLOGIAK. SAIAKUNTZA MAKINAREN DESKRIPZIOA

3.4.1 Existitzen diren arauak

Lehenik eta behin, literaturan proposatu diren saiakuntza kuasiestatiko eta dinamiko batzuk aurkeztuko dira.

Konpresio kuasiestatikoko saiakuntzetarako arau ugari proposatzen dituzte honako hauek: ASTM (ASTM D571-95) ASTM D945, ISO (ISO 7743) eta UNE (UNE 53536:2001). Saiakuntzaren abiaduren balioa 12±0,3 mm/min-koa da UNEn eta ASTMn; aldiz, 10 mm/min-koa da ISOn. Saiakuntzarako probeta zilindrikoa da, 28,6±0,1 mm eta 29±0,5 mm bitarteko diametroa eta 12,5±0,5 mm-ko altuera dituena kasu guztietan.

Saiakuntza prozedura horien arteko desberdintasun nagusia da ISOn saiakuntza makinarekin kontaktuan dauden gainazalak lubrifikatuta egon behar dutela. Saiakuntzako piezak lubrifikatuta badaude, konpresioa homogeneoa da. Lubrikazio barik espezimenaren barril efektua eman liteke, eta honen ondorioz, barne tenstio altuak sor litezke, ez direnak natura uniaxialekoak.

Guztiek esaten dute probetek saiakuntzako tenperatura estandarretan egon behar luketela denbora tarte batez neurketa eta saiakuntza egin aurretik. ASTMn eta ISOn denbora tarte hori gutxienez 3 ordukoa da, eta UNEn soilik 30 minutukoa.

Saiakuntza dinamikoak: a) bibrazio behartu ez-erresonatzaileko saiakuntzak, b) bibrazio behartu erresonatzaileko saiakuntzak, c) bibrazio askeko metodoak, eta d) uhin hedapeneko metodoak.

3.4.2 Saiakuntzetan aplikaturiko metodologia

Deformazio abiadura handiko konpresio saiakuntzetan, makina-burua 4 abiaduratan (V) jarri da: 0,004, 0,04, 0,4 eta 4 m/s. Abiadura bakoitzean, dentsitate bakoitzeko bi probeta frogatu dira, abiadura handienean izan ezik, hor probeta bakarra frogatu baita. Horrela, 4 deformazio abiadura $\dot{\varepsilon}$ lortu dira probeten luzera bakoitzeko ($\dot{\varepsilon} = \frac{V}{L_o}$):

3-7 taula. Deformazio abiadurak probeten bi dimentsioetarako

	$\dot{\varepsilon}$ (s^{-1})			
Probeta handiak ($L_0 = 70mm$)	0.057	0.57	5.7	57
Probeta txikiak ($L_0 = 40mm$)	0.1	1	10	100

Saiakuntza prozeduran makinaren desplazamendua antzematen da: laginaren azken altuera 21,5 mm-tan ezartzen du, hasierako altuera 40,5 mm-koa denean (probeta txikiak, hau da, deformazioa $\varepsilon = \frac{\Delta L}{L} = \frac{40.5 - 21.5}{40.5} = 0.469$ eta azken altuera 38,4 mm-tan jartzen du 69,5 mm-ko hasierako altuera duten probetetan (probeta handiak; deformazioa $\varepsilon = \frac{\Delta L}{L} = \frac{69.5 - 38.4}{69.5} = 0.447$). Saiakuntza makinako segurtasun arrazoiak direla-eta, ezin izan da saiakuntza egin deformazio maila handiagoetan.

Beraz, aztertutako deformazio abiadurak aldatu egiten dira: probeta handietan 0.057 s^{-1} ($\dot{\varepsilon} = \frac{v}{L} = \frac{0.004\ m/s}{0.070\ m}$)-tik 57.14 s^{-1} ($\frac{4\ m/s}{0.070\ m}$)-ra eta probeta txikietan 0.1s^{-1} tik 100 s^{-1}-ra.

Ez da saiakuntzen aurre-baldintzatzerik egin saiakuntzaren aurretik. Hala ere, ez da agertu barril itxurarik probetetan saiakuntzak egin bitartean. Beraz, gertakari hori albo batera utz daiteke zehaztasuna galdu gabe.

Saiakuntzaren emaitzak neurtu eta datuak erregistratu egin dira datuak hartzeko sistema baten bidez. Saiakuntza gelako batez besteko tenperatura 25 ºC-koa izan da.

3.4.3 Saiakuntza makinaren deskripzioa

Talkekiko erresistentzia kasuek oro har eskatzen dute hiru motatako saiakuntza sistemak ezartzea deformazio abiaduraren arabera. Egoera kuasiestatikoetan eta 0,1/s-tik beherako deformazio abiaduretan frogak egiteko, ohiko karga bastidoreak erabili beharko lirateke, izan mekanikoak edo izan serbohidraulikoak. 0,1/s-tik gorako deformazio abiaduretan, makina serbohidraulikoak eta barra motako makinak erabili beharko lirateke. Mota

serbohidraulikoko sistemek normalean 0,1 eta 500/s bitarteko (kasu berezietan 1000/s-ra iritsiz) deformazio abiadurak hartzen dituzte. Bestalde, barra motako sistemek 100 eta 1000/s bitarteko eta hortik goragoko deformazio abiadurak hartzen dituzte. 3-8 irudian[96], modu eskematikoan dago azalduta hiru saiakuntza sistemetarako deformazio abiaduren tartea.

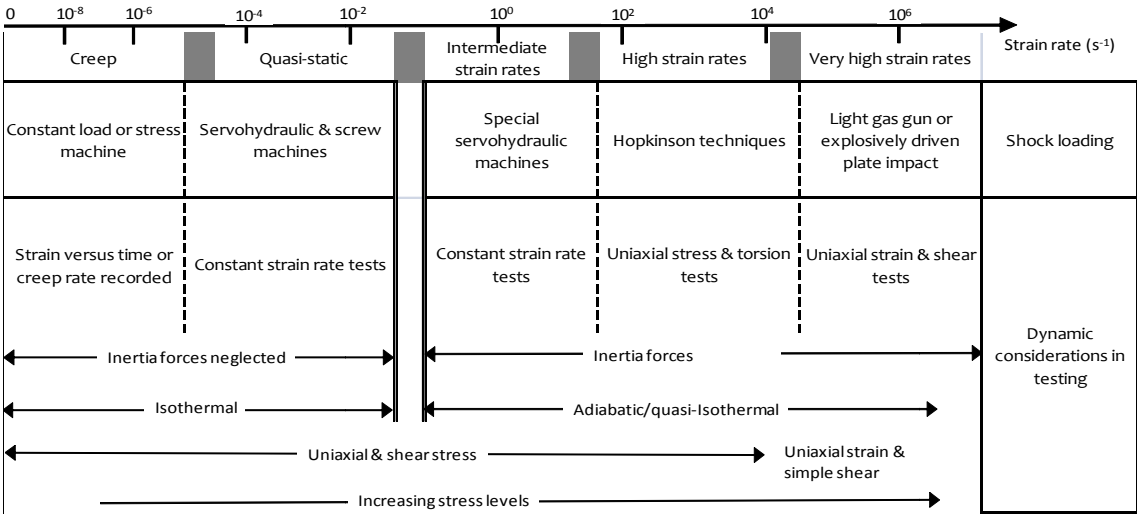

3-8 irudia. Froga mekanikoen alderdi dinamikoak

3-9 irudian, ikerketa honetan erabilitako MTS 819.10 abiadura handiko saiakuntza sistema serbohidraulikoaren argazkia dago. Makina horretan, saiakuntza estatikoak, dinamikoak eta abiadura handikoak (18 m/s-rainokoak) egin daitezke.

3-9 irudia. MTS abiadura handiko saiakuntza sistema, LEARTIKEReko saiakuntza mekanikoen laborategian

Ezinbestekoa da espezimenaren luzeran gertaturiko aldaketekin lotuta dagoen kargaren indarra neurtzea, saiakuntza uniaxialen bitartez material baten portaera mekanikoa

deskribatzeko. Ondorioz, hornituta dago, batetik, funtzionamenduan aplikatutako indarrak neurtzeko Kistler[97] markako 60 kN-ko karga zelula piezoelektriko batez eta, bestetik, aktuadorearen desplazamendua neurtzeko sentsore magnetostriktibo batez (Temposonics®), historikoki erabili den LVDT kontzeptua ordezkatuz.

Datuak hartzeko, National Instrument-eko PCI 6110 txartela erabili zen: 5.000.000 puntu/segunduko abiaduran erregistratzen ditu datuak. Saiakuntza esperimentaletako emaitzak hurrengo atalean azaltzen dira.

3.5 EMAITZAK ETA EZTABAIDA

3.5.1 90/10 proportzioa

Probetetan ez denez antzeman barril efekturik, ondoriozta daiteke deformazio eremua homegeneoa izan dela saiakuntzetan zehar.

3-10 irudian, 0,9 g/cm^3-ko dentsitateko probeta handiei dagozkien konpresio saiakuntzen emaitzak azaltzen dira modu grafikoan:

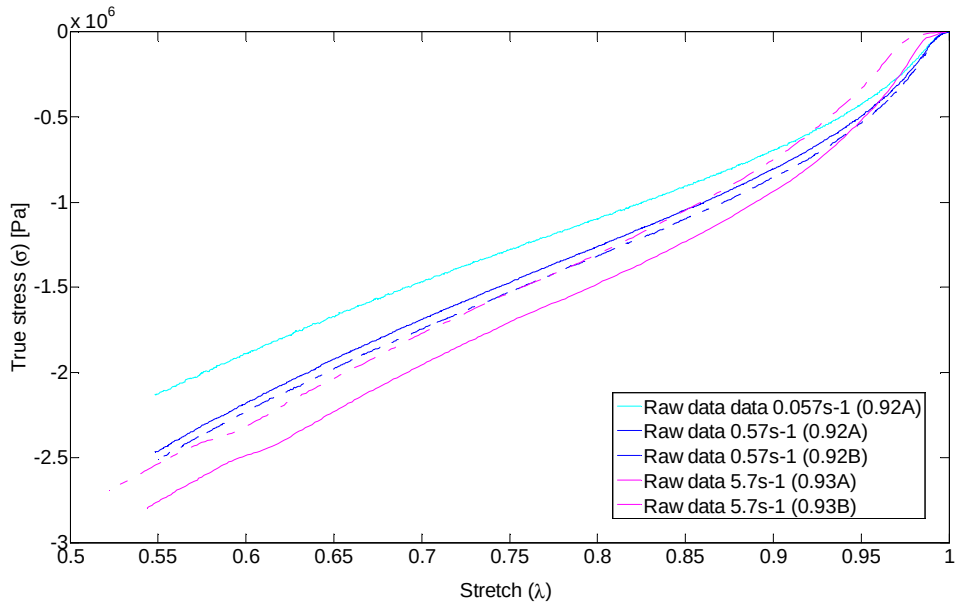

3-10 irudia. Tentsio-luzapen kurbak 0,9 g/cm^3-ko dentsitaterako, deformazio abiadura desberdinetan (probeta HANDIAK, 90/10 proportzioa). Parentesi artean, benetako dentsitatea eta frogatutako probeta (A edo B) daude adierazita.

Irudiak erakusten du konpresiopean zein den kautxuaren portaera. Kurba bakoitza deformazio abiadura bati dagokio; hiru deformazio abiadura azaltzen dira (0,057, 0,57 eta 5,7 s^{-1}), eta kolore bereko kurbek deformazio abiadura berbera daukate. Deformazio (luzapen) jakin baterako, tentsioaren balioak askoz ere altuagoak dira deformazio abiadura handiagoen eraginpean, deformazio abiadura txikien eraginpean baino. Bestalde, kurben ez-linealtasuna areagotu egiten da deformazio abiadura handiagoetan, hau da, modulu elastikoa aldagarria da eta luzapenarekin areagotzen da, material hiperelastikoekin gertatu ohi den bezala. Efektu biskoelastiko ez-lineal esanguratsua antzeman daiteke kargaren historian; izan ere, tentsioa ez da linealki areagotzen deformazio abiadurarekin. Tentsio-luzapen kurba desberdinen kurbadura aldatzeak nabarmentzen du efektu hori. 0,7 g/cm^3, 0,8 g/cm^3 eta 1 g/cm^3-ko dentsitateei dagozkien konpresio saiakuntzek efektu hori erakusten dute, hurrenez hurren **¡Error! No se encuentra el origen de la referencia.** irudian, **¡Error! No se encuentra el origen de la referencia.** irudian eta **¡Error! No se encuentra el origen de la referencia.** irudian azaltzen den bezala.

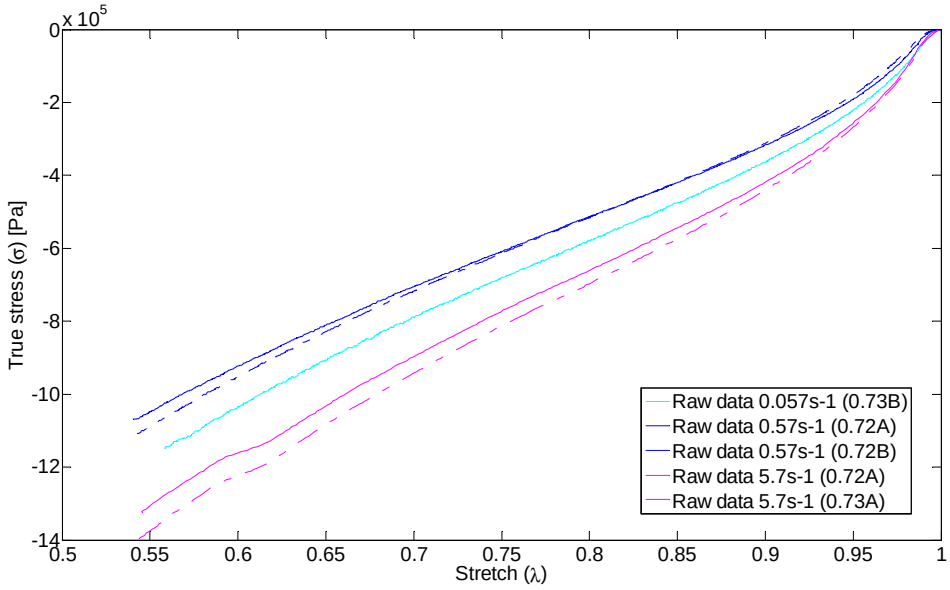

3-11 irudia. Tentsio-luzapen kurbak 0,7 g/cm^3-ko dentsitaterako, hainbat deformazio abiaduratan (probeta HANDIAK, 90/10 proportzioa). Parentesi artean, benetako dentsitatea eta frogatutako probeta (A edo B) daude adierazita.

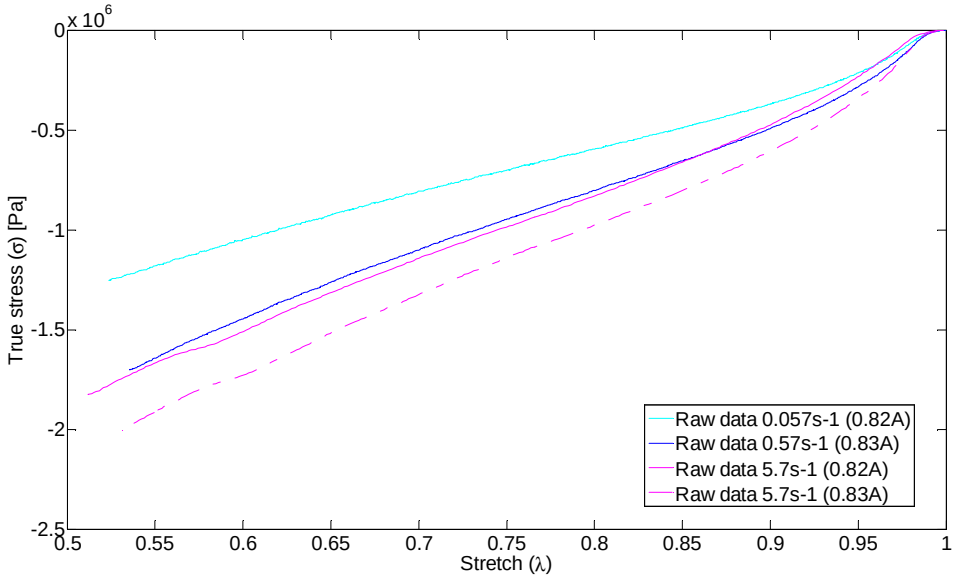

3-12 irudia. Tentsio-luzapen kurbak 0,8 g/cm^3-ko dentsitaterako, hainbat deformazio abiaduratan (probeta HANDIAK, 90/10 proportzioa).

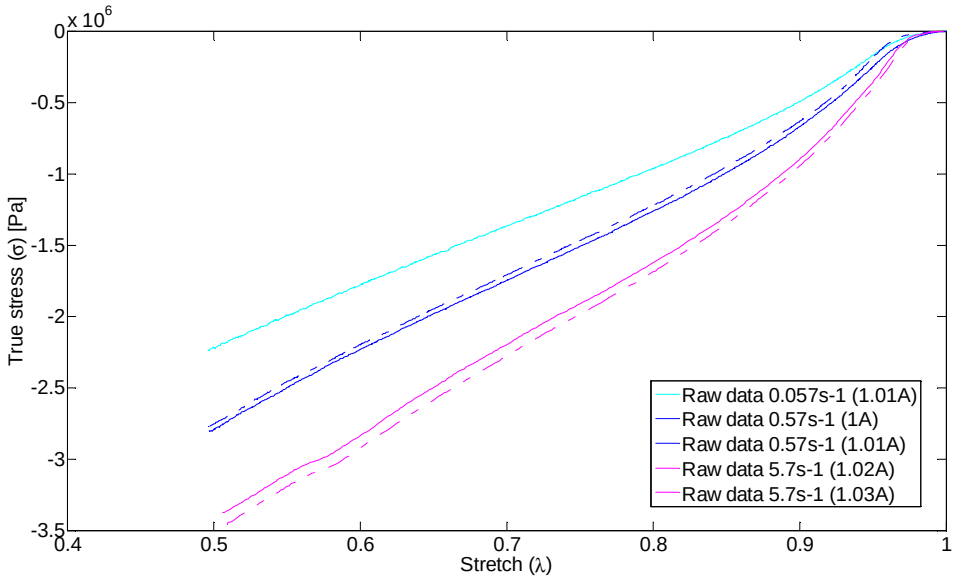

3-13 irudia. Tentsio-luzapen kurbak 1 g/cm^3-ko dentsitaterako, hainbat deformazio abiaduratan (lagin HANDIAK, 90/10 proportzioa).

Jarraian, probeta txikiei dagozkien saiakuntzen emaitzak azaltzen dira:

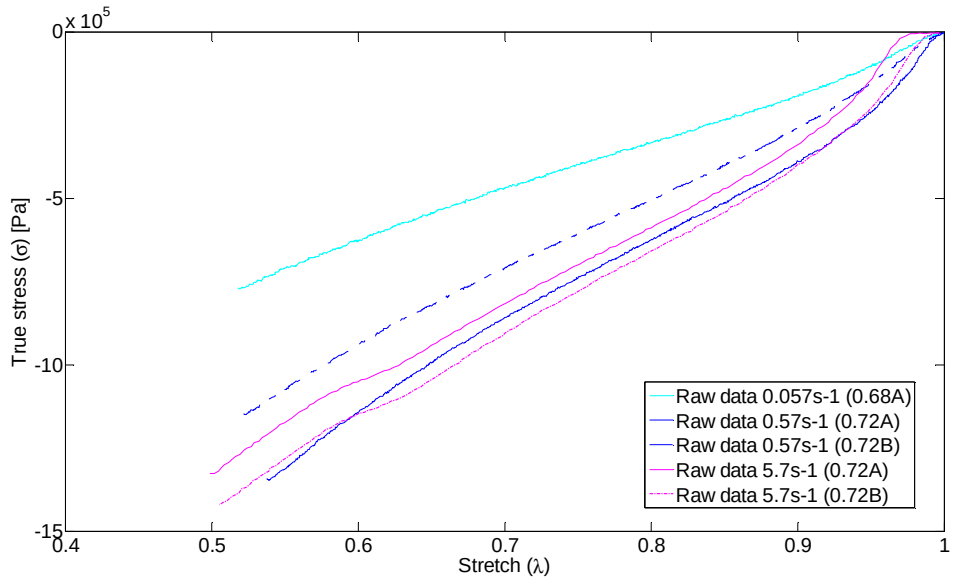

3-14 irudia. Tentsio-luzapen kurbak 0,7 g/cm^3-ko dentsitaterako, hainbat deformazio abiaduratan (lagin TXIKIAK, 90/10 proportzioa). Parentesi artean, benetako dentsitatea eta frogatutako lagina (A edo B) daude adierazita.

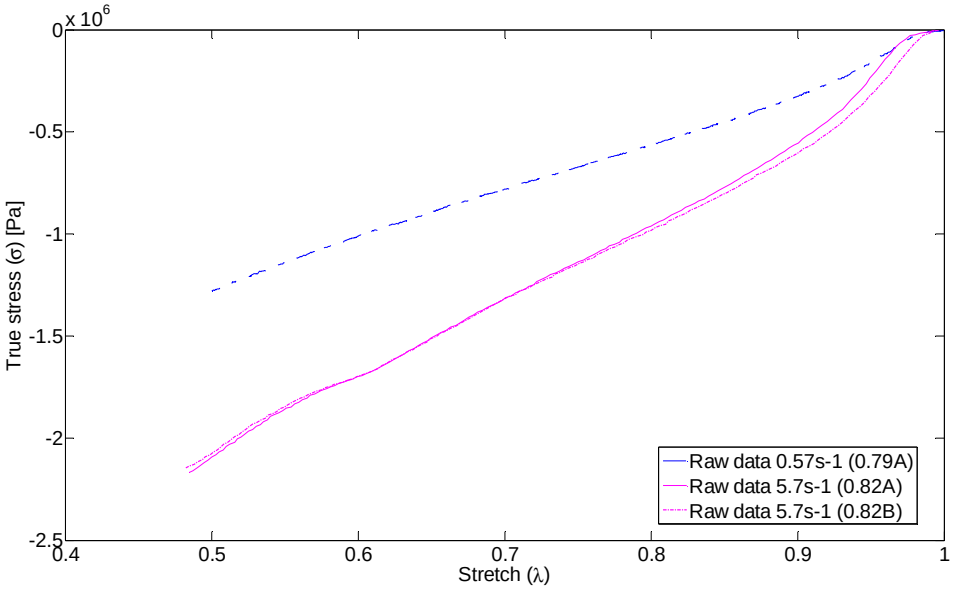

3-15 irudia. Tentsio-luzapen kurbak 0,8 g/cm^3-ko dentsitaterako, hainbat deformazio abiaduratan (lagin TXIKIAK, 90/10 proportzioa). Parentesi artean, benetako dentsitatea eta frogatutako lagina (A edo B) daude adierazita.

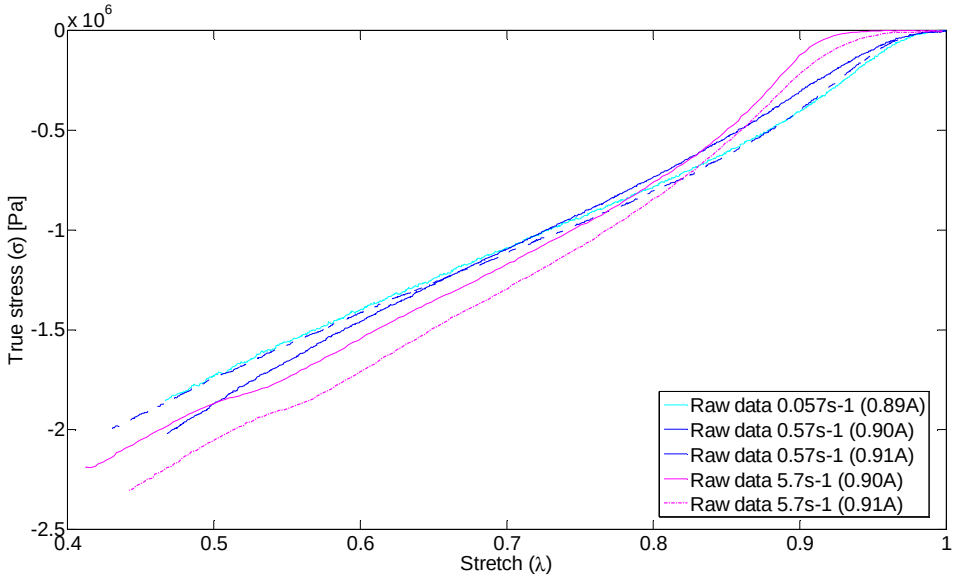

3-16 irudia. Tentsio-luzapen kurbak 0,9 g/cm^3-ko dentsitaterako, hainbat deformazio abiaduratan (lagin TXIKIAK, 90/10 proportzioa).

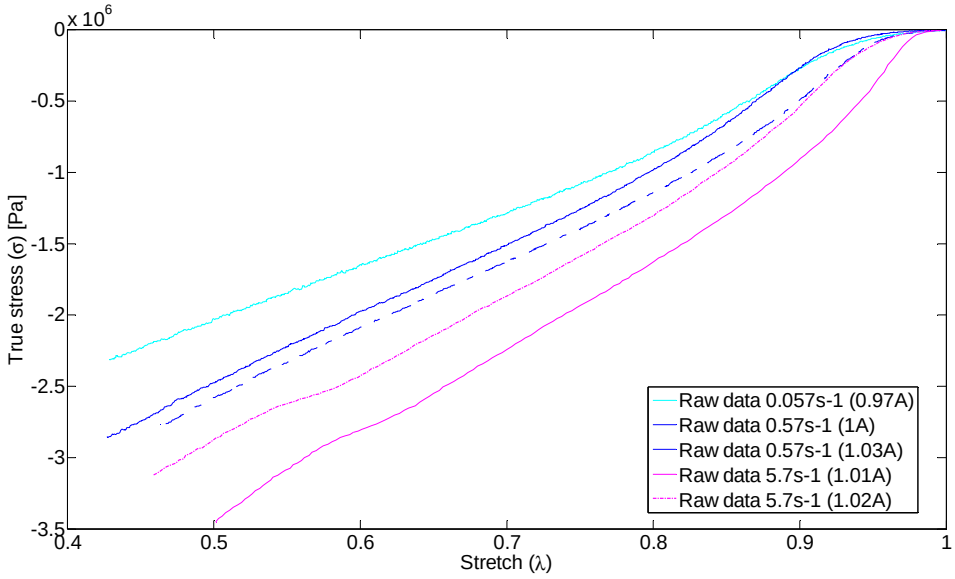

3-17 irudia. Tentsio-luzapen kurbak 1 g/cm^3-ko dentsitaterako, hainbat deformazio abiaduratan (lagin TXIKIAK, 90/10 proportzioa).

3-11 iruditik3-17 irudira, 3-10 irudiarekin konparatuz, joera berdinak ikusi dira, hau da, materialen joera hiperelastikoa nabarmendu daiteke tentsio-luzapen erlazio ez linealean. Baita ere agertzen da kurben kurbaturetan desplazamendu bat, itxura biskoelastiko ez

lineala erakusten duena. Izan ere, tentsioa ez da linealki handitzen deformazio abiadurarekin. Hurrengo taulan aurreko emaitzak daude laburbilduta:

3-8 taula. Tentsio-luzapen kurbak probeta handientzat 0.7 g/cm^3, 0.8 g/cm^3, 0.9 g/cm^3 eta 1 g/cm^3 dentsitateentzat

PROBETA HANDIAK	
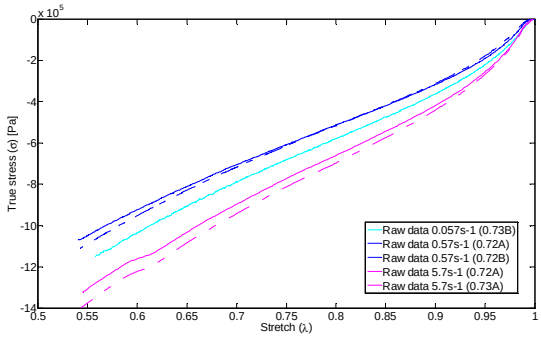 (a)	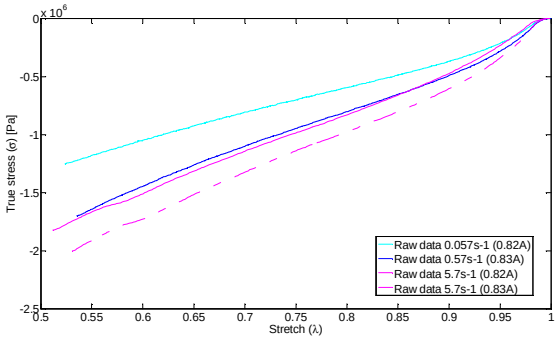 (b)
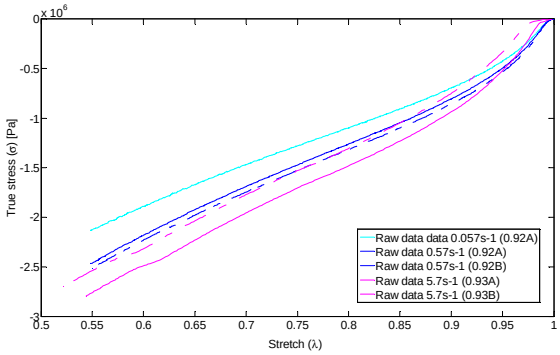 (c)	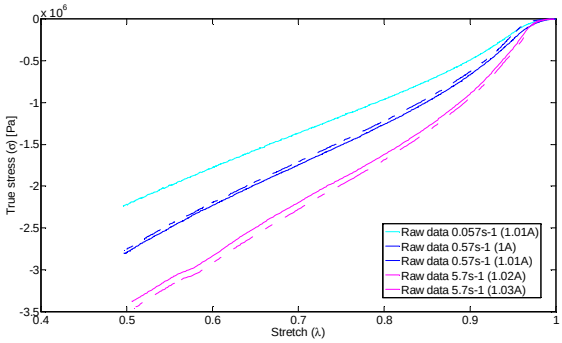 (d)

Ikus daitekeenez, 0,7 g/cm^3-ko dentsitateko (a) kasuan izan ezik, deformazio abiadurak modu progresiboan aldatzen dira. Kasu guztietan (dentsitate guztietan) azaltzen da portaera hiper-biskoelastikoa.

3-9 taula. Tentsio-luzapen kurbak probeta txikientzat eta 0.7 g/cm^3, 0.8 g/cm^3, 0.9 g/cm^3 eta 1 g/cm^3 dentsitateentzat (90/10 proportzioa)

PROBETA TXIKIAK	
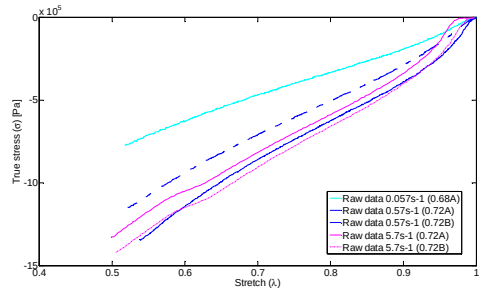 (a)	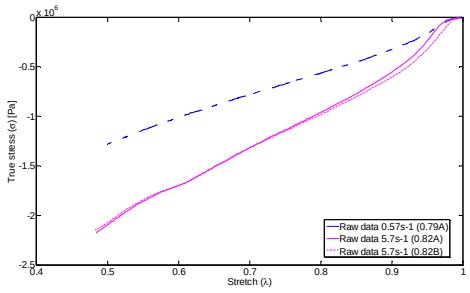 (b)
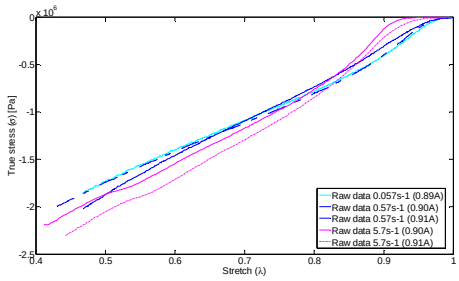 (c)	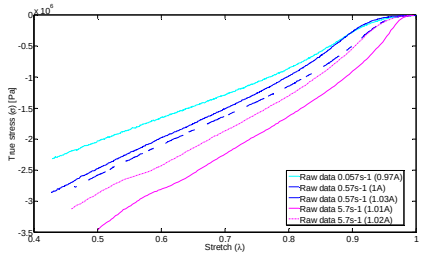 (d)

Ondoren, 3-18 irudiak probeta handi eta txikien tentsio-luzapen diagramak erakusten ditu deformazio abiadura desberdinentzat, 1 g/cm^3 dentsitatearen kasurako. Ikus daitekeenez, deformazio abiadura berdinarentzat, hau da, kolore berdindun kurbentzat, luzapenaren balio batentzat tentsioa oso antzerakoa da, itxaroten zen moduan. Hortaz, tamainaren eragina ez dela horren garrantzitsua ondoriozta daiteke.

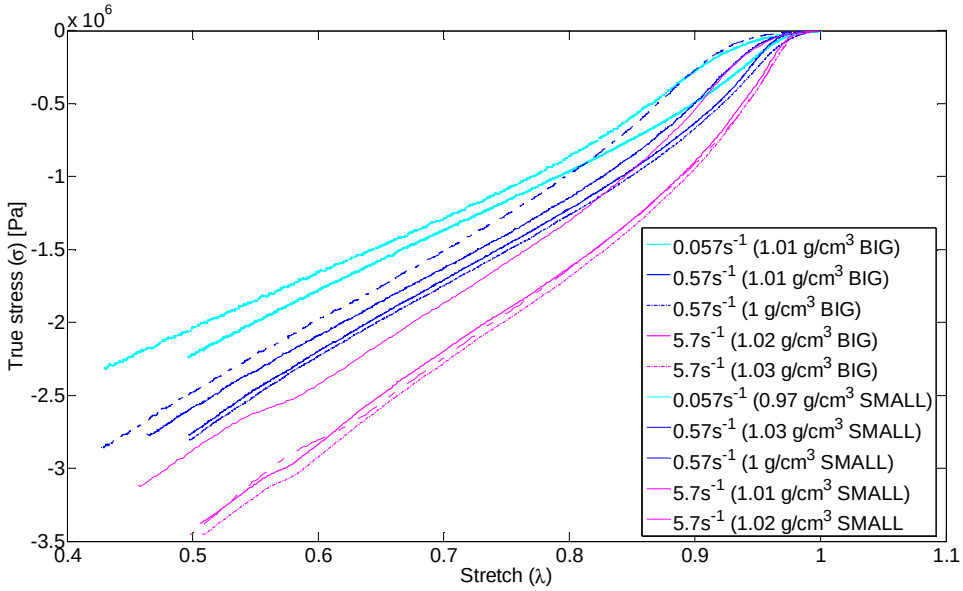

3-18 irudia. Lagin handien eta txikien tentsio-luzapen kurbak 1 g/cm^3-ko dentsitaterako, hainbat deformazio abiaduratan (90/10 proportzioa).

Material honen aplikazioan probeta handiak nahiago dira aplikazio potentziala kontsideratzen bada, kautxu birziklatu gehiago daukatelako eta hesien estalduren antz handiagoa dutelako.

Jarraian ageri den grafikoa ere interesgarria da, deformazio abiadura bera duten dentsitateak alderatzen baitira.

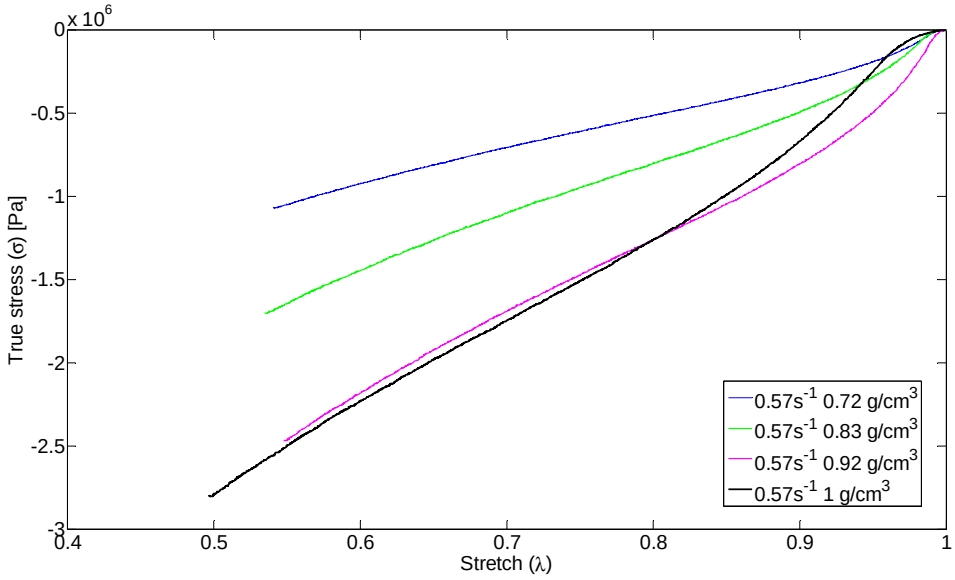

3-19 irudia. Tentsio-luzapen kurbak 0,7, 0,8, 0,9 eta 1 g/cm^3-ko dentsitateetarako, 0,57 s^{-1}-ko deformazio abiaduran (90/10 proportzioa)

3-19 irudian ikus daitekenez, dentsitate handiagoko materialak eremu zabalagoa du kurba azpian. Horrenbestez, interesgarria litzateke dentsitate handiagoko material bat erabiltzea errepideetako hesiak estaltzeko, talkan energia gehiago xurga dezan.

3.5.2 75/25 proportzioa

0.7 g/cm^3, 0.8 g/cm^3 eta 0.9 g/cm^3 dentsitateei dagozkien konpresiozko saiakuntzak ondoko tauletan laburbiltzen dira, lehendabizi probeta handientzat eta ostean probeta txikientzat; 1 g/cm^3 dentsitateari dagozkion emaitzak, probeta txikien kasurako, bigarren taula horretan aurki daitezke.

3-10 taula. Tentsio-luzapen kurbak probeta handientzat eta 0.7 , 0.8 eta 0.9 g/cm^3 dentsitateentzat (75/25 proportzioa)

PROBETA HANDIAK	
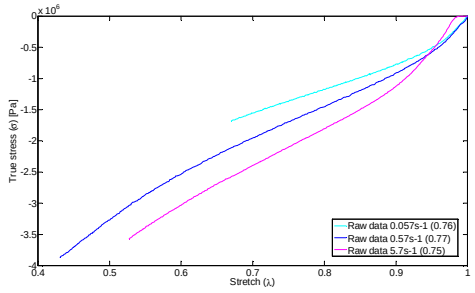 (a)	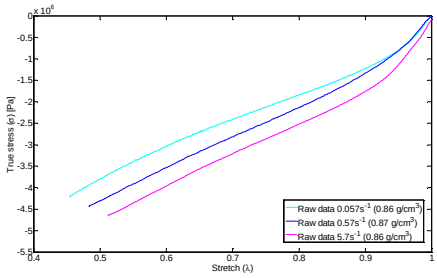 (b)
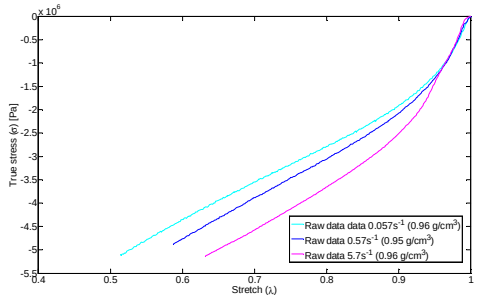 (c)	
Deformazio abiadurak progresiboki aldatuz doazela ikus daiteke. Kasu guztietan (dentsitate guztiak) portaera hiper-biskoelastikoa erakusten da.	

3-11 taula. Tentsio-luzapen kurbak probeta txikientzat eta 0.7, 0.8, 0.9 eta 1 g/cm^3 dentsitateentzat (75/25 proportzioa)

PROBETA TXIKIAK	
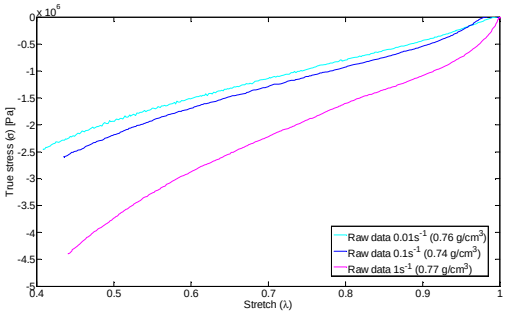 (a)	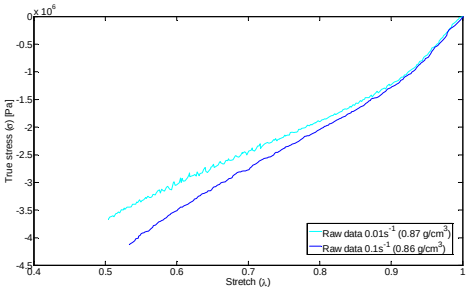 (b)
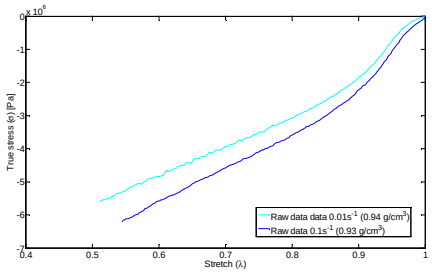 (c)	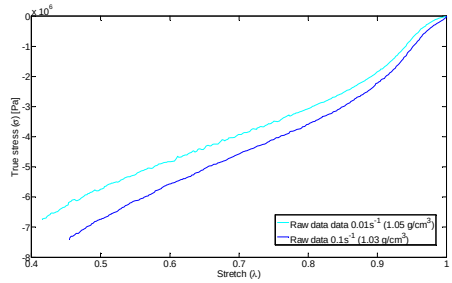 (d)

Ondoren, bi irudik 0.9 g/cm^3 dentsitateko probetak konparatzen dituzte, 3-20 irudiak 75/25 eta 90/10 proportzioak, probeta handientzat, and 3-21 irudiak 60/40, 75/25 eta 90/10 proportzioak, probeta txikientzat, hurrenez-hurren.

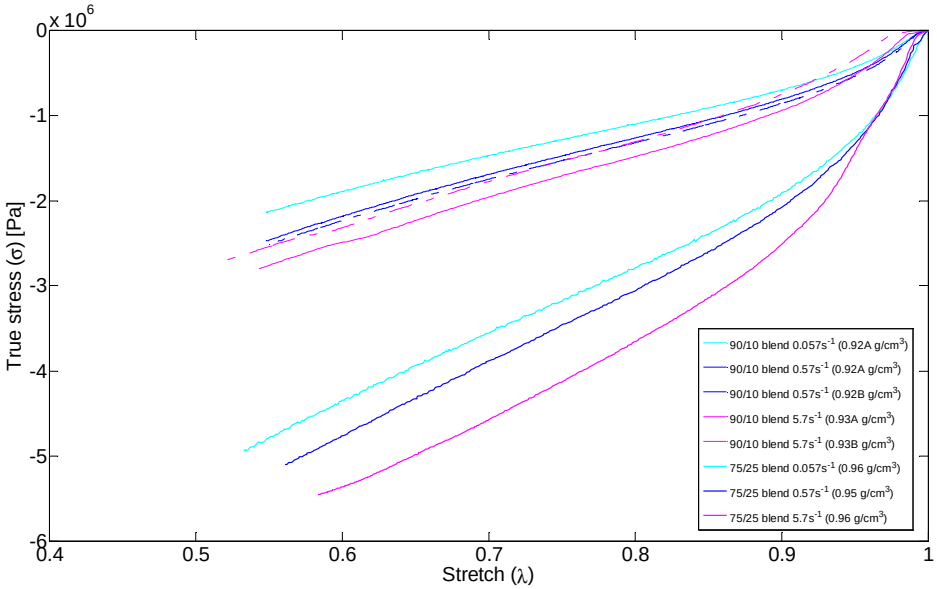

3-20 irudia. Tentsio-luzapen kurben konparaketa probeta HANDIENTZAT eta 0.9 g/cm^3 dentsitateentzat 75/25 eta 90/10 proportziodun nahasteentzat

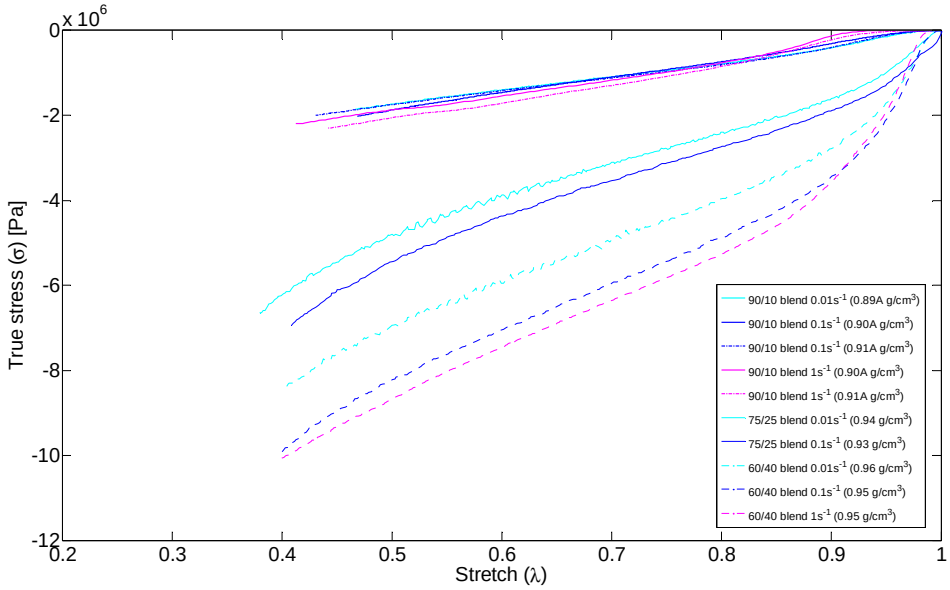

3-21 irudia. Tentsio-luzapen kurben konparaketa probeta TXIKIENTZAT eta 0.9 g/cm^3 dentsitateentzat, 60/40, 75/25 eta 90/10 proportziodun nahasteentzat

Ikus daitekeenez, zurruntasuna handituz doa PEren proportzioa nahastean handituz doan heinean; ondorioz, 60/40 proportzioa da zurruntasun handiena erakusten duena. Tentsioa 0.5 baliodun luzapen baten kasuan deformazio abiadura berdinarentzat, gutxi gora-behera 4 aldiz altuagoa da 60/40 proportziodun nahastearentzat 90/10 proportziodunarekiko, 3-21

irudian erakusten denez. Energia absorbatzeko gaitasuna nahastearen PE proportzioarekin batera handitzen da. Hala ere, konpromezuko soluzioa kontsideratu da, zeinetan ahalik eta kautxu kopuru handiena birziklatzen den, nahastearen abantailak modu nabarian galdu gabe; hortaz, 90/10 nahastea aukeratu da errepideetako hesietan estaldura moduan erabiltzeko.

3.5.3 60/40 proportzioa

0.7 g/cm^3, 0.8 g/cm^3, 0.9 g/cm^3 eta 1 g/cm^3 dentsitateei eta probeta txikiak izanik, konpresiozko saiakuntzen emaitzak ondoko taulan erakusten dira (ikusi Eranskina xehetasun gehiagorako):

3-12 taula. Tentsio-luzapen kurbak 0.7 g/cm^3, 0.8 g/cm^3, 0.9 g/cm^3 eta 1 g/cm^3 dentsitateentzat eta probeta txikiak (60/40 proportzioa)

PROBETA TXIKIAK	
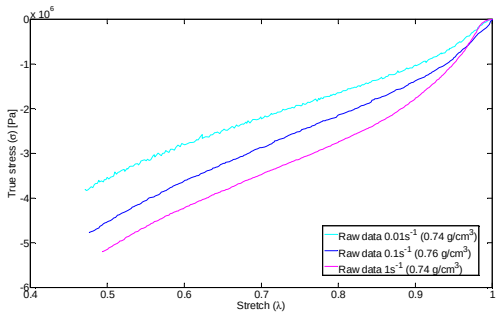 (a)	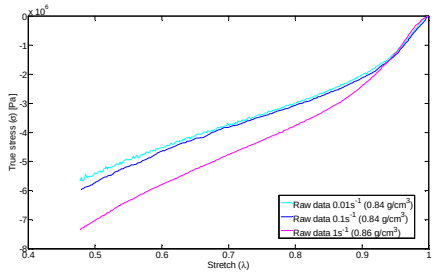 (b)
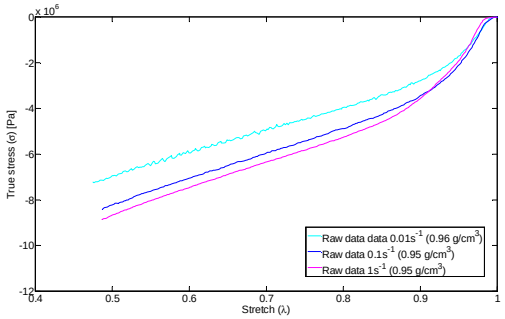 (c)	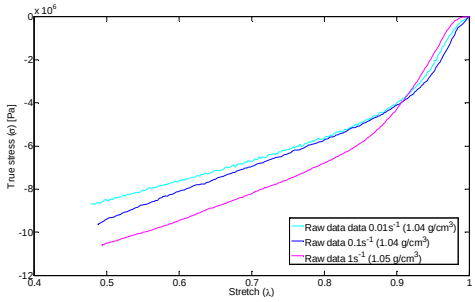 (d)

4.
EMAITZAK FILTRATZEKO METODOA

4.1 PROBLEMAREN DESKRIBAPENA

"System ringing" edo "erresonantzia-sistema" makina serbo-hidraulikoen bidez egiten diren abiadura altuko materialen saiakuntza dinamikoetan gehien eragiten duen faktoreetako bat da. Bitarteko abiaduretan burututako saiakuntzek, deformazio abiaduren 1 s^{-1}–etik 100 s^{-1}–rainoko tartean, zenbait zailtasun esperimental aurkezten dituzte[98]. Normalean, tarte horretan mugitzen den deformazio abiaduretan egiten diren saiakuntza esperimentalak abiadura handiko makina serbo-higraulikoetan egiten dira[13]. 10-60 s^{-1} bitarteko eremuan agertzen diren bibrazioak kritikoak izaten dira, lortzen diren tentsio-deformazioaren erantzunak hondatzen baitituzte. Arazo hau mota honetako saiakuntzetan materialen karakterizazio egoki bat egiteko oztopo nagusietako bat da. Bibrazio hauek, "system ringing" moduan ezagutzen direnak, saiakuntza makinaren modu nagusien eszitazioek sortuak dira eta frekuentzia natural batean ala gehiagotan oszilazioak eragiten dituzte[14], neurtutako materialaren erantzuna hondatuz (ondulazio bereizgarriak eraginez materialen kurbetan, beharrezko emaitzak zorrozki distortsionatuz).

"System ringing" honen efektu negatiboei heltzeko, neurtutako materialaren kurbei behe-paseko iragazkien teknika numerikoak aplikatu izan zaizkie nagusiki. Hala ere, praktika estandar hau kontu handiz aplikatu behar da, iragazteak zuzendutako seinaleak distortsionatzeko joera du eta[99]. Hainbat ikertzailek konfirmatu izan dute adierazpen hau beraien saiakuntzen bitartez. Dutton[100]-ek ondorioztatu zuenez, ez dago iragazkirik kurbak

leundu ditzakeenik datuak kaltetu barik, eta Rehrmann eta bestek[101] efektu negatiboak filtratutako seinaleen atzerapen bat eta fase aldaketa batean datzatela, eta baita informazio galera kargaren igoeran saiakuntzaren hasieran. Zhu eta bestek[14] iragazkiaren mozketa frekuentziaren identifikazio egokiaren garrantzia nabarmendu zuten eta, ildo berdinean, Larour[102]-ek erakutsi zuen zuzendutako seinale desberdinak aukeraturiko mozketa frekuentziaren arabera lortuak direla erakutsi zuen, emaitza finala aukeraketa subjetibo honen menpekoa dela azpimarratuz. Xia eta bestek[12] nabarmendu zuten iragazte prozesuaren zehaztasuna aukeraturiko iragazte algoritmoarekiko oso menpekoa dela, eta Bardenheier eta bestek[103] aplikaturiko iragazte algoritmoaren arabera leundutako soluzio desberdinak lortu zituzten.

Aipatutako mugak direla eta, gomendatu izan da oszilazioak beste medio batzuen bidez gutxitzea, iragazte algoritmoak esperimental datuei aplikatu aurretik[104]. Zuzenketa honek bibrazio hauek sortarazten dituzten faktoreen aurretiazko ezagutza izatera behartzen du, eta helburu honekin, beharrezkoa da makina serbo-hidraulikoaren erantzun dinamikoa modelatzea. Xiao[98] izan zen saiakuntza dinamikoetan "system ringing" hau kuantitatiboki neurtzeko eredu matematiko bat erabili zuen lehenengo autorea. Oinarrizko askatasun gradu bakarreko eredua erabili zuen (SDOF) bibrazioen anplitudeak, frekuentziak eta erortze-abiadurak iragartzeko, eta karga abiaduraren eta frekuentzia naturalaren eraginak deskribatu zituen "ringing"aren magnitudean. SDOF hau modu zabalduan erabilia izan da ondorengo laneatan erreferentziatzat hartuaz. Hala ere, ikertzaile hauetako batzuek emaitza esperimental eta analitikoen arteko desberdintasunak eman dituzte aditzera, erroreak bibrazio erantzun hau frekuentzia anitzek menperatua dagoela esleituz[14,105,106]. Hortaz, saiakuntza sistema dinamikoa Xiaok aurkeztu zuen SDOFa baino konplexuagoa da. Zhu eta bestek[14] ikerketa garatuagoa aurkeztu zuten, modu eta frekuentzia nagusiak analisi modal baten bidez antzemanez eta modu hauen garrantzia determinatuz bibrazio-erantzunean. Berriz ere, modu nagusien efektuak SDOF ereduen bidez aztertu ziren, erresonantzia-frekuentzia bakoitza bakarka kontuan hartuz. Aitortu zuten SDOF ereduak ezin dituela bibrazio-ezaugarri horiek bikoiztu eta askatasun gradu anitzeko ereduak (MDOF) bibrazio hauen estimazio hobea sortuko lukeela ondorioztatu zuten.

Azken ideia honi lotuta, lan honek abiadura altuko makina serbo-hidrauliko baten eredu dinamiko xehea aurkezten du, zeinetan hainbat bibrazio modu kontsideratu izan diren. Eredua parametro modaletan oinarritzen da, hots, moduak, frekuentzia naturalak eta moteltze faktoreak; makinarengan egindako analisi modal esperimental (EMA) baten bidez

lortuak, eta bibrazio-erantzuna simulatzeko gai dena. Denboraren eremuan simulazioak egin dira, makinaren sarrera-irteera portaera iragartzeko kautxua saiatu denean; sarrera bezala eragingailuaren bapateko kolpea espezimenaren kontra hartu da eta irteera bezala karga-zelula piezoelektrikoaren posizioko erantzuna hartuta. Simulaturiko indarren seinaleen frekuentzia edukiak antzeman ditu prozesuan parte hartzen duten frekuentzia garrantzitsuak; eta esperimentalki kautxuaren saiakuntzetan neurtutako indarren seinaleekin konparaketak iragarpen analitikoen efikazia frogatu du. Balioztatze azterketa honen ondoren, eredua hurrengo pauso batean erabili da, non simulaturiko indarren ondulazioak esperimentalki neurtutako karga-zelulako indarren seinaleei kenduz. Indarren seinale erresultanteak jatorrizko neurtutakoak baino askoz leunagoak dira eta zuzenketa prozedua azken iragazte pausoarekin burutzen da. Bi faktorek bermatzen dute azken iragazte pauso honen aplikazioa. Batetik, bibrazioen frekuentzia edukiaren ezagutzak mozketa frekuentziaren identifikazio zehatza baimentzen du, zein iragazki egoki baten diseinurako baldintza den[14]. Bestetik, iragazi beharreko datuen ondulazio txikiek posible egiten dute azken kurbak distortsio arbuiagarriarekin lortzea. Hortaz, datuak zuzendu ondoren, azken materialen kurbak lortzen dira, abiadura altuko indarra vs. denbora erreala adierazten dutena.

4.1.1 Abiadura altuko kautxuaren karakterizazioa

Erabilitako pneumatikoetako kautxu birziklatuaren karakterizaziorako egindako konpresiozko saiakuntzen artean, 4 m/s-ko eragingailuaren abiadura daukaten haiek, hau da, abiadura altuenetakoak, "ringing" erako bibrazioak sortarazten dituzte, karga-zelulen neurketak kutsatuz. 4-1 irudiak karga-zelularen konpresiozko indarra vs. denbora neurketa eta sentsore magnetostriktiboaren desplazamendua vs. denbora neurketa erakusten ditu, 4 m/s-ko abiaduran egindako saiakuntza bati dagozkionak, 60/40 proportzioko nahastearenak, espezimenaren birziklatutako kautxua %57a izanik, LLDPEa %40a eta TiO_2–a %3a.

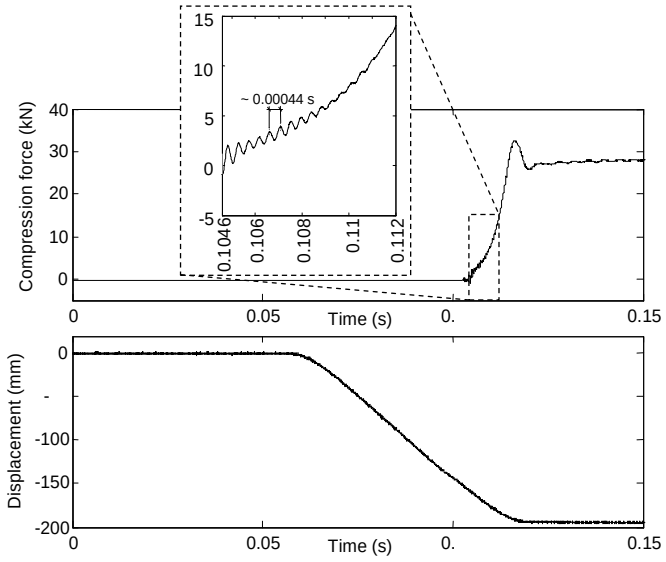

4-1 irudia. Konpresiozko indarra vs. denbora eta desplazamendua vs. denboraren neurketak.

Indarra vs. Denbora kurba hori ez da egokia materialaren karakterizaziorako, karga prozesuan nahi ez diren ondulazioak agertzen direlako (gutxi gora-behera 0.1046 s eta 0.112 s bitartean 4-1 irudian ikusten den saiakuntzan). Bibrazio hauen jatorriari eta naturari buruzko ezagutza lortzeko, bi pausoko prozedura jarraitu da. Lehenengo, frekuentzia nagusiaren hasierako estimazio bat egin izan da bi tontorren artean igarotako denboraren alderantzizkoa kalkulatuz (ikusi 4-1 irudia): $f_{estim} \approx 1/0.00044 = 2272.7\ \text{Hz}$. Bigarrenez, kalkulu zehatzago bat garatu izan da Fourierren Transformatu Azkarraren (FFT) bitartez indarraren seinalearen frekuentzia edukia ateraz. Emaitza optimoak lortzeko, transformatu honek sarrera bezala batazbesteko balio modura zeroa duen seinalea behar du, nahi ez diren frekuentziaren osagai baxuak ekiditzeko, zeinek geroago agertzen den 4-2 irudiko frekuentzia edukiaren itxura txarragotuko luketeenak. Beraz, goi-paseko iragazkia aplikatu da. Mozketa frekuentzia modura 1000 Hz hartu da, aurreko pausoan estimaturiko frekuentzia gordez. Etapa honetan iragazte algoritmoak sartzen duen distortsioa ez da garrantzitsua helburua ez delako seinale zuzendu bat lortzea, baizik eta beharrezkoa ez den informazioa kentzea; iragazkiak hau modu egokian egiten du. 4-2 irudiak FFT grafikoa aurkezten du, non frekuentzia espezifiko batetan kontribuzio altua nabarmentzen den, kontribuzio txikiagoa agertuz frekuentzia baxuago bateaan. Gertuagoko begirada batek frekuentzia nagusia 2320 Hz ingurukoa dela erakusten du, aurreko estimazioarekin bat etorriaz. Bigarren frekuentzia 1920 Hz ingurukoa da.

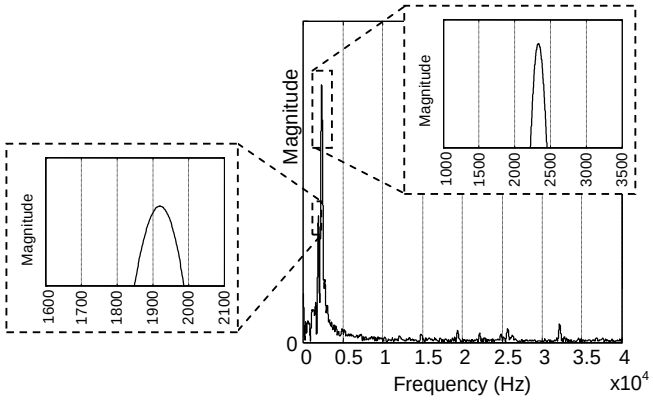

4-2 irudia. Neurtutako indarraren seinalearen FFTa.

4.1.2 Analisi Modal Esperimentala (EMA)

Saiakuntza sistemaren ezaugarri dinamikoak determinatzeko eta 4-2 irudian ikus daitekeen portaera iragartzen duen eredu bat sortzeko helburuarekin, EMA bat egin da 4-3 irudian erakusten den geometrian oinarrituz. Mailu instrumentatu bat erabili da eszitatzaile moduan, bi lokalizazio eta norabide desberdinetan ("Excitation" moduan adierazita 4-3 irudian), modu desberdinak era eraginkorrean eszitatzeko ideiarekin. Sarrera bakoitzarentzat, irudi berean erakusten diren 28 puntuetan erantzunak neurtu dira. Helburu honekin azelerometro triaxialak erabili dira. Neurketen frekuentzia eremua 0 Hz eta 4000 Hz bitartean ezarri da, 4-2 irudiarekin bat etorriz, eszitatutako frekuentzia nagusiak modu zabalean batuz. Beraz, bi azelerazio/indar frekuentziako erantzuneko funtzio (FRF) sorta jaso dira, 84 askatasun graduri dagozkienak. FRF hauetatik, parametro modalen sistema atera da erreferentzia anitzeko minimo karratuen frekuentzia estimatzaile konplexu bat erabiliz. 19 modu lortu dira interesatzen den frekuentzia eremuan, dagozkien frekuentzia naturalekin eta moteltze faktoreekin batera.

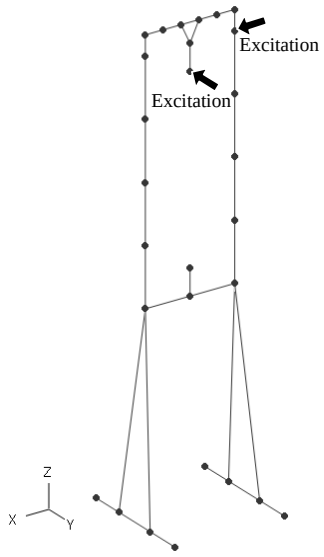

4-3 Irudia. EMAren geometria.

4.2 MAKINAREN EREDU DINAMIKOA

4-3 irudian erakusten den sistemaren mugimenduaren ekuazio orokorra kontsideratuz, zeinen portaera dinamikoa bigarren ordenako ekuazio diferentzial sorta baten bidez lor daitekeen[107]:

$$\boldsymbol{M}\ddot{z}(t)+\boldsymbol{C}\dot{z}(t)+\boldsymbol{K}z(t)=\boldsymbol{L}_u f(t) \tag{4.1}$$

Non:

- **M**, **C** eta **K** masa, moteltze eta zurruntasun matrizeak diren, hurrenez hurren.
- *z(t)* sistemako askatasun graduen desplazamendu bektorea den eta $\dot{z}(t)$ eta $\ddot{z}(t)$ bere denborarekiko deribatuak diren.
- $f(t)$ bektoreak egituran eragiten duten indarrak definitzen dituen eta $\mathbf{L_u}$ beraien eragin-matrizea den, sarrerako indarrek egituran nola eragiten duten adierazten duena.

Energiaren barreiadurarentzat adierazpen matematikoa formulatzea oso zaila da, barreiadura hau faktore askok eragiten bait dute, hara nola barne marruskadura histeretikoa, marruskadura lehor eta biskosoak, moteltze elementuak, etab. Tradizionalki eredu sinplifikatuak erabili izan dira; lan honetan eredurik zabalduenetako bat

kontsideratuko da, moteltze biskosoa (indar barreiatuak abiadurarekiko proportzionalak dira).

(4.1) ekuazioa koordenatu fisikoetan deskribatuta dago eta 4.1.2 ataleko EMAko emaitzek koordenatu modaletan deskribatutako formulazioa behar dute. Aldagai aldaketa bat egiten da ondokoari jarraituz:

$$z(t) = \Phi\, q(t) \tag{4.2}$$

Non $q(t)$ amplitude modalen bektorea den (84×1 dimentsioduna) eta $\mathbf{\Phi}$ matrizeak bere zutabeetan masa normalizatua duten moduen bektoreak ditu (84×19 dimentsioduna). (4.1) ekuazioan ordezkatuz, ezkerretik $\mathbf{\Phi^T}$ biderkatuz eta ortogonaltasun erlazioak erabiliz[108], zera lortzen da:

$$\ddot{q}(t) + 2\xi\Omega\dot{q}(t) + \Omega^2 q(t) = \Phi^{\mathrm{T}}\, \mathrm{L_u}\ f(t) \tag{4.3}$$

$\dot{q}(t)$ eta $\ddot{q}(t)$ $q(t)$ -ren deribatuak dira denborarekiko eta $f(t)$-k egituran eragiten duten indarrak definitzen ditu. $\mathbf{L_u}$ indar hauen eragin-matrizea da, sarrerako indarrek egituran nola eragiten duten adierazten duena. $\mathbf{\Omega}$ eta ξ matrize diagonalak dira, frekuentzia naturalak eta moteltze faktoreak dituztenak beren baitan, hurrenez hurren (19×19 dimentsiodunak).

M eta **K** matrizeek ortogonaltasun baldintzak betetzen dituzte, jarraian azalduko direnak.

Sistema kontserbakor baten erantzun askea kontuan hartuz, hots, moteltze barik (sistema dinamiko baten estudioaren abiapuntu gisa):

$$\boldsymbol{M}\ddot{z}(t) + \boldsymbol{K}z(t) = 0 \tag{4.4}$$

Ekuazio hau egituraren frekuentzia naturalak eta bibrazio moduak lortzeko erabil daiteke; sistema linealen kasuan, makinaren dinamika parametro hauen bidez guztiz definituta dago. Ekuazio honen soluzioak ondoko itxura du:

$$z(t) = \psi_i e^{jw_i t} \tag{4.5}$$

w_i egituraren i. frekuentzia naturala da eta ψ_i beroni lotutako bibrazio modua.

(4.5) ekuazioa (4.4) ekuazioaren barruan ordezkatuz, balio eta bektore propioen problema bat lortzen da:

$$\begin{aligned} &\left(\boldsymbol{K}-\lambda_i \boldsymbol{M}\right)\psi_i = 0 \\ &\lambda_i = w_i^2 \end{aligned} \tag{4.6}$$

M eta **K** matrizeak simetrikoak dira, **M** positibo definitua da (bere balio propio guztiak dira positiboak) eta **K** positibo semi-definitua (bere balio propio guztiak dira ez negatiboak). Hau kontuan hartuz, balio propio bakoitza aurreko ekuazioan erreala da eta ez negatiboa. Ekuazio honek bibrazio modua definitzen duenez baina ez bere anplitudea, berau eskalatzea posible da.

Frekuentzia naturalen eta bibrazio moduen kopurua egituraren askatasun graduen berdina da, N. Moteltze gabeko sistemaren soluzio osoa normalean NxN matrize bik emana dator:

$$\boldsymbol{\Omega}^2 = \begin{bmatrix} w_1^2 & 0 & \dots & 0 \\ 0 & w_2^2 & \dots & 0 \\ \vdots & \vdots & \ddots & \vdots \\ 0 & 0 & \dots & w_N^2 \end{bmatrix} \tag{4.7}$$

$$\boldsymbol{\psi} = [\psi_1, \psi_2, \dots, \psi_N] \tag{4.8}$$

Frekuentzia natural hauek sistemak bibratzeko joera duen frekuentziak adierazten dituzte eta bibrazio moduek, era berean masa eta zurruntasun matrizeak ortogonalizatzen dituen koordenatuen transformazioa definitzen duen propietate bat dute:

$$\psi_j^T \boldsymbol{K} \psi_i = 0 \tag{4.9}$$

$$\psi_j^T \boldsymbol{M} \psi_i = 0 \tag{4.10}$$

Non ψ_j eta ψ_i bibrazio modu desberdin bi diren. Ortogonaltasun baldintza hauek notazio matrizialean adieraz daitezke, ondoko eran:

$$\psi^T \boldsymbol{K} \psi = k_r \tag{4.11}$$

$$\psi^T \boldsymbol{M} \psi = m_r \tag{4.12}$$

k_r zurruntasun modalaren matrize diagonala eta m_r masa modalaren matrize diagonala dira.

Matrize bi hauen arteko erlazioa hurrengoa da:

$$k_r = \Omega^2 m_r \tag{4.13}$$

ψ matrizea eskala faktore arbitrario baten menpe dago, beraz k_r eta m_r ez dira bakarrak. Ohikoa izaten da eskala edo normalizazio moduan masa modal unitarioa erabiltzea. Kasu honetan, bibrazio moduen matrizea ϕ moduan idazten da eta ondoko propietateak ditu:

$$\phi^T \boldsymbol{K} \phi = \boldsymbol{\Omega}^2 \tag{4.14}$$

$$\phi^T \boldsymbol{M} \phi = \boldsymbol{I} \tag{4.15}$$

Non **I** matrize unitarioa den.

(4.2) ekuazioa (4.1)-en barruan sartuz:

$$\boldsymbol{M}\phi\{\ddot{q}(t)\} + \boldsymbol{C}\phi\{\dot{q}(t)\} + \boldsymbol{K}\phi q(t) = \boldsymbol{L_u} f(t) \tag{4.16}$$

(4.16) ekuazioa ϕ^T terminoaz aurre-biderkatuz eta kontuan izanik ortogonaltasun baldintza hauek:

$$\boldsymbol{I}\ddot{q}(t) + \phi^T \boldsymbol{C}\phi\dot{q}(t) + \boldsymbol{\Omega}^2 q(t) = \phi^T \boldsymbol{L_u} f(t) \tag{4.17}$$

Kontsideratu behar da **C** matrizearen kalkulatzeko era, prozedura analitikoa neketsua da eta. Normalean prozedura sinplifikatuak erabiltzen dira, hara nola moteltze proportzionala edo Rayleigh-en moteltzea eta moteltze modala. Hemen, bigarren hau erabiltzen da analisi modaletik lortzeko hobeto moldatuta baitago. Modu bakoitzaren moteltzearen magnitudea moteltze kritikoaren portzentai baten modura adierazten da; lortutako emaitzak egokiak dira moduen moteltzea moteltze kritikoa baino gutxiago bada.

Modu honetan, modu bakoitzarentzat moteltze modala ξ_i moteltze kritikoaren frakzio baten modura kontsideratu da eta honela definitu da:

$$\phi^T \boldsymbol{C} \phi = \boldsymbol{diag}(2 \cdot \boldsymbol{\xi_i} \cdot \boldsymbol{w_i}) \tag{4.18}$$

Eta (4.17) ekuazioa, (4.3) ekuazioaren moduko N ekuazio desakoplatutan bihurtu da; ekuazio bakoitzak bibrazio modu baten portaera deskribatzen du.

Non:

$$\boldsymbol{\xi} = \begin{bmatrix} \xi_1 & 0 & \dots & 0 \\ 0 & \xi_2 & \dots & 0 \\ \vdots & \vdots & \ddots & \vdots \\ 0 & 0 & \dots & \xi_N \end{bmatrix} \tag{4.19}$$

Modu bakoitzarentzat ξ_i balioak esperimentalki lortu dira.

(4.3) ekuazioa guztyiz definitu da parametro modaletan, EMAtik atera direnak 4.1.2. atalean.

Egoera-espazio errepresentazioak sistemaren erantzuna sarrerako indarren aurrean aztertzeko modu egoki bat ematen du; honela, errepresentazio honetan sistema lineal aldaezina denboran deskribatzen da, lehenengo ordenako ekuazio diferentzial sorta baten moduan. (4.20) eta (4.21) ekuazioek garapen honen forma orokorra deskribatzen dute:

$$\dot{x}(t) = Ax(t) + Bu(t) \tag{4.20}$$

$$y(t) = Cx(t) + Du(t) \tag{4.21}$$

(4.20) ekuazioa egoera ekuazioa da: sistemaren barne dinamika deskribatzen du, eta (4.21) ekuazioa irteera ekuazioa da.

Non:

- **A**, **B**, **C** eta **D** egoera-espazioko matrize errealak diren, denborarekiko independenteak, sistemaren dinamika adieraziz,

- $u(t)$ sistemaren sarrerako bektorea den ($f(t)$-ren berdina),

- $x(t)$ egoera bektorea den eta $\dot{x}(t)$ bere deribatua, eta

- $y(t)$ sistemaren irteerako bektorea den.

A, **B**, **C** eta **D** matrizeak egoera bektorearen aukeraketaren menpeko dira; hortaz, egoera-espazioaren errepresentazio desberdinak dira posibleak sistemaren sarrera eta irteerentzat. Egoera-espazioaren matrizeak eremu modalean definitzeko, egoera bektorearen definizo egoki bat ondokoa da[109]:

$$x(t) = \begin{bmatrix} \boldsymbol{\Omega} q(t) \\ \dot{q}(t) \end{bmatrix} \tag{4.22}$$

(4.3) ekuazioan ordezkatuz, **A** eta **B** matrizeak izango dira:

$$\mathbf{A}=\begin{bmatrix}\mathbf{0} & \mathbf{\Omega}\\ -\mathbf{\Omega} & -2\boldsymbol{\xi}\mathbf{\Omega}\end{bmatrix} \qquad \mathbf{B}=\begin{bmatrix}\mathbf{0}\\ \mathbf{\Phi}^{\mathrm{T}}\mathbf{L}_{\mathbf{u}}\end{bmatrix} \tag{4.23}$$

C eta **D** matrizeak behar diren irteeren menpekoak izango dira, beraz, eredua aukeraturiko askatasun graduen desplazamenduak, abiadurak eta azelerazioak simulatzeko erabil daiteke.

Egoera-espazioaren helburua irteerako askatasun gradu desberdinen desplazamenduak, abiadurak eta azelerazioak lortzea da. Nahi den terminoaren arabera, irteerako ekuazioa honela irakur daiteke:

Desplazamenduak:

Desplazamenduen kasuan, irteerako ekuazioa ondokoa da: $\{y(t)\}=\left[L_y\right]^T\{z(t)\}$

$$\{y(t)\}=\left[L_y\right]^T[\phi]\{\eta(t)\}=[\phi]_y[\Omega]^{-1}\{z(t)\}=Cz+Df \tag{4.24}$$

Abiadurak:

Abiaduren kasuan, irteerako ekuazioa ondokoa da: $\{y(t)\}=\left[L_y\right]^T\{\dot{z}(t)\}$

Azelerazioak:

Azelerazioen kasuan, irteerako ekuazioa ondokoa da: $\{y(t)\}=\left[L_y\right]^T\{\ddot{z}(t)\}$

$$y=\left(-[\phi]_y[\Omega]-2[\phi]_y[\xi][\Omega]\right)z+[\phi]_y\mu^{-1}[\phi]_u^{\ T}\{f(t)\}=Cz+Df \tag{4.25}$$

Behin eredua garatuta, garrantzitsua da bere zehaztasuna egiaztatzea. Hurrengo atalak lan honen markoan egindako egiaztapenak deskribatzen ditu.

4.3 EREDUAREN EGIAZTATZEA

Eredu matematikoak balioztatzeko modu arrunt bat simulaturiko eta neurturiko FRFak konparatzean datza. 4.3.1 azpiatalak egiaztatze hau deskribatzen du. Gainera, denboraren eremuan kautxuaren abiadura altuko konpresiozko saiakuntza bat simulatu da bibrazioen

frekuentzia edukia aurresateko, emaitza esperimentalki lortutakoarekin konparatuz. Hau 4.3.2. azpiatalean laburbiltzen da.

4.3.1 FRFen konparaketa

FRFen azelerantzia esperimentala, 4.1.2. azpiataleko analisi modaletik lor daitekeena, egoera-espazio ereduaren bitartez erreproduzitu daiteke. Kalkulu hauek azelerazioak lortzeko **C** eta **D** matrizeen definizio egokia behar dute, ondoko eran[109]:

$$\mathbf{C} = \left[\mathbf{L}_y^T \boldsymbol{\Phi}\boldsymbol{\Omega} \quad -2\mathbf{L}_y^T \boldsymbol{\Phi}\boldsymbol{\xi}\boldsymbol{\Omega}\right] \qquad \mathbf{D} = \mathbf{L}_y^T \boldsymbol{\Phi}\boldsymbol{\Phi}^T \mathbf{L}_u \tag{4.26}$$

$\mathbf{L}_y$ beharrezko irteeren eragin-matrizea da.

4-4 irudiak irteerako j askatasun graduaren eta sarrerako i askatasun graduaren arteko FRFak konparatzen ditu. Irteerako askatasun gradua aukeratu izan da, goiko muturraren eta espezimenaren arteko kolpea ematen den posizioan eta norabidean, makinaren indarraren bidean zehar transmititzen diren moduak detektatzeko ideiarekin.

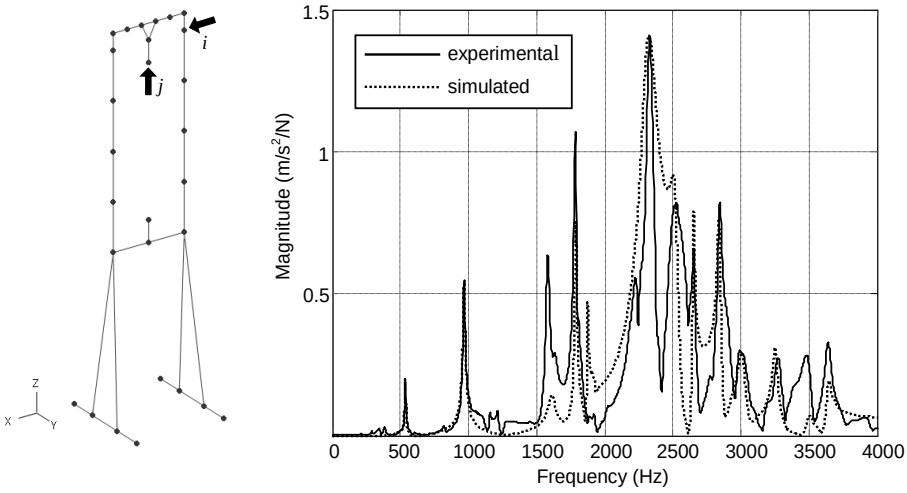

4-4 irudia. Irteerako j eta sarrerako i askatasun graduen arteko azelerantzia esperimental eta simulatuen FRFak

Irudi honek erakusten duenez, egoera-espazio eredu modalak sistemaren portaera dinamikoa modu egokian islatzen du. Interesgarria da anplituderik altueneko tontorra 2320 Hz ingurutan ematen dela, 4.1.2. azpiatalean detektaturiko frekuentzia bera izanik.

4.3.2 Denbora eremuko simulazioak

Konpresiozko kolpea kautxuzko espezimenean bapatean aplikaturiko bulkada-indar batekin konparagarria da. Idealizazio matematiko honek, aurreko ikerkuntza lanetan modu zabalean hartua[14,98], makinaren erantzunaren denborazko eboluzioa simulatzeko modu egokia ematen du, bulkada-indarrak modu errazean programa daitezkeelarik.

Matlab programaren Simulink plataforma erabili da simulazio hauek gauzatzeko. Egoera-espazio ereduan, bulkada-indarra 4-5 irudian erakutsitako bi "input" askatasun graduetan eragiten duelarik simulatu da $\mathbf{L_u}$ bektorearen definizio egoki baten bidez. Sisteman bi indar sartzen diren arren, magnitude berekoak dira, pistoian eta goiko buruan kolpean zehar auto-orekatzaileak diren indarrak adierazten dituztelako, eta ondorioz, $\mathbf{L_u}$–ren zutabe bakarra da beharrezkoa.

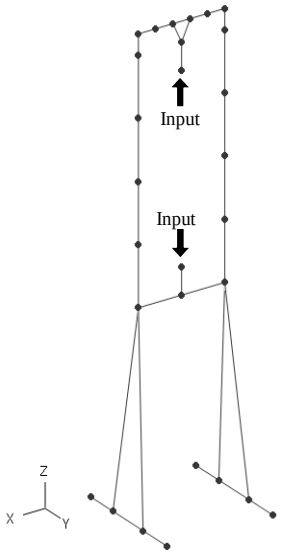

4-5 irudia. Sarrerako askatasun graduak denboraren eremuko simulazioetarako.

Bulkada-indar batekin lan egiten demean bere magnitudearen estimazio egokia da. Hurrengo atalak lan honetan jarraitutako estrategia eztabaidatzen da bulkada-indar horren balioa lortzeko.

4.3.2.1. Bulkada-indarraren magnitudearen estimazioa

Bulkada bat indarraren denboran zeharreko integral moduan definitzen da $\int f(t)dt$ eta magnitude oso handia duen indarra deskribatzen du, denbora tarte oso labor batean eragiten duena. Idealki, denbora tartea zerorantz hurbiltzen da eta indarra infinitorantz,

baina denbora integral finitu batekin. Denboraren eremuko simulazio ingurune batean ez da posible indar infinitorik aplikatzea, ezta zero denbora tartea definitzea ere, beraz, praktikan, *f* indar bat aplikatzen da Δ*t* denbora kopuru diskretu batean zehar. Egoera hau 4-6 irudian deskribatzen da.

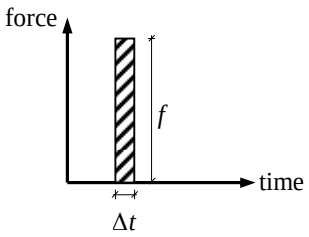

4-6 irudia. *f* magnitudeko bulkada-indarra Δ*t* denbora iraupen batekin.

Beraz, estimazio prozesua *f* balioaren determinazioan datza, Δ*t* denbora tartean eragiten duena, erantzun moduan makinaren portaera erreala islatzen duen emaitza ematen duelarik.

Helburu honekin aukeratutako erantzunak kontrol puntu batzuen azelerazioak izan dira; kontrol puntu horietan azelerometroak ipini izan diren 4-1 irudiko saiakuntzan zehar. Simulaturiko azelerazioak egoera-espazio eredua erabiliz lortu dira, $\mathbf{L}_y$ bektorearen definizio egoki batekin. Kautxuzko espezimena makinarekin alderatuz oso malgua dela kontsideratu da, beraz material honi dagokion zurruntasun gehigarririk ez zaio gehitu ereduari. Hortaz, Δ*t* definitu ostean, *f*-ren balioa modu iteratioboan aldatzen joan da erantzun simulatuaren eta neurtutakoaren artean korrespondentzia egokia lortu arte.

Behin bulkada-kargaren magnitude egokia estimatuta, ereduaren egiaztatze prozesuan hurrengo pausoa karga-zelulak neurtutako indarra aurresatea da, simulazioen zehaztasun maila determinatzeko asmoz.

4.3.2.2. Karga-zelulak neurtutako indarraren simulazioa

4-7 irudiak karga-zelula piezoelektrikoaren irudia aurkezten du, zein goiko muturrean kokaturik dagoen. Zelula honek neurtutako indarra estimatu daiteke, zelula malguki elementu baten bitartez karakterizatuz egindako ereduaren bitartez. Izan ere, malgukiaren amaierako desplazamenduak kalkulaturik daudela kontuan hartuz (*1* eta *2* puntuak 4-7 irudian), karga-zelulako indarra (F_{LC}) lor daiteke, bere zurruntasuna (K_{LC}) malgukiaren luzera aldaketarekin ($x_2 - x_1$) biderkatuz.

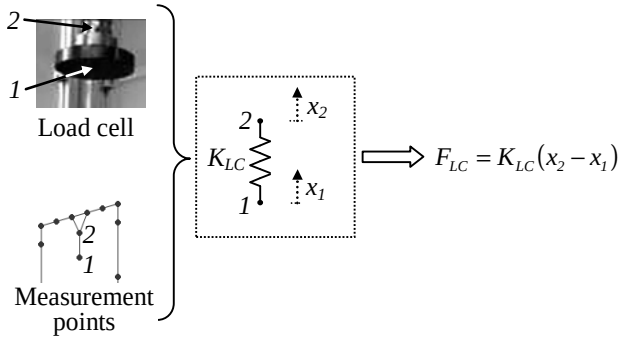

4-7 irudia. Karga-zelularen idealizazio matematikoa.

x_1 eta x_2 aldagaiak eredu modaletik kalkula daitezke (4-7 irudi berberean erakusten dira *1* eta *2* puntuei dagozkien neurketa puntuak). **C** eta **D** matrizeak moldatu egin behar dira desplazamenduak eman ditzaten irteera moduan, ondokoari jarraituz[109]:

$$\mathbf{C} = \left[\mathbf{L}_y^T \boldsymbol{\Phi} \boldsymbol{\Omega}^{-1} \quad \mathbf{0}\right] \qquad \mathbf{D} = \mathbf{0} \tag{4.27}$$

Hortaz, 4.3.2.1. azpiatalean lortutako bulkada magnitudea sarrera moduan aplikatu da eta *2* eta *1* puntuen desplazamendu axialak ereduaren bitartez estimatu dira. Puntu hauen arteko diferentzia K_{LC}-gatik biderkatu behar da, zein fabrikatzailearen katalogotik[97]. Indar simulatuaren denboran zeharreko seinale erresultantea 4-8 irudian erakusten da, seinale honen FFTarekin batera.

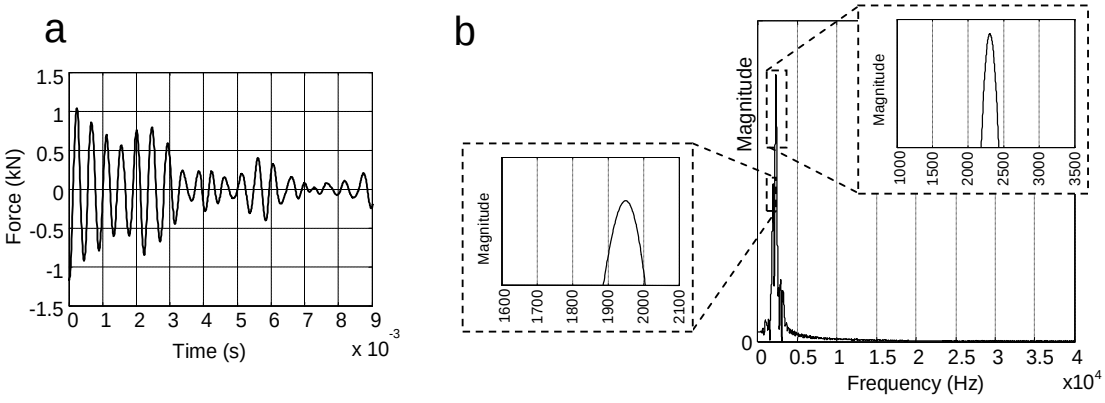

4-8 irudia. Simulaturiko karga-zelulako indar seinalearen (a) Denboran zeharreko eboluzioa eta (b) FFTa.

Antzekotasun argia ikusten da neurtutako karga-zelulako indar seinalearen (4-2 irudia) eta simulaturikoaren (4-8b irudia) frekuentzien edukien artean.

Hortaz, ereduaren balioztatze prozesuak simulazioen zehaztasuna ziurtatzen du; eredua hurrengo etapan egingo den indar seinalearen zuzenketarako egokia dela adieraziz.

4.4 KARGA-ZELULAK NEURTUTAKO INDARRAREN ZUZENKETA

Ereduak 4-8a irudian aurresandako indarraren seinaleak, karga-zelulak neurtutako osagai oszilakor iragankorra estimatzen du; osagai hau 4-1 irudiko materialaren saiakuntzan zehar makinaren erresonantzien eszitazioaren ondorioa da. Beraz, zati oszilakor hau ezabatu daiteke, simulaturiko erantzuna neurtutako seinaleari kenduz gero.

Ideia hau kontuarekin aplikatu behar da bi seinaleen arteko edozein fase-aldaketa ekiditzeko. Izatez, 4-1 eta 4-8a irudietako denboraren ardatzak independenteak dira eta korrelazio zehatzak aldibereko denbora uneen determinazioa kontu handiarekin egitea eskatzen du. Helburu hau lortu da bi seinaleak irudi berdinean gainezarriz eta erantzun simulatua tontor biren denbora uneak parekatu arte trasladatuz. Prozedura hau 4-9 irudian azaltzen da.

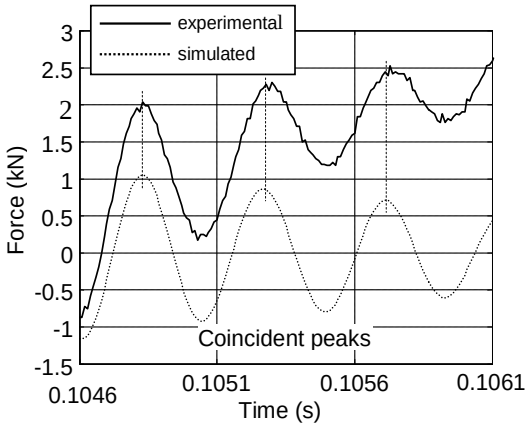

4-9 irudia. Indarraren seinale esperimentalaren eta simulatuaren arteko konparaketa denbora korrelazio egoki baten kasuan, erantzun simulatua trasladatu ondoren.

4-9 irudiko seinale simulatua orain seinale esperimentalari kentzeko prest dago. Eragiketa honek 4-10 irudiko kurba sortzen du.

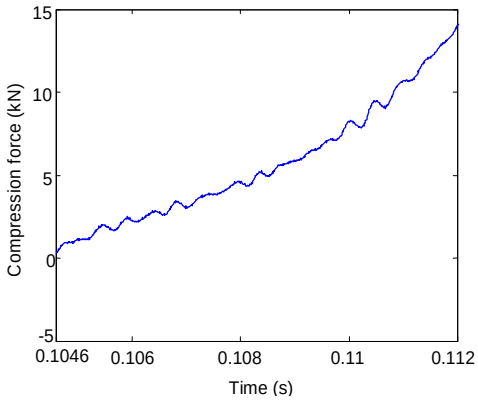

4-10 irudia. Karga-zelularen indar seinalea oszilazio simulatuak kenduta ostean.

Oszilazioak, guztiz kendu ez arren, modu nabarmenean txikitu dira. Hain zuzen ere, 4-1 irudiko jatorrizko datu esperimentalekin konparatuz, ikus daiteke tontorren anplitudeak modu argian txikitu egin direla.

Seinale berria egokiagoa da iragazkia aplikatzeko jatorrizko neurketa esperimentala baino, sarreran aipatu bezala. Beraz, 4-10 irudiko seinaleari behe-paseko iragazkia pasatu zaio, 1600 Hz-tako mozketa frekuentziaduna. Mozketa frekuentzia hau 4-8 irudian agertzen den oszilaziodun frekuentzia iragazi ahal izateko eran aukeratu da. Kurba erresultantea 4-11 irudian erakusten da.

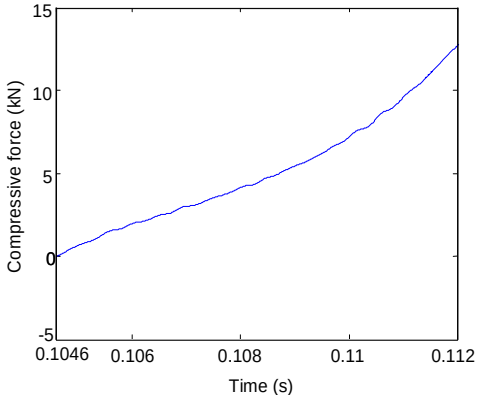

4-11 irudia. Iragazi ostean azken indarraren seinalea.

Emaitza final honek portaera leuna erakusten du, non erantzun oszilakorra kendua izan den. Beraz, makinaren kontribuzio dinamikoa kendu izan da eta kurbak saiakuntzako materialaren portaera erreala islatzen du; honek zera esan nahi du, seinalea egokia dela ondorengo analisietarako, materialaren karakterizaziorako abiadura altuetan.

Azkenik, 4-12 irudiak karga-zelulak neurtutako indar seinalea simulatutako oszilazioak kenduta gero eta azken indar seinalea iragazita gero erakusten ditu.

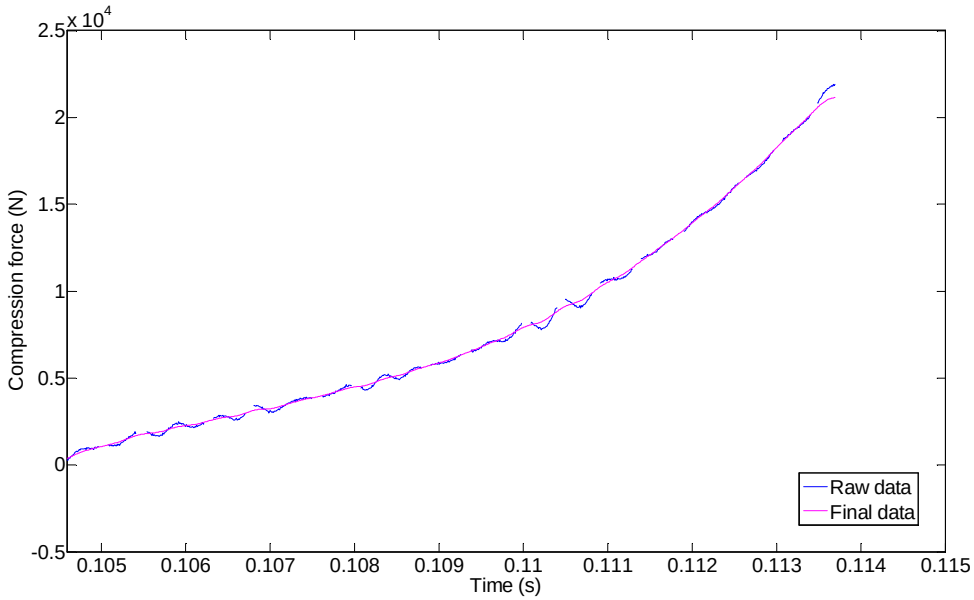

4-12 irudia. Karga-zelulak neurtutako indar seinalea simulatutako oszilazioak kenduta gero vs. Indar seinale finala iragaztearen ostean

4.5 APLIKAZIOA BESTE DENTSITATE MATERIAL BATZUETARA

Aurretiaz esan bezala, ikasitako kurba materialaren dentsitatea 0.75 g/cm^3 da, 60/40 proportziorako. Metodologia hau beste dentsitate material batzuei aplikatu zaie, hain zuzen ere 0.84, 0.93 eta 1.04 g/cm^3. Hurrengo irudiek hasierako indarra versus denbora erakusten dute, oszilazioak kenduta gero ateratzen diren indarren seinaleekin batera, dentsitate hauentzat.

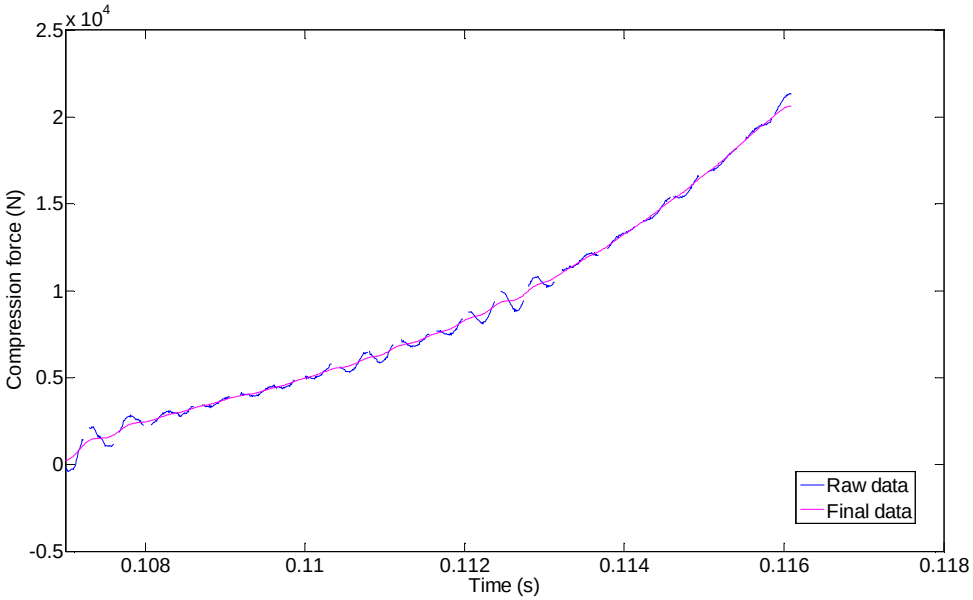

4-13 irudia. 0.84 g/cm^3 dentsitatearen kasuan hasierako eta bukaerako indarren seinaleak.

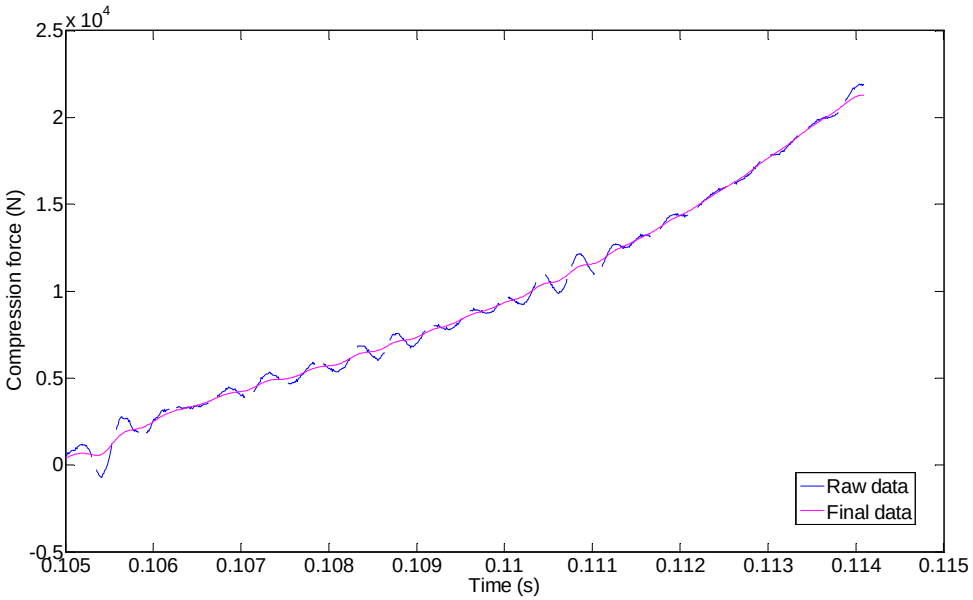

4-14 irudia. 0.93 g/cm^3 dentsitatearen kasuan hasierako eta bukaerako indarren seinaleak.

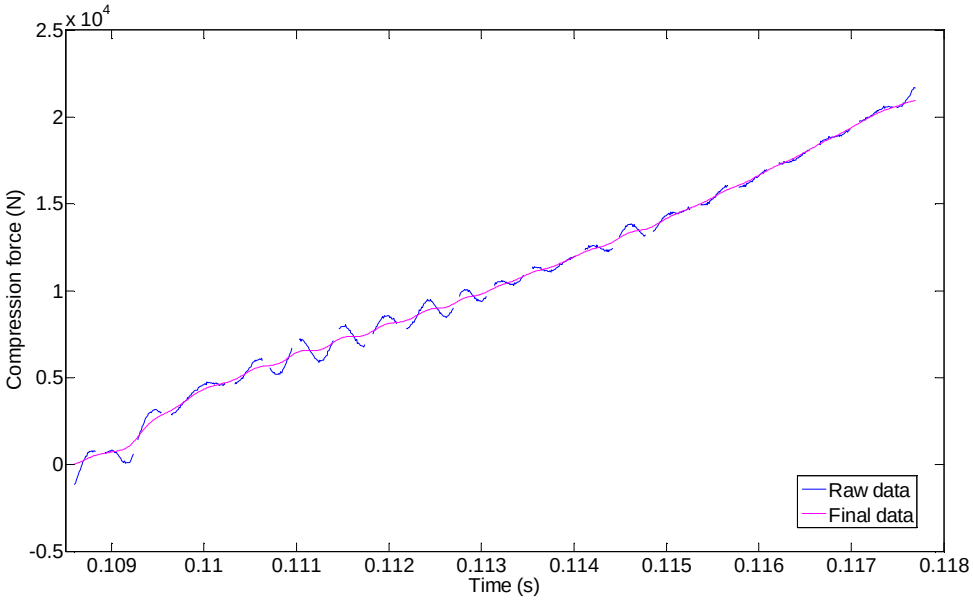

4-15 irudia. 1.04 g/cm^3 dentsitatearen kasuan hasierako eta bukaerako indarren seinaleak.

Ondoren, metodologia berdina aplikatu zaie materialaren beste proportzioei, hau da, 75/25 proportzioa eta 90/10 proportzioa, eta beraiei dagozkien dentsitateei.

<u>75/25 proportion</u>:

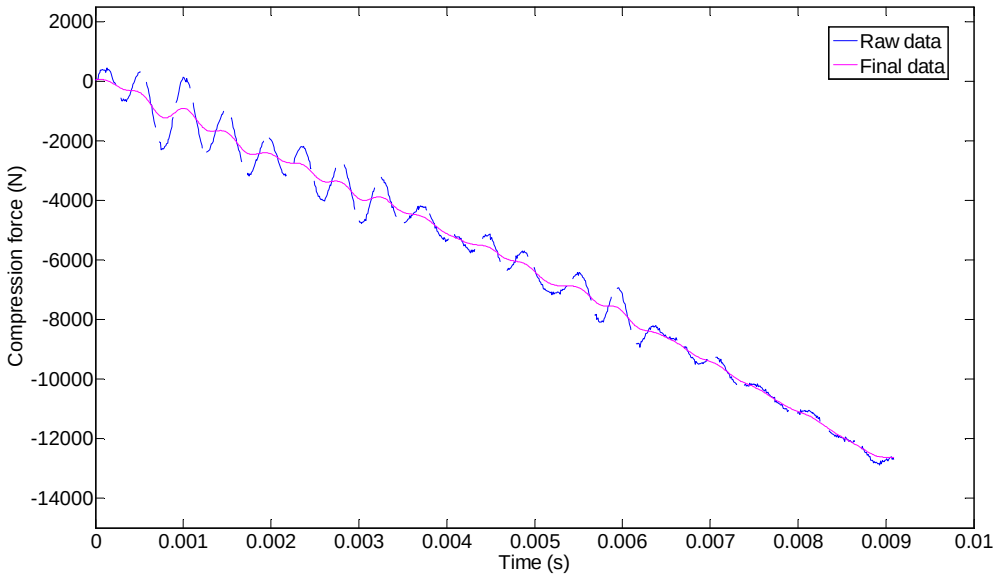

4-16 irudia. 0.77 g/cm^3 dentsitatearen kasuan hasierako eta bukaerako indarren seinaleak (probeta HANDIAK).

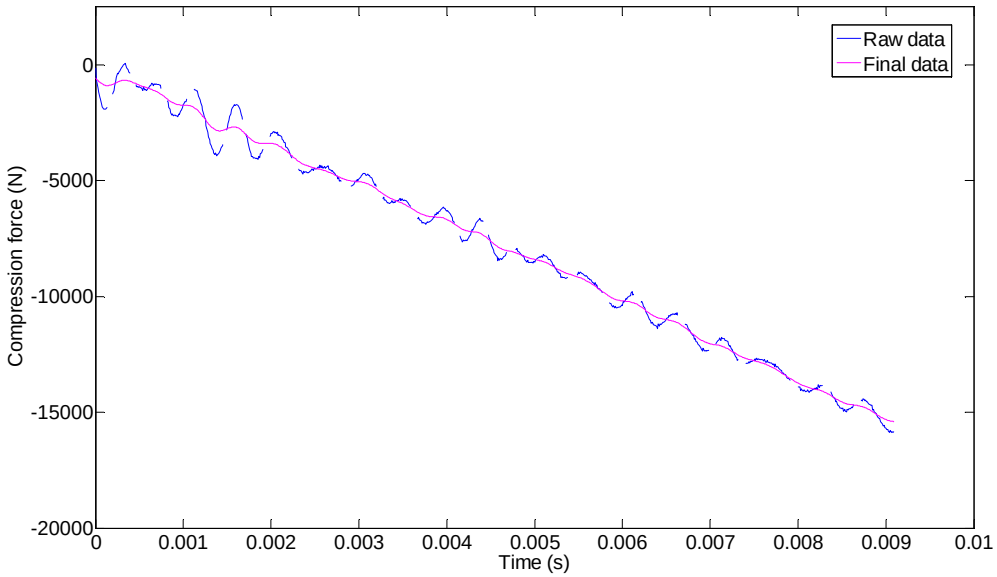

4-17 irudia. 0.85 g/cm^3 dentsitatearen kasuan hasierako eta bukaerako indarren seinaleak (probeta HANDIAK).

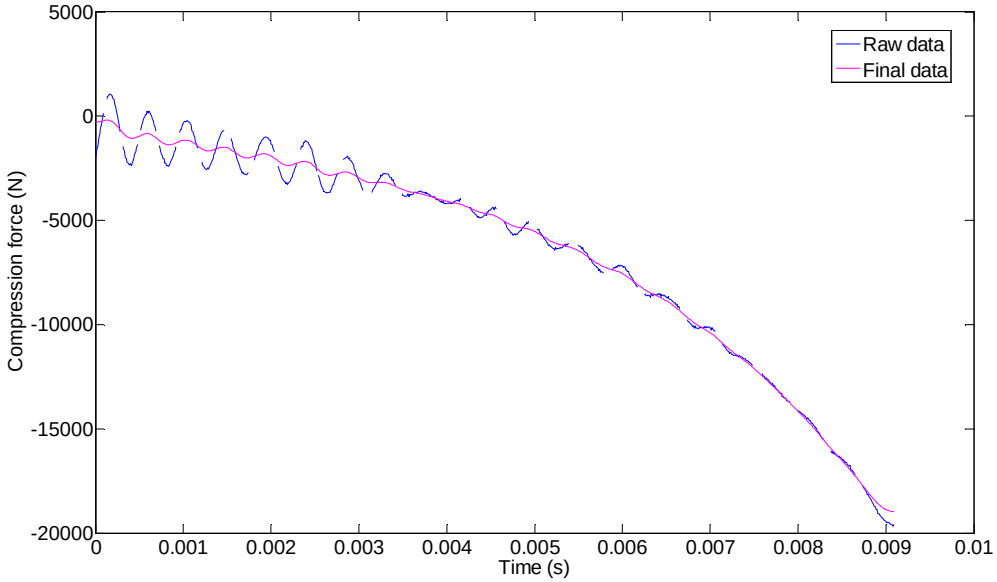

4-18 irudia. 0.73 g/cm^3 dentsitatearen kasuan hasierako eta bukaerako indarren seinaleak (probeta TXIKIAK).

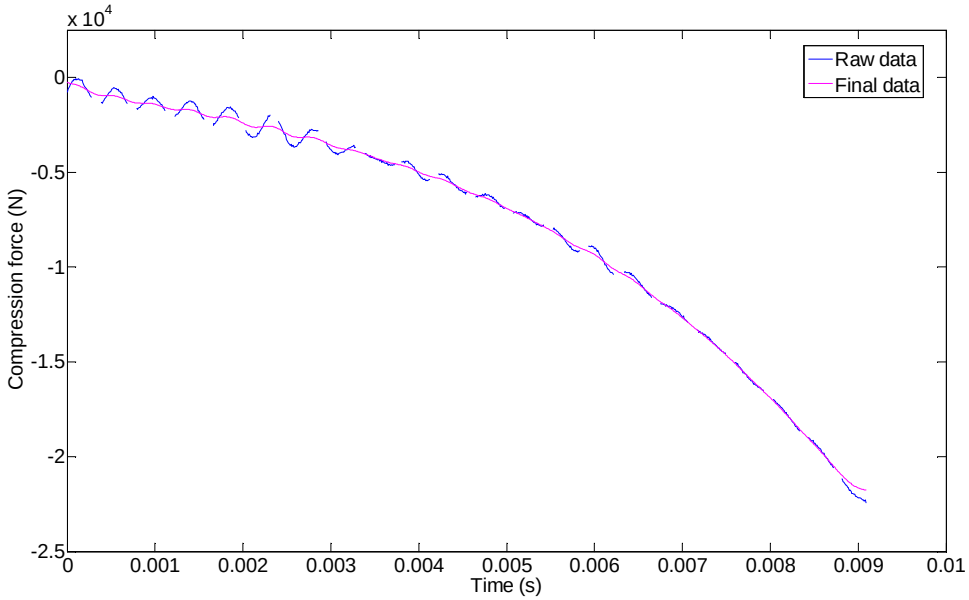

4-19 irudia. 0.83 g/cm³ dentsitatearen kasuan hasierako eta bukaerako indarren seinaleak (probeta TXIKIAK).

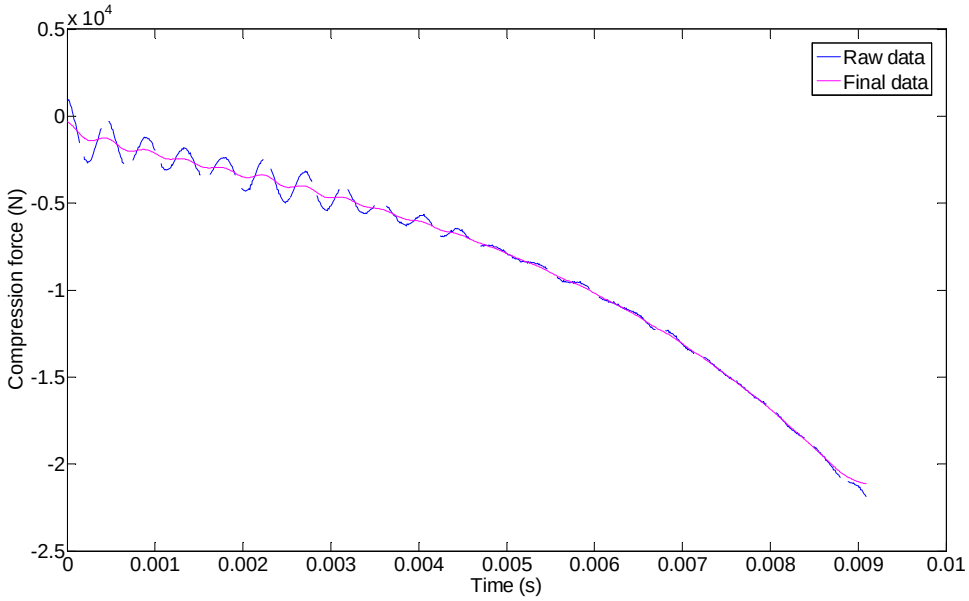

4-20 irudia. 0.93 g/cm³ dentsitatearen kasuan hasierako eta bukaerako indarren seinaleak (probeta TXIKIAK).

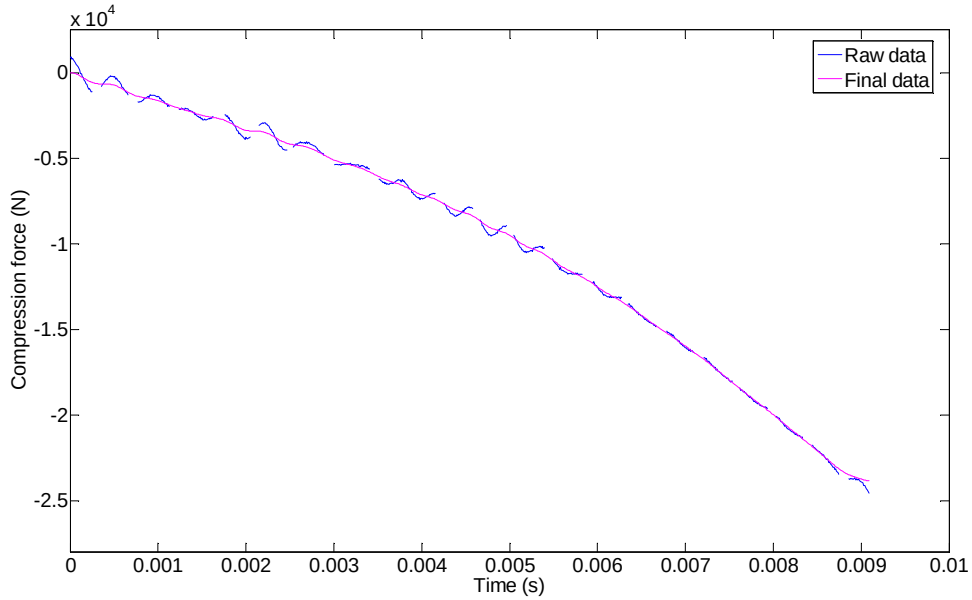

4-21 irudia. 1.07 g/cm^3 dentsitatearen kasuan hasierako eta bukaerako indarren seinaleak (probeta TXIKIAK).

<u>90/10 proportion</u>:

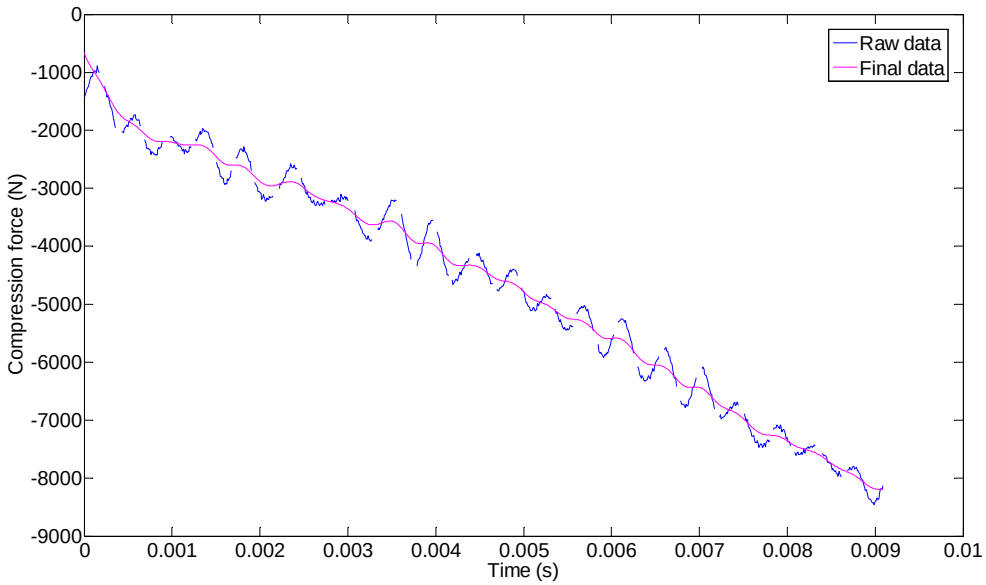

4-22 irudia. 0.73 g/cm^3 dentsitatearen kasuan hasierako eta bukaerako indarren seinaleak (probeta HANDIAK).

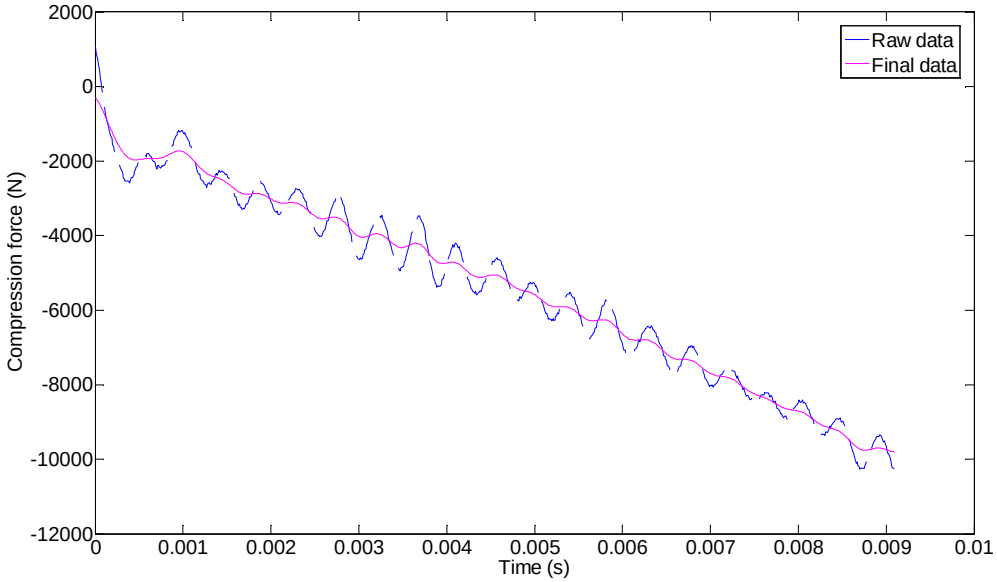

4-23 irudia. 0.83 g/cm³ dentsitatearen kasuan hasierako eta bukaerako indarren seinaleak (probeta HANDIAK).

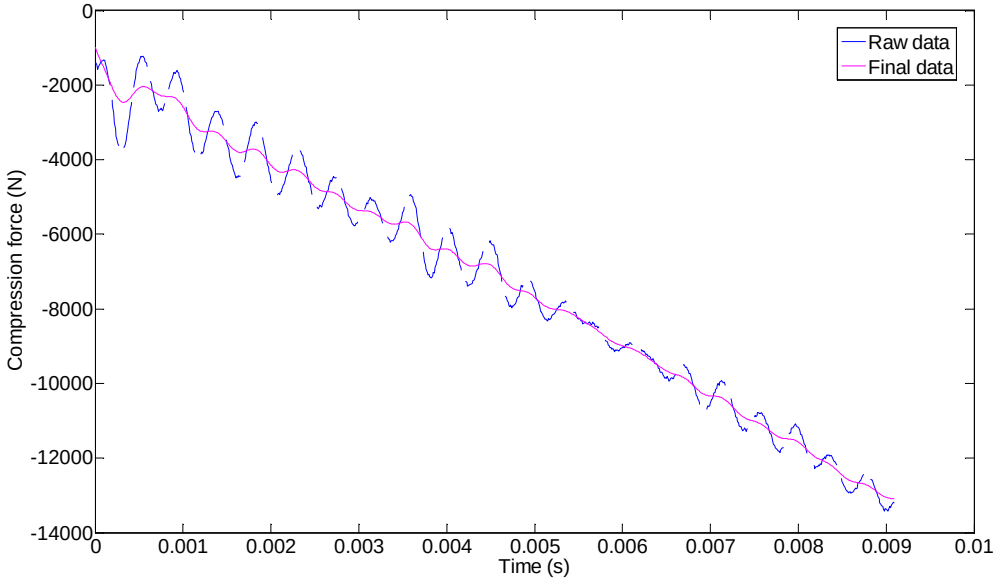

4-24 irudia. 0.93 g/cm³ dentsitatearen kasuan hasierako eta bukaerako indarren seinaleak (probeta HANDIAK).

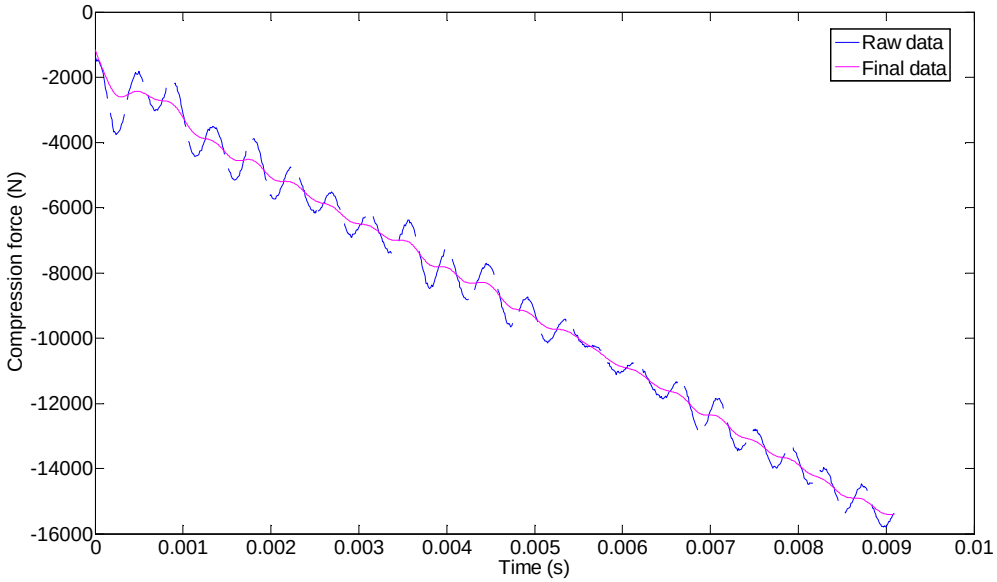

4-25 irudia. 1.02 g/cm³ dentsitatearen kasuan hasierako eta bukaerako indarren seinaleak (probeta HANDIAK).

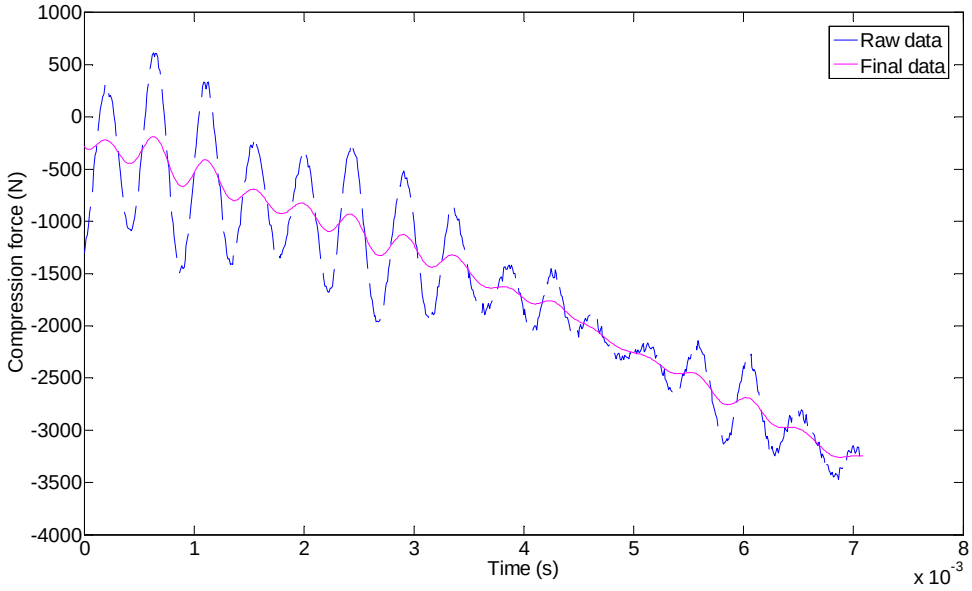

4-26 irudia. 0.82 g/cm³ dentsitatearen kasuan hasierako eta bukaerako indarren seinaleak (probeta TXIKIAK).

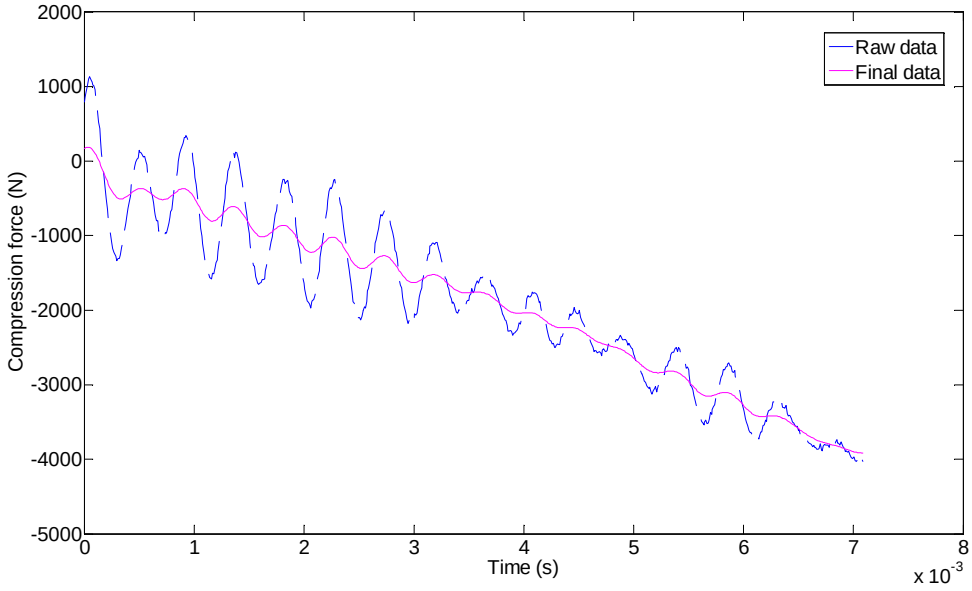

4-27 irudia. 0.92 g/cm³ dentsitatearen kasuan hasierako eta bukaerako indarren seinaleak (probeta TXIKIAK).

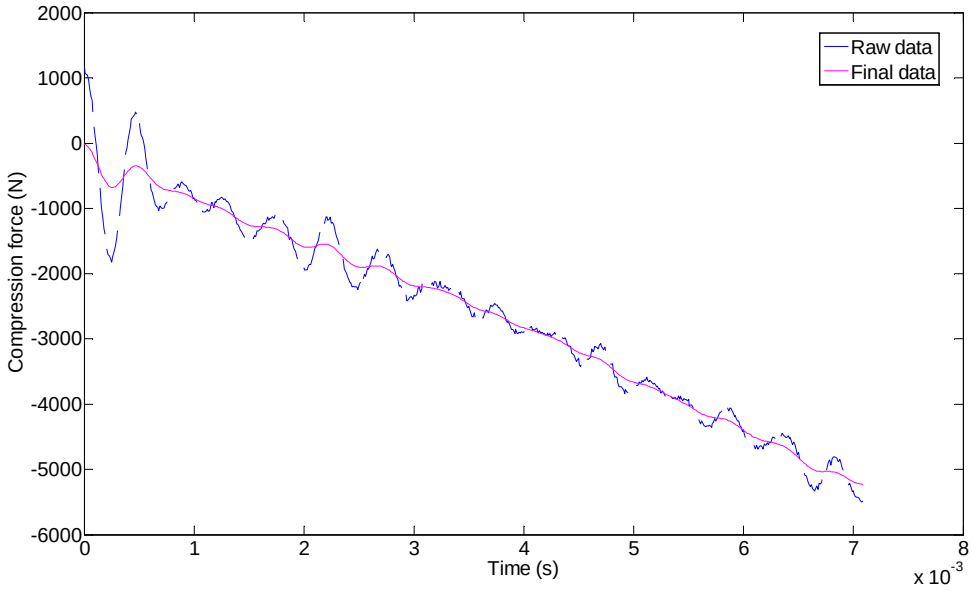

4-28 irudia. 0.99 g/cm³ dentsitatearen kasuan hasierako eta bukaerako indarren seinaleak (probeta TXIKIAK).

4.6 EZTABAIDA

Makina serbo-hidraulikoetan abiadura altuko materialen karakterizaziotik "ringing"aren ondorioz ematen diren ondulazioak ezabatzeko prozedura berri hau efikaza dela ikusi da. Metodoaren ezaugarri bereizgarria saiakuntza sistemaren propietate dinamikoen eredu modal baten bitartez egiten den deskribapena da; eredu honek bibrazio modu nagusiak kontsideratzen ditu makinaren portaeraren sarrera-irteeran. Hau esploratu gabeko ikerketa area da, egin berri den literaturako aurreko lanek askatasun gradu bakarreko ereduak kontsideratu izan dituztelarik; horrela, emaitza simulatuak eta esperimentalak konparatzerakoan, erroreak agertzen izan dira.

Garatutako eredua karga-zelulak neurtutako indarraren osagai iragankorra simulatzeko gai da, saiatzen ari den materiala inpultso baten eran eszitatzen denean. Osagai hau datu esperimentaletatik kentzen da bibrazioen anplitudeak asko txikitzen direlarik; horrela material kurba egokia egiten da ondoren iragazi ahal izateko.

Beraz, lan honen kontribuzio nagusia makina eredu baten garapena da, "ringing"aren ondorioz ematen diren oszilazioak minimizatzea posible egiten duena, datuak filtratu aurretik, filtro pausoa efikazagoa egiten duena jatorrizko neurketa esperimentalei zuzenean aplikatuz baino. Efikazia hau kautxuzko espezimen batean frogatu da, baina prozedura beste material batzuetara zabal liteke, zeinen zurruntasun propietateak ez diren mesprezagarriak.

5. MATERIALAREN EKUAZIO OSAGARRIA

5.1 SARRERA

Birziklatutako kautxuarekin eta LLDPE-arekin egindako hiru nahasteren probetak egin dira eta berauekin deformazio abiadura altuko konpresiozko saiakuntzak egin dira. Deformazio abiadura altuenaren datu esperimentalak zuzenduak izan dira AME-aren bitartez. Kapitulu honetan nahaste honen portaera azaltzen duen ekuazio osagarri bat aukeratzen eta garatzen da, hain zuzen ere, Yang-en eredua, 2.4 atalean aurkeztua. Ereduaren sei parametroak doitzen dira; lehendabiziko hiru hiperelastikoak minimo karratuen doiketa estrategiarekin, gainontzeko hiru biskoelastikoak doitzeko optimizazio algoritmo bat aplikatzen den bitartean. Algoritmo honi Particle Swarm Optimization (PSO) deritzo eta xehetasunez azaltzen da; bere erraztasunarengatik, sendotasunarengatik eta konbergentzia azkarrarengatik aukeratua izan da. Parametro gutxi batzuen doiketa soilik du beharrezko eta optimo globalera iristeko gai da, optimizatu nahi den funtzioa oso ez-lineala izanda ere[110]. Modu arrakastatsuan aplikatu izan da Kontrol-Ingeniaritzan edota Informatikan[111,112] eta Materialen Zientziaren[113,114] eremu batzuetan ere. Algoritmoa 90/10 nahasteari aplikatu zaio, 0.9 g/cm^3 dentsitatedun probeta handiei hain zuzen ere, 0.057, 0.57 and 5.7 s^{-1} deformazio abiadurekin. Ondoren, Yang-en eredua deformazio abiadura altuenari aplikatu zaio, hots, 57 s^{-1} deformazio abiadurari, eta balio hauek zuzenduriko balio esperimentalekin konparatu dira.

Kapitulua ondoren azaltzen den moduan antolatu da. Lehendabizi, Yang-en eredua garatu da 5.2. atalean. Gero, Particle Swarm (PSO) algoritmoa aurkeztu da 5.3. atalean. Jarraian, lortutako emaitzak erakusten dira 5.4. atalean. Azkenik, eta doiketa prozesuan aurkitutako zailtasunek parametroen ikasketa teorikoa eragin dute berauei buruz informazio gehiago eskuratzeko asmoz, 5.5. atalean. Kapitulua eztabaida labur batekin amaitzen da.

5.2 YANG-EN EREDUAREN AUKERAKETA

Lan honetan aukeraturiko eredu hiper-biskoelastikoa Yang eta bestek[68] proposaturikoa da 2.4. atalean esan bezala, 2. kapituluan. Eredua aukeratzearen arrazoia ikertzaileen komunitateak xehetasunez aztertu izan duela da[71,83,115-118]; kautxu erako materialen portaera zehaztasunez deskribatzen du deformazio abiadura eremu zabal batean. Lehendabizi hiru dimentsiotarako garatzen da eta ondoren, konpresio uniaxialeko kasuan aplikatzen da.

5.2.1 Yang-en ereduaren aurkezpena

Proposaturiko materialaren eredua osagai hiperelastiko bat osagai biskoelastiko batekin paraleloan ipiniz eratzen den material ereduen konbinaziotik dator. Zati hiperelastikoari dagokionez, hiru parametroko seriera moztutako Rivlinen eredua materialaren atal hau deskribatzeko aproposa dela ikusi da. Zati biskoelastikoari dagokionez, K-BKZ ereduaz osaturik dago, Yang-en aldaketarekin, Maxwell-en eredu orokortura eramanez. Kautxu erako material konprimaezinen deformazio handien hiru dimentsioko portaera hiper-biskoelastikoa deskribatzen du. Tentsio totala osagai bien batura da:

$$\sigma = \sigma^e + \sigma^v \tag{5.1}$$

Non σ^e tentsioak propietate hiperelastiko kuasiestatikoa adierazten duen eta σ^v tentsioa deformazio abiaduraren eta deformazioaren historiaren menpeko materialaren erantzuna den. Eredu honen adierazpen reologikoa proposa daiteke: orekako malguki bat Maxwell elementu batekin paraleloan ipinita; Maxwell elementu hau, bitarteko malguki bat eta segidan motelgailu biskoso[7] bat jartzean datza. Adierazpen hau 5-1 irudian erakusten da:

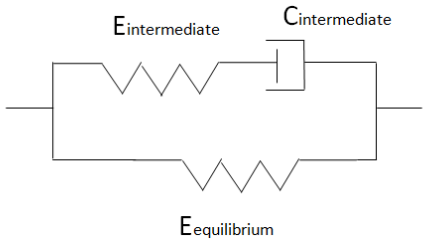

5-1 irudia. Eredu hiper-biskoelastikoaren adierazpen reologikoa

Ereduko malguki biak dira hiperelastikoak. Motelgailu biskosoak tentsioa (edo indarra, azken finean) bitarteko malgukian deformazio abiadurarekin aldatzea baimentzen du.

- Deformazio abiadura oso baxua denean, motelgailua ez denez aktibatzen, deformazioa orekako malgukiak zuzentzen du soilik;

- Deformazio abiadura oso altua demean, motelgailuak ez du denbora nahikoa deformatzeko eta "makil" baten modukoa da, eta beraz, bitarteko malgukia bere balio maximora hurbiltzen da.

Deformazio abiaduraren balio bi hauen bitartean, materiala deformazio abiaduraren menpeko da eta lege konstitutibo bisko-hiperelastiko baten bidez azaltzen da.

Cauchy-ren tentsio tentsorearen eta ezkerreko Cauchy-Green-en deformazio tentsorearen arteko erlazioa material hiperelastiko batentzat (ikusi Eranskina xehetasun gehiagorako):

$$\sigma^e = 2\left(\frac{\partial \psi}{\partial I_1} + I_1 \frac{\partial \psi}{\partial I_2}\right) b - 2\frac{\partial \psi}{\partial I_2} b^2 - pI \qquad (5.2)$$

Kontuan izanik saiakuntzak konpresiopean egiten direla (deformazio abiadura handiko konpresioko saiakuntzak), azken terminoa "$-pI$" da. Eta (2.14) ekuazioak dioenetik, Rivlin-en eredua 3 parametroren kasurako:

$$\psi = C_{10}(I_1 - 3) + C_{01}(I_2 - 3) + C_{11}(I_1 - 3)(I_2 - 3) \qquad (5.3)$$

Espezimen konprimaezin eta isotropo bati karga uniaxiala aplikatzen zaiola kontsideratzen da. Luzapen nagusiak $\lambda_1 = \lambda = 1 + \varepsilon_{11}$ dira, kargaren norabidean (ε_{11} deformazio nagusia delarik norabide berdinean) eta, ondorioz, $\lambda_2 = \lambda_3 = \lambda^{-1/2}$. Beraz, (5.2) ekuazioan:

$$\sigma_{11}^{e} = 2\frac{\partial \psi}{\partial I_1}\lambda^2 + 2\frac{\partial \psi}{\partial I_2}(I_1\lambda^2 - \lambda^4) - P \tag{5.4}$$

$$\sigma_{22}^{e} = 0 = \sigma_{33}^{e} \tag{5.5}$$

ψ inbarianteekiko deribatuz eta ordezkatuz:

$$\begin{aligned}\sigma_{11}^{e} &= 2\left[C_{10} + C_{11}(I_2 - 3)\right]\lambda^2 + 2\left[C_{01} + C_{11}(I_1 - 3)\right](I_1\lambda^2 - \lambda^4) - P = \\ &= 2\lambda^2 C_{10} + 4\lambda C_{01} + C_{11}\left[2\lambda^2(I_2 - 3) + 4\lambda(I_1 - 3)\right] - P\end{aligned} \tag{5.6}$$

P adierazpen horretatik kentzeko $\sigma_{22}^{e} = 0$ erabiltzen da.

$$P = 2\lambda^{-1}C_{10} + 2\lambda^{-1}(I_2 - 3)C_{11} + 2\left(I_1\lambda^{-1} - \lambda^{-2}\right)C_{01} + 2(I_1 - 3)\left(I_1\lambda^{-1} - \lambda^{-2}\right)C_{11} \tag{5.7}$$

Aurreko adierazpenak luzapenaren menpe idazten badira, tentsio kuasiestatikoarentzat adierazpen finala ondokoa da:

$$\sigma_{11}^{e} = 2(\lambda^2 - \lambda^{-1})C_{10} + 2(\lambda - \lambda^{-2})C_{01} + 6(\lambda^3 - \lambda^2 - \lambda + \lambda^{-1} + \lambda^{-2} - \lambda^{-3})C_{11} \tag{5.8}$$

C_{10}, C_{01} eta C_{11} saiakuntza unidimientsionaletik determinaturiko parametroak izanik. (5.8) ekuazioa doitzerako orduan saiakuntza kuasiestatikoetako luzapen eta tentsioaren datuak hartu behar dira kontuan. Hemen minimo karratuen doiketa erabili da tentsioaren errore erlatiboa minimizatzeko helburuarekin.

Propietate biskoelastikoei dagokienez, (2.41) ekuazioa kontuan hartu behar da hiru dimentsiotako kasurako. Hemen $\Omega_{\tau=-\infty}^{t}\{C(\tau)\}$ matrize funtzionalak deformazioaren historiak tentsioarengan duen eragina deskribatzen du. Lortzen zaila denez gero, zenbait hurbilketa egin dituzte Lockett-ek[86] eta Yang eta bestek[68,69]. Material hiperelastikoentzat bitarteko malguki moduan kontsideratu dute[7]:

$$\sigma^{v} = F\frac{\partial \psi}{\partial E}F^{T} \tag{5.9}$$

$\frac{\partial \psi}{\partial E} = S$ kontsidera daiteke ondoko adierazpen moduan:

$$\frac{\partial \psi}{\partial E} = \int_{-\infty}^{t} \frac{\partial u}{\partial E}(I_1, I_2, I_3, t-\tau)d\tau \tag{5.10}$$

Nukleoa den funtzioa, $u\left(I_1,I_2,I_3,t-\tau\right)$, bi zatiren biderkaketa moduan proposa daiteke; bata, deformazioaren menpeko dena, eta bestea, denboraren menpeko dena:

$$u\left(I_1,I_2,I_3,t-\tau\right)=U(I_1,I_2,I_3)\cdot m(t-\tau) \tag{5.11}$$

Hemen $m(t-\tau)$ memoria funtzioa da, erlaxazio funtzioa t denborarekin gutxituz doana; orokorrean, Prony deritzen serie esponentzialekin osaturiko seriea moduan kontsideratzen da:

$$m(t-\tau)=\sum_{i=1}^{N} m_i \cdot \exp\left(-\frac{t-\tau}{\theta_i}\right) \tag{5.12}$$

Non:

- m_i ponderazio-faktoreak izanik $\sum_{i=1}^{N} m_i = 1$ betetzen dutelarik

- θ_i erlaxazio denborak dira.

(5.10) ekuazioa (5.9) ekuazioan sartuz ondoko adierazpena lortzen da:

$$\sigma^v = F(t)\cdot \int_{-\infty}^{t} \left(\frac{\partial U}{\partial E}\left(I_1,I_2,I_3\right)\cdot m(t-\tau)\right) d\tau \cdot F^T(t) \tag{5.13}$$

Yang-en kontribuzioa eredu honetan U-ren definiziotik dator, ondoko moduan:

$$U\left(I_1,I_2,I_3\right)=\phi\left(I_1,I_2,I_3\right)\cdot \dot{E}(\lambda) \tag{5.14}$$

Non ϕ funtzioa honela definitzen den:

$$\phi(I_1,I_2)=C_2+C_3(I_2-3) \tag{5.15}$$

Deformazioaren historiaren efektua tentsioaren gainean (5.12) ekuazioan erlaxazio denbora konstante bakarra (N=1) sartuz hartu da kontuan. Suposaketa hau Yang eta bestek[68] esandakoarekin bat dator eta eredu material bat formulatzean beharrezkoak diren parametroen kopurua minimizatzearen helburua betetzen du; helburu hau, beti ere datu esperimentalekin korrelazioa modu esanguratsuan konprometitu gabe. Yang eta bestek beraien ikerketa lanean Maxwell-en eredu orokortuak deskriba dezakeen deformazio abiaduren tarteari buruzko azterketa egin zuten eta tentsioaren eta motelgailuari lotutako

deformazio abiaduraren arteko erlazio bat lortu zuten; honen arabera, motelgailua deformazio abiaduraren n.erroarekiko proportzionala litzateke. Hortaz, horrelako eredua deformazio abiaduren tarte handiago bat lortzeko erabil liteke.

Erantzun biskoelastiko erresultantea ondoko adierazpenak emana dator:

$$\sigma_{11}^{v} = \lambda^2 \int_o^t \lambda[C_2 + C_3(I_2(\tau) - 3)] \exp\left(-\frac{t-\tau}{C_4}\right) \dot{\lambda} d\tau + \\ + \frac{1}{2}\lambda^{-1} \int_o^t \lambda^{-2}[C_2 + C_3(I_2(\tau) - 3)] \exp\left(-\frac{t-\tau}{C_4}\right) \dot{\lambda} d\tau \tag{5.16}$$

Non I_2 deformazioaren bigarren inbariantea den,

$$I_2 = \frac{1}{2}\left[I_1^2 - \mathrm{tr}(B^2)\right] = \lambda^{-2} + 2\lambda \tag{5.17}$$

Eta B ezkerreko Cauchy-Green deformazio tentsorea, ondoko eran definituta dagoena:

$$B = \begin{bmatrix} \lambda^2 & 0 & 0 \\ 0 & \lambda^{-1} & 0 \\ 0 & 0 & \lambda^{-1} \end{bmatrix} \tag{5.18}$$

Zati biskoelastikoa zaila da minimo karratuen hurbilketa estandarrean inplementatzea; zailtasuna konboluzio integralaren determinazioan datza. Hemen definitzen den algoritmoa doiketa anitzeko prozedura ez linealean oinarritzen da, Doman[119]-ek ezarri bezala, eta inplementatzen erlatiboki erraza da; azterketa honetan Matlab-en egin da.

(5.16) ekuazioko hiru parametro biskoelastikoak (C_2, C_3 eta C_4) PSO hurbilketaren bitartez doitu dira. Doiketa algoritmoaren garapena hurrengo atalean deskribatzen da.

Formulazio honekin deskribatzen den portaera biskoelastikoa Maxwell-en eredu orokortuaren parekoa da; motelgailu biskosoa eta malguki elastikoa seriean konektatuta daudelarik. Deformazioaren menpeko malgukiaren modulu ez-lineala $E = C_2 + C_3(I_2 - 3)$, eta motelgailuaren biskositatea $\eta = E \cdot C_4$ dira, non C_4 ereduraren erlaxazio denbora konstantea den.

Ekuazio osagarri osoa (5.8) eta (5.16) ekuazioen batuketatik lortzen da:

$$\sigma_{11} = 2(\lambda^2 - \lambda^{-1})C_{10} + 2(\lambda - \lambda^{-2})C_{01} + 6(\lambda^3 - \lambda^2 - \lambda + \lambda^{-1} + \lambda^{-2} - \lambda^{-3})C_{11} +$$
$$+\lambda^2 \int_0^t \lambda[C_2 + C_3(I_2(\tau) - 3)]\exp\left(-\frac{t-\tau}{C_4}\right)\dot{\lambda}d\tau + \qquad (5.19)$$
$$+\frac{1}{2}\lambda^{-1}\int_0^t \lambda^{-2}[C_2 + C_3(I_2(\tau) - 3)]\exp\left(-\frac{t-\tau}{C_4}\right)\dot{\lambda}d\tau$$

5.3 DOIKETA ESTRATEGIA

C_{10}, C_{01} eta C_{11} parametroak minimo karratuen doiketaren bitartez determinate dira, aurreko atalean esan bezala. Zati biskoelastikoari dagokionez, hala ere, minimo karratuen hurbilketa estandarra inplementatzen zaila da; zailtasuna konboluzio integralaren determinazioan datza[120]. Hemen definitzen den algoritmoa doiketa anitzeko prozedura ez linealean oinarritzen da, Doman-ek[119] ezarri bezala eta inplementatzen erlatiboki erraza da; azterketa honetan Matlab-en egin da.

(5.16) ekuazioko hiru parametro biskoelastikoak (C_2, C_3 eta C_4) Particle Swarm Optimization (PSO) hurbilketaren bitartez doitu dira. Doiketa algoritmoaren garapena ondoko azpiatalean deskribatzen da, 0.9 g/cm^3 dentsitateari aplikatzen zaiolarik.

5.3.1 PSO metodoa

5.2.1.1 Algoritmoaren aurrekariak

PSO optimizazio teknika estokastikoa da multzoen inteligentzian oinarritutakoa. 1995ean garatu zuten James Kennedy and Russell Eberhart-ek, funtzio jarrai ez-linealak optimizatzeko asmoarekin. Metodoak bere jatorria metodologia nagusi bitan du: batetik, bizitza artifiziala orokorrean eta hegazti-andana eta arrain-sarda bereziki; eta beste aldetik, eboluzio-konputazioa, eta honi lotuta algoritmo genetikoak. Ez da konputazionalki garestia, ezta memoriaren beharrizanei begira, ezta denbora kontsumoaren aldetik[110].

Algoritmo hau bere erraztasunarenagtik, sendotasunarengatik eta konbergentzia azkarra izateagatik aukeratu da. Parametro gutxi batzuen doiketa soilik da beharrezkoa eta optimo globalera iristeko gai da, optimizatu nahi den funtzioa oso ez-lineala izanda ere[110]. Kontrol

Ingeniaritzan edota Informatikan[111,112] modu arrakastatsuan aplikatu izan da eta Materialen Zientziaren arlo batzuetan ere[114,121].

PSO batean helburua emandako kostu funtzio baten balio minimoa lortzean datza. Normalean, mota honetako algoritmoak bere balioa iterazioetan zehar hobetzen joatea bermatzen du. Hortaz, helburua ondoko eran defini daiteke:

$$Cost = f(\vec{p}) \tag{5.20}$$

$$\vec{p} = (p_1, p_2, \ldots, p_n) \tag{5.21}$$

$$\vec{p}_{optim} = Argmin_{\vec{p}}\, f(\vec{p}) \tag{5.22}$$

Proposaturiko optimizazio algoritmoak multzo bat osatuz bilatze-espazioan zehar mugituz doazen N partikula definitzen ditu eta k partikula bakoitzak bere posizio bektorea du, $\vec{p}_k$. Partikulen osizioen osagaiak doitu beharreko parametroak dira. Beraz partikula bakoitzak $c(\vec{p}_k)$ kostu bat du bere posizioari lotuta. Kostu funtzioaren optimizazioa partikulak parametroen-espazioan zehar mugitzen direnean soluziorik onena bilatuz lortzen da, ondorengo mugimenduaren ekuazioen bitartez:

$$\overrightarrow{v_k}(t_{n+1}) = w \cdot \overrightarrow{v_k}(t_n) + f_p \cdot r_p \cdot \left(\vec{p}_{k,opt} - \vec{p}_k(t_n)\right) + f_g \cdot r_g \cdot \left(\vec{p}_{globalopt} - \vec{p}_k(t_n)\right) \tag{5.23}$$

$$\vec{p}_k(t_{n+1}) = \vec{p}_k(t_n) + \overrightarrow{v_k}(t_n) \tag{5.24}$$

t_{n+1} eta t_n uneko eta aurreko iterazio denborak dira. Ekuazio bi hauek hainbat alditan edo iteraziotan aplikatzen dira.

Ekuazioetan sartutako parametroak 5-1 taulan definituta daude.

(5.23) ekuazioko inertzia-pisuaren koefizienteari dagokionez, txikitze ez-lineala duen inertzia-pisu bat kontsideratu da, funtzio ahur batekin Zheng eta beste[114]-k diotenarekin bat datorrelarik:

$$w = (w_{\max} - w_{\min})\frac{k^2}{k_{\max}^2} + (w_{\min} - w_{\max})\frac{2k}{k_{\max}} + w_{\max} \tag{5.25}$$

w_{max} eta w_{min} inertzia-pisu maximo eta minimoa dira, hurrenez hurren, eta k_{max} iterazio kopuru maximoa da. Inertzia-pisu handi batek bilaketa globala errazten du, inertzia-pisu txiki batek bilaketa lokala errazten duen bitartean[112].

5-1 taula. PSO algoritmoaren parametroak

Parametroa	Definizioa	Balioa edo balio-tartea
r_p	k. partikulak lortutako posizio optimora duen erakarpen-indarra	0 eta 1 balioen arteko ausazko balio uniformea. Balio hau iterazio bakoitzean kalkulatzen da
r_g	Partikula guztiek lortutako optimo globalera duten erakarpen-indarra	0 eta 1 balioen arteko ausazko balio uniformea. Balio hau iterazio bakoitzean kalkulatzen da
f_p	Azelerazio koefiziente honek garrantzi handiagoa ematen dio partikula bakoitzaren konbergentziari posizio optimorantz	Balio konstante positibo bat da
f_g	Azelerazio koefiziente honek garrantzi handiagoa ematen dio konbergentziari posizio optimo globalerantz	Balio konstante positibo bat da
w	Partikulen inertzia	Balio positibo bat da
$\vec{p}_k(t_n)$	k. partikularen posizioa t_n unean adierazten duen parametroa	Parametroen eremu eskualde posible batean hasierazten da modu estokastiko batean
$\overrightarrow{v_k}(t_n)$	k. partikularen abiadura t_n unean adierazten duen parametroa	Ausazko balio txikietan hasierazten da
$\vec{p}_{k,opt}$	k. partikularen parametro posiziorik onena	Partikulen hasierako posizioetan hasierazten da
$\vec{p}_{globalopt}$	Partikula guztien posizio parametro onena	Partikula guztien posizio onenetan hasierazten da

R^2 determinazio koefizientearen definizio klasikoa aplikatu da ereduaren doiketaren ontasuna neurtzeko datu esperimentalekiko; honetan oinarrituz, GE errore globala hurrengo erlazioaren bitartez definitzen da:

$$GE = \frac{\sum_{i=0}^{M-1}\left[\hat{\sigma}_n\left(i\Delta t, A_2, A_3, A_4\right) - \sigma_n(i\Delta t)\right]^2}{\sum_{i=0}^{M-1}\left[\overline{\sigma}_n - \sigma_n(i\Delta t)\right]^2} \tag{5.26}$$

M doiketan parte hartzen duten datu kopurua da, Δt denbora pausoa da, σ_n tentsioaren balio esperimentala da luzapen puntu bakoitzean, $\hat{\sigma}_n$ ekuazio osagarriaren bidez kalkulaturiko tentsioa da eta $\overline{\sigma}_n$ batezbesteko tentsio esperimentala da. Iragarritako balioak esperimental balioetara hurbiltzen diren heinean, GE zerorantz hurbiltzen da. Aurreko ekuazioaren hedadurak kurba anitzerako ondoko adierazpena ematen du:

$$GE_{total} = \sum GE_N \tag{5.27}$$

N doitu beharreko kurba kopurua da, hots, deformazio abiadura desberdinei dagozkien kurbak. R^2 determinazio koefizientea kontsideratu da eredu teorikoaren doiketaren ontasunaren adierazle moduan datu esperimentalekiko. Kurba desberdinen aldibereko doiketaren determinazio koefizientea lortu da GE_{total} kurben kopurutik kenduta eta ostean kurba kopuruaz zatituta[122]. Ebatzi beharreko optimizazio problema errorearen minimizazioa da; hau da, helburu-funtzioa den ($1-R^2$) minimizatzea zerorantz, hasierako parametroak aldatuz joanez:

$$Error = \left(1 - R^2\right) = \frac{GE_{total}}{N} \tag{5.28}$$

Oinarrizko optimizazio sekuentzia ondokoa da:

1. Luzapena, denbora eta materialaren konstanteak emanik, $\hat{\sigma}_n$ tenstioaren balioak ateratzen da. C_2, C_3 eta C_4 parametroen hasierako balioak literaturatik hartu dira. Batezbesteko tentsio esperimentala ere saiakuntza guztientzat deformazio-abiadura bakoitzean kalkulatzen da ($\overline{\sigma}_n$).Iterazio kopuru maximoa ezartzen da.

2. Helburua den funtzioa kalkulatzen da (5.28) ekuaziaren bidez.

3. Aurreko iterazioetako materialaren konstanteak erabiliz, eta helburua den funtzioaren uneko eta aurreko balioak konparatuz, helburu-funtzio hori minimizatuko duten koefiziente berriak iragartzen dira.

Bestela esanda, partikula bakoitzaren uneko kostu funtzioa, $c(\vec{p}_k)$, partikularen posizio onena, $\vec{p}_{k,opt}$, baino hobea bada, kostu funtzio honek $\vec{p}_{k,opt}$ ordezkatuko du eta uneko posizioak partikularen posizio onena ordezkatzen du.

Partikularen posizio onena, $\vec{p}_{k,opt}$, partikula guztien posizio onenarekin konparatzen da, $\vec{p}_{globalopt}$. Uneko $\vec{p}_{k,opt}$, $\vec{p}_{globalopt}$ baino hobea bada, orduan posizio global onena ordezkatzen du eta uneko posizioak partikulen posizio onena ordezkatzen du.

4. Errepikatu iterazio kopuru maximoa lortzen den arte.

Partikula bakoitzak bere soluziorik onena du (fitness) iterazio bakoitzean, **pbest** deitua, pertsonal onena; eta partikula guztien soluzio onena iterazio bakoitzean **gbest** deitzen da, global onena. Balio bi hauek 5-2 irudiko fluxu-diagraman erakusten dira:

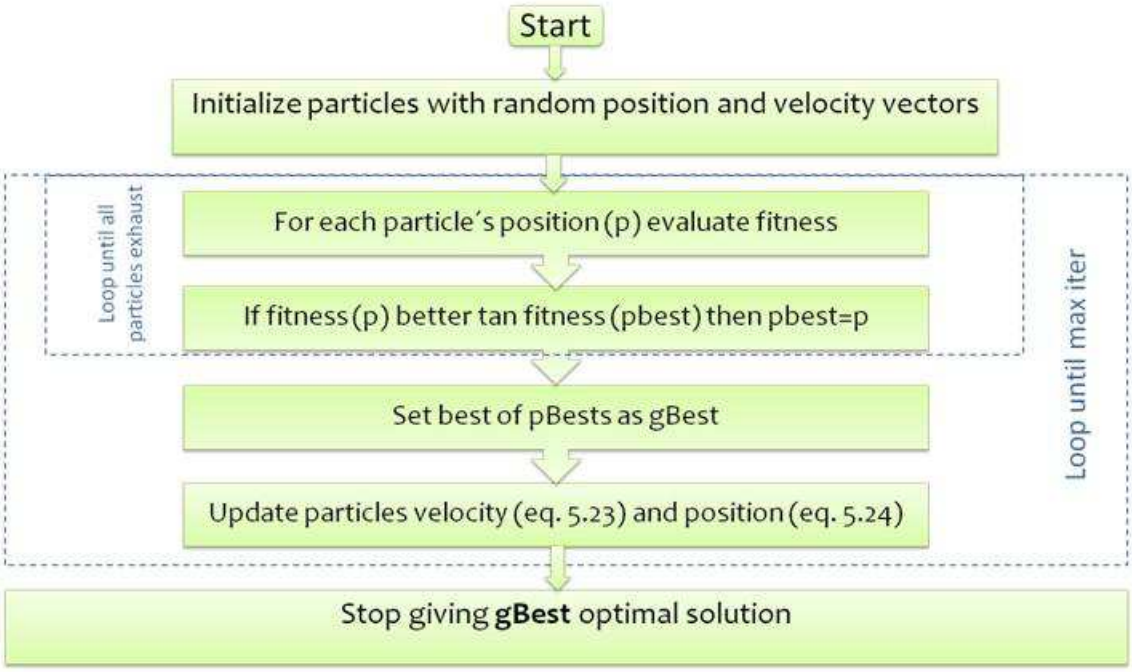

5-2 irudia. PSO algoritmoaren fluxu-diagrama

5.2.1.2. Algoritmoaren abantailak

Algoritmo honen abantaila nagusienetako bat zera da, kostu funtzioarengan ia ez dagoela murrizketarik. Teknika honen emaitzak hasierako parametroen estimazioekiko sentikorra dela egia izanda ere, soluzioa etengabe hobetuz doa (beti da aurreko iterazioan baino hobea); hau ez da honela gertatzen jeitsiera-gradientearen algoritmoarekin.

All particles in PSO algoritmoan partikula guztiak populazioaren osagai mantentzen dira algoritmoa exekutatu ahala. Aurreko iterazioetan kalkulaturiko balioak berrerabiliak dira algoritmo genetikoekin baino modu zuzenago batean.

5.3.2 PSO-ren aplikazioa Yang-en ereduari (zati hiperelastikoa minimo karratuen bidez)

Proposaturiko ereduaren C_{10}, C_{01} eta C_{11} parametro hiperelastikoak datu esperimentaletara doituak izan dira minimo karratuen hurbilketaren bitartez; modu honetan errore erlatiboa tentsio nominalean minimizatu egin da. Deformazio abiadurarik geldoenari dagozkion datu esperimentalak ($0.057s^{-1}$), kuasiestatiko kontsideratu den saiakuntzarenak, erabili izan dira. Materiala guztiz konprimaezina dela kontsideratu da parametro hiperelastiko hauek lortzerakoan.

Hortaz, minimizatu beharreko errore erlatiboa (5.29) ekuazioan ematen da:

$$relative\_error = \sum_{i=1}^{N} \left(\frac{\sigma_i^{theoretical} - \sigma_i^{experimental}}{\sigma_i^{experimental}} \right)^2 \tag{5.29}$$

$\sigma_i^{theoretical}$ (5.8) ekuazioko tentsio teorikoari dagokio eta $\sigma_i^{experimental}$ esperimentalki neurtutako tentsioari dagokio.

Parametro biskoelastikoei dagokienez, kautxu-erako materialentzat literaturan[68] agertzen diren balioak hartu dira hasierako estimazio modura C_2, C_3 eta C_4 parametroentzat. Parametro hauek aurretik azaldu den PSO doiketa anitzeko algoritmo ez-linealaren bitartez doitu dira, partikulen posizio bektoreen osagaiak izanik. Proposaturiko ereduaren eta Maxwell-en eredu orokortuaren artean dagoen analogiari jarraituz, 5.2 atalean deskribatu dena, C_2, C_3 eta C_4 positiboak izatea beharrezkoa da E-ren balio positivo bat eman dezaten. Eskakizun hauek zentzu fisikoa ematen diote ereduari.

5.4 EMAITZAK

5.4.1 0.057, 0.57 eta 5.7 s^{-1} deformazio abiadurak (guztiak, altuena izan ezik)

5.3.2.1. PSO-ren aplikazioa Yang-en ereduari. Ereduaren parametroen lortzea

PSO 90/10 proportzioko nahasteari aplikatu zaio, hain zuzen ere 0.9 g/cm^3 dentsitatedun probeta handiei. Ondoren, parametroen lorpena azpiatal bitan banatzen da, hiperelastikoa batetik eta biskoelastikoa bestetik; izan ere, lehendabizikoak minimo karratuekin lortzen dira eta PSO biskoelastikoei soilik aplikatu zaie[123].

a) Parametro hiperelastikoak

90/10 proportzioko eta 0.9 g/cm^3 dentsitatedun nahaste bati dagozkion koefiziente hiperelastikoak 5-2 taulan erakusten dira, kurben doikuntzan ateratako R^2 determinazio koefizientearekin batera.

5-2 taula. Koefiziente hiperelastikoak eta determinazio koefizientea

	C_{01} (Mpa)	C_{10} (Mpa)	C_{11} (Mpa)	R^2
0.92A_0.057	-1,56	2,8	0,24	0,9946
0.93A_0.057	-1,52	2,7	0,23	0,9927

¡Error! No se encuentra el origen de la referencia.5-3 irudiak 0.9 g/cm^3 dentsitaterako tentsio-luzapen kurbak erakusten ditu; materialaren erantzun elastiko ez-lineala hauteman daiteke eta proposaturiko ereduaren zati hiperelastikoaren korrespondentzia ona datu esperimentalekin. Emaitza hauek kurbek iragarritako desbiderazioak datu esperimentaletatik %1a baino txikiagoak direla erakusten dute.

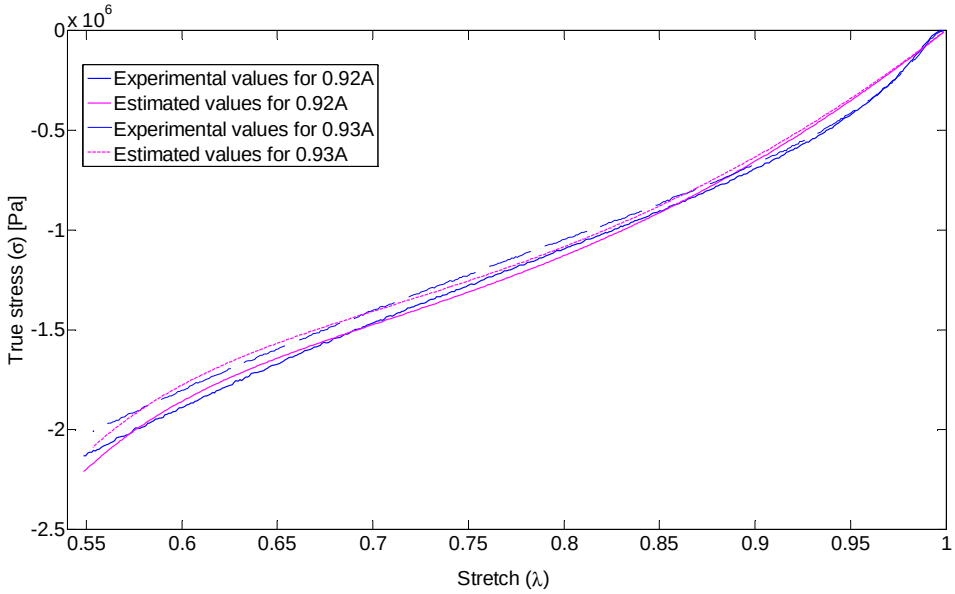

5-3 irudia. Tentsio-luzapen kurba kuasiestatikoak 0.9 g/cm^3 dentsitaterako vs. eredu teorikoaren osagai hiperelastikoa

Gainontzeko dentsitateetako saiakuntzei dagokienez, ereduaren eta emaitza esperimental kuasiestatikoen arteko konparaketa jarraian erakusten da:

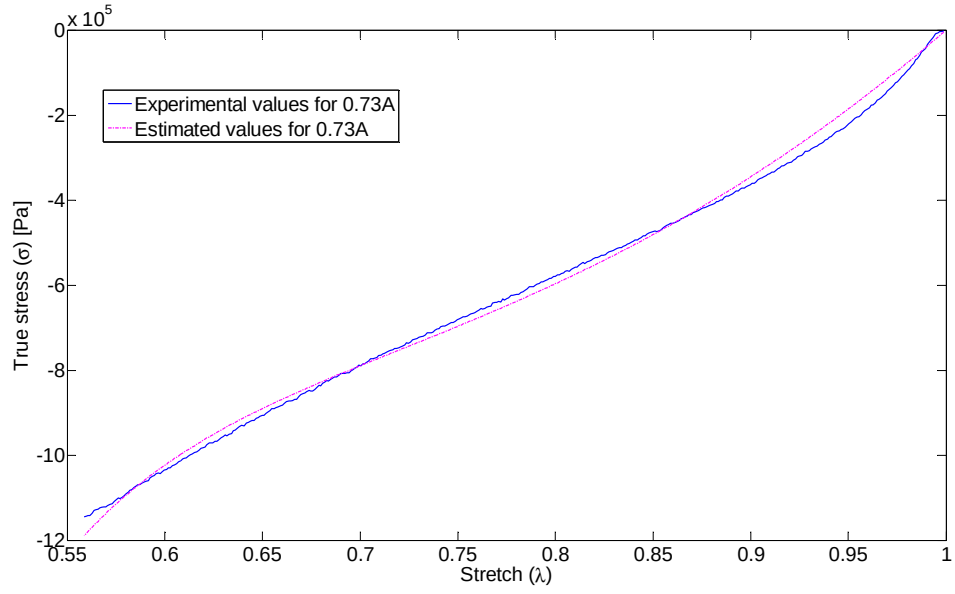

5-4 irudia. Tentsio-luzapen kurba kuasiestatikoak 0.7 g/cm^3 dentsitaterako vs. eredu teorikoaren osagai hiperelastikoa

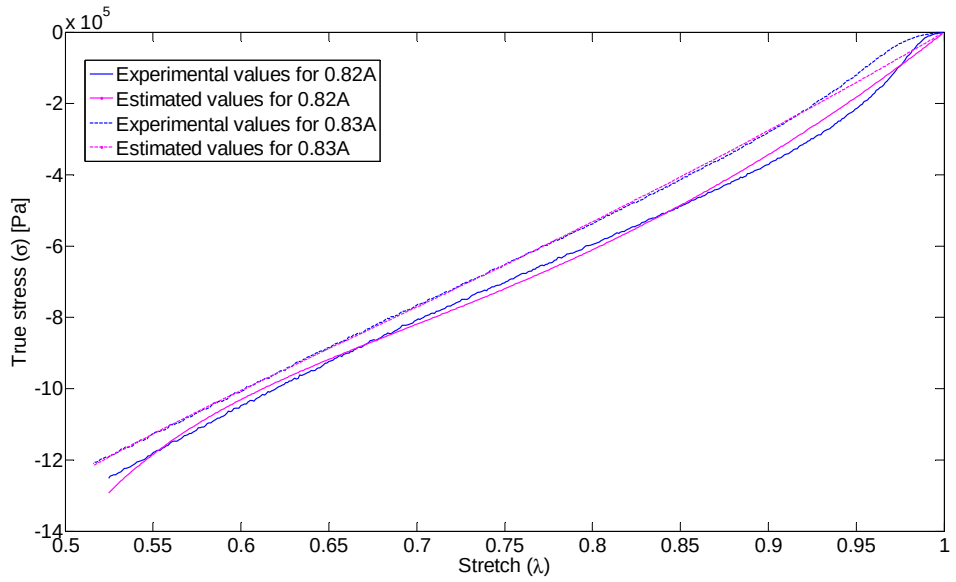

5-5 irudia. Tentsio-luzapen kurba kuasiestatikoak 0.8 g/cm^3 dentsitaterako vs. eredu teorikoaren osagai hiperelastikoa

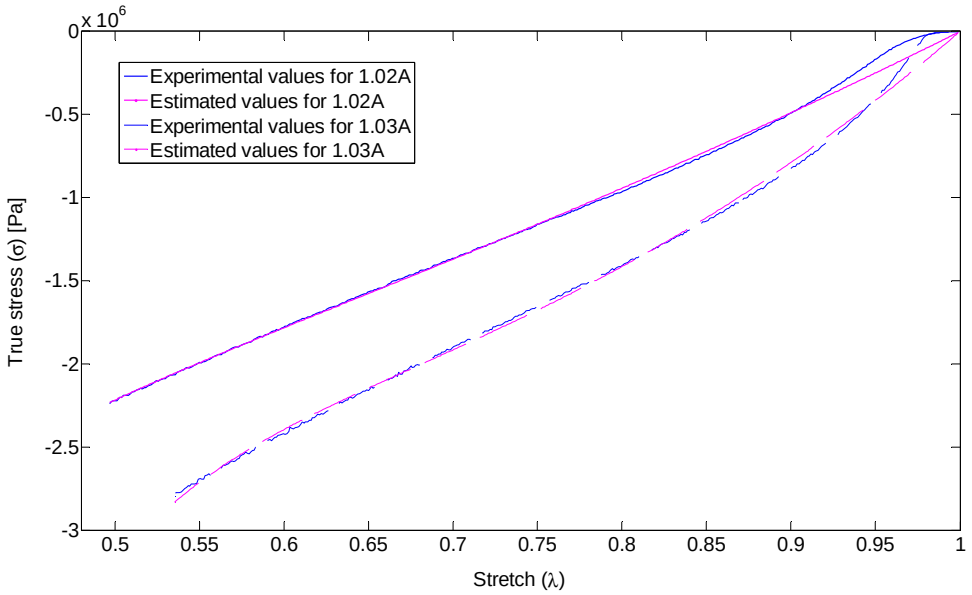

5-6 irudia. Tentsio-luzapen kurba kuasiestatikoak 1 g/cm^3 dentsitaterako vs. eredu teorikoaren osagai hiperelastikoa

b) Parametro biskoelastikoak

5-7 irudiak bilaketa-espazioa adierazten du, hots, hiru parametroen balio posibleen tartea 0.9 g/cm^3 dentsitatearen kasuan; iterazio bakoitzeko puntu desberdinak erakusten dira bertan. Puntu hauek C_2, C_3 eta C_4 parametroen balio desberdinek osatutako triadak dira 5.3.1. atalean azaldu bezala. Prozesu iteratiboaren hasieran bilaketa espazioa zabala da. Ondorengo iterazioentzat espazio hau estutzen doa, kostu funtzioaren balioa txikitu egiten da eta puntu gehienak triadaren posizio optimorantz zuzentzen dira.

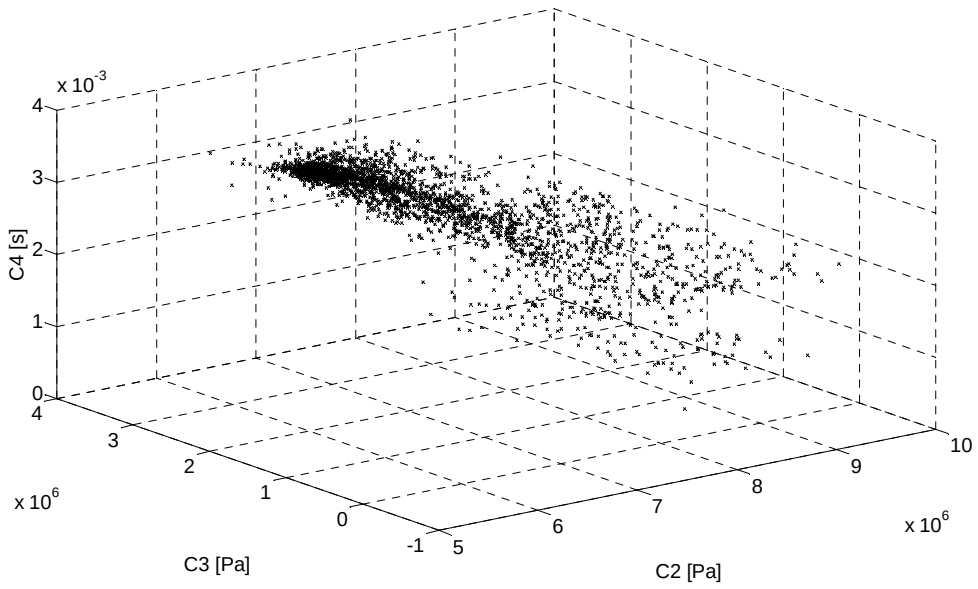

5-7 irudia. Parametro biskoelastikoen balio desberdinak PSO-ren exekuzioan zehar hirukote optimoarekin bat egin arte (0.9 g/cm^3 dentsitatearen kasua)

5-8, 5-9 eta 5-10 irudiek (1-R^2) kostu funtzioa edo errorea erakusten dute algoritmoaren iterazioetan zehar C_2, C_3 eta C_4 parametroekin konparatuz (0.9 g/cm^3 dentsitatearen kasua). Ikus daitekeenez, kostu funtzioaren balioak iterazio bakoitzean txikituz doaz bilaketa espazioan, parametroek berauen baliorik onenetara iristen doazen heinean; hau da, hasiera batean sakabanatuta aurkitzen diren puntuen puntu baterantz konbergentzia ematen da, iterazioak igaro ahala. Puntu hau grafiko bakoitzean dagokion parametroaren balio optimoa izango da, 5-3 taulan ikus daitekeenez. R^2 koefizientearentzat lortutako balioak ere taula honetan erakusten dira.

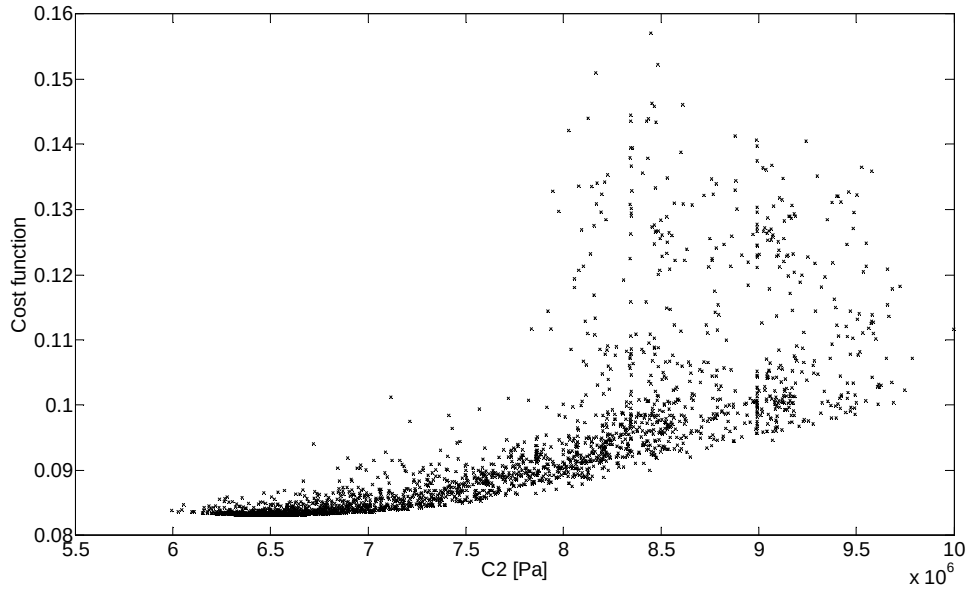

5-8 irudia. (1-R^2) kostu funtzioa vs. C_2

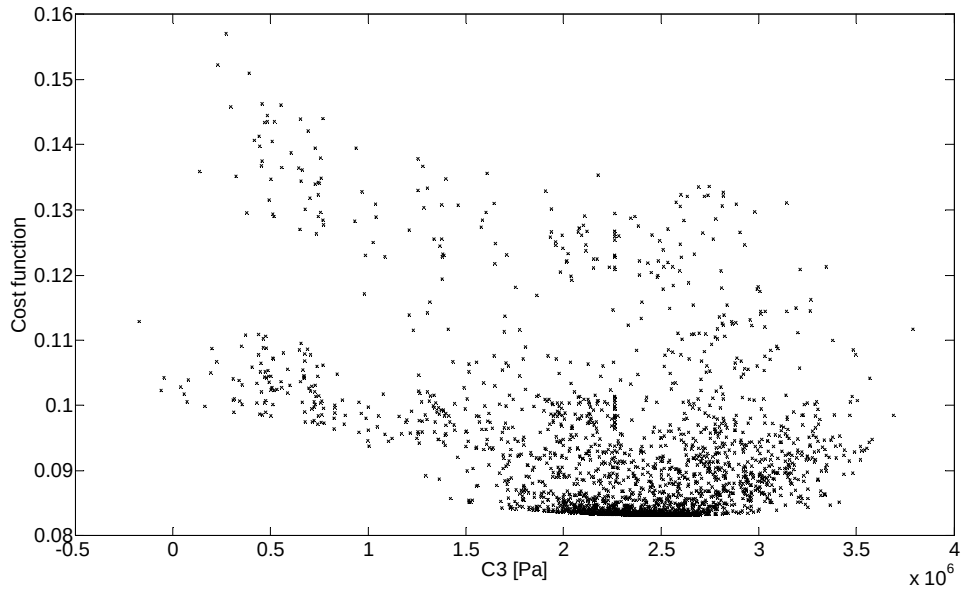

5-9 irudia. (1-R^2) kostu funtzioa vs. C_3

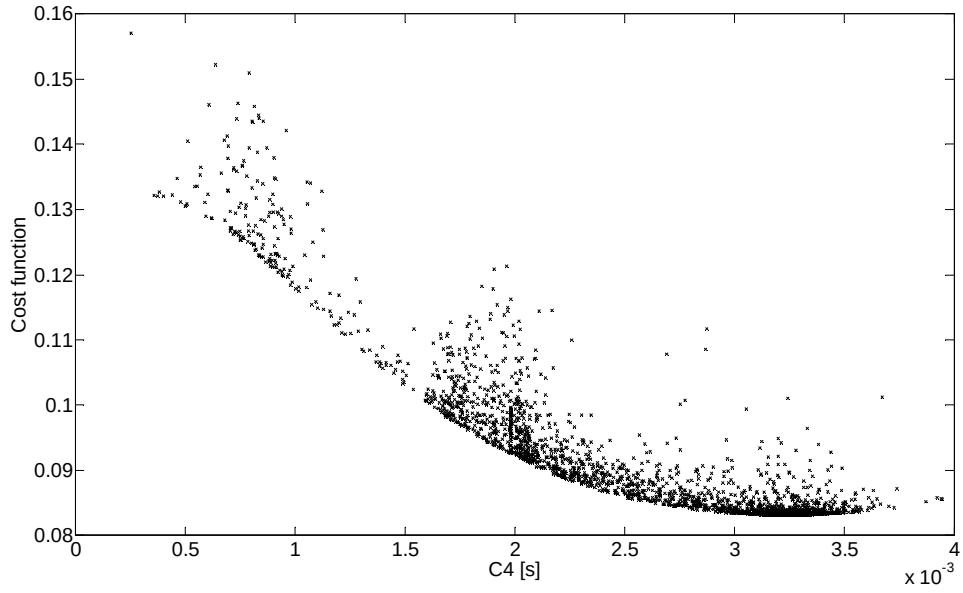

5-10 irudia. ($1-R^2$) kostu funtzioa vs. C_4

5-3 taula. Parametro biskoelastikoentzat balioak eta R^2 kurba desberdinentzat (0.9 g/cm^3 dentsitatearen kasurako)

Parameter	Value
C2 [Pa]	6,5117E+06
C3 [Pa]	2,5077E+06
C4 [s]	3,2202E-03
Cost function	0,08317
R2_0,57 (a)	0,9954
R2_0,57 (b)	0,9905
R2_5,7 (a)	0,9701
R2_5,7 (b)	0,9608

Kurba teorikoen eta datu esperimentalen arteko konparaketa 5-11 irudian erakusten da; 0.57s^{-1} eta 5.7s^{-1} deformazio abiadurentzat datu esperimentalak erakusten ditu proposaturiko ereduarekin konparatuz.

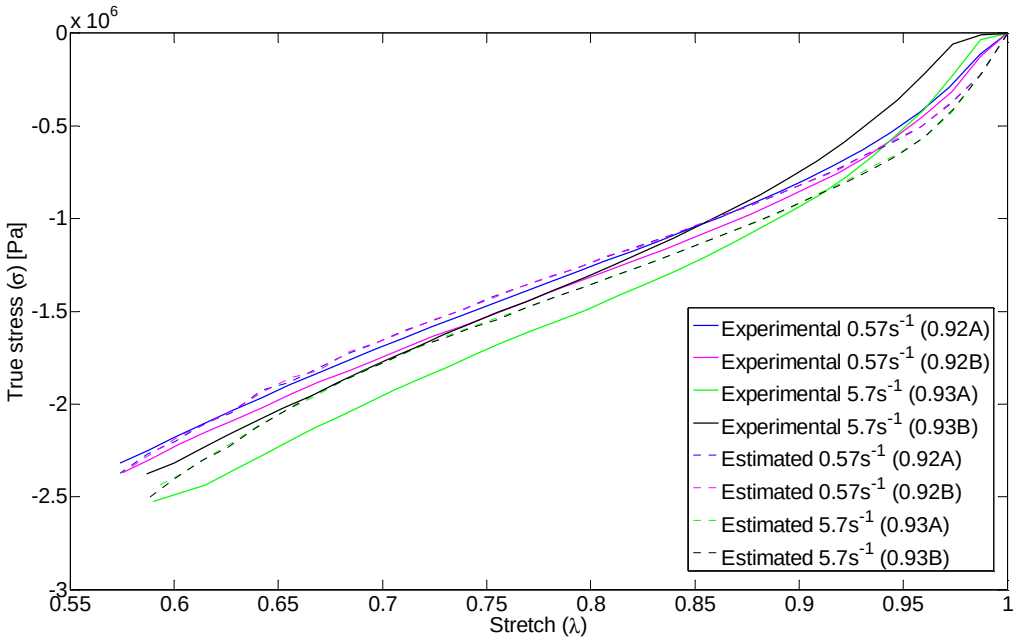

5-11 irudia. Datu esperimentalen eta kurba teorikoen arteko konparaketa 0.9 g/cm^3 dentsitaterako

1 eta 0.9 bitarteko luzapen tarteek hasierako hutsuneak ixten dabiltzan saiakuntzako fasea beren baitan dutela antzeman daiteke, saiakuntza esperimentalen hasierako etapetan zehar; saiakuntzen lehen zati hau, ondorioz, ereduaren doiketa neurketa esperimentalekiko egiterakoan ez da kontuan hartzen. Ondorioz, eredua nahiko ondo doitzen da bere datu esperimental homologoekiko; iragarritako kurben desbiderazioak kurba esperimentalekiko sekziorik txarrenean %10a inguru dira.

PSO optimizazio algoritmoari dagokionez, teknika honen emaitzak parametroen hasierako hurbilketekiko sentikorrak direla egia bada ere, konbergentzia egokia du datu esperimentalekiko korrelazio ona duten azken emaitza batzuetara.

Azkenik,. Kurba teorikoen eta neurketa esperimentalen arteko konparaketa 0.7 g·cm^{-3}, 0.8 g·cm^{-3} eta 1 g·cm^{-3} dentsitateei dagokienez, grafikoki erakusten da ondorengo 5-12, 5-13 eta 5-14 irudietan:

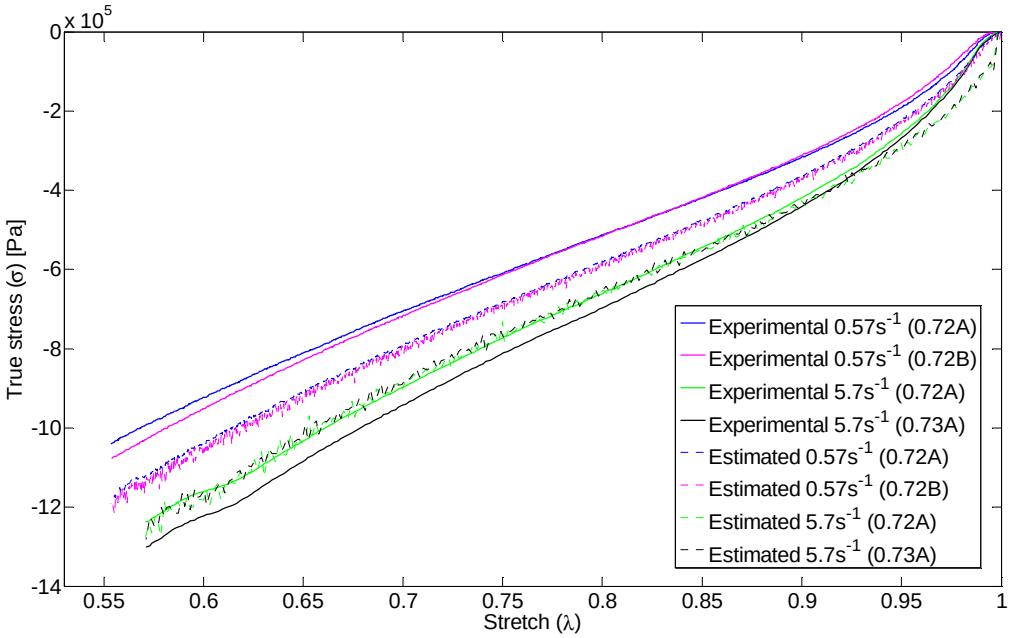

5-12 irudia. Datu esperimentalen eta kurba teorikoen arteko konparaketa 0.7 g/cm³ dentsitaterako

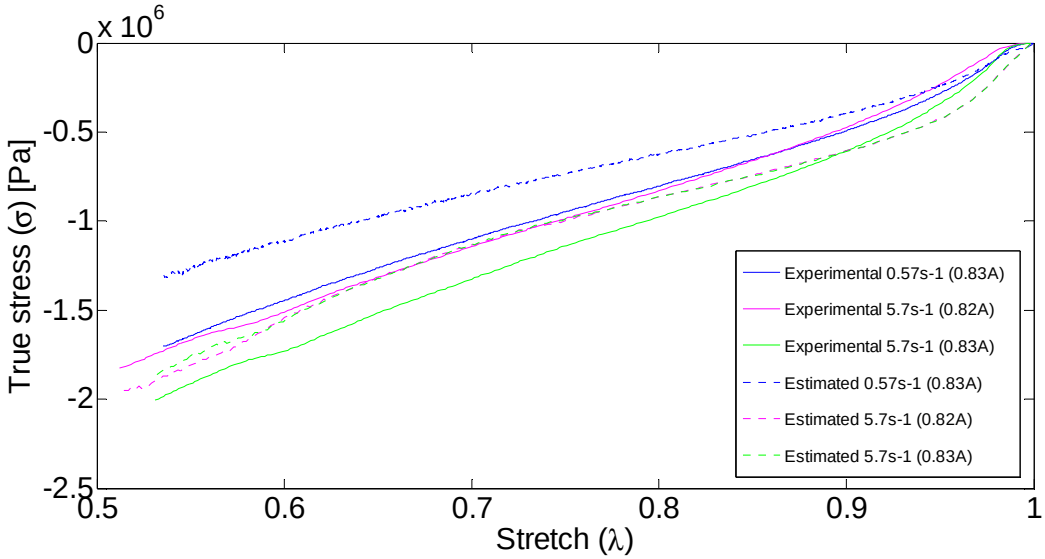

5-13 irudia. Datu esperimentalen eta kurba teorikoen arteko konparaketa 0.8 g/cm³ dentsitaterako

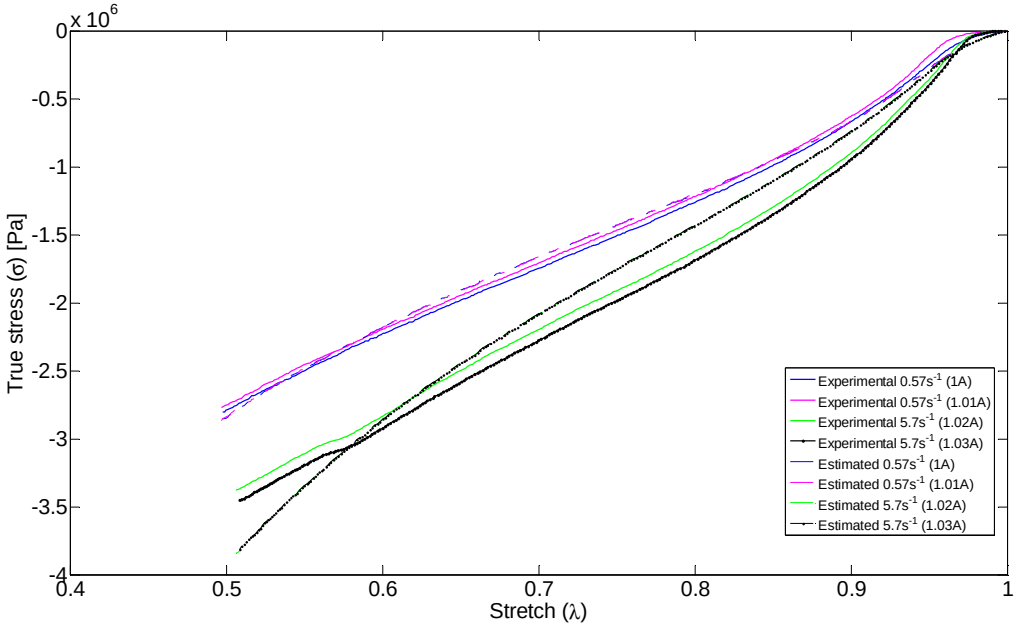

5-14 irudia. Datu esperimentalen eta kurba teorikoen arteko konparaketa 1 g/cm^3 dentsitaterako

5.4.2 57 s^{-1} deformazio abiadura (altuena)

5.3.3.1. Yang-en ereduaren aplikazioa zuzendutako deformazio abiadura altuenetara. Parametro biskoelastikoak PSOtik lortuta

PSO algoritmoa zuzendutako deformazio abiadura altuenetan aplikatu da, 90/10 proportzioko nahasteari eta probeta handiak kontsideratuz soilik. Datu esperimentalen konparazioa Yang-en eredutik iragarritako datuekin, dentsitate desberdinen kasurako, ondorengo 5-15, 5-16, 5-17 eta 5-18 irudietan erakusten da. Ereduak iragarritako tentsio-luzapen kurbek zera erakusten dute, berau ondo egokitzen dela nahaste honen portaera bisko-hiperelastikora, deformazio abiadura altuenean ere.

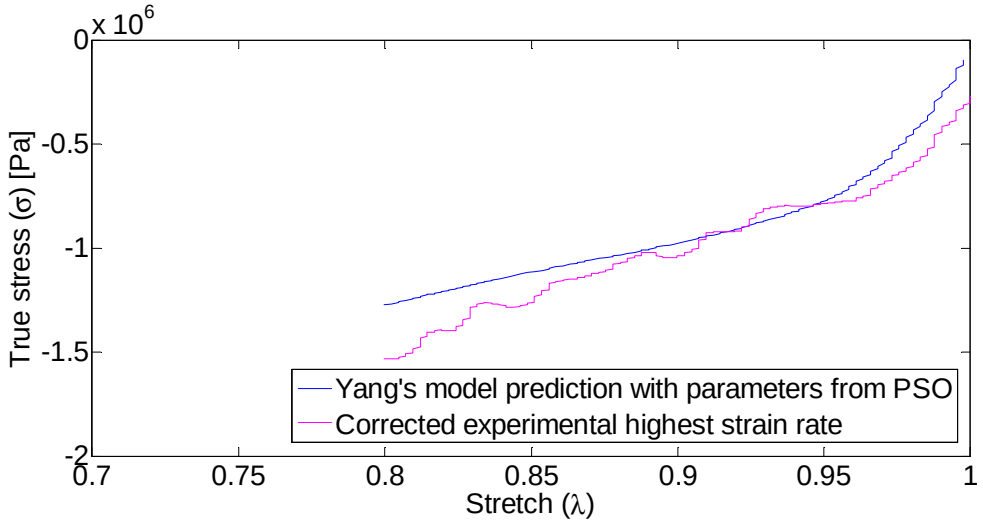

5-15 irudia. Yang-en ereduaren aplikazioa deformazio abiadura altuenera 0.7 g/cm³ dentsitaterako

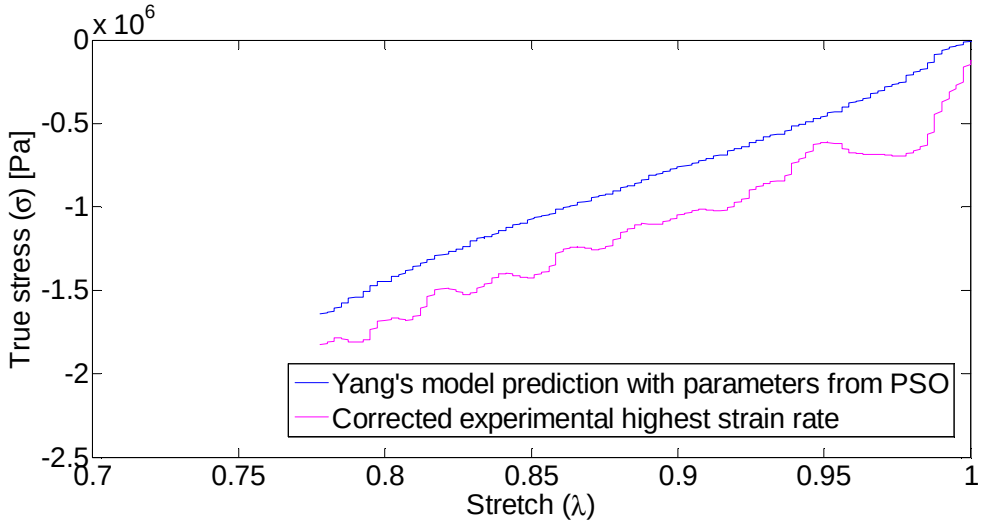

5-16 irudia. Yang-en ereduaren aplikazioa deformazio abiadura altuenera 0.8 g/cm³ dentsitaterako

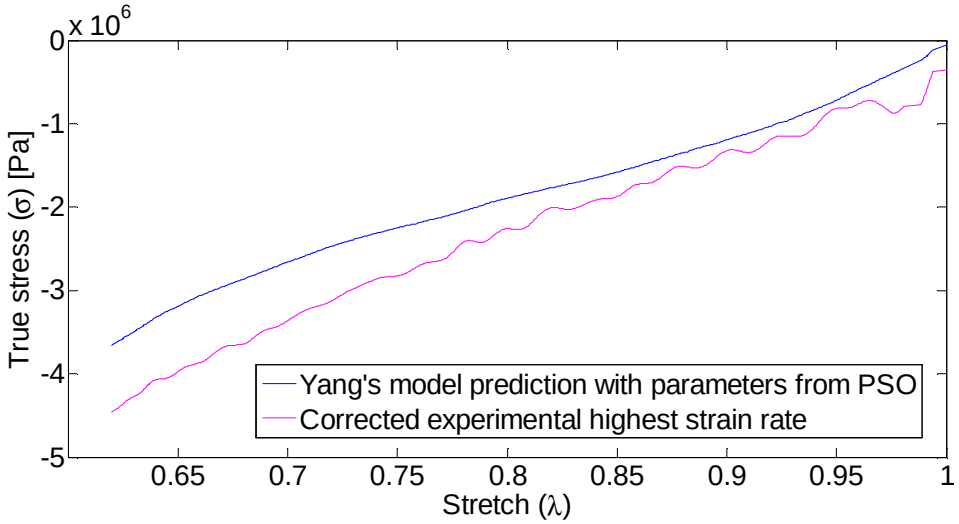

5-17 irudia. Yang-en ereduaren aplikazioa deformazio abiadura altuenera 0.9 g/cm^3 dentsitaterako

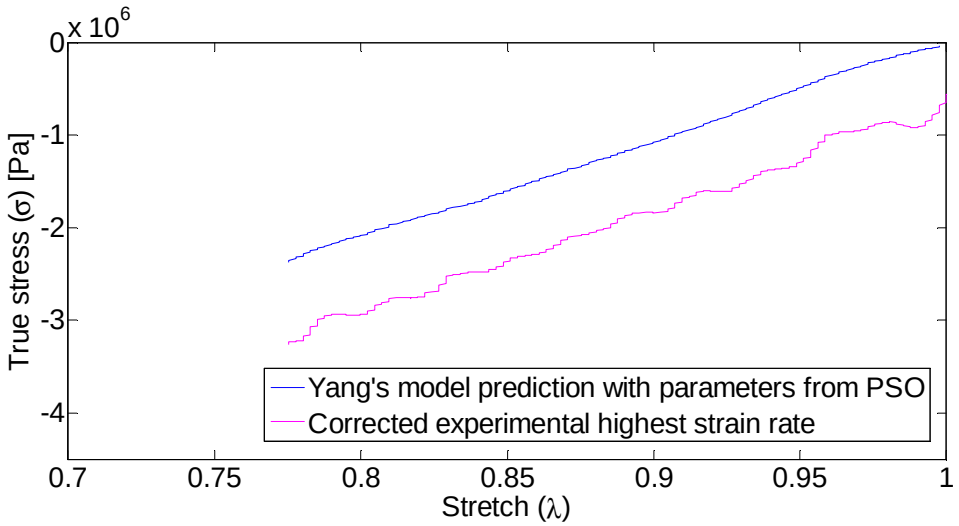

5-18 irudia. Yang-en ereduaren aplikazioa deformazio abiadura altuenera 1 g/cm^3 dentsitaterako

5.5 EREDUAREN IKASKETA TEORIKOA: PARAMETRO BAKOITZAREN ERAGINA

Batezbesteko errore karratua (MSE), J, hemen kontsideratuko da Yang-en ereduaren estimazioa, $f(p,t)$, datu esperimental errealen ordez, σ_{11}, kontuan hartzerakoan agertzen diren erroreen karratuen batezbesteko neurketa moduan; hau da, estimatzailearen eta estimatzen denaren arteko diferentzia.

$$J = \frac{1}{2}\int \left(\sigma_{11} - f(p,t)\right)^2 dt \tag{5.30}$$

Non *p*-k ereduaren parametroak adierazten dituen.

5.3 atalean definituriko optimizazio algoritmoak J-ren deribatuak parametro guztiekiko kalkulatzen ditu, $\frac{dJ}{dp}$; ondorioz, iterazio bakoitza ondoko eran kalkulatzen da:

$$\hat{p}_{k+1} = \hat{p}_k - \alpha \frac{\partial J}{\partial p} \tag{5.31}$$

(5.30) eta (5.31) ekuazioak elkarrekin erlazionatuz:

$$\begin{aligned} \hat{p}_{k+1} &= \hat{p}_k - \alpha 2 \frac{1}{2}\int \left(\sigma_{11} - f(p,t)\right)\left(-\frac{\partial f}{\partial p}\right)_{dt} dt = \\ &= \hat{p}_k + \alpha \int \left(\sigma_{11} - f(p,t)\right)\frac{\partial f}{\partial p} dt \end{aligned} \tag{5.32}$$

Integralaren barneko lehenengo terminoak errorea adierazten du, $e = \sigma_{11} - f(p,t)$, eta bigarren terminoa, $\frac{\partial f}{\partial p}$, sentikortasun funtzioa da; kasu honetan, $f(p,t) = \sigma_{Yang}$. Integral honek bi termino hauen arteko biderkaketa eskalarra adierazten du:

$$< e, \frac{\partial f}{\partial p} >= \int e \frac{\partial f}{\partial p} dt = \|e\| \left\| \frac{\partial f}{\partial p} \right\| \cos\varphi \tag{5.33}$$

Antzeman daitekeenez, erroreak iterazio bakoitzean eragiten du, baina sentikortasun funtzioak ere bai; hau da, algoritmoak errorearen balioa txikitzeko joera du. Eta zenbat eta eragin handiagoa izan parametroek funtzioarekiko, algoritmoak orduan eta kontuan gehiago hartzen du estimazio zehatzagoa lortu arazi lezakeen informazioa.

(5.19) ekuazioa kontsideratzen bada,

$$\frac{\partial \sigma_{Yang}}{\partial p} = \frac{\partial \sigma_{Hyper}}{\partial p} + \frac{\partial \sigma_{Visco}}{\partial p} \tag{5.34}$$

Jarraian, parametro hiperelastikoekiko deribatuak egiten dira, kontuan hartuz berauek ez direla azaltzen ereduaren zati biskoelastikoan:

$$\frac{\partial \sigma_{Yang}}{\partial C_{10}} = \frac{\partial \sigma_{Hyper}}{\partial C_{10}} = 2(\lambda^2 - \lambda^{-1}) \tag{5.35}$$

$$\frac{\partial \sigma_{Yang}}{\partial C_{01}} = \frac{\partial \sigma_{Hyper}}{\partial C_{01}} = 2(\lambda - \lambda^{-2}) \tag{5.36}$$

$$\frac{\partial \sigma_{Yang}}{\partial C_{11}} = \frac{\partial \sigma_{Hyper}}{\partial C_{11}} = 6(\lambda^3 - \lambda^2 - \lambda + \lambda^{-1} + \lambda^{-2} - \lambda^{-3}) \tag{5.37}$$

Zati biskoelastikoari dagokionez, bi integral dituena bere baitan; ondoko eran formulatu daiteke:

$$\sigma_{Visco} = \lambda^2 s_1 + \frac{1}{2}\lambda^{-1} s_2 \tag{5.38}$$

Non:

$$s_1 = \int_0^t \lambda[C_2 + C_3(I_2 - 3)]e^{-\frac{t-\tau}{C_4}} \dot{\lambda} d\tau \tag{5.39}$$

$$s_2 = \int_0^t \lambda^{-2}[C_2 + C_3(I_2 - 3)]e^{-\frac{t-\tau}{C_4}} \dot{\lambda} d\tau \tag{5.40}$$

Kontuan izanik Laplace-ren Transformatua eta s_1 eta s_2 gaien denborarekiko deribatuak eginez,

$$\dot{s}_1 = -\frac{1}{c_4} s_1 + g_1 \tag{5.41}$$

$$\dot{s}_2 = -\frac{1}{c_4} s_2 + g_2 \tag{5.42}$$

Non:

$$g_1 = \lambda[C_2 + C_3(I_2 - 3)]\dot{\lambda} \tag{5.43}$$

$$g_2 = \lambda^{-2}[C_2 + C_3(I_2 - 3)]\dot{\lambda} \tag{5.44}$$

Parametro biskoelastikoekiko deribatuak ondoren egiten dira, kontuan izanik ez direla ereduaren zati hiperelastikoan azaltzen:

$$\frac{\partial \sigma_{Visco}}{\partial p} = \lambda^2 \frac{\partial s_1}{\partial p} + \frac{1}{2}\lambda^{-1}\frac{\partial s_2}{\partial p} \tag{5.45}$$

$$\frac{d}{dt}\left(\frac{\partial s_1}{\partial p}\right) = -\frac{1}{c_4}\frac{\partial s_1}{\partial p} + \frac{\partial g_1}{\partial p} \tag{5.46}$$

$$\frac{d}{dt}\left(\frac{\partial s_2}{\partial p}\right) = -\frac{1}{c_4}\frac{\partial s_2}{\partial p} + \frac{\partial g_2}{\partial p} \tag{5.47}$$

C_2, C_3 eta C_4 parametroetarako partikularizatuz:

$$\frac{\partial \sigma_{Yang}}{\partial C_2} = \frac{\partial \sigma_{Visco}}{\partial C_2} = \lambda^2 \frac{\partial s_1}{\partial C_2} + \frac{1}{2}\lambda^{-1}\frac{\partial s_2}{\partial C_2} \tag{5.48}$$

$$\frac{d}{dt}\left(\frac{\partial s_1}{\partial C_2}\right) = -\frac{1}{c_4}\frac{\partial s_1}{\partial C_2} + \frac{\partial g_1}{\partial C_2} \tag{5.49}$$

$$\frac{d}{dt}\left(\frac{\partial s_2}{\partial C_2}\right) = -\frac{1}{c_4}\frac{\partial s_2}{\partial C_2} + \frac{\partial g_2}{\partial C_2} \tag{5.50}$$

Non $\frac{\partial s_1}{\partial C_2}$ eta $\frac{\partial s_2}{\partial C_2}$ (5.49) eta (5.50) ekuazioetatik lortzen diren, numerikoki ebatziz:

$$\frac{\partial s_1(k)}{\partial C_2} = \frac{\partial s_1(k-1)}{\partial C_2} + \Delta t\left(-\frac{1}{c_4}\frac{\partial s_1(k-1)}{\partial C_2} + \frac{\partial g_1}{\partial C_2}\right) = \frac{\partial s_1(k-1)}{\partial C_2}\left(1 - \frac{\Delta t}{c_4}\right) + \Delta t(\lambda\dot{\lambda}) \tag{5.51}$$

$$\frac{\partial s_2(k)}{\partial C_2} = \frac{\partial s_2(k-1)}{\partial C_2} + \Delta t\left(-\frac{1}{c_4}\frac{\partial s_1(k-1)}{\partial C_2} + \frac{\partial g_2}{\partial C_2}\right) = \frac{\partial s_2(k-1)}{\partial C_2}\left(1 - \frac{\Delta t}{c_4}\right) + \Delta t(\lambda^{-2}\dot{\lambda}) \tag{5.52}$$

Prozedura berbera jarraituz gainontzeko parametroekin:

$$\frac{\partial \sigma_{Yang}}{\partial C_3} = \frac{\partial \sigma_{Visco}}{\partial C_3} = \lambda^2 \frac{\partial s_1}{\partial C_3} + \frac{1}{2}\lambda^{-1}\frac{\partial s_2}{\partial C_3} \tag{5.53}$$

$$\frac{d}{dt}\left(\frac{\partial s_1}{\partial C_3}\right) = -\frac{1}{c_4}\frac{\partial s_1}{\partial C_3} + \frac{\partial g_1}{\partial C_3} \tag{5.54}$$

$$\frac{d}{dt}\left(\frac{\partial s_2}{\partial C_3}\right) = -\frac{1}{c_4}\frac{\partial s_2}{\partial C_3} + \frac{\partial g_2}{\partial C_3} \tag{5.55}$$

$$\frac{\partial s_1(k)}{\partial C_3}=\frac{\partial s_1(k-1)}{\partial C_3}+\Delta t\left(-\frac{1}{c_4}\frac{\partial s_1(k-1)}{\partial C_3}+\frac{\partial g_1}{\partial C_3}\right)=\frac{\partial s_1(k-1)}{\partial C_3}\left(1-\frac{\Delta t}{c_4}\right)+ \tag{5.56}$$
$$+\Delta t(\lambda\dot{\lambda})(I_2-3)$$

$$\frac{\partial s_2(k)}{\partial C_3}=\frac{\partial s_2(k-1)}{\partial C_3}+\Delta t\left(-\frac{1}{c_4}\frac{\partial s_2(k-1)}{\partial C_3}+\frac{\partial g_2}{\partial C_3}\right)=\frac{\partial s_2(k-1)}{\partial C_3}\left(1-\frac{\Delta t}{c_4}\right)+ \tag{5.57}$$
$$+\Delta t(\lambda^{-2}\dot{\lambda})(I_2-3)$$

$$\frac{\partial \sigma_{Yang}}{\partial C_4}=\frac{\partial \sigma_{Visco}}{\partial C_4}=\lambda^2\frac{\partial s_1}{\partial C_4}+\frac{1}{2}\lambda^{-1}\frac{\partial s_2}{\partial C_4} \tag{5.58}$$

$$\frac{d}{dt}\left(\frac{\partial s_1}{\partial C_4}\right)=-\frac{1}{c_4}\frac{\partial s_1}{\partial C_4}+\frac{\partial g_1}{\partial C_4} \tag{5.59}$$

$$\frac{d}{dt}\left(\frac{\partial s_2}{\partial C_4}\right)=-\frac{1}{c_4}\frac{\partial s_2}{\partial C_4}+\frac{\partial g_2}{\partial C_4} \tag{5.60}$$

$$\frac{\partial s_1(k)}{\partial C_4}=\frac{\partial s_1(k-1)}{\partial C_4}+\Delta t\left(-\frac{1}{c_4}\frac{\partial s_1(k-1)}{\partial C_4}+\frac{\partial g_1}{\partial C_4}\right)=\frac{\partial s_1(k-1)}{\partial C_4}\left(1-\frac{\Delta t}{c_4}\right)+ \tag{5.61}$$
$$+\frac{1}{C_4^{\,2}}\int_o^t\lambda\left[C_2+C_3(I_2-3)\right]e^{-\frac{t-\tau}{C_4}}\dot{\lambda}d\tau$$

$$\frac{\partial s_2(k)}{\partial C_4}=\frac{\partial s_2(k-1)}{\partial C_4}+\Delta t\left(-\frac{1}{c_4}\frac{\partial s_2(k-1)}{\partial C_4}+\frac{\partial g_2}{\partial C_4}\right)=\frac{\partial s_2(k-1)}{\partial C_4}\left(1-\frac{\Delta t}{c_4}\right)+ \tag{5.62}$$
$$+\frac{1}{C_4^{\,2}}\int_o^t\lambda^{-2}\left[C_2+C_3(I_2-3)\right]e^{-\frac{t-\tau}{C_4}}\dot{\lambda}d\tau$$

Ekuazio hauek Matlab-en sartu dira eta numerikoki ebatzi dira. Jarraian, denbora vs $\frac{\partial \sigma_{Visco}}{\partial p}$ erlazioak irudikatu dira sei parametroentzat.

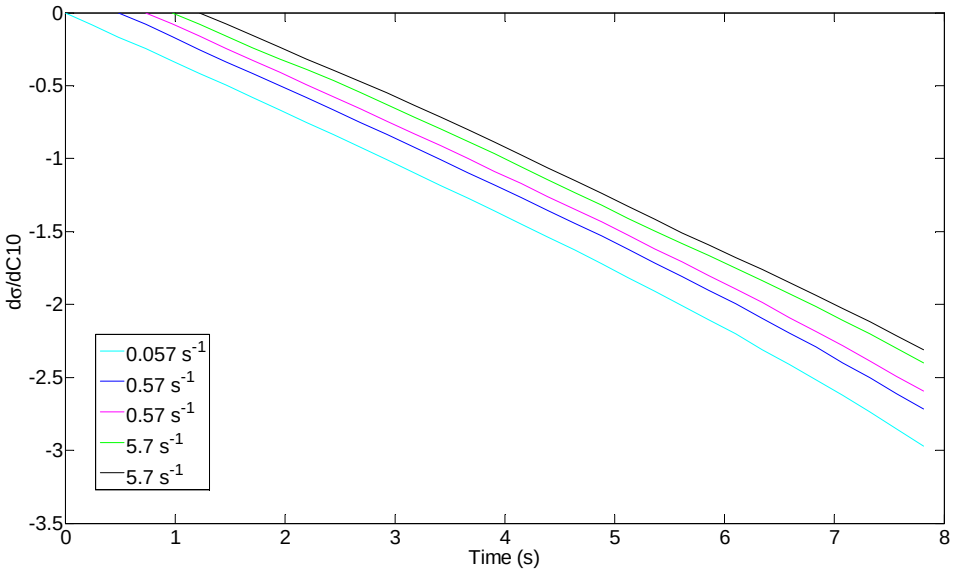

5-19 irudia. Saiakuntza desberdinen sentikortasuna C10 parametro hiperelastikoarekiko

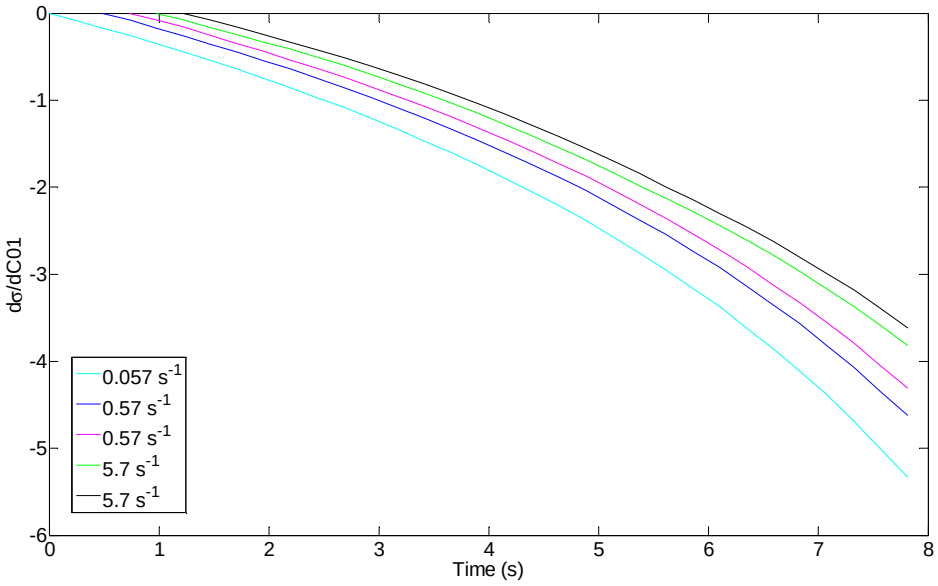

5-20 irudia. Saiakuntza desberdinen sentikortasuna C01 parametro hiperelastikoarekiko

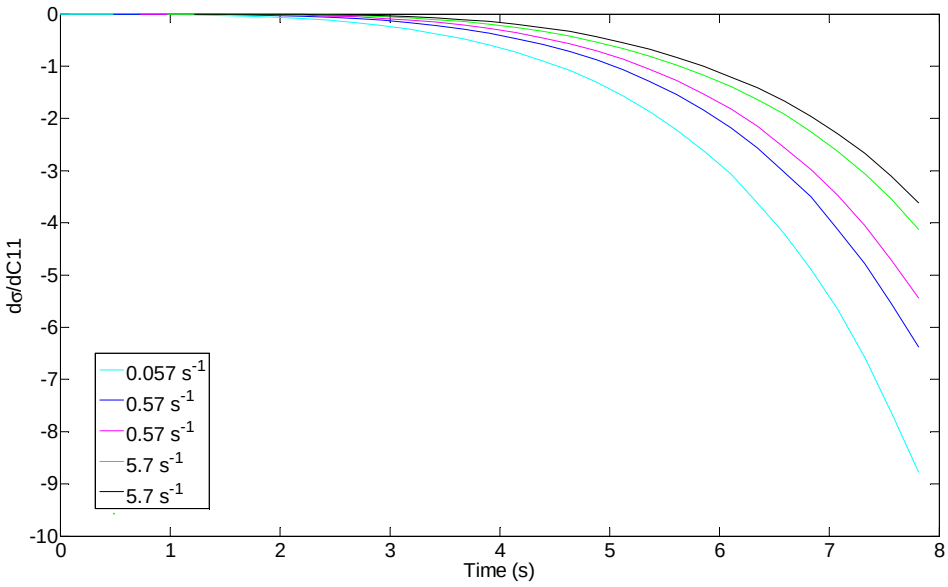

5-21 irudia. Saiakuntza desberdinen sentikortasuna C11 parametro hiperelastikoarekiko

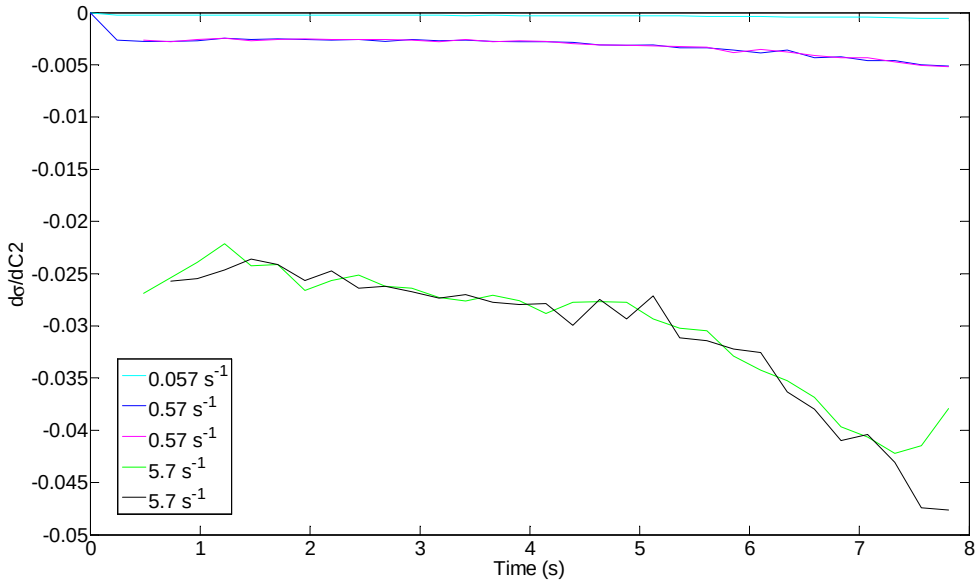

5-22 irudia. Saiakuntza desberdinen sentikortasuna C2 parametro hiperelastikoarekiko

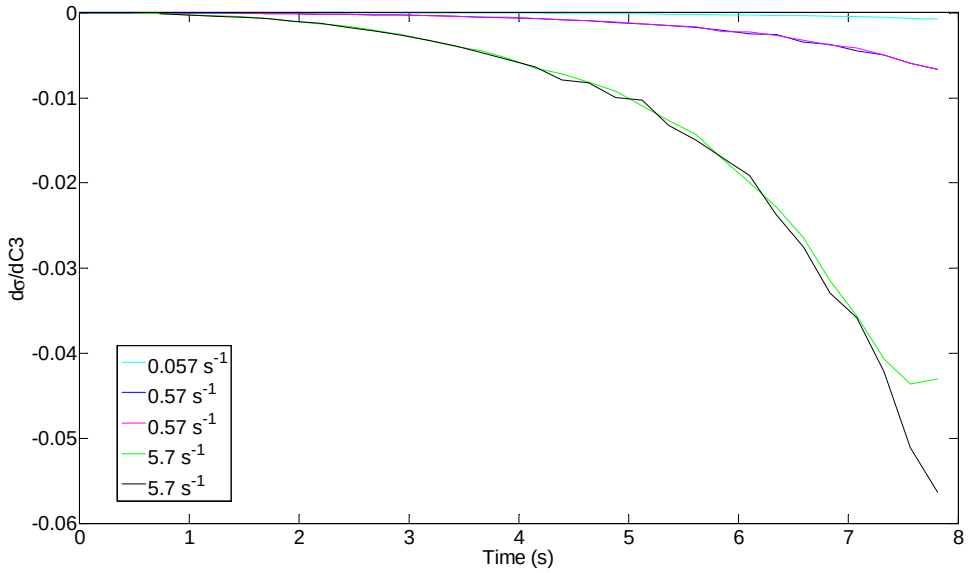

5-23 irudia. Saiakuntza desberdinen sentikortasuna C3 parametro hiperelastikoarekiko

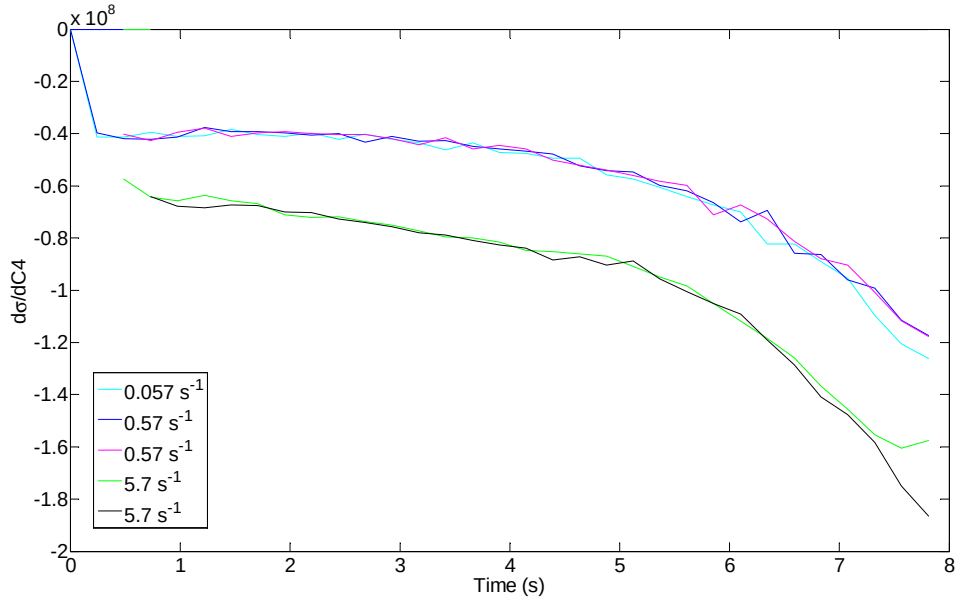

5-24 irudia. Saiakuntza desberdinen sentikortasuna C4 parametro hiperelastikoarekiko

Cauchy-ren tentsioaren sentikortasuna hiru parametro hiperelastikoekiko 5-19, 5-20 eta 5-21 irudietan ikus daiteke. Deformazio abiadura desberdinei dagozkien saiakuntza

esperimentaletako datuak erabili izan dira. $\frac{\partial \sigma_{Yang}}{\partial C_{10}}$ sentikortasunaren balio maximoa -3 balioari dagokio (adimentsionala) 8 s-tara gutxi gora-behera, kontuan izanik deformazio abiadura txikienari dagokikon kurbaren datuak, hots, hain zuzen ere parámetro hiperelastikoak doitzeko erabili izan diren datuak. $\frac{\partial \sigma_{Yang}}{\partial C_{01}}$ versus denbora aztertzen bada, balio maximo hori -5.5 baliorarte igotzen da 8 s-tara, eta hirugarren parametro hiperelastikoaren kasuan, $\frac{\partial \sigma_{Yang}}{\partial C_{11}}$, balio maximo hau -9 baliorarte igotzen da 8 s-tara. Honek adierazten du hiru parametro hiperelastikoen eragina antzekoa dela beraien artean, C_{11} parametroaren eragina gainontzeko biena baino pixkat altuagoa izanik; hala ere, eraginaren magnitude ordena berdina dute.

5-22, 5-23 eta 5-24 irudiak hartzen dira kontuan ondoren, parámetro bsikoelastikoen eragina aztertzeko. $\frac{\partial \sigma_{Yang}}{\partial C_{2}}$ eta $\frac{\partial \sigma_{Yang}}{\partial C_{3}}$ parametro hiperelastikoen sentikortasunarekiko magnitude ordena bi txikiagoak diren artean $\frac{\partial \sigma_{Yang}}{\partial C_{4}}$ parametro hiperelastikoen sentikortasunarekiko zazpi magnitude ordena handiagoa da. Azterketa honek zera erakusten du, C10, C01, C11, C2 eta C3 parametroen eragin txikia C4 parametroarekin alderatuz, eredu materialarekiko.

5.6 EZTABAIDA

Yang-en eredua aukeratu izan da materialaren portaera azaltzeko. Ereduaren parametroak 90/10 proportziodun eta 0.9 g/cm^3 dentsitatedun nahastearentzat doitu dira, probeta handiak kontsideratuz. Lehenengo hiru parametro hiperelastikoak minimo karratuen doiketa teknikaren bidez doitu dira. Emaitzek erakusten dutenez, iragarritako kurben eta datu esperimentalen arteko desberdintasunak %1a baino txikiagoak dira. Parametro biskoelastikoen determinazioa PSO algoritmoan oinarritutako doiketa ez-lineal anitzaren bidez egin da, minimo karratuekin neketsua zelako inplementatzea eta ez du beti soluzio optimora jotzen. Kasu honetan, iragarritako kurben desbiderazioak datu esperimentaletatik sekziorik txarrenean %10a inguru dira.

Algoritmoak funtzio ez-lineal honen sendotasuna eta minimo globalera iristeko gaitasuna erakusten du, hurbilketa inteligente batean oinarrituta dagoelako optimizazio problemaren bertsio askorekin, partikulak deituak. Hurbilketa honek optimizazio problemaren minimo lokaletatik urruntzea baimentzen du. Are gehiago, algoritmoak ez dio optimizazio funtzioari murrizketa matematiko garrantzitsurik inposatzen. Optimizazio metodo ona dela erakutsi du, erraza, moldaerraza eta parametro gutxi batzuen bitartez soluzio optimora azeleratzen duena.

Neurtutako R_2 balioa 0.99 izan da; honek proposaturiko ereduaneurketa esperimentalekin modu egokian bat datorrela adierazten duelarik. Eredu osagarriak materialaren portaera ondo iragartzen du $0.057s^{-1}$ eta $5.7s^{-1}$ bitarteko deformazio abiadura eremuan eta %45erarteko deformazioentzat. Deformazio abiadura altuagoetarako, eragin ez-linealak nabariagoak dira, eta ondorioz, eredu honen termino kopuru mugatuarekin zailagoa egiten da portaera deskribatzea. PSO algoritmoak optimizazio metodo efizientea dela erakutsi du lan honetan kontuan hartu den arean.

Parametroen ikasketa teorikoa egitea erabaki da ereduaren parametroen eragina honeto ulertzen saiatzeko, PSOren emaitzak hasierako parametroen hurbilketekiko sentikorrak direla kontuan hartuz. Ikasketak argia isuri du C_4 parametro biskoelastikoa aukeratzerakoan kontua eduki beharraren gainean; izan ere, ereduaren gaineko bere eragina gainontzeko parametroena baino zazpi magnitude ordena altuagoa da.

6. MATERIALAREN AZPIRRUTINA ERATZEKO METODOLOGIA

6.1 SARRERA

Kapitulu honetan, Ansys elementu finituen softwarean –LS Dyna dauka softwareak analisi esplizituak egiteko– Yang-en eredua inplementatzeko metodologia aurkeztuko da. Gogorarazi beharra dago materialaren aplikazio potentziala dena, errepideetako hesien estaldura gisa erabiltzea, eta, horregatik, talkak simulatzea da xedea. Lehenik, deformazio handiko eta portaera ez-linealeko material batean epe labur batez iraungo duten konpresio saiakuntzen simulazioak burutu nahi dira; hori da, hain zuzen ere, analisi esplizitua egitearen arrazoia.

Nahiz eta kautxu birziklatuz eta LLDPEz egindako nahasketa ia konprimaezina den, kontuan hartu behar da konprimagarritasunaren menpeko ekuazio konstitutiboa, FE kodean inplementatu ahal izateko. 6.2 atalean, Yang-en eredutik abiatuta Cauchy-ren tentsioaren adierazpena kalkulatu da. Bada, adierazpen horretan oinarriturik, aintzat hartzekoa da konprimagarritasunaren alderdia. Horrez gain, ereduaren zati biskoelastikorako beste metodologia bat erabili da, Midpoint Metodoa hain zuzen ere, 6.2 atalean azaltzen den bezala. Hori dela eta, parametro berriak berriz ere kalkulatzeko asmoz, PSO algoritmoa aplikatu da ekuazioan, metodologia horri jarraituz.

6.2 PSO BIDEZ PARAMETRO BERRIAK LORTZEA

Kautxuaren tankerako materialak ia bolumen konstantean deformatzen dira, eta konprimaezintzat jotzen dira. Horregatik da I_3 (1.17) ekuazioan unitatearen parekoa. Berez, kautxuak konprimagarritasun finitua du, eta, txikia izan arren, ez da hutsala egoera guztietan. Materialaren eredua FE kodean inplementatzeko xedez, kapitulu honetan deformazio gradientea bi zatitan banatu da: zati isokorikoa (zati distortsionala) eta zati bolumetrikoa (zati dilatazionala):

$$F = \left(J^{1/3} I\right)\overline{F} = J^{1/3}\overline{F} \tag{6.1}$$

Eta horrenbestez:

$$C = \left(J^{2/3} I\right)\overline{C} = J^{2/3}\overline{C} \tag{6.2}$$

$$\overline{I}_1 = J^{-2/3} I_1 \tag{6.3}$$

$$\overline{I}_2 = J^{-4/3} I_2 \tag{6.4}$$

Non:

$$\det \overline{F} = \overline{\lambda}_1 \overline{\lambda}_2 \overline{\lambda}_3 = 1 \tag{6.5}$$

$$\det \overline{C} = 1 \tag{6.6}$$

Non $\overline{\lambda}_a = J^{(-1/3)}\lambda_a, a = 1, 2, 3$. Kontuan hartuta $\frac{\partial I_3}{\partial C} = I_3 C^{-1}$ eta $I_3 = \det b = J^2$:

$$\frac{\partial J^2}{\partial C} = J^2 C^{-1} \tag{6.7}$$

Eta katearen arauari jarraituz:

$$\frac{\partial J}{\partial C} = \frac{J}{2} C^{-1} \tag{6.8}$$

$$\frac{\partial J^{-2/3}}{\partial C} = -\frac{1}{3} J^{-2/3} C^{-1} \tag{6.9}$$

Deformazio energia ere bi zatitan bana daiteke, energia askea erreproduzitzen duen alderdia gehituta, soilik aurreko energia askearekiko bolumen aldaketarekin lotuta dagoena, eta sareko deformazioari dagokion alderdia:

$$\psi(C)=\psi_{vol}(J)+\psi_{isoc}(\overline{C}) \tag{6.10}$$

Literaturan, hainbat deformazio energia daude zehaztuta. Alde bolumetrikoa konprimagarritasun koefizientearen (K) menpe dago. Halaber, kontuan hartzekoa da Petiteau-ren[40] irizpidea, Simo-k[79] proposaturikoa (sinpleenetariko bat) hautatzen duena. Gogoratu beharra dago material ia konprimaezina deskribatzea dela helburua; ondorioz, K balio altuarekin aukeratu da parametro hiperelastikoekin alderatuz gero.

$$\psi_{vol}(J)=U(J)=\frac{K}{2}(J-1)^2\,LnJ \tag{6.11}$$

Ondorengo adierazpena tentsioaren alde bolumetrikoa kalkulatzeko erabili da, B Eranskineko (1.49) ekuazioan erakusten den moduan:

$$\sigma_{hyper\_vol}=\frac{\partial\psi_{vol}}{\partial J}I=\left(K(J-1)LnJ+\frac{K}{2}(J-1)^2\frac{1}{J}\right)I \tag{6.12}$$

Deformazio energiaren zati isokoroari dagokionez, 2. kapituluan jasotako deformazio energietako batekin egin daiteke hurbilketa: $\psi_{isoc}(\overline{C})=\overline{\psi}$. Hortaz, B Eranskineko (1.49) ekuaziotik abiatuta lor daiteke zati hori:

$$\sigma_{hyper\_isoc}=2J^{-1}dev\left[\left(\frac{\partial\psi_{isoc}}{\partial\overline{I}_1}+\overline{I}_1\frac{\partial\psi_{isoc}}{\partial\overline{I}_2}\right)\overline{b}-\frac{\partial\psi_{isoc}}{\partial\overline{I}_2}\overline{b}^2\right] \tag{6.13}$$

(5.3) ekuazioa kontuan hartuz: $\psi_{isoc}=C_{10}(\overline{I}_1-3)+C_{01}(\overline{I}_2-3)+C_{11}(\overline{I}_1-3)(\overline{I}_2-3)$.

(6.13) ekuaziotik abiatuta:

$$\sigma_{hyper\_isoc}=2J^{-1}dev\left[\left[C_{10}+C_{11}(\overline{I}_2-3)+\overline{I}_1\left(C_{01}+C_{11}(\overline{I}_1-3)\right)\right]\overline{b}-\left(C_{01}+C_{11}(\overline{I}_1-3)\right)\overline{b}^2\right] \tag{6.14}$$

Kontuan hartuta $\det(F)=\lambda_1\lambda_2\lambda_3=J$ eta konpresio unixialeko kasua ($\lambda_2=\lambda_3$) dela, honela formula daiteke F:

$$F=\begin{pmatrix}\lambda & 0 & 0\\ 0 & \left(\frac{J}{\lambda}\right)^{1/2} & 0\\ 0 & 0 & \left(\frac{J}{\lambda}\right)^{1/2}\end{pmatrix} \tag{6.15}$$

(6.1) ekuazioa aintzat hartuta, adierazpen hau lortzen da b-rentzat:

$$\begin{aligned}\overline{b}=(\overline{F}\overline{F}^{T})=J^{-1/3}&\begin{pmatrix}\lambda & 0 & 0\\ 0 & \left(\frac{J}{\lambda}\right)^{1/2} & 0\\ 0 & 0 & \left(\frac{J}{\lambda}\right)^{1/2}\end{pmatrix}J^{-1/3}\begin{pmatrix}\lambda & 0 & 0\\ 0 & \left(\frac{J}{\lambda}\right)^{1/2} & 0\\ 0 & 0 & \left(\frac{J}{\lambda}\right)^{1/2}\end{pmatrix}=\\ =J^{-2/3}&\begin{pmatrix}\lambda^2 & 0 & 0\\ 0 & \frac{J}{\lambda} & 0\\ 0 & 0 & \frac{J}{\lambda}\end{pmatrix}=\begin{pmatrix}J^{-2/3}\lambda^2 & 0 & 0\\ 0 & \frac{J^{1/3}}{\lambda} & 0\\ 0 & 0 & \frac{J^{1/3}}{\lambda}\end{pmatrix}\end{aligned} \tag{6.16}$$

Yang-en ereduaren alderdi biskoelastikoari erreparatuz eta hurrengo urratsa erantzunaren zenbakizko integrazioa izanik, Petiteau-ren[40] hurbilketa bera egiten da:

$$\overline{\sigma}_{visco}=\frac{1}{J}dev\left[\overline{F}_n\overline{H}_n\overline{F}_n^{T}\right] \tag{6.17}$$

n denbora une bati dagokio $\overline{\sigma}_{visco}$ horrek. (5.13)-(5.16) ekuazioetako Yang-en ereduari jarraituz, $\overline{H}_n$ honela adieraz daiteke:

$$\overline{H}_n=\int_{-\infty}^{t}[C_2+C_3(\overline{I}_2(\tau)-3)]\exp\left(-\frac{t-\tau}{C_4}\right)\dot{\overline{E}}d\tau \tag{6.18}$$

Adierazpen hori bi zatitan banatuz gero:

$$\bar{H}_n = \int_{-\infty}^{t_{n-1}} [C_2 + C_3(\bar{I}_2(\tau) - 3)] \exp\left(-\frac{t_n - t_{n-1}}{C_4}\right) \exp\left(-\frac{t_{n-1} - \tau}{C_4}\right) \dot{\bar{E}} d\tau + \\ + \int_{t_{n-1}}^{t_n} [C_2 + C_3(\bar{I}_2(\tau) - 3)] \exp\left(-\frac{t_n - \tau}{C_4}\right) \dot{\bar{E}} d\tau \tag{6.19}$$

Eta kontuan hartuta $\Delta t = t_n - t_{n-1}$ dela:

$$\bar{H}_n = \exp\left(-\frac{\Delta t}{C_4}\right) \bar{H}_{n-1} + \int_{t_{n-1}}^{t_n} [C_2 + C_3(\bar{I}_2(\tau) - 3)] \exp\left(-\frac{t_n - \tau}{C_4}\right) \dot{\bar{E}} d\tau \tag{6.20}$$

Ondoren, Midpoint Metodoa aplikatu da. Lehen ordenako hurbilketa bat da, non τ $\frac{t_n + t_{n-1}}{2}$ balioaren bitartez hulbiltzen den:

$$\bar{H}_n = \exp\left(-\frac{\Delta t}{C_4}\right) \bar{H}_{n-1} + \exp\left(-\frac{\Delta t}{2C_4}\right) \left[C_2 + C_3 \left(\bar{I}_2 \left(\frac{t_n + t_{n-1}}{2} \right) - 3 \right) \right] \int_{t_{n-1}}^{t_n} \dot{\bar{E}} d\tau \tag{6.21}$$

Azkenik, $E = \frac{1}{2}(C - I)$ ordezkatuz:

$$\bar{H}_n = \exp\left(-\frac{\Delta t}{C_4}\right) \bar{H}_{n-1} + \exp\left(-\frac{\Delta t}{2C_4}\right) \left[C_2 + C_3 \left(\bar{I}_2 \left(\frac{t_n + t_{n-1}}{2} \right) - 3 \right) \right] \frac{1}{2} (\bar{C}_n - \bar{C}_{n-1}) \tag{6.22}$$

$C_{10}, C_{01}, C_{11}, C_2, C_3, C_4$ materialaren sei parametro horiez gain, J bolumen indizea ere ezezaguna da. Haren balioa gutxi gorabehera $J = 1$ denez, lehenik eta behin PSO aplikatzeko eta parametroa kalkulatzeko hurbilketa hori egiten da. 5. kapituluan bezala, 90/10-eko proportzioko eta 0,9 g/cm^3-ko dentsitateko probeta handiak hartu dira kontuan.

C_{10}, C_{01}, C_{11} parametro hiperelastikoak lortu dira batezbesteko errore koadratikoaren bitartez. Balioak 6-1 taulan aurki daitezke. 5-2 taulan lortutako balioekin alderatuz gero, ikus daiteke, espero bezala, oso antzekoak direla. Hemen balioak altuxeagoak dira, baina ez modu esanguratsuan. 6-1 irudian tentsio-luzapen kurbak azaltzen dira, bai datu esperimentalei dagozkienak, bai ereduari jarraiki lortutako emaitzei dagozkienak. Honako hauek dira parametro hiperelastikoen balioak:

6-1 taula. Parametro hiperelastikoen balioak 90/10-eko proportzioa eta 0,9 g/cm^3-ko dentsitatea duen nahasketarako, konprimagarritasuna aintzat hartuta eta Midpoint metodoa aplikatuta

Parametroa	Balioa
C_{10} [MPa]	3.08
C_{01} [MPa]	-1.47
C_{11} [MPa]	0.22

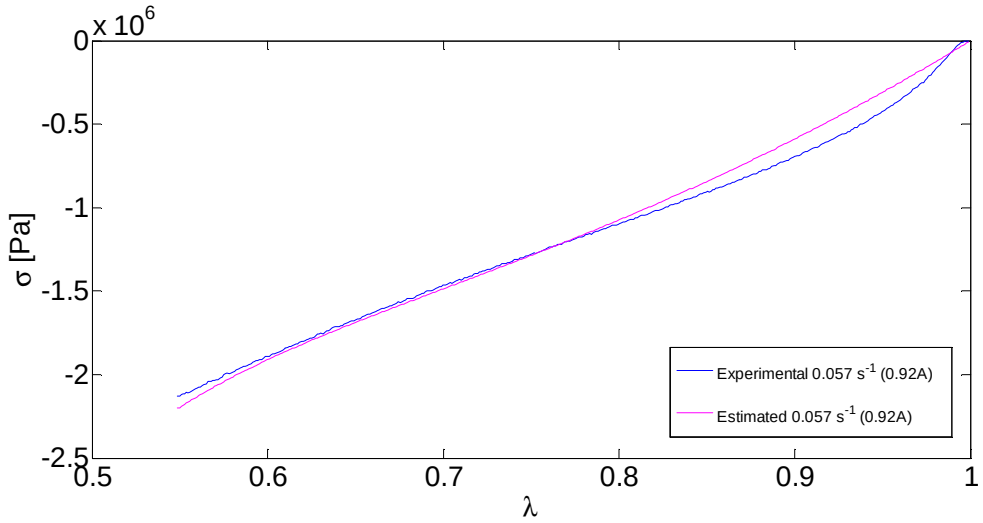

6-1 irudia. Tentsio-luzapen kurba kuasiestatikoak vs. eredu teorikoaren osagai hiperelastikoa 0,9 g/cm^3-ko dentsitaterako, konprimagarritasuna kontuan hartuta eta Midpoint metodoa aplikatuta

Parametro biskoelastikoei dagokienez, PSO aplikatu da. 6-2 irudian, parametro biskoelastikoek algoritmoan zehar hartzen dituzten hainbat balio ikus daitezke, triada optimoa lortu arte. 6.2. taulan ageri dira triada optimoaren balioak.

6-2 taula. Parametro biskoelastikoen balioak 90/10-eko proportzioa eta 0,9 g/cm^3-ko dentsitatea duen nahasketarako, konprimagarritasuna aintzat hartuta eta Midpoint metodoa aplikatuta

Parametroa	Balioa
C_2 [MPa]	12.29
C_3 [MPa]	1.03
C_4 [s]	0.0056

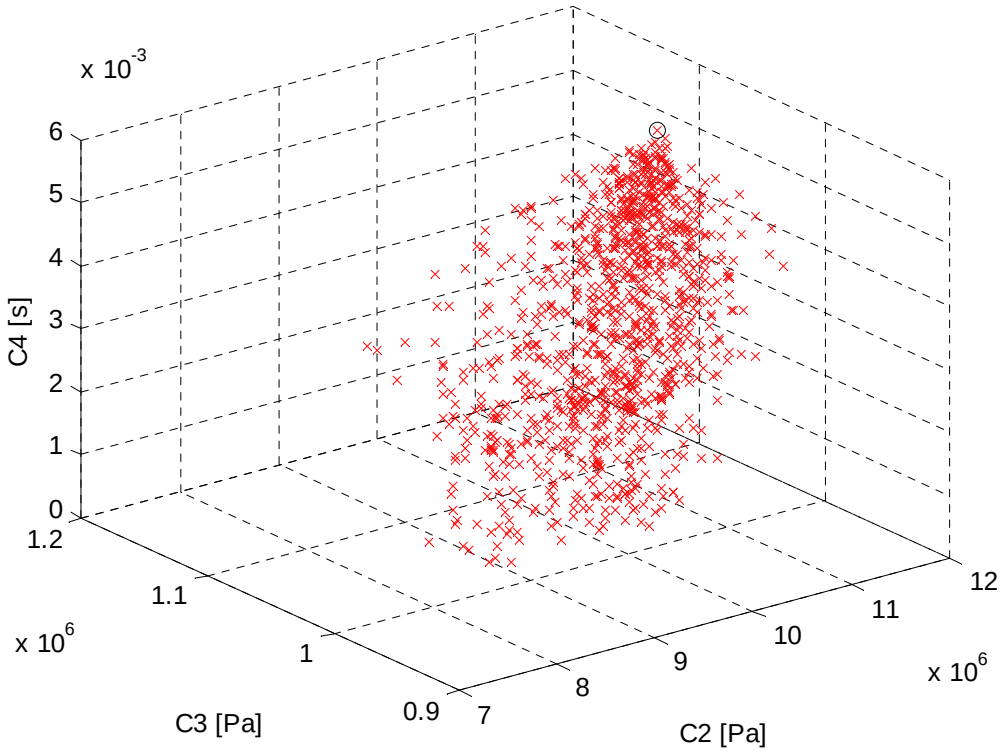

6-2 irudia. Parametro biskoelastikoen balioak PSOn, triada optimoan bat egin arte (0,9 g/cm³-ko dentsitatean), konprimagarritasuna kontuan hartuta eta Midpoint metodoa aplikatuta

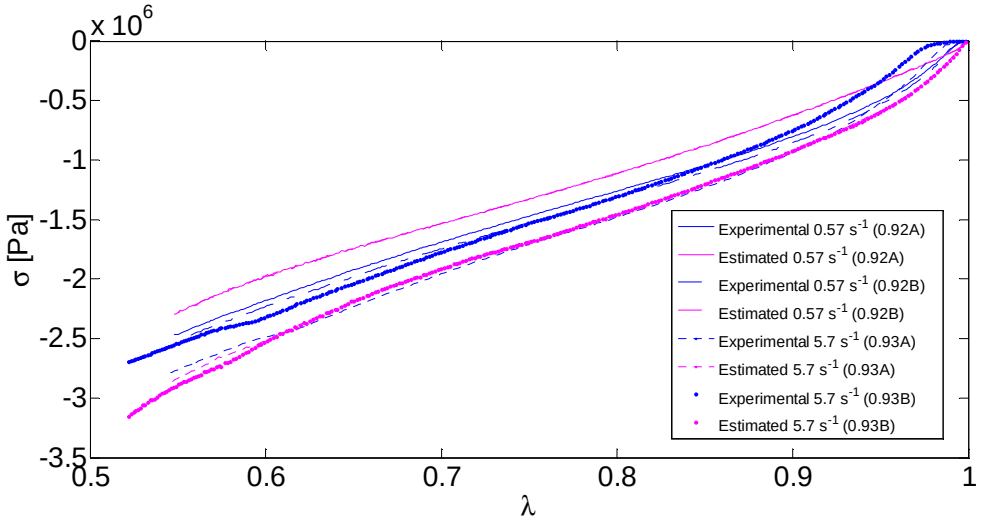

6-3 irudia. Datu esperimentalen eta kurba teorikoen arteko konparazioa 90/10-eko proportzioa eta 0,9 g/cm³-ko dentsitatea duen nahasketarako, konprimagarritasuna kontuan hartuta eta Midpoint metodoa aplikatuta

6-3 irudian, datu esperimentalei zein emaitza teorikoei dagozkien tentsio-luzapen kurbak azaltzen dira, 90/10-eko proportzioko eta 0,9 g/cm^3-ko dentsitateko probeta handietan.

6.3 ERANTZUN KONSTITUTIBOA LORTZEKO MATERIALAREN AZPIRRUTINARAKO ALGORITMOA

Behin ereduaren sei parametroak berriz kalkulatuta, materialaren ekuazio konstitutiboa FE kodean inplementatzeko metodologia aurkeztuko da. Petiteau-k[40] proposaturiko algoritmoan oinarritzen da, baina Yang-en ereduari aplikatuta. Urratsak honela laburbildu daitezke:

- ✓ t_n une batean eta dagokion λ_n luzapenean, aurreko uneko honako informazio hau hartzen da kontuan: $\overline{C}_{n-1}$ eta $\overline{H}_{n-1}$ (biak dira beharrezkoak (6.22) ekuazioan).
- ✓ F_n , $J = \det(F_n)$ eta $\overline{F}_n = J^{-1/3} F_n$ kalkulatzen dira.
- ✓ $\overline{b}_n = \overline{F}_n \overline{F}_n^T$ Cauchy eta Green-en ezkerreko deformazio tentsorearen zati isokoroa kalkulatzen da, (6.13) ekuazioan erabiltzeko $\overline{I}_1 = tr(\overline{b}_n)$ eta $\overline{I}_2 = \frac{1}{2}\left[\overline{I}_1^2 - tr(\overline{b}_n^2)\right]$ inbarianteekin batera.
- ✓ Tentsio hiperelastikoa kalkulatzen da, (6.14) ekuazioan Rivlin-en eredua deformazio energiaren adierazpenean txertatu ostean lortutako zati isokoroaren eta (6.12) ekuazioaren zati esferikoaren batura gisa.
- ✓ Tentsio biskoelastikoa kalkulatzen da ondoren, (6.22) ekuazioa (6.17) ekuazioan ordezkatuz.
- ✓ $\overline{C}_{n-1}$ eta $\overline{H}_{n-1}$ balioak eguneratzen dira, $\overline{C}_n$ eta $\overline{H}_n$ berauen balioetan gordez.
- ✓ Azkenik, honela kalkulatzen da Cauchy-ren tentsioa guztira:

$$\sigma_n = \left(\sigma_n^{hyper\_vol} + \overline{\sigma}_n^{hyper\_isoc}\right) + \overline{\sigma}_n^{visco} \tag{6.23}$$

Aintzat hartu behar da J ezazaguna dela, hau da, ekuazioa haren menpekoa dela. Horrenbestez, beharrezkoa da $\sigma_{22} = \sigma_{22\_hyper} + \sigma_{22\_visco} = 0$ ekuazioa (edo modu berean $\sigma_{33} = 0$) ebaztea, une bakoitzean J-k duen balioa eskuratzeko. Algoritmo hori Matlab-en txertatu da lehenik. 6-4 irudian azaltzen dira hortik ateratako emaitzak, 90/10-eko

proportzioko eta 0,9 g/cm^3-ko dentsitateko probeta handiak erabilita. Ikus daitekeenez, azpirrutinatik ateratako emaitzak bat datoz emaitza esperimentalekin.

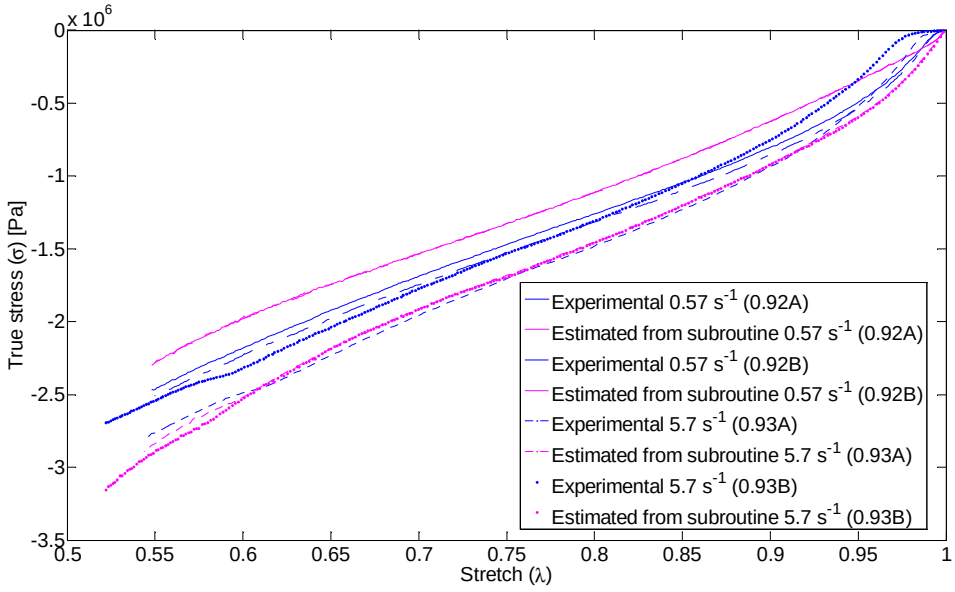

6-4 irudia. Datu esperimentalen eta algoritmoaren bitartez lortutako kurba teorikoen arteko konparazioa 90/10-eko proportzioa eta 0,9 g/cm^3-ko dentsitatea duen nahasketarako

6.4 EZTABAIDA

Lan honetan aurkezturiko nahasketan Yang-en ekuazio konstitutiboa inplementatzeko metodologia azaldu da. Materialak errepideetako hesiak estaltzeko duen erabilera potentziala dela-eta, analisi esplizituak egitea izan da Ansys EF kodean txertatzeko aukerarik onena. Horregatik da aintzat hartzekoa LS Dyna. Ekuazio konstitutiboan konprimagarritasunak duen erabilera ere gogoan izan behar da, FE simulazioek baldintza hori betetzea eskatzen baitute. Horiek horrela, eredua aurkeztean konprimagarritasuna barne hartu da eta PSO aplikatu da ekuazioan, parametroak berriz kalkulatzeko eta inplementaziorako baliorik onenak lortzeko.

Ondoren, materialaren azpirrutinaren algoritmoa aurkeztu eta Matlab-en inplementatu da, parametroen balio berriak txertatuta. Emaitzek erakusten dute eredua bat datorrela alderdi esperimentalarekin. LS Dyna-n, Matlab kodearen bitartez konpresio saiakuntzen simulazioak sartzea da hurrengo urratsa, eta FE eredua datu esperimentaletara egokitzea.

Ondorioz, eta lan honetatik harago, etorkizuneko ikerketa ildoa izan daiteke errepideetako hesiak LS Dyna-ren bidez garatzea.

7.

ONDORIOAK ETA ETORKIZUNERAKO KONTSIDERAZIOAK

Hiru nahaste egin dira pneumatikoetako kautxu birziklatuarekin eta dentsitate txikiko polietileno linealarekin (LLDPE) itsasgarri moduan, material bakoitzaren proportzio desberdinekin eta koloratzailelez erabili den TiO_2-ren proportzio konstante batekin nahaste guztietan. Proportzio hauek 90/10, 75/25 eta 60/40 deitu izan dira, non bigarren terminoak LLDPEren portzentaia adierazten duen, eta lehenengoak, TiO_2-ren %3a eta gainontzekoa kautxu birziklatua diren. Material honen aplikazio potentziala errepideetako hesietan estaldura moduan litzateke, motoziklistak kolpeen aurrean babesteko asmoarekin. Erabilera hau inpaktuen barne dago; hortaz, nahastearen karakterizazio mekanikoak abiadura altuko konpresiozko saiakuntzak barneratzen ditu.

Literaturan ondo ezagutzen den eredu osagarri hiper-biskoelastikoa aukeratu da materiala karakterizatzeko, hain zuzen ere Yang-en eredua. Eredu honek hiru parametroko Rivlinen eredua dauka zati hiperelastiko moduan eta zati biskoelastikoan beste hiru parametro aurkezten ditu, K-BKZ ereduan oinarrituz, egileen ekarpena gehituz. Zati hiperelastikoa minimo karratuen doiketa teknikaren bitartez doitu da. Konboluzioko integralean oinarrituta dagoen zati biskoelastikoko parametroei dagokienez, doitzeko oso zailak izanik, Particle Swarm Optimization (PSO) algoritmoa aukeratu da parametro hauen balioak lortzeko. PSO algoritmoak optimizazio metodo ona dela erakutsi du, sinplea, moldagarria,

eta soluzio optimora iristeko parametro gutxi batzuen definizioa soilik behar duena, optimizatu beharreko funtzioa oso ez lineala bada ere. Nahaste honekin lortu nahi den helburu nagusia ahalik eta kautxu gehien birziklatu ahal izatea denez, printzipioz 90/10 nahastea aukeratu da azterturiko hiruren artean. Konpromezuko soluzio bat nahi izan da hartu, gainontzeko nahasteek energia absorbatzeko gaitasun handiagoa dutela aitortuz, baina zurruntasun handiagoa ere badute, eta interesatzen dena ahalik eta gehien birziklatzea da. Ereduaren parametroak 90/10 nahasketarako eta 0.9 g/cm^3 dentsitatearentzat doitu dira.

Lau dentsitate desberdin aztertu dira, lau abiadura desberdinetan, 0.004 eta 4 m/s abiaduren tartean; abiadura hau makinaren segurtasun arrazoiek mugatu dute. Abiadurarik altuenean materialaren kurbek ondulazio bereizgarri batzuek aurkeztu dituzte, normalean "ringing" (erresonantzia) moduan ezagutzen direnak literatura espezializatuan. Datu esperimental hauek ezin dira jatorrizko eran erabili distortsionatuta daude eta. Hortaz, Analisi Modal Esperimentala (EMA) kontsideratu da makina serbo-hidraulikoaren ezaugarri dinamikoak xehetasunez ikasteko asmoz. Analisi honetatik saiakuntzetan zehar eszitatu izan diren, datu esperimentala kaltetu dutelarik, saiakuntza-makinaren modu nagusiak atera dira. Hortik askatasun gradu anitzeko eredu bat eraiki da EMAtik lortutako frekuentzia naturalen, moduen eta moteltze faktoreen bitartez. Eredu matematiko honek "system ringing" horretan nagusiki eragin duten moduak ebatzi ditu. Bulkada-karga baten bidez eszitatu izan da karga-zelulak neurtutako indarraren frekuentzia edukia modu egokian simulatuz. Ostean, erantzun simulatuaren zati oszilakorra kendu zaio neurtutako indar seinaleari. Jarraian, seinale berriaren ondulazioak modu nabarmenean txikituta, egokia suertatu da behe-paseko iragazki bat aplikatzeko, 1600 Hz-tako mozketa frekuentziaduna. Modu honetan emaitza finalaren oszilazioak minimizatuta jada erabilgarria da.

Aurretiaz proposaturiko Yang-en eredua Ansys Elementu Einituetako software-an inplementatzeko metodologia aurkeztu da ondoren; analisi esplizituetarako LS Dyna erabiltzen duena. Ekuazio osagarri hau ez dago oraindik software honetan inplementaturik eta ondorioz, materialaren azpirrutina bat garatu da, lehendabizi Matlaben. Konpresiozko saiakuntzen simulazioak egin nahi dira, denbora une laburrean deformazio handiak jasaten dituen eta portaera ez lineala aurkezten duen material batengan; analisi esplizitua egitearen arrazoia hori da. Lan honetan materialaren azpirrutina inplementatzeko algoritmoa azaltzen da; azpirrutina hau elementu finituetan sartzeko prozesua etorkizuneko lana da, tesi honetako estudiotik abiatuz egin beharrekoa.

ETORKIZUNEKO LAN-ILDOAK:

Etorkizuneko lanean kontuan hartu beharreko alderdi nagusiak jarraian laburbiltzen dira:

- Etorkizuneko lerro posible bat karga-zelulak neurtzen duen indarraren zuzenketa hobetzean datza. Lan hori "eskuz" egin izan da eta interesgarria litzateke prozesuaren automatizazioren bat burutzea, seinale bien bat datozen denbora uneak lokalizatzeko, seinale esperimentala eta simulatua, biak grafiko berdinean gainezartzen direnean bat egiten duten tontorrak lortzeko asmoz.

- Lan honetan saiakuntza esperimentalak abiadura konstantean egin izan dira. Saaikuntzako abiadura hau konstante beharrean aldakorra izanez gero, honek informazio gehiago emango lieke datu esperimentalei. Horrela, ereduaren parametroen eragina handiagoa izango litzateke eta errazagoa parametro horiek identifikatzerakoan sortzen den errorea kontrolatzea. Ate ireki bat da aspektu hau sakontasun handiagoarekin ikasteko.

- Parametroen eragina aztertu denean ikusi izan da Yang-en eredua bere parametro biskoelastikoetako batekiko bereziki sentikorra dela, hain zuzen ere C_4. Analisi honetatik ateratako informazioarekin ondorioztatu daiteke lehendabizi parametro hau doitzea eta ondoren, ereduko gainontzekoei ekitea egokiagoa litzatekeela; doiketaren emaitzak zehatzagoak izango liratekeela pentsa daiteke, nahiz eta lan honetan egindako errorea %10-15a baino txikiagoa den gutxi gora-behera.

- LS Dynan deformazio abiadura altuko konpresiozko simulazioetara joan, datu esperimentalekin balioztaturiko elementu finituetako eredu bat lortzeko. Ondoren, errepideetako hesi baten elementu finituetako eredu bat, materialaren nahasketarekin estaldura duelarik, egin ahal izango litzateke eta maniki baten kolpea hesi honen kontra simulatu. Lehendabizi, datu esperimentalen deformazio abiadura berdinetara, eta ondoren, arauetan ezarritako abiaduretara. Behin eredu egokia lortu dela, prototipo bat fabrikatuko litzateke, saiakuntza errealak egin ahal izateko beronekin. Esperimentazioa garestia denez eta denbora daramanez, aurretasen duen eredu honen erabilerak gastu horiek laburtuko lituzke.

- Beste ikerketa-lerro posible bat parametroen identifikaziorako erabili den algoritmoaren hobekuntzari lotuta dago. PSO hobetzeko literatura zabala existitzen da: algoritmo moldakorrak, emaitza onak erabiltzea ala ez iterazio zenbakiaren ordez algoritmoa geratzeko metodo moduan, etab.

- Ereduaren erantzun biskoelastikoak analisi gehiago behar dezake, parametro biskoelastikoen identifikazioa errazteko asmoz. Bere alde egonkorra aztertzen bada, erantzun biskoelastiko honentzat adierazpen algebraiko bat proposatu liteke. Ikertzeko lerro interesgarria ematen du, konboluzioko integralean oinarrituriko eredu biskoelastikoak alboratu egin direla dirudi eta berauen konplexutasun matematikoa dela eta zati batean.

ERREFERENTZIAK

7.1

1. De SK, Isayev A, Khait K. Rubber recycling. boca raton, FL: CRC press, taylor & francis group. ; 2005.

2. Myhre M, MacKillop DA. Rubber recycling. *Rubber Chemistry and Technology*. 2002;75(3):429-474.

3. Rajeev R, De S. Thermoplastic elastomers based on waste rubber and plastics. *Rubber chemistry and technology*. 2004;77(3):569-578.

4. Stevenson K, Stallwood B, Hart AG. Tire rubber recycling and bioremediation: A review. *Bioremediation J*. 2008;12(1):1-11.

5. Shim J, Mohr D. Rate dependent finite strain constitutive model of polyurea. *Int J Plast*. 2011;27(6):868-886.

6. Shim J, Mohr D. Rate dependent finite strain constitutive model of polyurea. *Int J Plast*. 2011;27(6):868-886. doi: http://dx.doi.org/10.1016/j.ijplas.2010.10.001.

7. Anani Y, Alizadeh Y. Visco-hyperelastic constitutive law for modeling of foam's behavior. *Mater Des*. 2011;32(5):2940-2948. doi: http://dx.doi.org/10.1016/j.matdes.2010.11.010.

8. FUNG Y. Stress, strain, growth, and remodeling of living organisms. *Z Angew Math Phys*. 1995;46:S469-S482.

9. Gil-Negrete N. On the modeling and dynamic stiffness prediction of rubber isolators. [Universidad de Navarra]. ; 2004 [Ph.D. thesis].

10. FEMA (The Federation of European Motorcyclist Associations). A project to develop recommendations to road traffic authorities for reducing injuries to motorcyclist in collision with crash barriers. *Final Report of the Motorcyclist & Crash Barriers Project*. 2000.

11. Haugou G, Markiewicz E, Fabis J. On the use of the non direct tensile loading on a classical split hopkinson bar apparatus dedicated to sheet metal specimen characterisation. *Int J Impact Eng*. 2006;32(5):778-798. doi: http://dx.doi.org/10.1016/j.ijimpeng.2005.07.015.

12. Xia Y, Zhu J, Zhou Q. Verification of a multiple-machine program for material testing from quasi-static to high strain-rate. *Int J Impact Eng*. 2015;86:284-294. doi: http://dx.doi.org/10.1016/j.ijimpeng.2015.07.010.

13. Petiteau J, Othman R, Guégan P, Le Sourne H, Verron E. Dynamic uniaxial extension of elastomers at constant true strain rate. *Polym Test*. 2013;32(2):394-401. doi: http://dx.doi.org/10.1016/j.polymertesting.2012.10.007.

14. Zhu D, Rajan S, Mobasher B, Peled A, Mignolet M. Modal analysis of a servo-hydraulic high speed machine and its application to dynamic tensile testing at an intermediate strain rate. *Exp Mech*. 2011;51(8):1347-1363. doi: http://dx.doi.org/10.1007/s11340-010-9443-2.

15. Roche N. Comportement vibro-acoustique de matériaux et structures à base de poudrettes de pneumatiques recyclés. 2010.

16. Navarro FJ, Partal P, Martínez-Boza FJ, Gallegos C. Novel recycled polyethylene/ground tire rubber/bitumen blends for use in roofing applications: Thermo-mechanical properties. *Polym Test*. 2010;29(5):588-595.

17. Amari T, Themelis NJ, Wernick IK. Resource recovery from used rubber tires. *Resour Policy*. 1999;25(3):179-188.

18. Sonnier R, Leroy E, Clerc L, Bergeret A, Lopez-Cuesta J. Polyethylene/ground tyre rubber blends: Influence of particle morphology and oxidation on mechanical properties. *Polym Test*. 2007;26(2):274-281.

19. Rocha MCG, Leyva ME, Oliveira MGd. Thermoplastic elastomers blends based on linear low density polyethylene, ethylene-1-octene copolymers and ground rubber tire. *Polímeros*. 2014;24(1):23-29.

20. Kumar CR, Fuhrmann I, Karger-Kocsis J. LDPE-based thermoplastic elastomers containing ground tire rubber with and without dynamic curing. *Polym Degrad Stab*. 2002;76(1):137-144.

21. Scaffaro R, Dintcheva NT, Nocilla MA, La Mantia FP. Formulation, characterization and optimization of the processing condition of blends of recycled polyethylene and ground tyre rubber: Mechanical and rheological analysis. *Polym Degrad Stab*. 2005;90(2):281-287. doi: 10.1016/j.polymdegradstab.2005.03.022.

22. Fainleib A, Grigoryeva O, Starostenko O, Danilenko I, Bardash L. Reactive compatibilization of recycled low density polyethylene/butadiene rubber blends during dynamic vulcanization. . 2003;202(1):117-126.

23. Sonnier R, Leroy E, Clerc L, Bergeret A, Lopez-Cuesta J. Compatibilisation of polyethylene/ground tyre rubber blends by γ irradiation. *Polym Degrad Stab*. 2006;91(10):2375-2379.

24. Grigoryeva O, Fainleib A, Tolstov A, Starostenko O, Lievana E, Karger-Kocsis J. Thermoplastic elastomers based on recycled high-density polyethylene, ethylene–propylene–diene monomer rubber, and ground tire rubber. *J Appl Polym Sci*. 2005;95(3):659-671.

25. de Sousa, Fabiula Danielli Bastos, Gouveia JR, de Camargo Filho, Pedro Mário Franco, et al. Blends of ground tire rubber devulcanized by microwaves/HDPE-part B: Influence of clay addition. *Polímeros*. 2015;25(4):382-391.

26. Ausias G, Thuillier S, Omnes B, Wiessner S, Pilvin P. Micro-mechanical model of TPE made of polypropylene and rubber waste. *Polymer*. 2007;48(11):3367-3376.

27. Guo B, Cao Y, Jia D, Qiu Q. Thermoplastic elastomers derived from scrap rubber powder/LLDPE blend with LLDPE-graft-(epoxidized natural rubber) dual compatibilizer. *Macromolecular Materials and Engineering*. 2004;289(4):360-367.

28. Naskar AK, Bhowmick AK, De S. Thermoplastic elastomeric composition based on ground rubber tire. *Polymer Engineering & Science*. 2001;41(6):1087-1098.

29. Scaffaro R, Dintcheva NT, Nocilla M, La Mantia F. Formulation, characterization and optimization of the processing condition of blends of recycled polyethylene and ground tyre rubber: Mechanical and rheological analysis. *Polym Degrad Stab*. 2005;90(2):281-287.

30. Zhu J, Zhang X, Liang M, Lu C. Enhancement of processability and foamability of ground tire rubber powder and LDPE blends through solid state shear milling. *Journal of Polymer Research*. 2011;18(4):533-539.

31. Mészáros L, Fejős M, Bárány T. Mechanical properties of recycled LDPE/EVA/ground tyre rubber blends: Effects of EVA content and postirradiation. *J Appl Polym Sci*. 2012;125(1):512-519.

32. Parenteau T, Bertevas E, Ausias G, Stocek R, Grohens Y, Pilvin P. Characterisation and micromechanical modelling of the elasto-viscoplastic behavior of thermoplastic elastomers. *Mech Mater*. 2014;71:114-125.

33. Drozdov A. Constitutive equations for the nonlinear viscoelastic and viscoplastic behavior of thermoplastic elastomers. *Int J Eng Sci*. 2006;44(3):205-226.

34. Drozdov A, Christiansen J. Thermo-viscoplasticity of carbon black-reinforced thermoplastic elastomers. *Int J Solids Structures*. 2009;46(11):2298-2308.

35. Austrell P. Modeling of elasticity and damping for filled elastomers. [Lund University]. ; 1997 [Ph.D. thesis].

36. Pouriayevali H, Guo YB, Shim VPW. A constitutive description of elastomer behaviour at high strain rates – A strain-dependent relaxation time approach. *Int J Impact Eng*. 2012;47(0):71-78. doi: http://dx.doi.org/10.1016/j.ijimpeng.2012.04.001.

37. Pouriayevali H, Arabnejad S, Guo YB, Shim VPW. A constitutive description of the rate-sensitive response of semi-crystalline polymers. *Int J Impact Eng*. 2013;62:35-47. doi: 10.1016/j.ijimpeng.2013.05.002.

38. Ciambella J, Paolone A, Vidoli S. A comparison of nonlinear integral-based viscoelastic models through compression tests on filled rubber. *Mech Mater*. 2010;42(10):932-944. doi: http://dx.doi.org/10.1016/j.mechmat.2010.07.007.

39. Ogden R, Saccomandi G, Sgura I. Fitting hyperelastic models to experimental data. *Comput Mech*. 2004;34(6):484-502.

40. Petiteau J. Experimental characterization and modelling of the behaviour of elastomers under fast dynamic loading. application to suspension mounts. Ecole Centrale de Nantes (ECN) (ECN) (ECN) (ECN); 2012.

41. Banks HT, Hu S, Kenz ZR. A brief review of elasticity and viscoelasticity for solids. *Advances in Applied Mathematics and Mechanics*. 2011;3(01):1-51.

42. Holzapfel GA. *Nonlinear solid mechanics.* Vol 24. Wiley Chichester; 2000.

43. Treloar LRG. *The physics of rubber elasticity.* Oxford University Press, USA; 1975.

44. Arruda EM, Boyce MC. A three-dimensional constitutive model for the large stretch behavior of rubber elastic materials. *Journal of the Mechanics and Physics of Solids*. 1993;41(2):389-412. doi: http://dx.doi.org/10.1016/0022-5096(93)90013-6.

45. Mooney M. A theory of large elastic deformation. *J Appl Phys*. 1940;11(9):582-592.

46. Rivlin R. The elasticity of rubber. *Rubber Chemistry and Technology*. 1992;65(3):51-66.

47. Yeoh O. Characterization of elastic properties of carbon-black-filled rubber vulcanizates. *Rubber chemistry and technology*. 1990;63(5):792-805.

48. Gent A. A new constitutive relation for rubber. *Rubber chemistry and technology*. 1996;69(1):59-61.

49. Marckmann G, Verron E. Comparison of hyperelastic models for rubber-like materials. *Rubber chemistry and technology*. 2006;79(5):835-858.

50. Steinmann P, Hossain M, Possart G. Hyperelastic models for rubber-like materials: Consistent tangent operators and suitability for treloar's data. *Arch Appl Mech*. 2012;82(9):1183-1217. http://dx.doi.org/10.1007/s00419-012-0610-z. doi: 10.1007/s00419-012-0610-z.

51. Verron E. Contribution expérimentale et numérique aux procédés de moulage par soufflage et de thermoformage. Ecole Centrale de Nantes; Université de Nantes; 1997.

52. Rivlin RS, Saunders D. Large elastic deformations of isotropic materials. VII. experiments on the deformation of rubber. *Philosophical Transactions of the Royal Society of London A: Mathematical, Physical and Engineering Sciences*. 1951;243(865):251-288.

53. Gent AN, Thomas AG. Forms for the stored (strain) energy function for vulcanized rubber. *Journal of Polymer Science*. 1958;28(118):625-628. doi: 10.1002/pol.1958.1202811814.

54. Beda T, Gacem H, Chevalier Y, Mbarga P. Domain of validity and fit of gent-thomas and flory-erman rubber models to data. *Parameters*. 2008;1:K2.

55. Carmichael A, Holdaway H. Phenomenological elastomechanical behavior of rubbers over wide ranges of strain. *J Appl Phys*. 1961;32(2):159-166.

56. Valanis K, Landel R. The Strain-Energy function of a hyperelastic material in terms of the extension ratios. *J Appl Phys*. 1967;38(7):2997-3002.

57. Ogden R, Saccomandi G, Sgura I. Fitting hyperelastic models to experimental data. *Comput Mech*. 2004;34(6):484-502.

58. Blatz P, Sharda SC, Tschoegl N. Strain energy function for rubberlike materials based on a generalized measure of strain. *Transactions of the Society of Rheology*. 1974;18(1):145-161.

59. Yeoh O, Fleming P. A new attempt to reconcile the statistical and phenomenological theories of rubber elasticity. *Journal of Polymer Science-B-Polymer Physics Edition*. 1997;35(12):1919-1932.

60. Shariff M. Strain energy function for filled and unfilled rubberlike material. *Rubber chemistry and technology*. 2000;73(1):1-18.

61. Pucci E, Saccomandi G. Some remarks about a simple history dependent nonlinear viscoelastic model. *Mech Res Commun*. 2015;68:70-76.

62. Noll W. A mathematical theory of the mechanical behavior of continuous media. *Archive for rational Mechanics and Analysis*. 1958;2(1):197-226.

63. Truesdell C, Noll W. The non-linear field theories of mechanics. Springer; 2004.

64. Fatt MSH, Bekar I. High-speed testing and material modeling of unfilled styrene butadiene vulcanizates at impact rates. *J Mater Sci*. 2004;39(23):6885-6899.

http://dx.doi.org/10.1023/B:JMSC.0000047530.86758.b9. doi: 10.1023/B:JMSC.0000047530.86758.b9.

65. Wineman A. Nonlinear viscoelastic solids—a review. *Mathematics and Mechanics of Solids*. 2009;14(3):300-366.

66. Drapaca C, Sivaloganathan S, Tenti G. Nonlinear constitutive laws in viscoelasticity. *Mathematics and Mechanics of Solids*. 2007;12(5):475-501.

67. Park S. Analytical modeling of viscoelastic dampers for structural and vibration control. *Int J Solids Structures*. 2001;38(44):8065-8092.

68. Yang L, Shim V, Lim C. A visco-hyperelastic approach to modelling the constitutive behaviour of rubber. *Int J Impact Eng*. 2000;24(6):545-560.

69. Yang L, Shim V. A visco-hyperelastic constitutive description of elastomeric foam. *Int J Impact Eng*. 2004;30(8):1099-1110.

70. Shim V, Yang L, Lim C, Law P. A visco-hyperelastic constitutive model to characterize both tensile and compressive behavior of rubber. *J Appl Polym Sci*. 2004;92(1):523-531.

71. Hoo Fatt MS, Xin Ouyang. Integral-based constitutive equation for rubber at high strain rates. *Int J Solids Structures*. 2007;44(20):6491-506. doi: 10.1016/j.ijsolstr.2007.02.038.

72. Ward I, Pinnock P. The mechanical properties of solid polymers. *British Journal of Applied Physics*. 1966;17(1):3.

73. Christensen R. A nonlinear theory of viscoelasticity for application to elastomers. *Journal of Applied Mechanics*. 1980;47(4):762-768.

74. Khajehsaeid H, Arghavani J, Naghdabadi R, Sohrabpour S. A visco-hyperelastic constitutive model for rubber-like materials: A rate-dependent relaxation time scheme. *Int J Eng Sci*. 2014;79:44-58. doi: 10.1016/j.ijengsci.2014.03.001.

75. Bergström J. *Large strain time-dependent behavior of elastomeric materials.* [Massachusetts Institute of Technology]. ; 1999.

76. Bergström J, Boyce M. Constitutive modeling of the time-dependent and cyclic loading of elastomers and application to soft biological tissues. *Mech Mater*. 2001;33(9):523-530.

77. Jongmin Shim, Mohr D. Rate dependent finite strain constitutive model of polyurea. *Int J Plast*. 2011;27(6):868; 868-886; 886. doi: 10.1016/j.ijplas.2010.10.001.

78. Shim J, Mohr D. Punch indentation of polyurea at different loading velocities: Experiments and numerical simulations. *Mech Mater*. 2011;43(7):349-360.

79. Simo J. On a fully three-dimensional finite-strain viscoelastic damage model: Formulation and computational aspects. *Comput Methods Appl Mech Eng*. 1987;60(2):153-173.

80. Drozdov AD. A constitutive model for nonlinear viscoelastic media. *Int J Solids Structures*. 1997;34(21):2685-2707.

81. Green AE, Rivlin RS. The mechanics of non-linear materials with memory. *Archive for Rational Mechanics and Analysis*. 1957;1(1):1-21.

82. Coleman BD, Noll W. The thermodynamics of elastic materials with heat conduction and viscosity. *Archive for Rational Mechanics and Analysis*. 1963;13(1):167-178.

83. Pouriayevali H, Guo Y, Shim V. A visco-hyperelastic constitutive description of elastomer behaviour at high strain rates. *Procedia Engineering*. 2011;10:2274-2279.

84. Drozdov AD, Dorfmann A. Finite viscoelasticity of filled rubber: Experiments and numerical simulation. *Arch Appl Mech*. 2003;72(9):651-672.

85. Bergström J, Boyce M. Large strain time-dependent behavior of filled elastomers. *Mech Mater*. 2000;32(11):627-644.

86. Lockett FJ. *Nonlinear viscoelastic solids.* Academic Press; 1972.

87. Bernstein B, Kearsley E, Zapas L. A study of stress relaxation with finite strain. *J Rheol*. 1963;7:391.

88. Kaye A. Non-Newtonian flow in incompressible fluids. 1962.

89. Tanner RI. From A to (BK)Z in constitutive relations. *The Society of Rheology*. 1988.

90. Chang W, Bloch R, Tschoegl N. On the theory of the viscoelastic behavior of soft polymers in moderately large deformations. *Rheologica Acta*. 1976;15(7-8):367-378.

91. Fung Y, Skalak R. Biomechanics: Mechanical properties of living tissues. 1981.

92. Morman Jr K. An adaptation of finite linear viscoelasticity theory for rubber-like viscoelasticity by use of a generalized strain measure. *Rheologica acta*. 1988;27(1):3-14.

93. AENOR. Standard on the evaluation of performance of the protection systems for motorcyclists on safety barriers and parapets - part 1: Terminology and test procedures. *UNE 135900-1:2008*. 2008.

94. AENOR. Standard on the evaluation of performance of the protection systems for motorcyclists on safety barriers and parapets - part 2: Performance clasess and aceptance criteria. *UNE 135900-2:2008*. 2008.

95. Mullins L. Softening of rubber by deformation. *Rubber Chemistry and Technology*. 1969;42(1):339-362.

96. Sierakowski R. Strain rate effects in composites. *Appl Mech Rev*. 1997;50:741-761.

97. Kistler. Quartz force links, manufacturer's catalog. . 2010.

98. Xiao X. Dynamic tensile testing of plastic materials. *Polym Test*. 2008;27(2):164-178. doi: http://dx.doi.org/10.1016/j.polymertesting.2007.09.010.

99. Yang X, Hector Jr L, Wang J. A combined theoretical/experimental approach for reducing ringing artifacts in low dynamic testing with servo-hydraulic load frames. *Exp Mech*. 2014;54(5):775-789. doi: http://dx.doi.org/10.1007/s11340-014-9850-x.

100. Dutton J. Dynamic tensile properties of thin sheet materials. Research Report 303; 2005.

101. Rehrmann T, Kopp R. Recent enhancements to determine flow stress data in high speed compression tests. . 2004;1st International Conference in High Speed Forming:71-80.

102. Larour P. Strain rate sensitivity of automotive sheet steels: Influence of plastic strain, strain rate, temperature, microstructure, bake hardening and pre-strain. [Doctoral Thesis: RWTH Aachen, Germany]. Lehrstuhl und Institut für Eisenhüttenkunde; 2010.

103. Bardenheier R, Rogers G. Dynamic impact testing. *Instron Ltd., High Wycombe, UK*. 2003.

104. Eriksen R,Normann Wilken. High strain rate characterisation of composite materials; high strain rate characterisation of composite materials. Doctoral Thesis ed. DTU Mechanical Engineering; 2014.

105. Silva FdA, Zhu D, Mobasher B, Soranakom C, Toledo Filho RD. High speed tensile behavior of sisal fiber cement composites. *Materials Science and Engineering: A*. 2010;527(3):544-552. doi: http://dx.doi.org/10.1016/j.msea.2009.08.013.

106. Zhu D, Mobasher B, Rajan S, Peralta P. Characterization of dynamic tensile testing using aluminum alloy 6061-T6 at intermediate strain rates. *J Eng Mech*. 2011;137(10):669-679.

107. Pneumont A. Vibration control of active structures. . 1997.

108. Ewins D. Modal testing: Theory, practice and application (mechanical engineering research studies: Engineering dynamics series). . 2003.

109. Preumont A. *Vibration control of active structures: An introduction.* Springer Science & Business Media; 2002.

110. Kennedy J, Eberhart R. *Particle swarm optimization.* Proceedings of IEEE International Conference on Neural Network: ; 1995, p.1945-1948:1948.

111. Poli R. Analysis of the publications on the applications of particle swarm optimisation. *Journal of Artificial Evolution and Applications*. 2008;2008:1-10.

112. Shi Y, Eberhart RC. Fuzzy adaptive particle swarm optimization. . 2001;1:101-106.

113. Cao YQ, Deng ZX, Li J, Liu HJ. Multi-parameter optimization algorithm of frequency-dependent model for viscoelastic damping material. *Advanced Materials Research*. 2010;129-131:416-420. doi: 10.4028/www.scientific.net/AMR.129-131.416.

114. Zheng X, Lin G, Wang J, Zhang Y. Parameter identification of nonlinear viscoelastic-plastic constitutive equation of soybean and cottonseed based on particles swarm optimization. Proceedings of IEEE International Workshop on Knowledge Discovery and Data Mining: ; 2008, p.101-106:552.

115. Khajehsaeid H, Arghavani J, Naghdabadi R, Sohrabpour S. A visco-hyperelastic constitutive model for rubber-like materials: A rate-dependent relaxation time scheme. *Int J Eng Sci*. 2014;79:44-58.

116. Moravec F, Holeček M. Microstructure-dependent nonlinear viscoelasticity due to extracellular flow within cellular structures. *Int J Solids Structures*. 2010;47(14):1876-1887.

117. Kraaij G, Zadpoor AA, Tuijthof GJ, Dankelman J, Nelissen RG, Valstar ER. Mechanical properties of human bone–implant interface tissue in aseptically loose hip implants. *Journal of the mechanical behavior of biomedical materials*. 2014;38:59-68.

118. Hao D, Li D, Liao Y. A finite viscoelastic constitutive model for filled rubber-like materials. *Int J Solids Structures*. 2015;64:232-245.

119. Doman D, Cronin D, Salisbury C. Characterization of polyurethane rubber at high deformation rates. *Exp Mech*. 2006;46(3):367-376.

120. Beda T, Casimir J, Atcholi K, Chevalier Y. Loaded rubber-like materials subjected to small-amplitude vibrations. *Chinese Journal of Polymer Science*. 2014;32(5):620-632.

121. Cao YQ, Deng ZX, Li J, Liu HJ. Multi-parameter optimization algorithm of frequency-dependent model for viscoelastic damping material. *Materials and Manufacturing Technology, Pts 1 and 2*. 2010;129-131:416-420. doi: 10.4028/www.scientific.net/AMR.129-131.416.

122. Salisbury C. *On the deformation mechanics of hyperelastic porous materials.* [University of Waterloo]. ; 2011 [Ph.D. thesis].

123. Uriarte I, Zulueta E, Guraya T, Arsuaga M, Garitaonandia I, Arriaga A. CHARACTERIZATION OF RECYCLED RUBBER USING PARTICLE SWARM OPTIMIZATION TECHNIQUES. *Rubber Chemistry and Technology*. 2015;88(3):343-358. http://dx.doi.org/10.5254/rct.15.85916. doi: 10.5254/rct.15.85916.

ANNEX A

7.2 A.1. EXPERIMENTAL CURVES FOR BLENDS 75/25 AND 60/40 (SUMMARIZED IN CHAPTER 3)

A.1.1. 75/25 BLEND

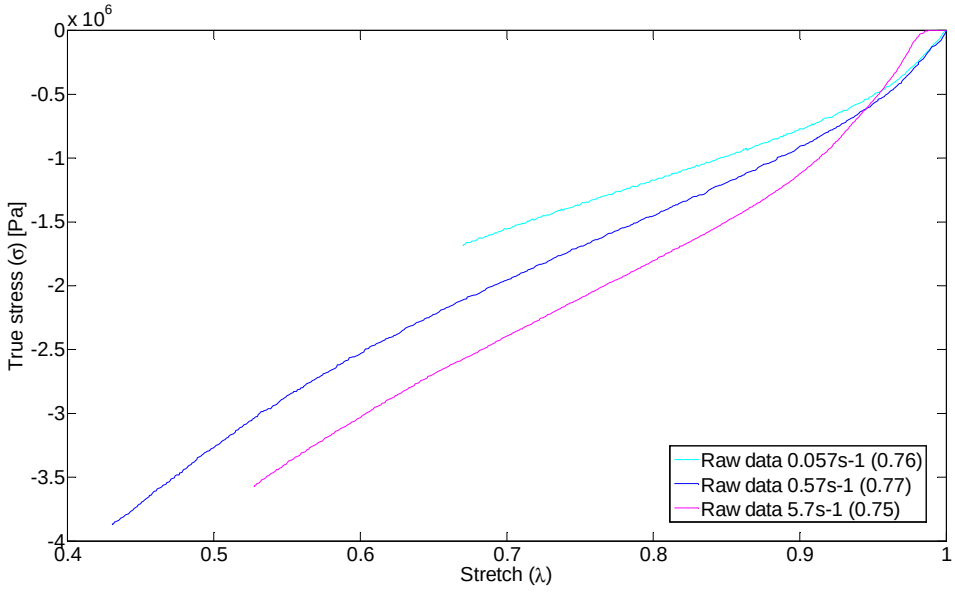

Fig. A - 1 Stress-stretch curves for density 0.7 g/cm^3 at different strain rates (BIG samples, 75/25 proportion).

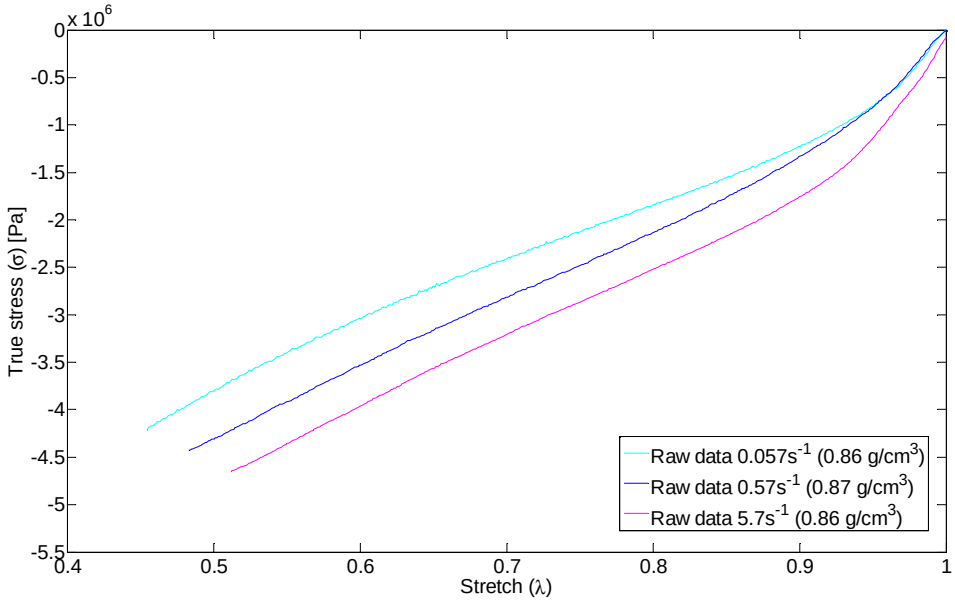

Fig. A - 2 Stress-stretch curves for density 0.8 g/cm³ at different strain rates (BIG samples, 75/25 proportion).

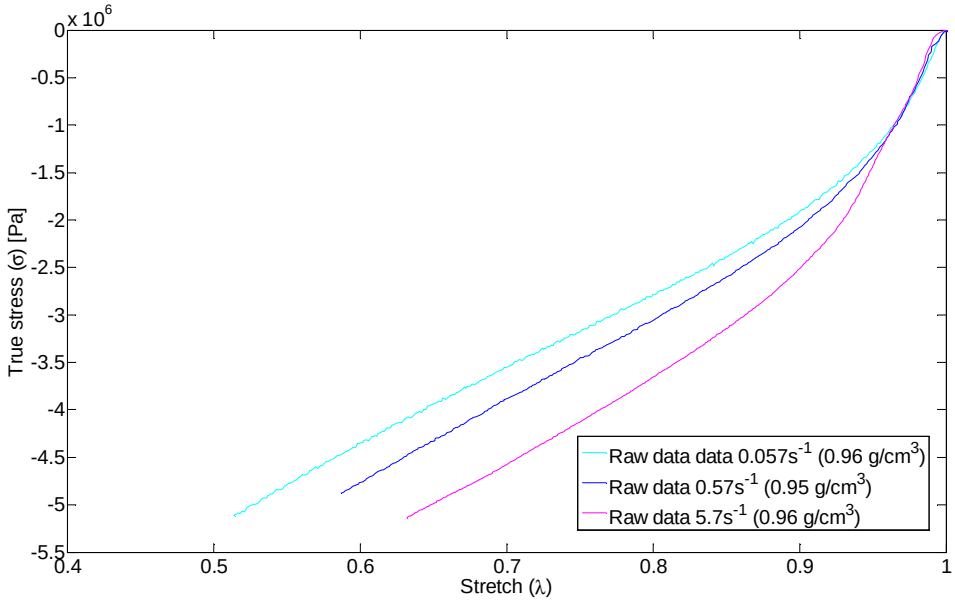

Fig. A - 3 Stress-stretch curves for density 0.9 g/cm³ at different strain rates (BIG samples, 75/25 proportion).

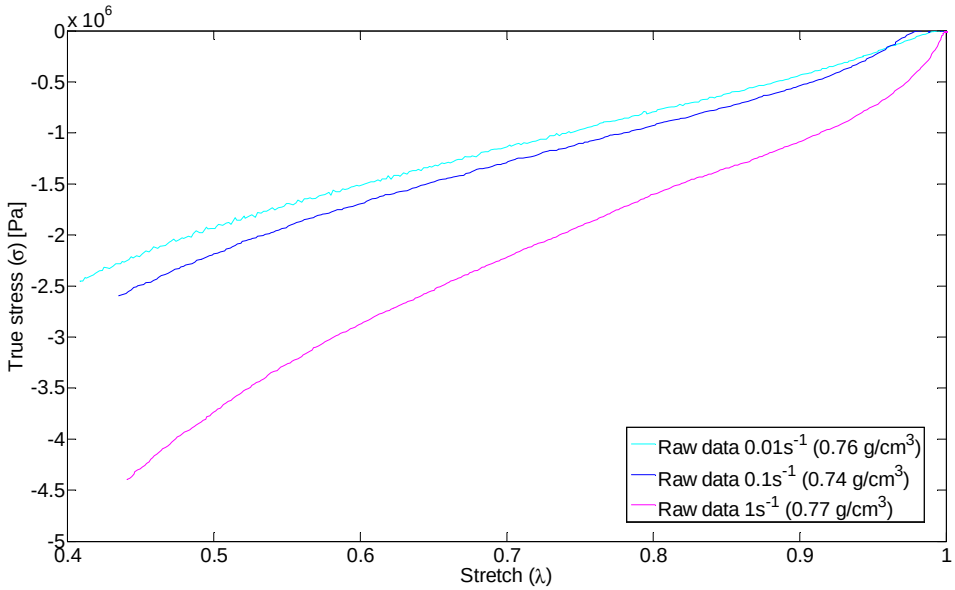

Fig. A - 4 Stress-stretch curves for density 0.7 g/cm³ at different strain rates (SMALL samples, 75/25 proportion).

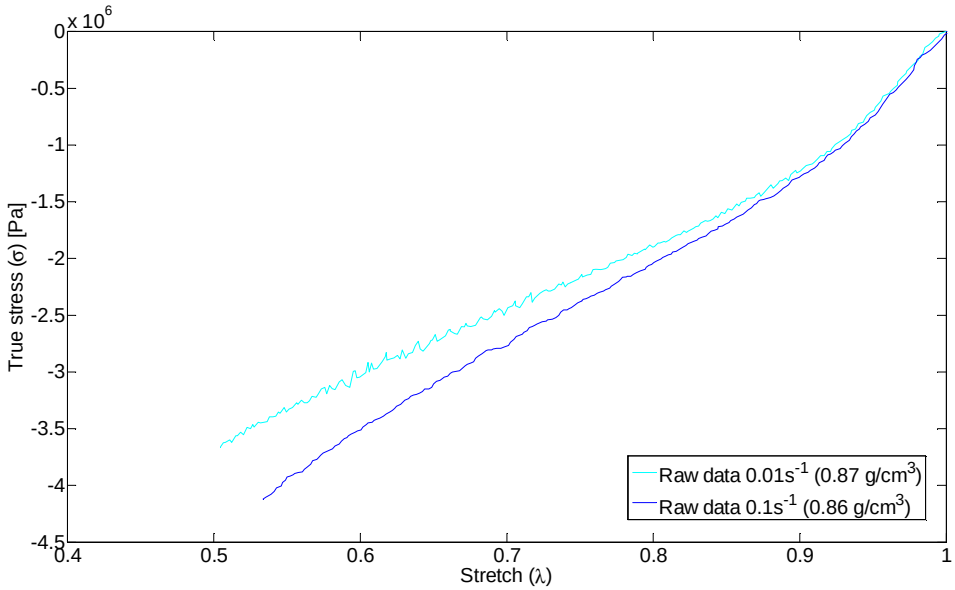

Fig. A - 5 Stress-stretch curves for density 0.8 g/cm³ at different strain rates (SMALL samples, 75/25 proportion).

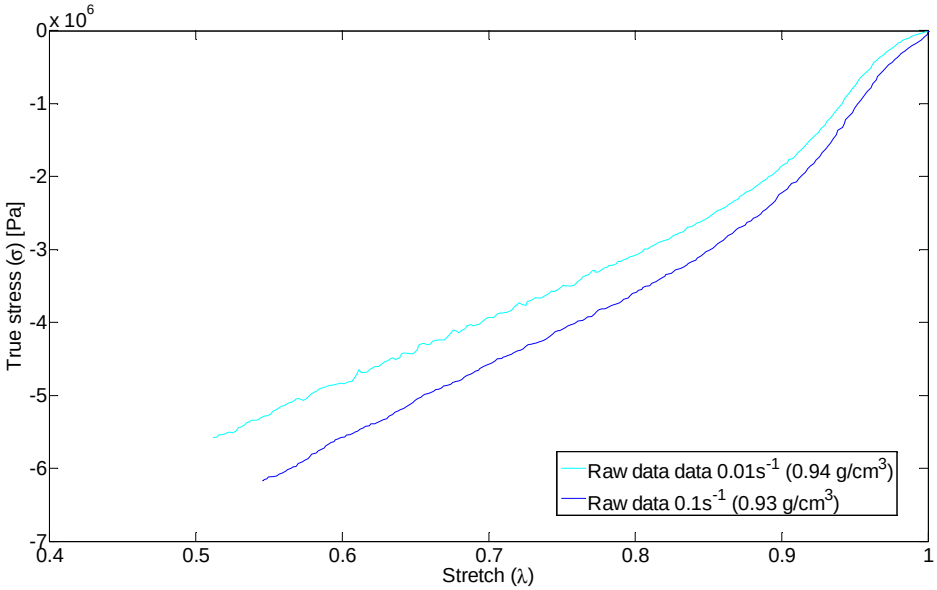

Fig. A - 6 Stress-stretch curves for density 0.9 g/cm³ at different strain rates (SMALL samples, 75/25 proportion).

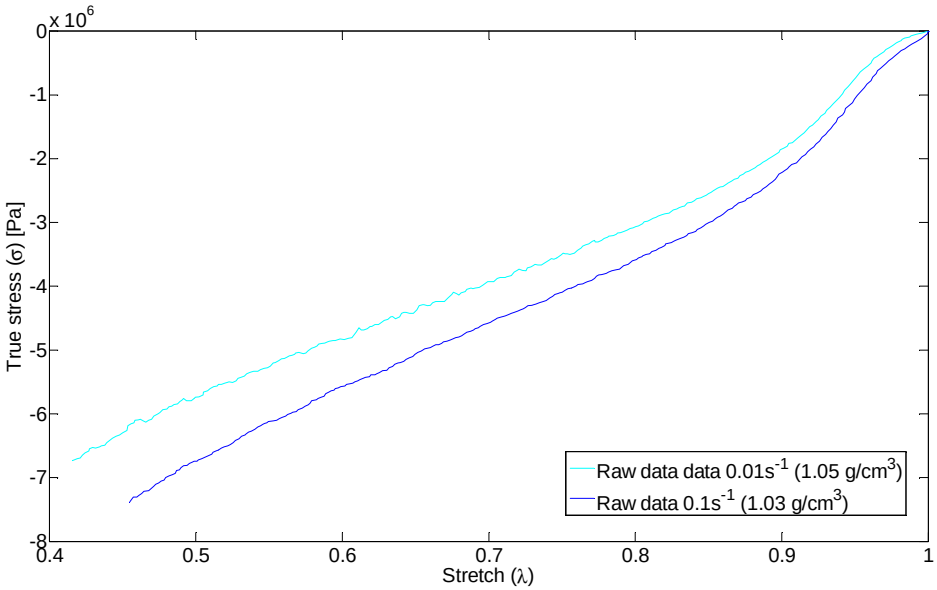

Fig. A - 7 Stress-stretch curves for density 1 g/cm³ at different strain rates (SMALL samples, 75/25 proportion).

A.1.2. 60/40 BLEND

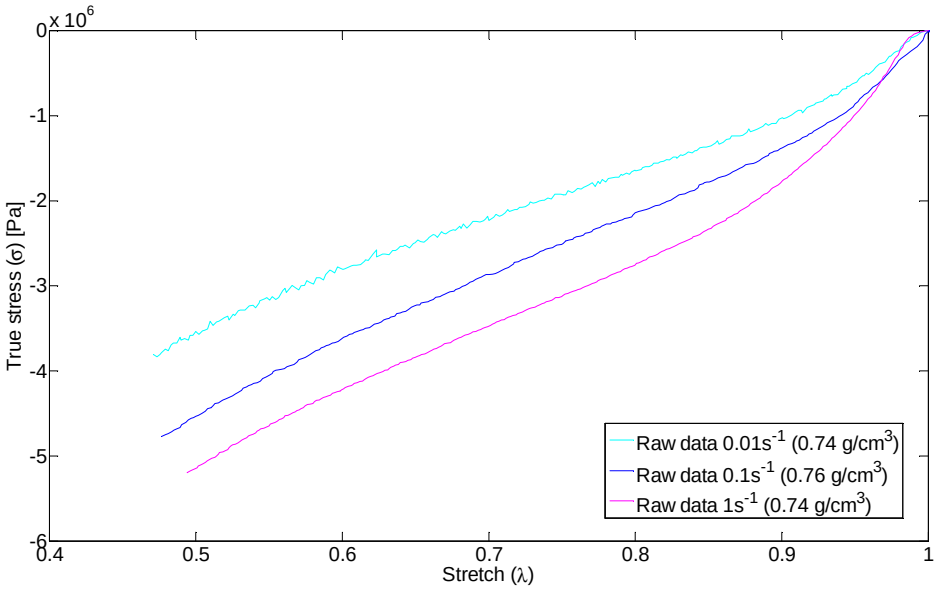

Fig. A - 8 Stress-stretch curves for density 0.7 g/cm3 at different strain rates (SMALL samples, 60/40 proportion).

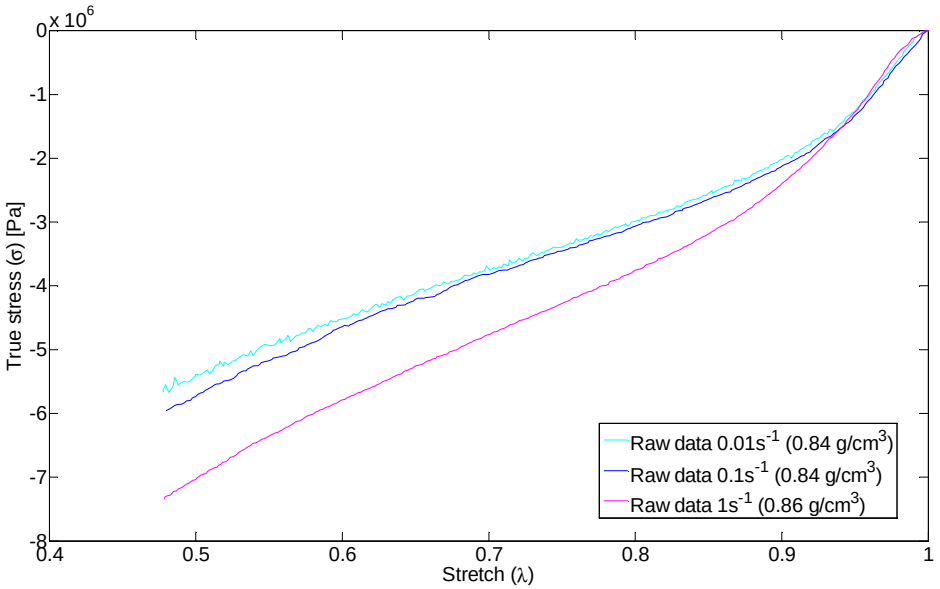

Fig. A - 9 Stress-stretch curves for density 0.8 g/cm^3 at different strain rates (SMALL samples, 60/40 proportion).

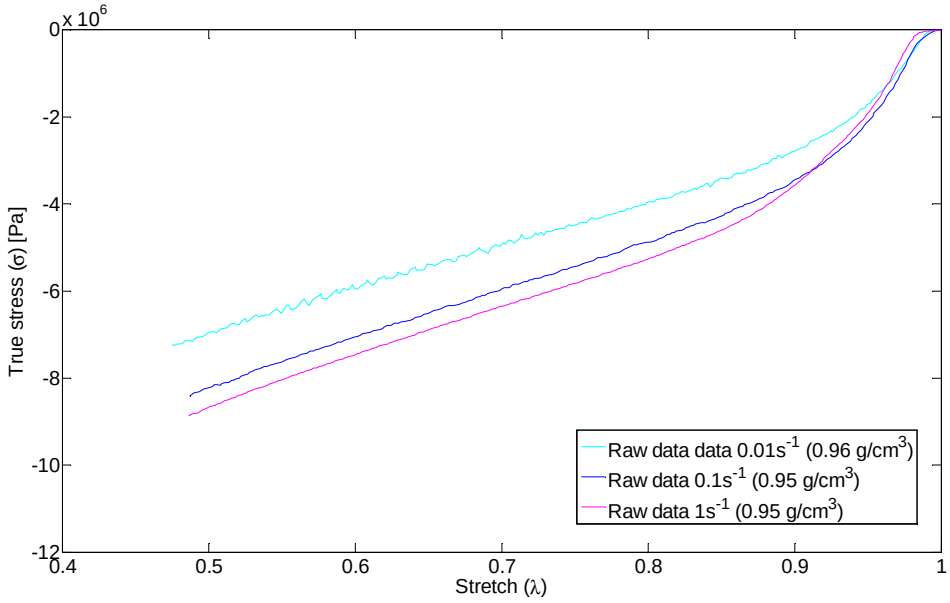

Fig. A - 10 Stress-stretch curves for density 0.9 g/cm³ at different strain rates (SMALL samples, 60/40 proportion).

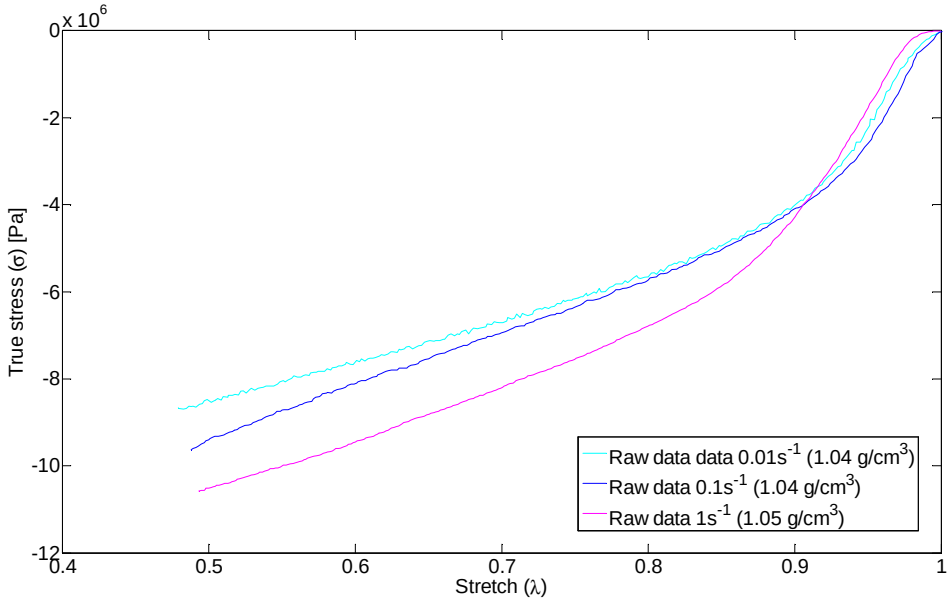

Fig. A - 11 Stress-stretch curves for density 1 g/cm³ at different strain rates (SMALL samples, 60/40 proportion).

ANNEX B

7.3 B.1. SOME REMARKS ON OBJECTIVITY, ISOTROPY AND INCOMPRESSIBILITY CHARACTERISTICS OF HYPERELASTIC MATERIALS

The **strain-energy function** is assumed to be **objective** (invariant to the change of the observer), that is, after a translation and a rotation of the **hyperelastic** material the amount of stored energy remains unchanged. If x^* is the position of a point in the space after a translation and a rotation of the point x from the reference configuration, they are related by the expression:

$$x^* = c(t) + Q(t)x \tag{1.1}$$

$$t^* = t + \alpha \tag{1.2}$$

Where the vector c(t) describes de rigid body translation; and the tensor Q –proper orthogonal tensor, det(Q)=1 – describes a rigid body rotation.

$$\begin{aligned} F(X,t) &= \frac{\partial x(X,t)}{\partial X} \\ F^*(X,t^*) &= \frac{\partial x^*(X,t^*)}{\partial X} \end{aligned} \tag{1.3}$$

$$F^* = \frac{\partial x^*}{\partial X} = Q\frac{\partial x}{\partial X} = QF \tag{1.4}$$

$$\psi(F) = \psi\left(F^*\right) = \psi(QF) \tag{1.5}$$

As any proper orthogonal tensor Q is valid in previous expression, if the transpose of the rotation tensor is considered, $Q = R^T$,

$$\psi(F) = \psi(QF) = \psi\left(R^T F\right) = \psi\left(R^T RU\right) = \psi(U) \tag{1.6}$$

Here, it can be concluded that $\boldsymbol{\psi}$ only depends on the **stretching part of F** (it is independent of the rotational part R). As $C = F^T F = U^T R^T RU = U^2$ ($R^T R = 1$ and $U^T = U$) and $E = \frac{U^2 - I}{2}$, $\boldsymbol{\psi}$ can be expressed as a function of these:

$$\psi(F) = \psi(C) = \psi(E) \tag{1.7}$$

If the derivative of the strain energy function is done, it is obtained the next expression:

$$\begin{aligned} \dot{\psi} &= tr\left[\left(\frac{\partial \psi(F)}{\partial F}\right)^T \dot{F}\right] = tr\left[\left(\frac{\partial \psi(C)}{\partial C}\right)^T \dot{C}\right] = tr\left[\left(\frac{\partial \psi(C)}{\partial C}\right)^T \left(\dot{F}^T F + F^T \dot{F}\right)\right] = \\ &= 2tr\left(\frac{\partial \psi(C)}{\partial C} F^T \dot{F}\right) \end{aligned} \tag{1.8}$$

From here it can be obtained:

$$\left(\frac{\partial \psi(F)}{\partial F}\right)^T = 2\frac{\partial \psi(C)}{\partial C} F^T \tag{1.9}$$

And taking into account that $PF^T = FP^T$, the Cauchy stress is:

$$\sigma = J^{-1} F\left(\frac{\partial \psi(F)}{\partial F}\right)^T = 2J^{-1} F \frac{\partial \psi(C)}{\partial C} F^T \tag{1.10}$$

The first Piola Kirchhoff stress tensor:

$$P = \left(\frac{\partial \psi(F)}{\partial F}\right) = 2F\frac{\partial \psi(C)}{\partial C} \tag{1.11}$$

The second Piola Kirchhoff stress tensor:

$$S = F^{-1} P = 2\frac{\partial \psi(C)}{\partial C} = \frac{\partial \psi(E)}{\partial E} \tag{1.12}$$

As $2E = C - I$.

If the material is **isotropic**, this is, if the response of the material is the same in all directions, and a superimposed rigid body motion is considered on the reference configuration of a material, being:

$$X^* = c(t) + Q(t)X \tag{1.13}$$

Where $F^* = \frac{\partial x}{\partial X^*}$.

$$F = \frac{\partial x}{\partial X} = \frac{\partial x}{\partial X^*} Q = F^* Q \rightarrow F^* = FQ^T \tag{1.14}$$

A hyperelastic material is isotropic if:

$$\psi(F) = \psi(F^*) = \psi(FQ^T) \tag{1.15}$$

Taking into account that $\psi(F) = \psi(C)$ if the material is hyperelastic, $\psi(C) = \psi(C^*) = \psi(F^{*T}F^*) = \psi(QF^TFQ^T) = \psi(QCQ^T)$.

If this expression holds for all symmetric tensors C and orthogonal tensors Q, $\psi(C)$ is an invariant of C (invariant under rotation), so it can be expressed in terms of the principal invariants of C.

$$\psi(C) = \psi[I_1(C), I_2(C), I_3(C)] = \psi[I_1(b), I_2(b), I_3(b)] \tag{1.16}$$

$$\begin{aligned} I_1(C) &= tr(C) \\ I_2(C) &= \frac{1}{2}\left[(tr(C))^2 - tr(C^2)\right] \\ I_3(C) &= \det(C) \end{aligned} \tag{1.17}$$

Remembering that $S = F^{-1}P = 2\frac{\partial \psi(C)}{\partial C}$ and differentiating $\psi(C)$:

$$\frac{\partial \psi(C)}{\partial C} = \frac{\partial \psi}{\partial I_1}\frac{\partial I_1}{\partial C} + \frac{\partial \psi}{\partial I_2}\frac{\partial I_2}{\partial C} + \frac{\partial \psi}{\partial I_3}\frac{\partial I_3}{\partial C} \tag{1.18}$$

$$\frac{\partial I_1}{\partial C}=\frac{\partial trC}{\partial C}=\frac{\partial (I:C)}{\partial C}=I$$
$$\frac{\partial I_2}{\partial C}=\frac{1}{2}\left(2(trC)I-\frac{\partial tr(C^2)}{\partial C}\right)=I_1 I-C \tag{1.19}$$
$$\frac{\partial I_3}{\partial C}=I_3 C^{-1}$$

$$S=2\frac{\partial \psi(C)}{\partial C}=2\left[\frac{\partial \psi}{\partial I_1}I+\frac{\partial \psi}{\partial I_2}(I_1 I-C)+\frac{\partial \psi}{\partial I_3}I_3 C^{-1}\right] \tag{1.20}$$

$$S=2\left[\left(\frac{\partial \psi}{\partial I_1}+I_1\frac{\partial \psi}{\partial I_2}\right)I-\frac{\partial \psi}{\partial I_2}C+I_3\frac{\partial \psi}{\partial I_3}C^{-1}\right] \tag{1.21}$$

$$\sigma=J^{-1}FSF^T \tag{1.22}$$

Taking into account that:

$$FIF^T=FF^T=b$$
$$FCF^T=\left(FF^T\right)^2=b^2 \tag{1.23}$$
$$FC^{-1}F^T=FF^{-1}F^{-T}F^T=I$$

Following expression is obtained:

$$\sigma=2J^{-1}\left[\left(\frac{\partial \psi}{\partial I_1}+I_1\frac{\partial \psi}{\partial I_2}\right)b-\frac{\partial \psi}{\partial I_2}b^2+I_3\frac{\partial \psi}{\partial I_3}I\right] \tag{1.24}$$

Remembering eq.5.88 from Holzapfel[42], $b^2=I_1 b-I_2 I+I_3 b^{-1}$, and replacing it in previous equation:

$$\begin{aligned}\sigma&=2J^{-1}\left[\left(\frac{\partial \psi}{\partial I_1}+I_1\frac{\partial \psi}{\partial I_2}\right)b-\frac{\partial \psi}{\partial I_2}\left(I_1 b-I_2 I+I_3 b^{-1}\right)+I_3\frac{\partial \psi}{\partial I_3}I\right]=\\&=2J^{-1}\left[\left(I_2\frac{\partial \psi}{\partial I_2}+I_3\frac{\partial \psi}{\partial I_3}\right)I+\left(\frac{\partial \psi}{\partial I_1}\right)b-I_3\frac{\partial \psi}{\partial I_2}b^{-1}\right]\end{aligned} \tag{1.25}$$

In the case of **incompressible** materials, the related constraint is $J=1$, and the strain energy function is defined as:

$$\psi=\psi(F)-p(J-1) \tag{1.26}$$

With p as Lagrange multiplier. It can be determined from the boundary conditions and equilibrium equations, as hydrostatic pressure.

Differentiating this equation with respect to F and taking into account that $\frac{\partial J}{\partial F} = JF^{-T}$,

$$P = \frac{\partial \psi(F)}{\partial F} - pF^{-T} \tag{1.27}$$

If previous equation is multiplied by F^{-1} from the left-hand side:

$$S = F^{-1}\frac{\partial \psi(F)}{\partial F} - pC^{-1} = F^{-1}2F\frac{\partial \psi(C)}{\partial C} - pC^{-1} = 2\frac{\partial \psi(C)}{\partial C} - pC^{-1} \tag{1.28}$$

If eq.**¡Error! No se encuentra el origen de la referencia.** is multiplied by F^T from the right-hand side:

$$\sigma = \frac{\partial \psi(F)}{\partial F}F^T - pI \tag{1.29}$$

As for the incompressible case the invariant $I_3 = \det C = \det b = 1$, the strain energy function may be expressed in terms of I_1 and I_2:

$$\psi(C) = \psi\left[I_1(C), I_2(C)\right] - \frac{1}{2}p(I_3 - 1) = \psi\left[I_1(b), I_2(b)\right] - \frac{1}{2}p(I_3 - 1) \tag{1.30}$$

Where $\frac{p}{2}$ is a Lagrange multiplier.

Taking into account that $S = 2\frac{\partial \psi(C)}{\partial C}$, if $\psi\left(I_1(C), I_2(C)\right)$ is derived:

$$\frac{\partial \psi(C)}{\partial C} = \frac{\partial \psi(I_1, I_2)}{\partial C} - \frac{\partial \frac{1}{2}p(I_3 - 1)}{\partial C} = I\frac{\partial \psi}{\partial I_1} + (I_1 I - C)\frac{\partial \psi}{\partial I_2} - \frac{1}{2}pI_3 C^{-1} \tag{1.31}$$

$$S = 2I\frac{\partial \psi}{\partial I_1} + 2(I_1 I - C)\frac{\partial \psi}{\partial I_2} - 2\frac{1}{2}pI_3 C^{-1} = 2\left(\frac{\partial \psi}{\partial I_1} + I_1\frac{\partial \psi}{\partial I_2}\right)I - 2\frac{\partial \psi}{\partial I_2}C - pC^{-1} \tag{1.32}$$

Taking into account eq. **¡Error! No se encuentra el origen de la referencia.** and the relationship between Cauchy stress and second Piola-Kirchhoff stress next expression is obtained:

$$\sigma = 2(\frac{\partial \psi}{\partial I_1} + I_1 \frac{\partial \psi}{\partial I_2})b - 2\frac{\partial \psi}{\partial I_2} b^2 - pI \tag{1.33}$$

Which is the **expression used by Yang et al.** for a hyperelastic, isotropic, incompressible material showm in eq.(5.2).

The strain energy can be also separated, as stated in eq. (6.10). Keeping in mind eq.**¡Error! No se encuentra el origen de la referencia.**:

$$S = 2\frac{\partial \psi_{isoc}}{\partial C} + 2\frac{\partial \psi_{vol}}{\partial J}\frac{\partial J}{\partial C} \tag{1.34}$$

From $\frac{\partial J}{\partial C} = \frac{J}{2} C^{-1}$:

$$S = 2\frac{\partial \psi_{isoc}}{\partial C} + J\frac{\partial \psi_{vol}}{\partial J} C^{-1} \tag{1.35}$$

In the isotropic case, $\psi_{isoc} = \psi_{isoc}(\overline{I}_1, \overline{I}_2)$; differentiating it:

$$\frac{\partial \psi_{isoc}}{\partial C} = \frac{\partial \psi_{isoc}}{\partial \overline{I}_1}\frac{\partial \overline{I}_1}{\partial C} + \frac{\partial \psi_{isoc}}{\partial \overline{I}_2}\frac{\partial \overline{I}_2}{\partial C} \tag{1.36}$$

Next, eq.(6.3) and eq.(6.4) are introduced in **¡Error! No se encuentra el origen de la referencia.** , and with

$$\frac{\partial I_1}{\partial C} = \frac{\partial trC}{\partial C} = \frac{\partial (I:C)}{\partial C} = I \tag{1.37}$$

$$\frac{\partial I_2}{\partial C} = \frac{1}{2}\left(2(trC)I - \frac{\partial tr(C^2)}{\partial C} \right) = I_1 I - C \tag{1.38}$$

Differentiating $\overline{I}_1$ and $\overline{I}_2$ over C:

$$\frac{\partial \overline{I}_1}{\partial C} = \frac{\partial J^{-2/3}}{\partial C} I_1 + J^{-2/3}\frac{\partial I_1}{\partial C} = -\frac{1}{3} J^{-2/3} C^{-1} I_1 + J^{-2/3} I \tag{1.39}$$

$$\frac{\partial \overline{I}_2}{\partial C} = \frac{\partial J^{-4/3}}{\partial C} I_2 + J^{-4/3}\frac{\partial I_2}{\partial C} = -\frac{2}{3} J^{-4/3} C^{-1} I_2 + J^{-4/3}(I_1 I - C) \tag{1.40}$$

Therefore:

$$S = 2\frac{\partial \psi_{isoc}}{\partial \bar{I}_1}\frac{\partial \bar{I}_1}{\partial C} + 2\frac{\partial \psi_{isoc}}{\partial \bar{I}_2}\frac{\partial \bar{I}_2}{\partial C} + J\frac{\partial \psi_{vol}}{\partial J}C^{-1} =$$
$$= 2\frac{\partial \psi_{isoc}}{\partial \bar{I}_1}\left(-\frac{1}{3}J^{-2/3}C^{-1}I_1 + J^{-2/3}I\right) + 2\frac{\partial \psi_{isoc}}{\partial \bar{I}_2}\left(-\frac{2}{3}J^{-4/3}C^{-1}I_2 + J^{-4/3}(I_1 I - C)\right) + J\frac{\partial \psi_{vol}}{\partial J}C^{-1} = \quad (1.41)$$
$$= 2J^{-2/3}\left[\frac{\partial \psi_{isoc}}{\partial \bar{I}_1}\left(I - \frac{1}{3}C^{-1}I_1\right) + J^{-2/3}\frac{\partial \psi_{isoc}}{\partial \bar{I}_2}\left(I_1 I - C - \frac{2}{3}C^{-1}I_2\right)\right] + J\frac{\partial \psi_{vol}}{\partial J}C^{-1}$$

This expression may be written as:

$$S = 2J^{-2/3}DEV\left[\frac{\partial \psi_{isoc}}{\partial \bar{I}_1}I - J^{-2/3}\frac{\partial \psi_{isoc}}{\partial \bar{I}_2}C^{-2}\right] + J\frac{\partial \psi_{vol}}{\partial J}C^{-1} \quad (1.42)$$

With $DEV(\bullet) = (\bullet) - \frac{1}{3}[(\bullet):C]C^{-1}$ as the deviatoric operator over the material configuration.

Remembering eq.**¡Error! No se encuentra el origen de la referencia.**, one gets next expression:

$$S_{deviatoric} = 2\left(\frac{\partial \psi_{isoc}}{\partial \bar{I}_1} + \bar{I}_1\frac{\partial \psi_{isoc}}{\partial \bar{I}_2}\right)I - 2\frac{\partial \psi_{isoc}}{\partial \bar{I}_2}\bar{C} \quad (1.43)$$

And the Cauchy stress becomes ($\sigma = J^{-1}FSF^T$):

$$\sigma = 2J^{-2/3}J^{-1}\left[\frac{\partial \psi_{isoc}}{\partial \bar{I}_1}F\left(I - \frac{1}{3}C^{-1}I_1\right)F^T + J^{-2/3}\frac{\partial \psi_{isoc}}{\partial \bar{I}_2}F\left(I_1 I - C - \frac{2}{3}C^{-1}I_2\right)F^T\right] + J\frac{\partial \psi_{vol}}{\partial J}FC^{-1}F^T \quad (1.44)$$

And considering eq. **¡Error! No se encuentra el origen de la referencia.** again:

$$\sigma = 2J^{-1}\left[J^{-2/3}\frac{\partial \psi_{isoc}}{\partial \bar{I}_1}\left(b - \frac{1}{3}I_1 I\right) + J^{-4/3}\frac{\partial \psi_{isoc}}{\partial \bar{I}_2}\left(I_1 b - b^2 - \frac{2}{3}I_2 I\right)\right] + \frac{\partial \psi_{vol}}{\partial J}I \quad (1.45)$$

Remembering that $\bar{b} = J^{-2/3}b$ and $\bar{b}^2 = \bar{I}_1\bar{b} - \bar{I}_2 I + \bar{b}^{-1}$ next expression is obtained:

$$\bar{b}^{-1} = -\bar{I}_1\bar{b} + \bar{I}_2 I + \bar{b}^2 \quad (1.46)$$

And therefore:

$$\sigma = 2J^{-1}\left[\frac{\partial \psi_{isoc}}{\partial \bar{I}_1}\left(\bar{b} - \frac{1}{3}\bar{I}_1 I\right) - \frac{\partial \psi_{isoc}}{\partial \bar{I}_2}\left(\bar{b}^{-1} - \frac{1}{3}\bar{I}_2 I\right)\right] + \frac{\partial \psi_{vol}}{\partial J}I \quad (1.47)$$

This expression may be written as:

$$\sigma = 2J^{-1} dev\left[\frac{\partial \psi_{isoc}}{\partial \bar{I}_1} \bar{b} - \frac{\partial \psi_{isoc}}{\partial \bar{I}_2} \bar{b}^{-1} \right] + \frac{\partial \psi_{vol}}{\partial J} I \tag{1.48}$$

With $dev(\bullet) = (\bullet) - \frac{1}{3} tr(\bullet) I$ as the deviatoric operator over the spatial configuration.

Considering eq. **¡Error! No se encuentra el origen de la referencia.** once more, if it is introduced into eq. **¡Error! No se encuentra el origen de la referencia.**:

$$\begin{aligned}
&\sigma = 2J^{-1} dev\left[\frac{\partial \psi_{isoc}}{\partial \bar{I}_1} \bar{b} - \frac{\partial \psi_{isoc}}{\partial \bar{I}_2} \left(-\bar{I}_1 \bar{b} + \bar{I}_2 I + \bar{b}^2 \right) \right] + \frac{\partial \psi_{vol}}{\partial J} I = \\
&= 2J^{-1} dev\left[\left(\frac{\partial \psi_{isoc}}{\partial \bar{I}_1} + \bar{I}_1 \frac{\partial \psi_{isoc}}{\partial \bar{I}_2} \right) \bar{b} - \frac{\partial \psi_{isoc}}{\partial \bar{I}_2} \left(-\bar{I}_2 I - \bar{b}^2 \right) \right] + \frac{\partial \psi_{vol}}{\partial J} I = \\
&= 2J^{-1} dev\left[\left(\frac{\partial \psi_{isoc}}{\partial \bar{I}_1} + \bar{I}_1 \frac{\partial \psi_{isoc}}{\partial \bar{I}_2} \right) \bar{b} - \frac{\partial \psi_{isoc}}{\partial \bar{I}_2} \bar{b}^2 \right] + \frac{\partial \psi_{vol}}{\partial J} I
\end{aligned} \tag{1.49}$$

eman ta zabal zazu

Universidad del País Vasco
Euskal Herriko Unibertsitatea

DOKTORETZA TESIA – PhD THESIS

PNEUMATIKOETAKO KAUTXU BIRZIKLATUZ FABRIKATURIKO MATERIAL BATEN KARAKTERIZAZIOA KOLPEEN AURREAN

CHARACTERIZATION OF RECYCLED RUBBER COMING FROM USED TIRES UNDER IMPACT LOADINGS

Egilea / Author:

Irantzu Uriarte Gallastegi

Zuzendariak / Supervisors:

Iker Garitaonandia Areitio Dr.

Teresa Guraya Díez Dr.

Bilbao, 2017 Maiatza / May

In moments of crisis only imagination is more important than knowledge

Albert Einstein (1879-1955)

ESKER ONAK

Ezagutzen nauen orok daki niretzat zeinen zailak diren honako hitz hauek. Izan ere, horrenbeste dut eskertzeko, horrenbeste jenderi, beldurra ematen didala inor ahazteagatik minduta senti daitekeenaren pentsatze hutsak.

Nire eskerrak txikitatik unibertsitaterainoko bidean nire ikastola maitean jakin-mina, zirrara berezi hori sorrarazi zidaten guztiei. Baita unibertsitatean izan nituen irakasle itzel horiei ere. Mikel, Andoni, Javi eta Josu, zueri bere eskerrik asko bihotzez. Izandako lan desberdinetako kide eta gaur egungo lagun berezi horiei. Ibilbide horrek egin nau gaur naizen profesionala.

Nire tesi zuzendari biok ezin ahaztu, Iker eta Teresa.

Lanean ditudan kideei esker berezia. Esteban, Ziortza eta Iñakiri, zuokin ikasgaiak partekatzea plazer bat delako eta tesi honetan aritu naizen artean lagundu izan didazuen guztiarengatik, ez lan kontuetan soilik. Sarritan gogorrak egiten diren momentuetan euskarri izan zaretelako, Rober eta Mikelekin batera. Zer esan lan honetan gehien lagundu izan didan pertsona horri buruz, Ekaitz, zure moduko jendez beteta behar luke mundu honek; lagun itzela egin dut bidean, Ciceron. Berarekin batera Gasteizen zaitudan lagun miñ horri, behar zaitudan oro hor egoteagatik, milesker! Ta noski sailean eta unibertsitatean zaituztedan gainontzeko lagunoi ere (Juan, Aloña, Nekane, Amaia, Edorta), jada elkarrekin bizi izandako hainbeste gauzengatik. Maider, Pilar, Itzi, Antón,…ikusten?, zerrenda luzeegia; parkatu norbait ez bazaituztet aipatu.

Kuadrillako lagun guztioi, denpora guzti honetan ni jasan izanagatik, nire eskerrik beroenak. Azkenean badirudi *dottore dottore* abestu ahal izango dugula (Venecia-n ote?). Nire beste lagun *Ladies* horiei ere milesker hor egoteagatik! Bidean ezagutu eta horren berezietan bihurtu zaretenoi ere eskerrak, Yolanda, nire *Xelebreak*, Ramon, Ibai, nire Death Star horren berezi horri.

Ta betiko moduan, ezin falta familia. Familiako guztioi bide honetan lagundu izanagatik. Batetik, aita-ama, Naia, amumi. Bestetik, Bego, Juan, Izas, izeko, osabak. Ta noski, Gari eta nire maitetxu biori, Izaro eta Laida, hor zaudetelako, beti.

Bidean joan zaidan persona garrantzitsuenari.

Amuma, zuretzat.

SUMMARY

Rubber is broadly demanded in a variety of engineering fields where high damping and energy dissipation capability is required. Used rubber tires represent an important percentage of waste polymeric material as the automotive industry requires an increasing amount of tires year after year. With the objective of recycling this material, significant quantities of protective systems adapted for two wheel vehicles have been designed, generically called Motorcyclist Protection Systems (MPS). Motivated by the benefits of using recycled rubber as a shock absorber in metallic road barriers, this thesis presents the work carried out on the characterization of a material based on used tires. Three blends of recycled rubber from used tires and Linear Low Density Polyethylene as adhesive have been performed, with different proportions of each material and a constant proportion of TiO_2 as colorant on all of them. This use is included into impacts; hence the mechanical characterization of the blend has encompassed high strain rate compression tests.

A visco-hyperelastic constitutive equation pretty well known in the literature has been chosen to characterize the material, i.e. Yang's model. The hyperelastic part has been adjusted by the least-squares fitting technique. Concerning the parameters of the viscoelastic part, based on convolution integral, resulted very difficult to adjust. Particle Swarm Optimization (PSO) algorithm has been selected to obtain the values of these parameters.

At the highest speed the material curves exhibited distinctive waves, usually called as "ringing" in the specialized literature. This data can not be used in its original form as it is distorted. Therefore, Experimental Modal Analysis (EMA) has considered essential to study in detail the dynamic characteristics of the servo hydraulic machine. Thus, it has done a multiple degree of freedom machine model by means of the natural frequencies, mode shapes and damping factors obtained from the EMA. That way the final data resulted treatable with an obvious reduction of the oscillations.

The methodology to implement the previously proposed Yang's model in the Finite Element software Ansys, with its solver for explicit analysis LS Dyna, has been introduced next. This constitutive equation is not implemented in this software yet and consequently, a material user subroutine has been developed first in Matlab. The algorithm to implement the material subroutine is explained in this work.

INDEX

List of figures

List of tables

ABBREVIATIONS AND SYMBOLS

a	non-dimensionalised modelling parameter
A_i	modelling parameters
$\boldsymbol{B}$	left Cauchy-Green deformation tensor
B_{ij}	components of $\boldsymbol{B}$
$\boldsymbol{C}$	right Cauchy-Green deformation tensor
$\dot{\boldsymbol{D}}$	non-dimensionalised strain rate
$\boldsymbol{E}$	Green-Lagrange strain tensor
$\dot{\boldsymbol{E}}$	strain rate tensor
$\boldsymbol{F}$	deformation gradient tensor
$\boldsymbol{I}$	unit tensor
I_i	invariants of $\boldsymbol{B}$
I'_i	invariants of $\boldsymbol{C}$
p	pressure
s	non-dimensionalised time
$\boldsymbol{S}$	non-dimensionalised stress tensor
t	time
W	strain energy potential
$\boldsymbol{x}$	position vector of a material particle at time t
$\boldsymbol{X}$	initial position vector of a material particle
β	integral variable of non-dimensionalised time
ε_{ij}	components of engineering strain
$\dot{\zeta}$	non-dimensionalised stretch rate
θ_i	relaxation time
λ	stretch
$\dot{\lambda}$	stretch rate
σ	Cauchy stress tensor
σ^0_{ij}	components of engineering stress
σ_{ij}	components of σ
τ	integral value of time
Ω	constitutive functional

1. INTRODUCTION

1.1 ANTECEDENTS

Rubber is broadly demanded in a variety of engineering fields where high damping and energy dissipation capability is required. Used rubber tires represent an important percentage of waste polymeric material as the automotive industry requires an increasing amount of tires year after year. Vulcanized rubber has a cross-linked three-dimensional network structure, which is not easily degradable by natural means, so there is widespread interest in rubber recycling[1-4]. This interest has been encouraged by waste disposal management trends all over the world, which try to provide alternative uses to end-of-life products not only because of environmental factors, but also for economic reasons.

The engineering applications of rubbers are broad and grow rapidly: structural bearings in army vehicles for blast protection[5,6]; or to protect buildings and bridges from earthquakes[7], tires, biological tissues[8], vehicle suspensions, vibration isolators[9], sealings, flexible joints and shock absorbers. Recycling of waste rubber by means of blending with Linear Low Density Polyethylene (LLDPE) is an interesting solution in this last application. The ability of rubber to absorb energy during impacts provides a very useful property for the design of protective coating on road barriers for motorcyclists who consistently call for more user-friendly and safer road barriers for two-wheel vehicle users[10]. Among the protective systems for road infrastructures, those constructed with metallic barriers are considered to be especially harmful for motorcycle riders, since an impact against their frame may cause serious injuries.

With the objective of satisfying the aforementioned demands, significant quantities of protective systems adapted for two wheel vehicles have been designed, generically called

Motorcyclist Protection Systems (MPS). Motivated by the benefits of using recycled rubber as a shock absorber in metallic road barriers, this thesis presents the work carried out on the characterization of a material based on used tires. This work is situated within the framework of an investigation project of the University of the Basque Country (UPV/EHU); the main objective of this project consists of studying the alternatives to regenerate/recycle rubber from used tires. It goes into detail about different recycling procedures, grinded particle sizes of vulcanized rubber, possible blend solutions to mix these rubber particles with other components and proportions of these blends.

It is important to understand the mechanical behavior of the material and specifically the rate-dependence of the blends to acquire knowledge on the proper characterization, so compression tests have been thoroughly conducted. Selection of a testing machine type or another depends on the range of application of the strain rate; there is not any universal facility that covers the whole strain rates domain[11,12]. Usually high rate servo-hydraulic testing systems[13] are preferred to carry experimental tests in the strain rate range from 1 s^{-1} to 100 s^{-1}. But there happens a problem with the machines in the range between 10-60 s^{-1} as there occur some vibrations that distort the stress-strain experimental response that make useless this data. These vibrations are known as system ringing in the specialized literature and they are produced by the excitation of predominant modes of the testing machine and create oscillations at one or more natural frequencies[14], damaging the experimental data.

Commonly researchers have performed the quantitative study of these vibrations considering the testing machine as a single degree of freedom system mainly, which has led to a general understanding of the variables involved in the process. However, discrepancies between analytical predictions and experimental observations have been detected using the single degree of freedom approach, so the need for further detailed study of machine dynamic characteristics has been reported. The work presented here addresses this requirement by means of a detailed characterization of the dynamic behavior of a MTS 819.10 high rate testing system.

1.2 OBJECTIVE OF THE THESIS

The main objective of this thesis consists in the mechanical characterization of the blend composed by recycled rubber and LLDPE to impacts, in order to study its potential

application as coating for road barriers. It is expected to obtain an adequate blend components proportion to comply with the requirements. With this purpose high strain rate compression tests have been carried out in a high speed servo-hydraulic machine. Thus, specific objectives of the thesis are:

- Three blends of recycled rubber and LLDPE are prepared, with different proportions of each component and four material densities. Four different machine speeds have been tested. In the highest speed waves have appeared in the force-time signal, known as system ringing. These oscillations convert into useless the experimental data. Therefore, it results necessary to perform an Experimental Modal Analysis of the testing machine, i.e. a MTS 819.10 machine in order to analyze the origin of these waves. Natural frequencies, mode shapes and damping factors will be obtained and it is hoped to develop a mathematical model of the process from these modal parameters. This mathematical model will be used to detect the modes that have the greatest influence in system ringing when testing rubber at high strain rates and to predict quantitatively the amplitudes of vibrations produced in the process. That way, it is expected to correct material curves.
- A material model is selected from the literature and its parameters are going to be adjusted by means of a Particle Swarm Optimization algorithm, which is selected because of its simplicity, robustness and rapid convergence. The PSO algorithm is a versatile optimization method that is able to turn away from local minimum and hence, reach the global minimum even if the function to optimize is highly nonlinear. The parameters to be fitted define the positions of the particles that move along a searching space, until they arrive to the global optimum.
- Next objective is to establish the methodology both in Matlab and in LS Dyna to implement this model in LS Dyna software. This will be done by creating a material subroutine as it does not exist in the software library. Therefore, it is expected to perform an explicit analysis of the high strain rate compression tests of the samples, i. e. simulations of the experimental tests.

1.3 CONTENTS AND STRUCTURE OF THE THESIS

This thesis has been divided in seven chapters. With the aim of providing a general overview of the thesis a brief description of each chapter is given below.

Chapter 2 presents existing materials based on recycled rubber and Polyethylene blends. Thereafter, it summarizes the main hyperelastic and viscoelastic existing material models to finish with the selection of Yang's model as the one used in the present work.

Next, a set of high strain rate compression tests have been performed as shown in Chapter 3. The samples of material used in these tests have been produced with three different component proportions, i.e. 60/40, 75/25 and 90/10; where the second number expresses LLDPE percentage in the blend while the first number (resting "3" denotes the rubber percentage). And four different densities, 0.7, 0.8, 0.9 and 1 g/cm^3.

A method to filter the experimental results corresponding to the highest strain rate is developed in Chapter 4. The corrupted material curves which show undesirable waves have been corrected subtracting the predicted undulations from the original measurements, obtaining smooth curves that reflect adequately the real material behavior at high strain rates. This way the stress-stretch curves corresponding to the highest strain rates are processed and it results possible to use them in further analysis performed in next chapter.

Yang's material constitutive equation is explained in Chapter 5. The three hyperelastic parameters of this model are fitted by least squares, while a Particle Swarm Optimization algorithm is applied to the viscoelastic part in order to adjust the three viscoelastic parameters. The experimental curves used to fit the parameters of the model correspond to the three slowest machine speeds, 0.004 m/s, 0.04 m/s and 0.4 m/s. Next the curves corresponding to the highest machine speeds (4 m/s) are compared to those obtained from the Yang's model with previously fitted parameters.

In Chapter 6 a material subroutine to be implemented in LS Dyna software is described, in order to perform simulations of the experimental compression tests with this constitutive equation.

And last, in Chapter 7 the main conclusions from this work and future research lines are summarized.

2.

STATE OF THE ART

2.1 INTRODUCTION

More than 3 millions of tons of used tires are generated by the industry of tires each year[15,16]. As the rubber is crosslinked due to the vulcanization, the way outs given to it are reduced to three main fields: the energetic valuation by the combustion/pyrolysis process, which covers approximately the 40% of the total amount of used tires; landfilling, 25% of the total amount; and recycling process, 35% of the total amount. This last option represents the best strategy for value recovery[17], both for environmental and economic reasons; it provides the highest value-added application for these products.

The idea of using this recycled rubber from used tires as coatings in road barriers provides a solution to this material. Its function will be to absorb the energy from the impacts of the motorcyclists and to protect them from severe injuries. The Low Density Polyethylene works as adhesive in order to agglutinate the rubber particles. After different tests with Ethylene Vinyl Acetate, different Polyethylenes, at last, Linear Low Density Polyethylene has been selected. This material allows configuring a blend with an up to 90% of recycled rubber. The maximization in the use of this recycled rubber has been a priority in this work.

The composite material coming from this blend is economic. It can be transformed by extrusion to obtain long and constant shear section products and it can maintain its elastic properties at temperatures above 60°C taking into account its application.

The present chapter is focused on the selection of an adequate mechanical constitutive model for the blend of recycled rubber and LLDPE. With this purpose, a review of existing

materials of this type is presented first, followed by a review of existing models with hyperelastic and viscoelastic properties.

2.2 MATERIALS BASED ON RECYCLED RUBBER WITH POLYETHYLENE

The original idea of this work came from the search of industrial applications where recycled rubber would be the main component. This rubber results from recycling plants with a particle size around 3 to 5 mm, or larger. That results in a more economic component than pulverized and easier to manipulate. These small particles obtained from waste tires that are ground, are also known as ground rubber tire (GRT). It is very important the control of its particle size and morphology[18,19]. This GRT is then compound with thermoplastics, being the most important among them low density polyethylene (LDPE)[20-22], high density polyethylene (HDPE)[18,23-25] and polypropylene (PP)[26], to obtain thermoplastic elastomers (TPE)[27].

Most of the literature concerning blends of polyethylene plus recycled rubber has usually worked with pulverized rubber[20,27-29]. Its objective has been related to the improvement of the toughness of the Polyethylene (PE) by means of the fabrication of a TPE. The prerequisites of manufacturing TPE containing GTR according to literature in order to improve the interphase adhesion between the components of the blend[24,29,30] are: using additional (fresh) elastomer, using compatibilizers or devulcanise the GRT at least partially[20].

Tipical GRT containing blend applications[31] include their use as covers of sport and recreation fields, tiles for roofs (see Fig. 2-2) blending with asphalt products (when the recycled rubber size is greater it is used in pavements), pneumatic tires, or added in small quantities to rubbers or thermoplastics. In this work it composes, together with the LLDPE, a TPE material used as coating in road barriers, as shown in Fig. 2-1Fig. 2-2 Fig. 2-3 and Fig. 2-4.

Fig. 2-1 Sample of recycled rubber and Linear Low Density Polyethyle blend with the shape of crash barrier and poles

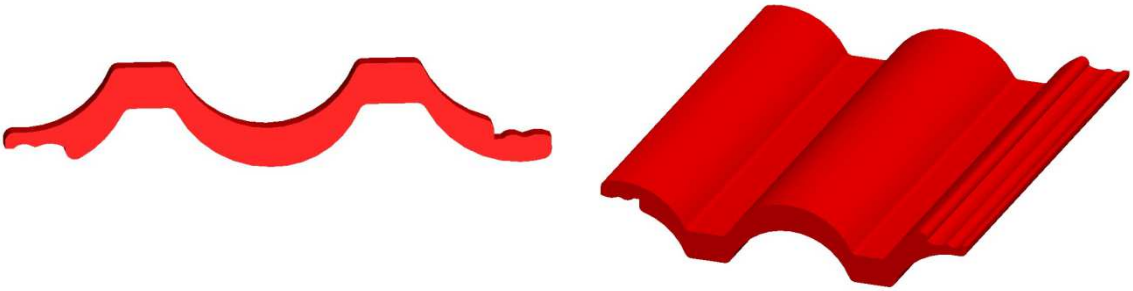

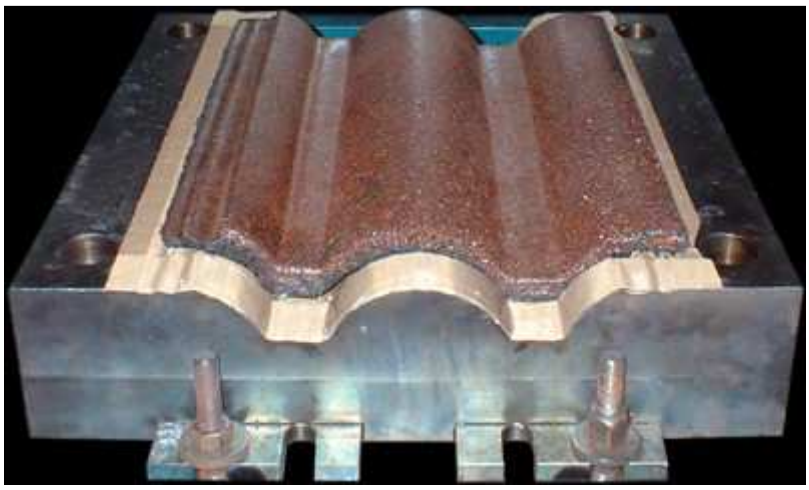

Fig. 2-2 Tiles for roofs

Numerous approaches which attempt to model the mechanical behavior of these TPE have been carried out by different researchers[32]. According to these studies, the significant non-

linear viscoelasticity that exhibit this blend has to be considered together with the hyperelastic property of the rubber. Three ways to define mechanical properties of these kinds of materials are shown in the existing literature. The first one, molecular approach where chain network is described[33]. The second one, a micromechanical or homogenization method, often used in the field of metallic materials but also with the polymers[26,32,34]; in this approach, the behavior of each constituent of the blend is taken into account. At last, the development of models based on phenomenological approach.

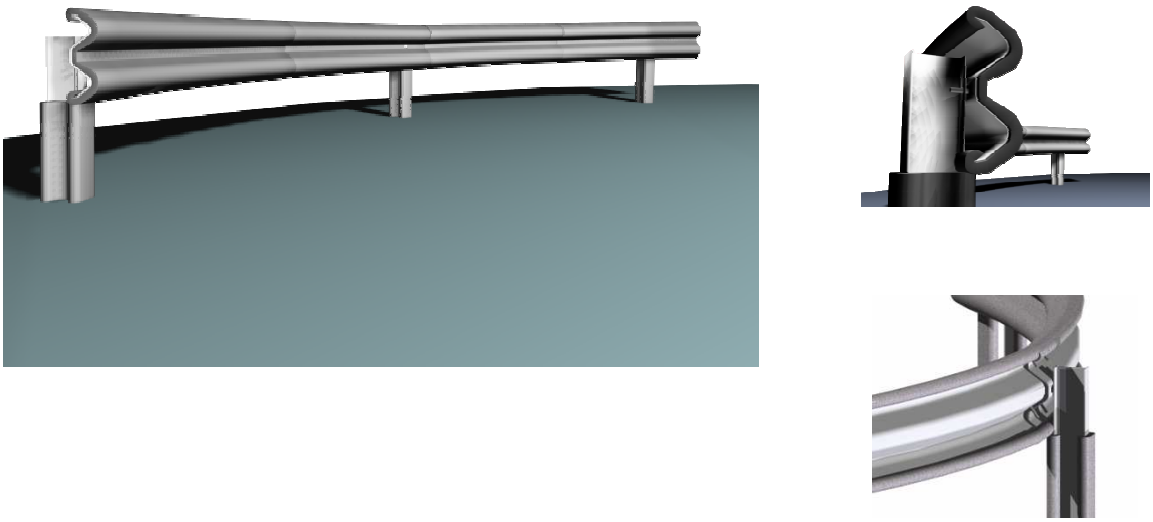

Fig. 2-3 Simulation of positioning of recycled rubber and Linear Low Density Polyethyle blend in road barrier

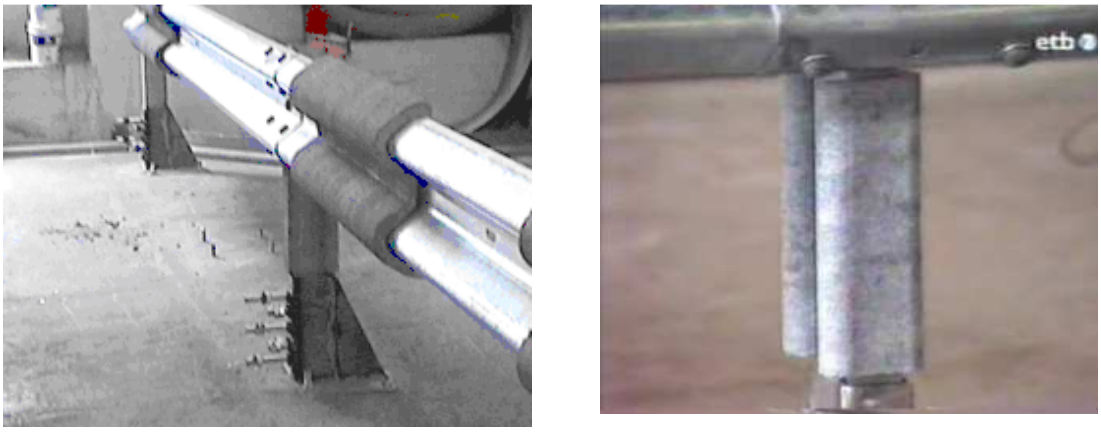

Fig. 2-4 Real example of the blend located in a road barrier. One of its greatest advantages is that it is easy and economic to place it and the flexibility to adapt it to different barrier configurations

These properties are further explained in subsequent sections.

2.3 EXISTING CONSTITUTIVE MATERIAL MODELS

A constitutive equation represents the relationship between the stress and the strain and temperature, that is, the real behavior of a material. The composite material characterized in this thesis requires considering firstly the hiperelasticity, as the rubber is its main component. When time and deformation rate effects of rubber are important, the viscoelastic behavior has to be considered.

Therefore, in what follows, a review of the existing models is performed. It results necessary to remark that it is important to use the minimum number of parameters in the constitutive equation that allows a proper definition of material behavior, i.e., to optimize the relation between number of parameters and the precision defining the material behavior.

One of the mechanical properties of vulcanized rubber, including rubber with fillers, is incompressibility[9]. It is an idealization, taking into account that volume changes due to hydrostatic pressure are small compared to those due to compression forces. In this work, the composite material is considered almost, and not totally, incompressible[9,35-39] to avoid numerical problems when the model is introduced in FE software.

2.3.1 Hyperelastic models

Rubber experiences large deformations when loaded and recovers almost entirely when unloaded. Recycled rubber is filled and this causes a fully non-linear behavior. The definition of a valid elastic matrix in order to relate the stress with the strain is, therefore, very difficult due to the fact that the terms in this matrix are dependant on the strain and not constant. The alternative comes by the use of the strain-energy function that exists for all elastic materials. Different strain-energies are defined in the literature; Petiteau gives some examples[40].

The aim of this section is to show the most widely known hyperelastic constitutive equations. Previously, some basic concepts of the continuum mechanics are reminded, taking into account that the studied material fills completely the space occupied and acts, in consequence, as a continuous medium[41].

When an external force is applied over a deformable body, this experiences a displacement, which can be divided into a rigid-body displacement and a deformation. Depending on the magnitude of this deformation, it can be studied by two theories: infinitesimal strain theory for small deformations and finite strain theory for large deformations, which is the case for elastomers. Viscoelasticity needs also to be considered usually; the focus of the thesis stands here.

These deformations can be studied by two points of view, the Lagrangian and the Eulerian descriptions. In the first one, the observer is in the referential configuration and observes the particles changing their position during the time. In the second one, the observer is located in the current configuration and it belongs to a moving coordinate system. As the Langrangian description prevails over the Eulerian in solid mechanics (the Eulerian form is used in fluid dynamics), it will be used from now on.

Therefore, if x is the position vector of a particle/material point in the current configuration - that is, the deformed system - and X is its position vector in the reference configuration - the undeformed system - their relationship is given by the mapping function h:

$$x = h(X, t) \tag{2.1}$$

Displacements of the particles are obtained by means of a matrix that is essential in nonlinear continuum mechanics. This matrix[42] is called deformation gradient matrix, denoted by F:

$$F_{ij} = \partial x_i / \partial X_i \tag{2.2}$$

Where *i* corresponds to the row number and *j* to the column number of the matrix.

This matrix defines completely the motion in the neighborhood of a point. This relationship describes how a material line element changes its length and direction by the deformation.

As F_{ij} depends on rigid body rotations, it is not adequate as measure of strain. It can be decomposed as F=RU (or F=VR), where U and V are positive definite and symmetric matrices and R is an orthogonal matrix, as shown in the polar decomposition theorem. U and V are suitable measures of strain as they do not involve any rigid body rotation; however, it is difficult to determine them in practice.

The left (B) and right (C) Cauchy-Green deformation tensors are:

$$B = FF^T \tag{2.3}$$

$$C = F^T F \tag{2.4}$$

These tensors can be used as a measure of strain, because rigid body motion does not affect them (see Annex B for further detail). They have the same deformation invariants I_1, I_2, I_3 that are obtained by:

$$I_1(C) = tr(C) \tag{2.5}$$

$$I_2(C) = \frac{1}{2}\left[\left(tr(C)\right)^2 - tr(C^2)\right] \tag{2.6}$$

$$I_3(C) = \det(C) \tag{2.7}$$

Stretch ratios are defined as the square roots of the eigenvalues of C (or B), denoted by λ_i^2. Principal invariants can be expressed by means of these in the following way:

$$I_1 = \lambda_1^2 + \lambda_2^2 + \lambda_3^2 \tag{2.8}$$

$$I_2 = \lambda_1^2\lambda_2^2 + \lambda_2^2\lambda_3^2 + \lambda_3^2\lambda_1^2 \tag{2.9}$$

$$I_3 = \lambda_1^2\lambda_2^2\lambda_3^2 \tag{2.10}$$

The hyperelasticity states the existence of a strain energy function from which the stress is derived. A hyperelastic material as elastic material is able to deform and recover its original form after removing the solicitation, without energy dissipation. It experiments large/finite strains which has a Helmholtz free energy function ψ defined for,

$$P = \frac{\partial \psi(F)}{\partial F} \tag{2.11}$$

Usually ψ is called strain-energy or stored-energy function and is a scalar-valued energy function (a hyperelastic material has a conservative nature). F is the previously defined deformation gradient and P is the first Piola-Kirchhoff stress tensor.

Clasically the stress tensors used for large strain problems are the nominal stress tensor or the first Piola-Kirchhoff stress tensor P and the Cauchy stress tensor or true stress tensor σ. The first Piola-Kirchhoff stress tensor relates the forces in the present configuration with the areas in reference/initial configuration. The Cauchy stress tensor, on its behalf, relates the forces in the present configuration with the areas in the present configuration. The relationship between Cauchy stress tensor and first Piola-Kirchhoff tensor is as follows:

$$\sigma = J^{-1} P F^{T} = J^{-1} \frac{\partial \psi(F)}{\partial F} F^{T} \tag{2.12}$$

Where J is the volume ratio.

The different expressions presented in the literature to describe the free strain energy are based on two main approaches:

1- Statistical or kinetic theory. It takes into account the physical properties of the polymer chains network, that is, its structure. Its fundamentals consider that the elastic force of the rubber comes almost fully from the decrease in entropy when applied extension is increased under constant pressure or constant volume conditions.
2- Phenomenological theory. It consists of a mathematical fitting procedure of different equations to experimental data. It does not analyze the problem from the physical viewpoint; it does not consider the microstructure of the material. It is based on a mathematical framework around the continuum mechanics.

Concerning the statistical models, Treloar model (known as neo-Hookean, developed by Treloar[43] in 1943) or Arruda-Boyce[44] model (1993) are the most representative ones. The main advantage of these models is that as they are based on a specific molecular model, they provide a physical explanation of the properties of the rubber. The problem with them is a lack of precision compared to experimental results.

Referring to the phenomenological approach, the first relevant model included in this theory has been proposed by Mooney[45] in 1940 based on purely phenomenological grounds. Later Rivlin[46] performed some changes creating the Mooney-Rivlin model, which is nowadays one of the most popular models. Based on Rivlin's form, when N=1 in the polynomial form, Mooney-Rivlin model (eq.(2.14)) is obtained and when the material parameter C_{01}=0 Neo-Hookean model is obtained. Some authors, Yeoh[47] among them, proposed a strain energy only dependant on I_1, as the influence of I_2 on the strain energy seems to be negligible when representing the behavior of filled rubbers. Gent[48] developed his own model with the peculiarity of I_1 having a maximum value, I_m.

The main issue with phenomenological models is to ensure the stability of the model, which usually requires restrictions or constraints; as there exists the possibility of getting parameters giving unphysical predictions, these constants must be selected carefully, preserving the physical reality. These constants must satisfy Drucker's stability principle. Another problem may be that these models are not capable of predicting other deformation modes than the one used to fit the constants.

Table 2-1 outlines the main strain energy functions derived from different phenomenological theories formulated in the literature as the selected model in this research is included into this group. Further information can be found in the reviews from Marckmann et al.[49], Steinmann et al.[50], Gil-Negrete[9], Holzapfel[42] or Verron[51].

Table 2-1 Main phenomenological models

Phenomenological Model	Strain energy (ψ)	
Mooney[45] (1940)	$\psi = C_1(I_1 - 3) + C_2(I_2 - 3)$	(2.13)
Rivlin's form[46] (1948)	$\psi = \sum_{i+j=1}^{N} C_{ij}(I_1 - 3)^i (I_2 - 3)^j$	(2.14)
Rivlin and Saunders[52] (1951)	$\psi = C(I_1 - 3) + f(I_2 - 3)$	(2.15)
Gent and Thomas[53,54] (1958)	$\psi = C_1(I_1 - 3) + C_2 \ln\left(\frac{I_2}{3}\right)$	(2.16)
Biderman[50] (1958)	$\psi = C_{10}(I_1 - 3) + C_{01}(I_2 - 3) + C_{20}(I_1 - 3)^2 + C_{30}(I_1 - 3)^3$	(2.17)
Carmichael and Holdaway[55] (1961)	$\psi = \sum_{i=1}^{3}\left[\phi(\lambda_i^2) - \phi(1)\right]$ *where* $\frac{d\phi(u)}{du} = \frac{1}{4u}\left[Ae^{\beta\left(\sqrt{u}-\sqrt{u^{-1}}\right)} - 2B(u + u^{-1} - 2)\right]$	(2.18)
Hart-Smith[49] (1966)	$\frac{\partial \psi}{\partial I_1} = Ge^{k_1(I_1-3)^2}$ *and* $\frac{\partial \psi}{\partial I_2} = G\frac{k_2}{I_2}$	(2.19)
Valanis and Landel[56] (1967)	$\psi = \psi(\lambda_1) + \psi(\lambda_2) + \psi(\lambda_3)$ *and* $\frac{d\psi}{d\lambda} = 2\mu \ln(\lambda)$	(2.20)

Alexander	$\psi = \frac{\mu}{2}\left\{ \begin{array}{l} C_1 \int e^{k(I_1-3)^2} dI_1 + C_2 \ln\left(\frac{(I_2-3)+\gamma}{\gamma}\right) \\ +C_3(I_2-3) \end{array} \right\}$	(2.21)
Ogden[57] (1972)	$\psi = \sum_{n=1}^{N} \frac{\mu_n}{\alpha_n}(\lambda_1^{\alpha_n} + \lambda_2^{\alpha_n} + \lambda_3^{\alpha_n} - 3)$	(2.22)
Blatz, Sharda and Tschoegl[58] (1974)	$\psi = \frac{2G}{\alpha} I_{E_\alpha} + B I_{E_\alpha}{}^{\beta}$	(2.23)
Haines-Wilson[49] (1975)	$\psi = C_{10}(I_1-3) + C_{01}(I_2-3) + C_{11}(I_1-3)(I_2-3) + +C_{02}(I_2-3)^2 + C_{20}(I_1-3)^2 + C_{30}(I_1-3)^3$	(2.24)
Yeoh[47] (1990)	$\psi = C_{10}(I_1-3) + C_{20}(I_1-3)^2 + C_{30}(I_1-3)^3$	(2.25)
Arruda-Boyce[44] (1993)	$\psi = \mu \sum_{i=1}^{5} \frac{C_i}{\lambda_m^{2i-2}}(I_1^i - 3)$	(2.26)
Gent[48] (1996)	$\psi = -\frac{E}{6}(I_m - 3) ln\left[1 - \frac{I_1-3}{I_m-3}\right]$	(2.27)
Yeoh and Fleming[59] (1997)	$\psi = \frac{A}{B}[1 - e^{(-B(I_1-3))})] - C_{10}(I_m-3) ln(1 - \frac{I_1-3}{I_m-3})$	(2.28)

Shariff[60] (2000)	$\sigma = \lambda_1 \frac{\partial \psi}{\partial \lambda_1} - p = E\sum_{i=0}^{n} \alpha_i \phi_i(\lambda)$ $\phi_0(\lambda) = \frac{2\ln(\lambda)}{3}$ $\phi_1(\lambda) = e^{(1-\lambda)} + \lambda - 2$ $\phi_2(\lambda) = e^{(\lambda-1)} - \lambda$ $\phi_3(\lambda) = \frac{(\lambda-1)^3}{\lambda^{3.6}}$ $\phi_j(\lambda) = (\lambda-1)^{j-1}, j = 4,5,\ldots n$	(2.29)
Beda (2005)	$\psi = \frac{K_0}{\beta}(I_2-3)^{\beta} + \frac{C_1}{\alpha}(I_1-3)^{\alpha} +$ $+C_2(I_1-3) + \frac{C_3}{\varsigma}(I_1-3)^{\varsigma}$ $0 < \alpha < 1$ $0 < \beta < 1$ $1 < \varsigma$	(2.30)
Pucci and Saccomandi[61] (2015)	$\psi = \frac{\mu}{2}\left[(I_1-3) + \frac{\beta}{2}(I_1-3)^2\right]$	(2.31)

2.3.2 Viscoelastic models

As previously stated, rubber has elastic properties that can be correctly explained by hyperelastic models both in quasi-static cases and also at very high strain rate cases[40,62] when large deformations occur. When the deformations are large and the applied forces are at moderate strain rates as shown in the Fig. 2-5, large strain viscoelasticity needs to be applied[40]. Viscoelastic materials dissipate energy without damage and they depend on the strain history, that is, these materials have a memory, a fading memory.

Reviews of nonlinear viscoelastic models can be found in[63,64].

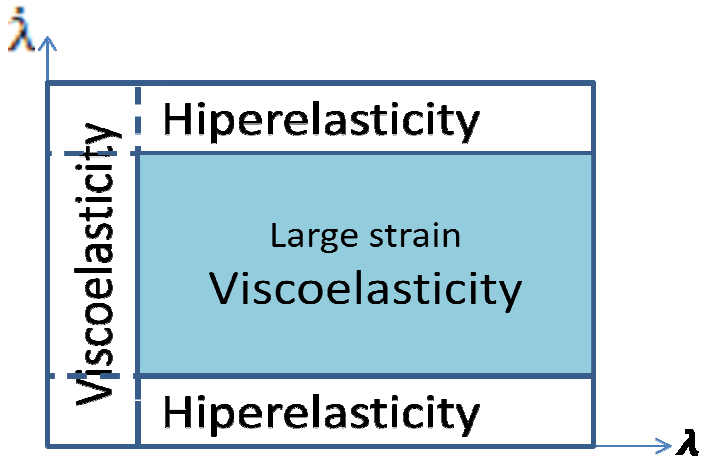

Fig. 2-5 Applicability of viscoelasticity (the axes correspond to strain (λ) and strain rate ($\dot{\lambda}$))

According to Fig. 2-5, and remembering that this material is aimed to be used as coating in road barriers for motorcyclists, that is, impacts, the case to be studied is concerned by large strain viscoelasticity. Therefore, the dynamic behavior of the material has to be modeled by means of the viscoelasticity.

Time and deformation rate have to be considered; usual phenomena related to time-dependency are:

- Hysteresis in cyclic loading, which means that loading and unloading curves do not remain the same.
- Rate dependency observable in the stress-strain relationship, this is, if a strain value is taken, there are different increasing stress values depending on the strain rate.
- Stress relaxation with time, which means that the stress will decrease with time at a step-strain loading.
- Creep, in which the strain increases with time at a step-stress loading.

It has been shown that depending on the strain, small-strain linear viscoelasticity or finite-strain viscoelasticity must be considered. In the first one, the response is linear, that is, the stress and the strain are related by the elastic modulus. Finite viscoelasticity, on the contrary, stablishes non-linear elastic behavior between stress and strain for large strains; the aim of this theory is to study the influence of the strain rate in large deformations.

In order to establish the basis of the large strain viscoelasticity, it is convenient to begin with a review of LINEAR VISCOELASTICITY[65]. This theory studies the influence of the strain rate in small deformations.

Linear viscoelasticity may be expressed by two different formulations:

1- Stress-deformation relationship, originally proposed by Bolzmann Superposition Principle. The application of this principle, also called convolution/hereditary integral approach, is very used; it states that the stress depends, not only on the deformation at an instant, but also on the whole deformation history. This means that current stress can be obtained by the superposition of stress responses to the whole inputs of increments of strains. The deformation history is taken into account by means of fading-memory functions, used to be called Prony series. Some researchers[66-69] use a phenomenological BKZ (known as BKZ due to its authors, Bernstein, Kearsley, Zapas) integral based on linear viscoelasticity. This way, the response of the model will be formed by addition of contribution of all the solicitations. If the material is isotropic, the uniaxial, isothermal stress-strain equation for a nonaging, linear viscoelastic material can be represented by the following Boltzmann superposition integral[70]:

$$\sigma(t) = \int_{-\infty}^{t} G(t-\tau)\frac{d\varepsilon(\tau)}{d\tau}d\tau \tag{2.32}$$

For applied strains being zero for $-\infty < t < 0$, eq. (2.32) can be written as:

$$\sigma(t) = \varepsilon_0 G(t) + \int_{0^+}^{t} G(t-\tau)\frac{d\varepsilon(\tau)}{d\tau}d\tau \tag{2.33}$$

Where ε_0 is the value of the sudden strain at t=0, current time is t and an earlier generic time is τ; where $\tau \in (0,t)$.

Eq. (2.33) follows from the memory hypothesis, smoothness assumptions and mathematical representation theorem (Christensen[71]). It will be considered that the reference state is undeformed and unstressed, that is, the integral is calculated from 0^+ and $\sigma(t) = 0 and \varepsilon(t) = 0$ for t<0.

2- On the other hand, by means of time derivatives of first and higher order in the stress and strain, based on Spring-Dashpot Models. In uniaxial cases, rheological models composed by springs and dashpots have been classically used. From these models, differential equations relating stress and strain are obtained. Later they are applied in tridimensional cases by tensor form.

In small deformations, models based on springs and dashpots and models based on convolution integrals are similar, giving identical results.

Linear viscoelasticity's application range is only valid in small deformations. As Drapaca[64] et al. state, a nonlinear constitutive law has to comply with the requirement of reducing the model to its correspondent linear model when the strains are small. Going in depth into LARGE STRAIN VISCOELASTICITY, the models to characterize the material's behavior when the deformations are large are finite viscoelastic models. Finite viscoelasticity is mainly formulated by two approaches[72]:

1- On one side, internal variables models, based on multiplicative decomposition of the gradient deformation tensor F into an elastic part and an inelastic part[73]. This approach at the beginning was formulated by Green and Tobolsky and followed by several researchers. Lubliner, Sidoroff, Bergström and Boyce[74], Shim and Mohr[75,76] among others. These models usually have been experimentally validated. This approach will not be presented in this work.

2- On the other side, by hereditary integral approach: these models use fading-memory polynomial functions to express the effects of strain history on the current stress (Simo[77], Drozdov[78]). Integral models are an extension on Boltzmann Principle to large strains. The origin remains in Green and Rivlin[79] and Coleman and Noll[80] (Finite Linear Viscoelasticity). Yang et al.[66] used a K-BKZ (where K corresponds to Kaye) type phenomenological model. Pouriayevali[36,81] used a model of integral form together with a strain-dependent relaxation time.

Some of these models are based on a phenomenological approach, while other ones are based on micromechanics. To go in depth in this second approach, the researchers may refer to Drozdov and Dorfmann[82], Bergström and Boyce[83] and the references cited therein.

This thesis focuses on hereditary integral approach. Therefore, the attention is paid on the constitutive models arising from this approach.

The theory of Green and Rivlin[79] predicts that the stress at time t is equal to the next sum of history integrals, for the unidimensional deformation case:

$$\sigma(t) = \int_0^t G_1(t-\tau)\frac{d\varepsilon(\tau)}{d\tau}d\tau + \int_0^t\int_0^t G_1(t-\tau_1)G_2(t-\tau_2)\frac{d\varepsilon(\tau_1)}{d\tau_1}\frac{d\varepsilon(\tau_2)}{d\tau_2}d\tau_1 d\tau_2 + \ldots \qquad (2.34)$$

They related the Cauchy stress to the strain history by this equation. Green and Rivlin used linear functional of the strain/deformation history (development of Frechet-Volterra). Where G_1, G_2,... are relaxation functions that are dependent on the truncature order performed.

Coleman and Noll[80] postulate the use of the Finite Linear Viscoelastic Theory (FLV), which only takes into account the dependency of the stress on the recent past deformation gradients which occurred in a very small neighborhood of that point. The stress is decomposed into an equilibrium stress, that is, stress response at an infinitely slow rate of deformation, and a viscosity-induced overstress. The relaxation function is specified as a measure for the material's memory. Most of the early constitutive laws for viscoelastic materials were developed in the context of the theory of fading memory. This way, linear integrals are used to define the deformation history to obtain the stress:

$$\sigma(t) = \sigma^{\infty}\{C(t)\} + F(t)\int_{-\infty}^{t} g\left(C(t), t-\tau\right)\frac{dE_t(\tau)}{d\tau}d\tau F^{T}(t) \qquad (2.35)$$

There is no generally accepted well-defined form for the constitutive equations for nonlinear viscoelastic solids, as there is for linear viscoelastic solids. A number of specific representations for the response functionals can be found in the literature and these are summarized in the book by Lockett[84], Wineman[63], and the more recent review article by Drapaca[64] et al.

Bernstein, Kearsley and Zapas[85] and Kaye[86] proposed another theory, known as K-BKZ. Tanner[87] reviews the connections of the model and its different versions with continuum mechanics, molecular theory and experiments. K-BKZ can be applied both to solids and to fluids. The most general expression for incompressible materials is:

$$\sigma(t) = -pI + 2\int_{-\infty}^{t}\left(\frac{\delta U}{\delta I_1}C_t^{-1}(\tau) - \frac{\delta U}{\delta I_2}C_t(\tau)\right)d\tau \qquad (2.36)$$

Where U is the potential, dependent on time and on I_1 and I_2.

By their part, Chang, Bloch and Tschoegl[88] developed a linear integral model, called CBT, based on the measure of generalized strain into the Boltzmann superposition integral; they separate the time and deformation effects in the relaxation function:

$$\sigma(t) = -pI + \frac{1}{n}\int_{-\infty}^{t} G(t-\tau)\left[B^{n/2}(t)\frac{dC_t^{\,n/2}(\tau)}{d\tau} + \frac{dC_t^{\,n/2}(\tau)}{d\tau}B^{n/2}(t) \right] d\tau \qquad (2.37)$$

Where n and G(τ) are material parameters.

Christensen[71] truncated to 1st order the eq.(2.34):

$$\sigma(t) = -pI + F(t)\left[g_o I + \int_o^t g_1(t-\tau)\frac{dE(\tau)}{d\tau}d\tau \right] F^T(t) \qquad (2.38)$$

The following table summarizes previously presented non-linear viscoelastic theories:

Table 2-2 Main non-linear viscoelastic models

MAIN NON-LINEAR VISCOELASTIC MODELS		
Green and Rivlin[79] (1957)	$\sigma(t)=\int_0^t G_1(t-\tau)\frac{d\varepsilon(\tau)}{d\tau}d\tau+$ $\int_0^t\int_0^t G_1(t-\tau_1)G_2(t-\tau_2)\frac{d\varepsilon(\tau_1)}{d\tau_1}\frac{d\varepsilon(\tau_2)}{d\tau_2}d\tau_1 d\tau_2+\ldots$	(2.34)
Coleman and Noll[80] (1961)	$\sigma(t)=\sigma^{\infty}\{C(t)\}+F(t)\int_{-\infty}^t g\left(C(t),t-\tau\right)\frac{dE_t(\tau)}{d\tau}d\tau F^T(t)$	(2.35)
Bernstein, Kearsley and Zapas[85] and Kaye[86] (1962)	$\sigma(t)=-pI+2\int_{-\infty}^t\left(\frac{\delta U}{\delta I_1}C_t^{-1}(\tau)-\frac{\delta U}{\delta I_2}C_t(\tau)\right)d\tau$	(2.36)
Chang, Bloch and Tschoegl[88] (1976)	$\sigma(t)=-pI+\frac{1}{n}\int_{-\infty}^t G(t-\tau)\left[B^{n/2}(t)\frac{dC_t^{n/2}(\tau)}{d\tau}+\frac{dC_t^{n/2}(\tau)}{d\tau}B^{n/2}(t)\right]d\tau$	(2.37)
Christensen[71] (1980)	$\sigma(t)=-pI+F(t)\left[g_0 I+\int_0^t g_1(t-\tau)\frac{dE(\tau)}{d\tau}d\tau\right]F^T(t)$	(2.38)
Fung[89] (1981)	$\sigma(t)=-pI+F(t)\left\{K^{(e)}[C(t)]+\int_0^t K^{(e)}[C(s)]\frac{\partial G(t-s)}{\partial(t-s)}ds\right\}F(t)^T$	(2.39)
Morman[90] (1988)	$\sigma(t)=-pI+\frac{E(t)}{E_e}\left(\Gamma_1 B+\Gamma_{-1}B^{-1}\right)$ $\Gamma_1=2\frac{\partial\psi(I_1(t-s),I_2(t-s))}{\partial I_1(t-s)}$ $\Gamma_{-1}=-2\frac{\partial\psi(I_1(t-s),I_2(t-s))}{\partial I_2(t-s)}$	(2.40)

2.4 SELECTED CONSTITUTIVE EQUATION

As the availability of information concerning the composite material proposed in the thesis regarding its microstructure and composition is limited, in this work, a phenomenological approach is preferred in the hyperelastic part of the model. Rivlin's form with 3 parameters is selected to characterize this hyperelastic part, taking into account its ablity to provide accurate response predictions, based on compression tests, and that it is mathematically easy to calculate. It is also implemented in all FE codes.

Concerning previously presented viscoelastic models, hereditary integral approach is preferred, and here K-BKZ model is chosen, with a modification introduced by Yang et al.[66]. This model is further explained in Chapter 5.

If the general form of the viscoelastic model for a homogeneous, isotropic and incompressible material is considered[84]:

$$\sigma = -p + F(t) \cdot \Omega^{t}_{\tau=-\infty} \{C(\tau)\} \cdot F^{T} \tag{2.41}$$

The matrix functional can be written as:

$$\Omega^{t}_{\tau=-\infty} \{C(\tau)\} = \int_{-\infty}^{t} \phi(I_1, I_2) m(t-\tau) \dot{E}(\tau) d\tau \tag{2.42}$$

Yang's contribution to this model comes from the definition of the function ϕ:

$$\phi(\tau) = C_2 + C_3 (I_2 - 3) \tag{2.43}$$

As one relaxation time term is selected into the relaxation function m(t-τ), it can be appreciated that few parameters (only three) are necessary to describe viscoelastic behavior.

The aim of the selected hyper-viscoelastic model is to represent the behaviour of the material as closely as possible with the minimum number of parameters.

3. EXPERIMENTAL MATERIAL TESTING

3.1 INTRODUCTION

The aim of this chapter is to investigate the mechanical behavior of a composed material constituted by vulcanized recycled rubber, LLDPE and titanium dioxide (TiO_2) to use as coating in road barriers, in order to absorb a part of the energy produced in an impact.

Elastomers show a great capacity to have large strains without breaking, while the stress rises as the material is compressed. Additionally, a non–linear viscoelastic effect is also identified for the rubber that shows dissipative properties. The LLDPE has a great energy absorption capacity.

As it is a special material its mechanical properties have not been characterized systematically, and taking into account the application where there will be an impact with this composite, the material will experience compressive stress states characterized by time-varying strain rates. Therefore, it results necessary to perform some tests under established conditions. Actually, compressive impact and weight-drop tests are the most common ways to measure the material's shock absorbing capability under compressive conditions. Following the results obtained from a previous study with weight-drop tests, here high strain rate tests are performed, at different loading rates, in order to know the properties of the compound presented, appreciating that this material has a significant dependence on strain rate in large deformations.

The requirements stated by the Standard on the evaluation of performance of the protection systems for motorcyclists on safety barriers and parapets - part 2: Performance

classes and acceptance criteria UNE 135900[91,92] are very strict. The Standard establishes that the impact tests have to be performed launching a dummy instrumented on its head and neck against the protection system at a 60 km/h speed. Some biomechanical parameters are measured in the test, which can not exceed determined values. Therefore, the procedure to follow would be to design the protection system to be homologated, to perform the corresponding tests with prototypes at real scales and to verify if the requirements of the norm are satisfied or not. If the test was satisfactory there would not be any problem, but if not, the necessary modifications should be done on the protection system and then, perform again the tests. Taking into account that these tests result very expensive, the trial-error procedure is unacceptable from an economic viewpoint. Hence, the aim in this work is to do simulations on Finite Element software in order to verify the behavior of the protection system.

The strain rate rank to consider is between 10^{-3} to 10^{3} s^{-1}, including the test speeds stablished in the Standard UNE 135900-2:2008[92]. As transient effects become increasingly significant as strain rate increases, large oscillations are observed on the force signals.

The tests have not been preconditioned in order to avoid the Mullins' effect[93]. Nevertheless, as it did not appear any barrel form on the samples during the test, this fact can be avoided without losing accuracy.

Next, proposed material model's parameters will be fitted with the experimental results. Thereafter, it results necessary to define the testing procedures to characterize the behavior of the material. As the experimental campaign is often expensive and time-consuming, the use of predictive analytical/numerical models that will be presented in Chapter 6 represents a valid alternative for estimating this quantity.

This chapter is organized in the next way. First, sample preparation for different proportions of recycled rubber and LLDPE are presented in 3.2. High strain rate test methodologies are introduced in section 3.4. Thereafter, a description of the testing machine is also given in this section3.4.3. To close the chapter, experimental results and some final comments are included in section 3.5.

3.2 SAMPLE PREPARATION

A blend of recycled rubber from used tires and Low Density Polyethylene has been used. The rubber has a particle size of between 0.8 – 3 mm, and the LLDPE is used as an adhesive to compact it. This blend is the material to be characterized. TiO_2 (in Fig. 3-3) is also used to give to the samples a colour as similar as possible to a road barrier, as this is its expected future application.

When the rubber is mixed with an adhesive and is compacted, the ability to absorb energy of the resultant product is determined by: the nature of the adhesive; the relative proportions of both materials; the final density of the mixture and the thickness of the material. As rubber is the major component of the mixture, the characterization of the material's response to impacts shows a particular difficulty. This results from the impossibility of testing the material under tension as it breaks easily under these circumstances and in consequence it is necessary to test it under compression.

Test repeatability is considered, and also the influence of the density and the thickness of the material on its ability to absorb impact energy. The possibilities of combining experimental techniques and numerical techniques in order to obtain a correct characterization of these kinds of materials are also evaluated. This allows selecting better material constitutive models.

Due to the lack of homogeneity in the raw material, it is pretended to combine the results with those results obtained from weight drop tests performed to plates of different densities and thicknesses in a Roswand IFW5 machine. Experimental compression results are used as data into the FE program Ansys-LS Dyna to simulate these compression tests.

3 different proportions of recycled rubber and LLDPE have been manufactured, as shown in Table 3-1:

Table 3-1 Proportions of recycled rubber to LLDPE in the different blends

	Recycled rubber	LLDPE	TiO_2 (constant proportion)
90/10	87%	10%	3%
75/25	72%	25%	3%
60/40	57%	40%	3%

It has been assumed in the present investigation that the lowest strain rate behavior of rubber is essentially the same as its static response; the experimental results confirm that such an assumption does not generate significant error.

It is necessary to triturate the recycled rubber as it is already vulcanized, as shown in Fig. 3-1.

Fig. 3-1 Grinded recycled rubber

At ambient temperature LLDPE is solid as it can be appreciated in Fig. 3-2 but when it is introduced in the extruder it flows at high temperatures and when it leaves it is solidified again, doing its adhesive function with the rubber pieces.

Fig. 3-2 LLDPE before it is extruded

Fig. 3-3 TiO_2 as colorant

The three components are introduced in a mixer as shown in Fig. 3-4 and they are turned some minutes to have a mixture as homogeneous as possible.

Fig. 3-4 Mixer

A dry extrusion has been performed, at 160°C.

This blend is introduced into the extruder (Fig. 3-5), where the LLDPE is melt and mixed with the rubber due to the extruder rotation and the temperature inside it.

Fig. 3-5 Extruder

The obtained blend is easy to manipulate. It is taken with the hands and tightened / compacted into the mould.

Fig. 3-6 The blend

Depending on the desired sample density, the blend shown in Fig. 3-6 will be tightened more or less. Once the mould is filled, it is left 24 hours at ambient temperature to cool the sample. After this time, the sample can be filled out and it is ready for tests.

3.3 CREATION OF THREE DIFFERENT BLENDS

3.3.1 First case 90/10

A mixture composed by 87% rubber joined to 10% LLDPE, with 3% TiO_2 has been manufactured. A set of 28 cylindrical specimens of nominal diameter 60 mm and thickness / height 70 mm has been manufactured, called "big" samples, divided in 4 main groups according to their density: 0.7, 0.8, 0.9 and 1 g/cm^3 (studied density rank has been 0.68-1.03 g/cm^3). Fig. 3-7 shows one of these samples. The tests have been performed in a MTS 819.10 servo-hydraulic machine at 4 different speeds: one speed (0.004 m/s) for quasistatic analysis, inducing a strain rate of 0.057 s^{-1} and three speeds (0.04 m/s, 0.4 m/s and 4 m/s) for dynamic analysis, inducing strain rates of 0.57, 5.7 and 57 s^{-1}, respectively. This enables to establish material behavior at medium-low strain rates that will result on several engineering applications, although they do not encompass the strain-rate range of all possible impact cases. At each speed, two samples of each density are tested, except at the highest speed, for whose only one sample is tested.

On the other hand, another set of 28 cylindrical specimens of nominal diameter 30 mm and thickness 40 mm, called "small" samples, has been manufactured. This set is also divided in the same groups with similar densities, and the tests have been performed at the same machine speeds, inducing the next strain rates: 0.1 s^{-1} for quasi-static analysis, and 1, 10 and 100 s^{-1} for dynamic analysis, respectively.

The nomenclature in the acquired data files is as follows: for the big samples the file name starts with G, being *G_speed_densityA* (or ending in *B* if there are two samples with the same density; and the speed is in m/s); for the small samples, the name is analogous, starting with *p*.

The names of some of the files corresponding to the big samples with density 0.7 g/cm^3 are shown as an example:

G_0.004_0.73B: big sample (G) + 0.004 m/s machine speed + 0.73 g/cm^3 density + B sample of a pair of two

p_0.4_0.72A: small sample (p) + 0.4 m/s machine speed + 0.72 g/cm^3 density + A sample

G_4_0.73A: big sample (G) + 4 m/s machine speed + 0.73 g/cm^3 density + A sample

Next, two tables are included –Table 3-2 for the big samples and Table 3-3 for the small ones– with all the densities and speeds:

Table 3-2 ***Tested big samples list for 90/10 proportion***

(Densities between 0.7 and 1 g/cm^3 and test speeds between 0.004 and 4 m/s)

BIG SAMPLES											
d=0.7 g/cm^3			d= 0.8 g/cm^3			d=0.9 g/cm^3			d=1 g/cm^3		
0.004	m/s	0.73B	0.004	m/s	0.82A 0.83A	0.004	m/s	0.92A 0.93A	0.004	m/s	1.01A 1.03A
0.04	m/s	0.72A 0.72B	0.04	m/s	0.83A 0.83B	0.04	m/s	0.92A 0.92B	0.04	m/s	1A 1.01A
0.4	m/s	0.72A 0.73A	0.4	m/s	0.82A 0.83A	0.4	m/s	0.93A 0.93B	0.4	m/s	1.02A 1.03A
4	m/s	0.73A	4	m/s	0.83A	4	m/s	0.93A	4	m/s	1.02A

Table 3-3 ***Tested small samples list for 90/10 proportion***

(Densities between 0.7 and 1 g/cm^3 and test speeds between 0.004 and 4 m/s)

SMALL SAMPLES												
d=0.7 g/cm^3			d= 0.8 g/cm^3			d=0.9 g/cm^3			d=1 g/cm^3		
0.004	m/s	0.68A 0.71A	0.004	m/s	0.77A	0.004	m/s	0.89A 0.91A	0.004	m/s	0.97A 0.99A
0.04	m/s	0.72A 0.72B	0.04	m/s	0.78A 0.79A	0.04	m/s	0.90A 0.91A	0.04	m/s	1A 1.03A
0.4	m/s	0.72A 0.72B	0.4	m/s	0.82A 0.82B	0.4	m/s	0.90A 0.91A	0.4	m/s	1.01A 1.02A
			4	m/s	0.82A	4	m/s	0.92A	4	m/s	0.99A

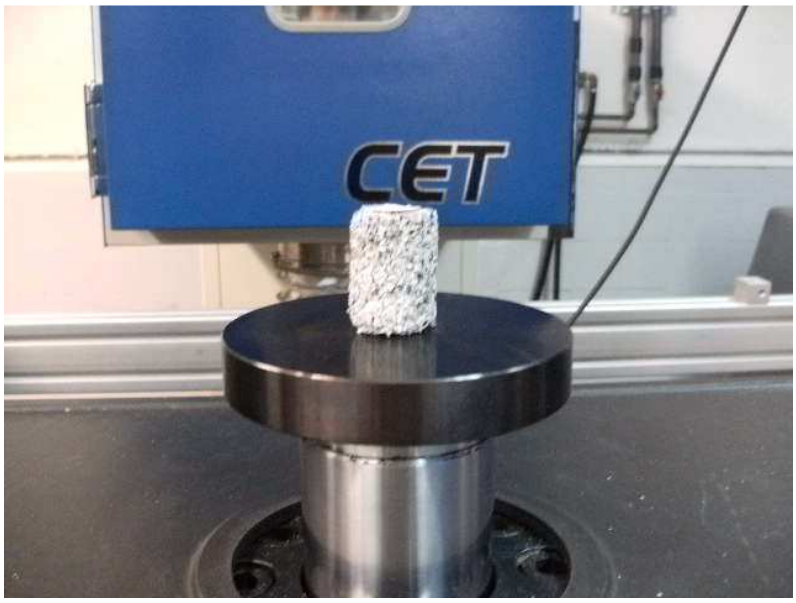

Fig. 3-7 ***Rubber recycled test sample detail***

3.3.2 Second case 75/25

A mixture composed by 72% rubber joined to 25% LLDPE, with 3% TiO_2 has been manufactured. A set of 11 cylindrical big specimens of nominal diameter 60 mm and thickness 70 mm has been manufactured (big samples), as well as a set of 16 cylindrical small specimens of nominal diameter 30 mm and thickness 40 mm, divided in 4 main groups according to their density: 0.7, 0.8, 0.9 and 1 g/cm^3. The tests have been performed in the same servo-hydraulic machine at 4 different speeds: one speed (0.004 m/s) for quasistatic

analysis, and three speeds (0.04 m/s, 0.4 m/s and 4 m/s) for dynamic analysis. This is summarized in Table 3-4 and Table 3-5.

Table 3-4 Tested big samples list for 75/25 proportion

BIG SAMPLES								
d=0.7 g/cm^3			d= 0.8 g/cm^3			d=0.9 g/cm^3		
0.004	m/s	0.76	0.004	m/s	0.86	0.004	m/s	0.96
0.04	m/s	0.77	0.04	m/s	0.87	0.04	m/s	0.95
0.4	m/s	0.75	0.4	m/s	0.86	0.4	m/s	0.96
4	m/s	0.77	4	m/s	0.85			

Table 3-5 Tested small samples list for 75/25 proportion

SMALL SAMPLES											
d=0.7 g/cm^3			d= 0.8 g/cm^3			d=0.9 g/cm^3			d=1 g/cm^3		
0.004	m/s	0.76	0.004	m/s	0.87	0.004	m/s	0.94	0.004	m/s	1.05
0.04	m/s	0.74	0.04	m/s	0.86	0.04	m/s	0.93	0.04	m/s	1.03
0.4	m/s	0.77	0.4	m/s	0.86	0.4	m/s	0.97	0.4	m/s	1.07
4	m/s	0.73	4	m/s	0.83	4	m/s	0.93	4	m/s	1.07

3.3.3 Third case 60/40

A mixture composed by 57% rubber joined to 40% LLDPE, with 3% TiO_2 has been manufactured. A set of 16 cylindrical small specimens of nominal diameter 30 mm and thickness 40 mm has been manufactured, divided in 4 main groups according to their density: 0.7, 0.8, 0.9 and 1 g/cm^3. The tests have been performed in the same servo-hydraulic machine at 4 different speeds: one speed (0.004 m/s) for quasistatic analysis, and three speeds (0.04 m/s, 0.4 m/s and 4 m/s) for dynamic analysis. This is summarized in Table 3-6.

Table 3-6 Tested small samples list for 60/40 proportion

SMALL SAMPLES											
d=0.7 g g/cm^3			d= 0.8 g/cm^3			d=0.9 g/cm^3			d=1 g/cm^3		
0.004	m/s	0.74	0.004	m/s	0.84	0.004	m/s	0.96	0.004	m/s	1.04
0.04	m/s	0.76	0.04	m/s	0.84	0.04	m/s	0.95	0.04	m/s	1.04
0.4	m/s	0.74	0.4	m/s	0.86	0.4	m/s	0.95	0.4	m/s	1.05
4	m/s	0.75	4	m/s	0.84	4	m/s	0.93	4	m/s	1.04

3.4 TEST METHODOLOGIES FOR THE HIGH STRAIN RATE COMPRESSION TESTS. DESCRIPTION OF THE TESTING MACHINE

3.4.1 Existing standards

First of all, a review of some of the existing quasi-static and dynamic tests proposed in literature is presented.

Different test standards for quasi-static compression tests are proposed by ASTM (ASTM D571-95) ASTM D945, ISO (ISO 7743) and UNE (UNE-ISO 7743:2016, previous UNE 53536:2001). Test rates are 12±0.3 mm/min into ASTM and 10 mm/min into ISO. Test sample is a cylinder specimen with diameters comprised between 28.6±0.1 mm and 29±0.5 mm and 12.5±0.5 mm height in all the standards.

The main difference among these test procedures is the inclusion of lubrication condition of specimen surfaces that are in contact with the testing machine into ISO. If test pieces are lubricated, the compression is homogeneous. Without lubrication barreling of the specimen could occur which would result in high internal stresses that are not of a uniaxial nature.

Both of them state that samples should be conditioned at standard test temperatures, for a period of time previous to their measurement and test; this time is of at least 3 hours for both ASTM and ISO.

Concerning dynamic tests, there exist a large number of testing machines to perform dynamic tests according to ISO 4664-1:2005[94]. They can be classified by vibration type, by testing machine type or by deformation mode.

a) Classification by vibration type. Two main dynamic tests exist, those using *free vibration* in which the sample is deformed and then released, doing some oscillations that decrease gradually due to the rubber damping; and *forced vibration* tests in which the oscillations are maintained by external means. These last test type include the forced non-resonant and the forced resonant vibration tests.

b) Classification by testing machine type. Small and big testing machines are considered here; depending on the purpose of the test, used vibration method, deformation mode or sample shape one or another should be used.

c) Classification by the deformation mode. This can be compression, shear stress, tension, bending or torsion of the sample.

3.4.2 Applied methodology for the tests

High strain rate compression tests have been carried out at 4 different machine crosshead speeds, V, as previously stated: 0.004, 0.04, 0.4 and 4 m/s. At each speed two samples of each density are tested, except at the highest speed, for which only one sample is tested. This way, 4 different strain rates $\dot{\varepsilon}$ are obtained for each sample length ($\dot{\varepsilon} = \frac{V}{L_o}$):

Table 3-7 Strain rates for both sample dimensions

	$\dot{\varepsilon}$ (s^{-1})			
Big samples ($L_0 = 70mm$)	0.057	0.57	5.7	57
Small samples ($L_0 = 40mm$)	0.1	1	10	100

In the test procedure, it is estimated a machine displacement that places the final height of the sample in 21.5 mm from a initial height of 40.5 mm (small samples; that is, a deformation $\varepsilon = \frac{\Delta L}{L} = \frac{40.5 - 21.5}{40.5} = 0.469$) and a final height of 38.4 mm for the samples with an initial height of 69.5 mm (big samples; deformation $\varepsilon = \frac{\Delta L}{L} = \frac{69.5 - 38.4}{69.5} = 0.447$). The security reasons on the testing machine have not permitted tests at higher strain levels.

The studied strain rates vary, therefore, from $0.057\ s^{-1}$ ($\dot{\varepsilon} = \frac{v}{L} = \frac{0.004\ m/s}{0.070\ m}$) to $57.14\ s^{-1}$ ($\frac{4\ m/s}{0.070\ m}$) for big samples and from $0.1 s^{-1}$ to $100\ s^{-1}$, for the small samples.

Test conditioning has not been conducted previous to the tests. Nevertheless, as it has not appeared any barrel form on the samples during the tests, this fact can be avoided without losing accuracy.

Test data has been measured and recorded by a data acquisition system. The average temperature in the testing room has been 25 ºC.

3.4.3 Description of the testing machine

Crashworthiness application cases generally require three types of testing systems depending on the strain rate range. For testing at quasi-static situations and strain rates below 0.1/s, conventional load frames, either mechanical or servo-hydraulic, should be used. For strain rates higher than 0.1/s, both servo-hydraulic and bar type machines should be used. The servo-hydraulic type system can normally encompass a strain rate range from 0.1 to 500/s (reaching 1000/s in special cases). On the other the hand, bar type systems cover the strain rates from 100 to 1000/s and higher. Fig. 3-8[95] is a schematic representation of the applicable range of strain rates for the three testing systems.

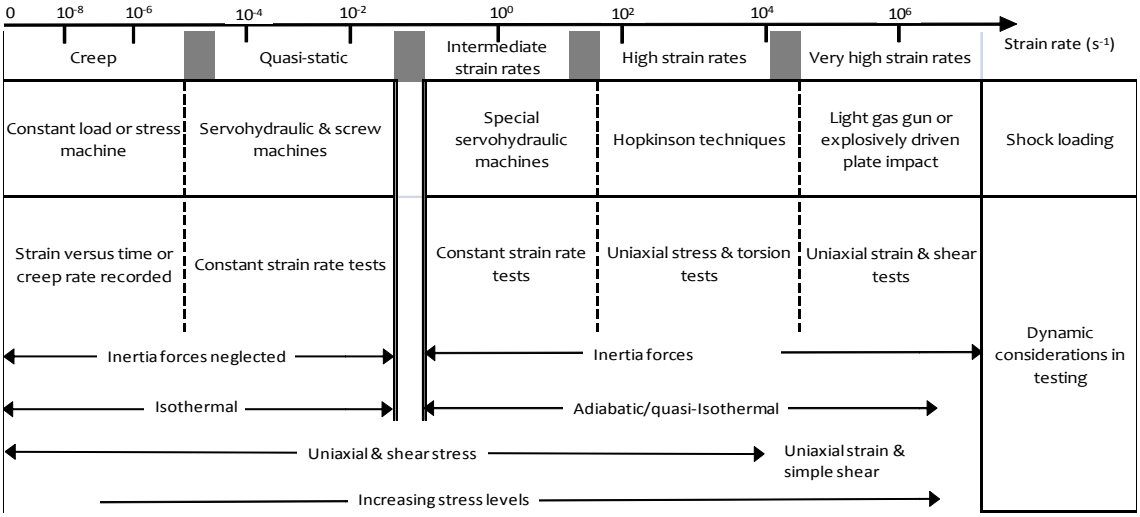

Fig. 3-8 Dynamics aspects of mechanical testing[95]

Fig. 3-9 presents a picture of the MTS 819.10 high rate servo-hydraulic testing system used in this research. Static, dynamic and high speed tests (up to 18 m/s) can be done in this machine.

Fig. 3-9 MTS High Rate Test System at mechanical testing laboratory of LEARTIKER

It is necessary to measure the loading force associated with the change in the length of the specimen in order to characterize the mechanical behavior of a material by uniaxial tests. With this purpose, it is equipped with a 60 kN piezoelectric load cell from Kistler[96] to measure forces exerted during operation and with a magnetostrictive sensor (Temposonics®) to measure actuator displacement, replacing the historically used LVDT concept.

A PCI 6110 card, with a 5.000.000 points/second recording speed, from National Instrument has been used for the data acquisition. The experimental results are reported in the next section.

3.5 RESULTS AND DISCUSSION

3.5.1 90/10 Proportion

As it has not been appreciated any barrel effect on the samples, it has been concluded that the deformation field has been homogeneous during the tests.

The compression test results corresponding to the density of **0.9 g/cm^3** and **big samples** are graphically shown in Fig. 3-10:

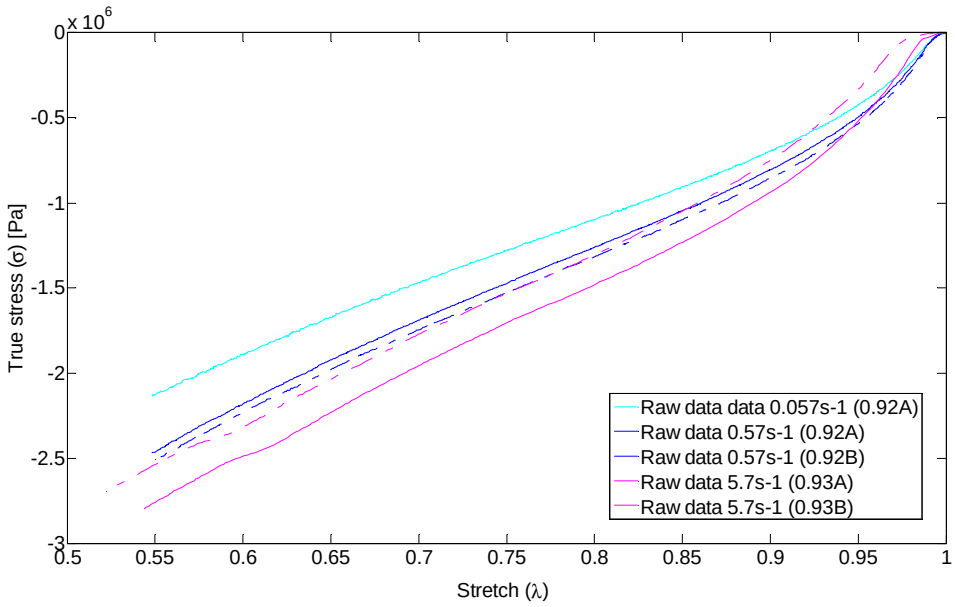

Fig. 3-10 Stress-stretch curves for density 0.9 g/cm^3 at different strain rates (BIG samples, 90/10 proportion). The terms in brackets refer to real density and to each tested sample (A or B).

This figure shows the behavior of rubber under compression, each curve corresponding to a strain rate. Three different strain rates (0.057, 0.57 and 5.7 s^{-1}) are shown, where curves with the same color have the same strain rate. For a given strain (stretch), the values of the stress under higher strain rates are much larger than those at low strain rates. It is noted that the non-linearity of the curves increases for higher strain rates, i.e., the elastic modulus is variable, increasing with the stretch, as occurs in hyperelastic materials. A significant non–linear viscoelastic effect can be appreciated throughout the loading history, since the stress does not increase linearly with the strain rate. This effect is evidenced by the shift in curvature of the different stretch-stress curves. It is noted that the non-linearity of the curves increases for higher strain rates. Compression tests corresponding to densities of 0.7 g/cm^3, 0.8 g/cm^3 and 1 g/cm^3 that are introduced next in Fig. 3-11, Fig. 3-12 and Fig. 3-13, respectively, show this effect.

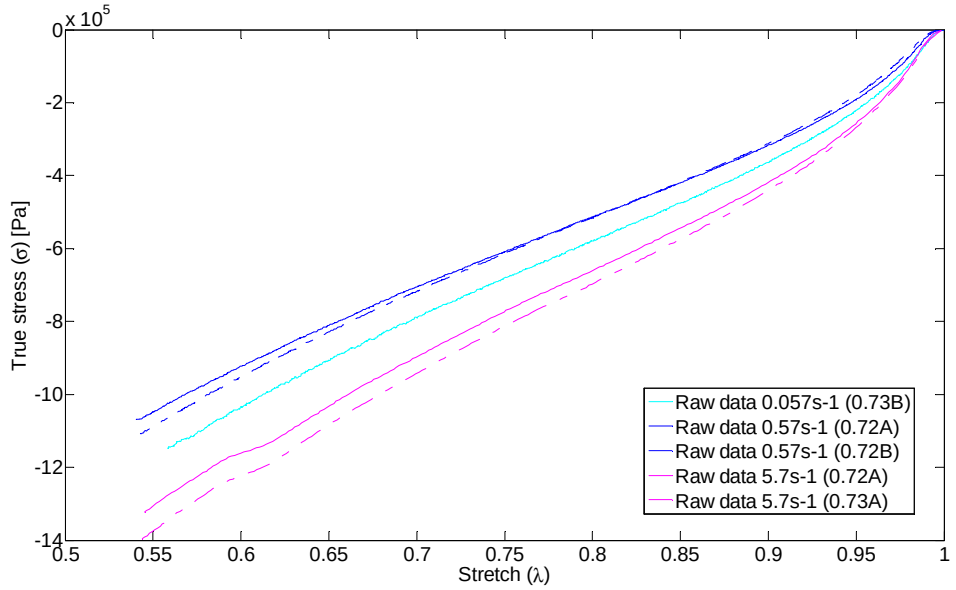

Fig. 3-11 Stress-stretch curves for density 0.7 g/cm^3 at different strain rates (BIG samples, 90/10 proportion). The terms in brackets refer to real density and to each tested sample (A or B).

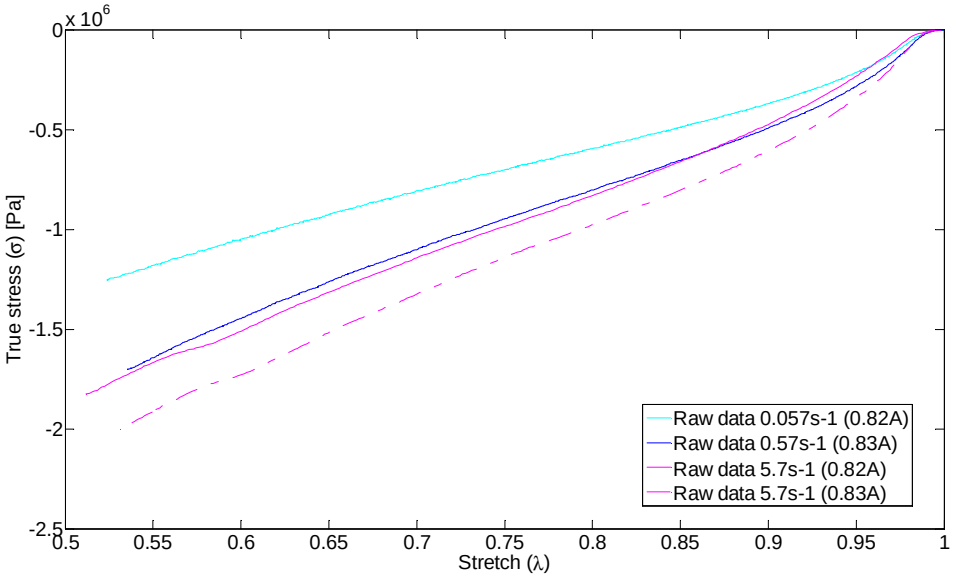

Fig. 3-12 Stress-stretch curves for density 0.8 g/cm^3 at different strain rates (BIG samples, 90/10 proportion).

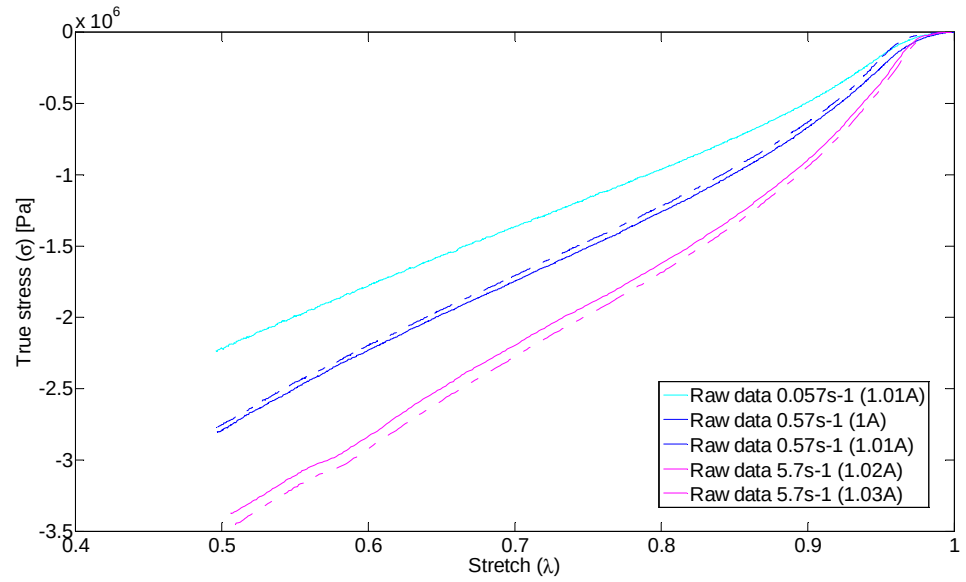

Fig. 3-13 Stress-stretch curves for density 1 g/cm^3 at different strain rates (BIG samples, 90/10 proportion).

Concerning to the small samples, these are detailed below in **Fig. 3-14**, Fig. 3-15, **Fig. 3-16** and **Fig. 3-17**:

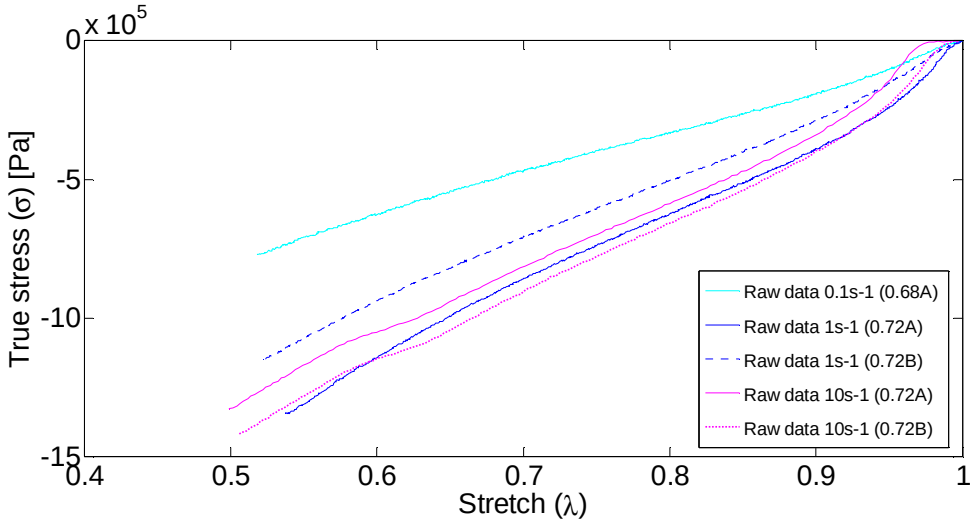

Fig. 3-14. Stress-stretch curves for density 0.7 g/cm^3 at different strain rates (SMALL samples, 90/10 proportion). The terms in brackets refer to real density and to each tested sample (A or B).

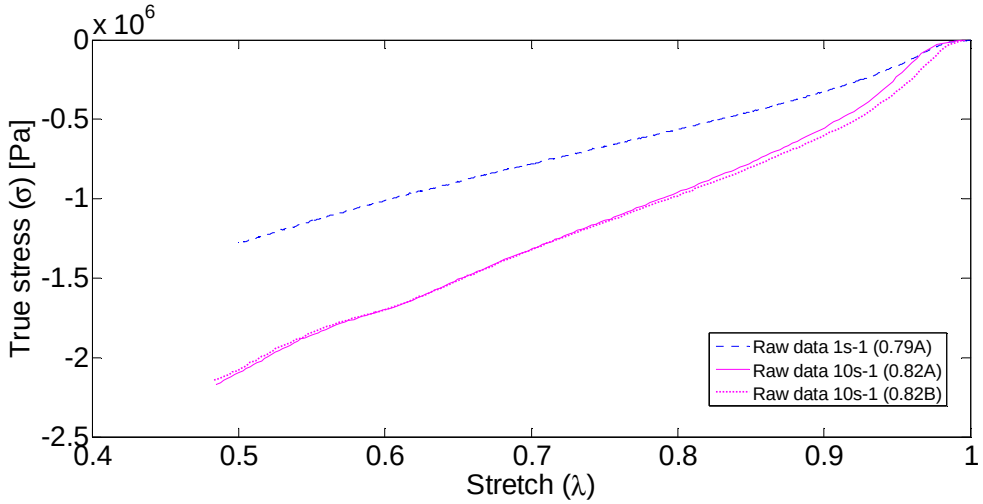

Fig. 3-15 Stress-stretch curves for density 0.8 g/cm^3 at different strain rates (SMALL samples, 90/10 proportion). The terms in brackets refer to real density and to each tested sample (A or B).

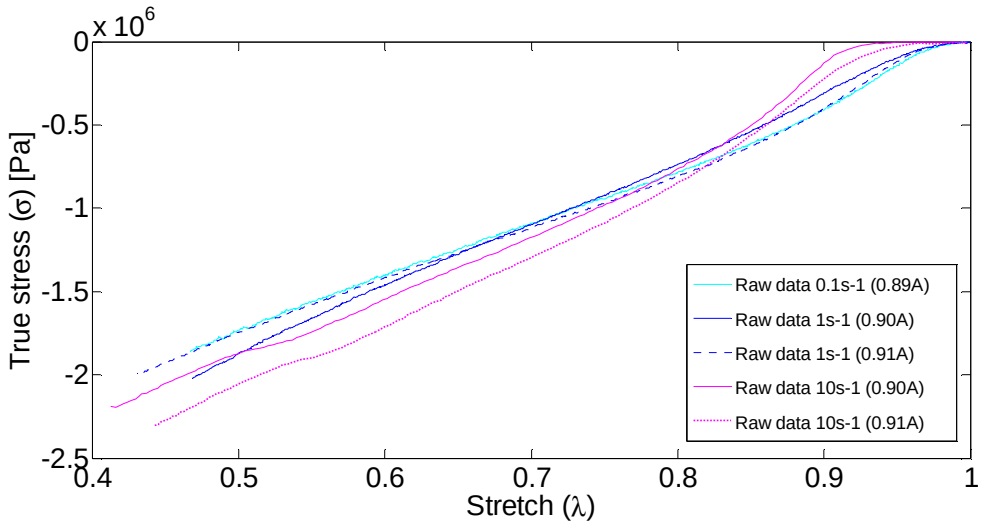

Fig. 3-16 Stress-stretch curves for density 0.9 g/cm^3 at different strain rates (SMALL samples, 90/10 proportion).

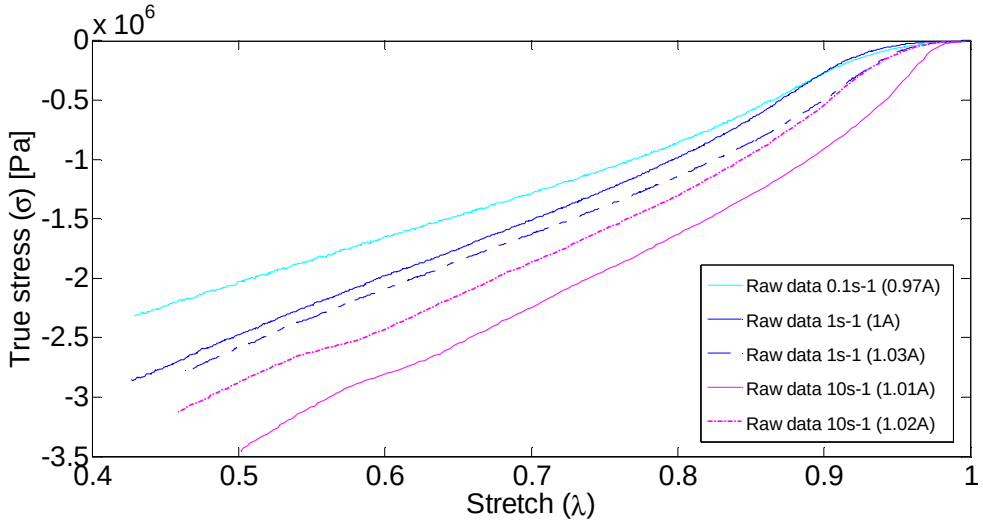

Fig. 3-17 Stress-stretch curves for density 1 g/cm^3 at different strain rates (SMALL samples, 90/10 proportion).

Compared to Fig. 3-10, similar tendencies have been observed in Fig. 3-11 to Fig. 3-17. That is, the hyperelastic behavior of the materials is appreciated in the non-linear stress-stretch relationship. A shift in the curvatures of the curves that shows a non-linear viscoelastic appearance is also observed. In fact, the stress does not increase linearly with the strain rate. The previous figures are summarized in Table 3-8 and Table 3-9:

Table 3-8 Stress-stretch curves for big samples with densities 0.7 g/cm^3, 0.8 g/cm^3 , 0.9 g/cm^3 and 1 g/cm^3

BIG SAMPLES	
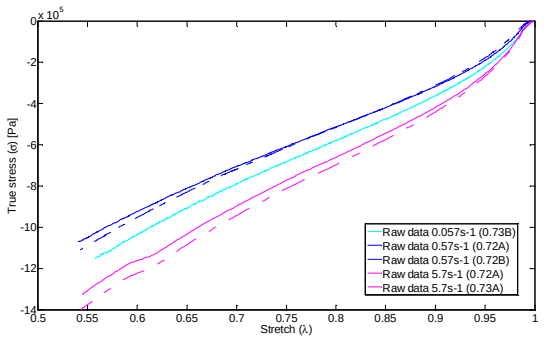 (a)	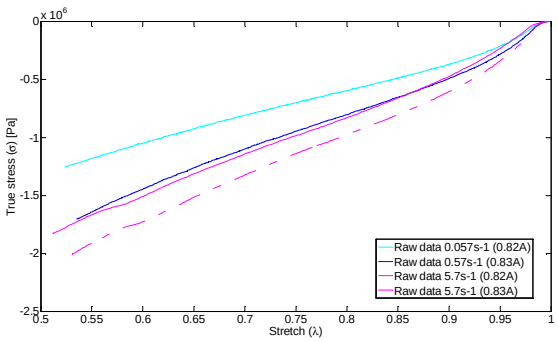 (b)
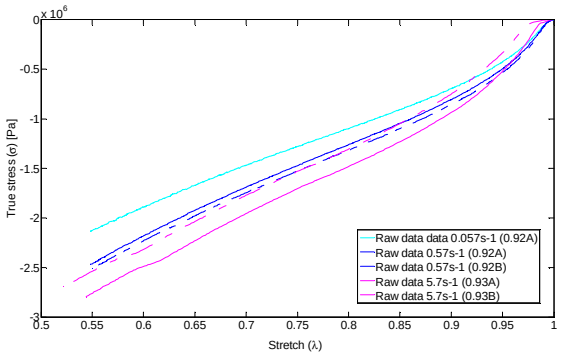 (c)	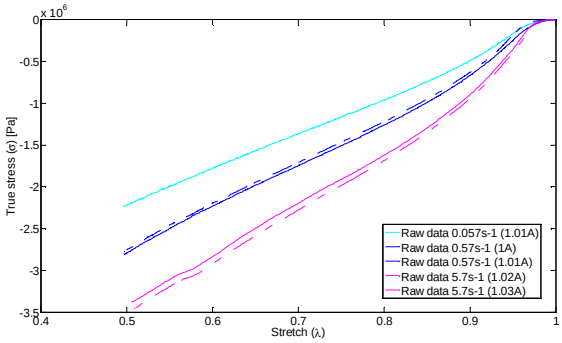 (d)

It can be appreciated that except for the 0.7 g/cm^3 case (a), the strain rates vary progressively. In all cases (all densities) hyper-viscoelastic behavior is exhibited.

Table 3-9 Stress-stretch curves for small samples with densities 0.7 g/cm^3, 0.8 g/cm^3, 0.9 g/cm^3 and 1 g/cm^3 (90/10 blends)

SMALL SAMPLES	
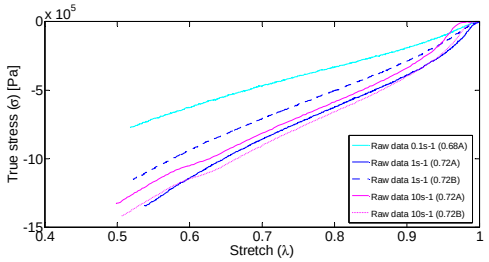 (a)	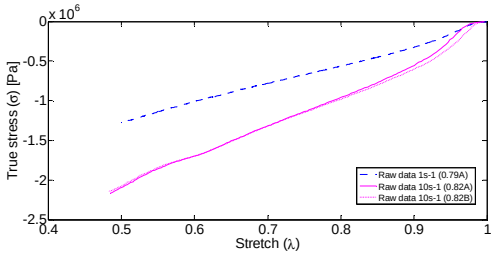 (b)
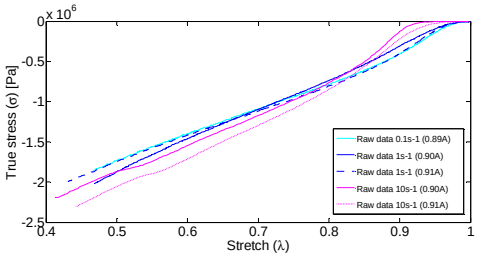 (c)	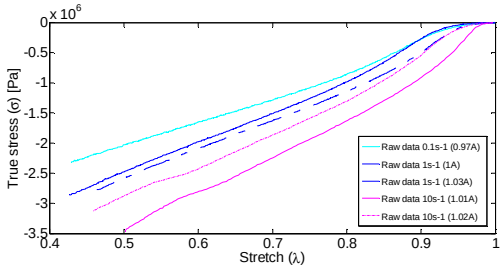 (d)

Next, Fig. 3-18 shows a comparison of stress-stretch curves of big and small samples for the different strain rates, for 1 g/cm^3 density. As it can be seen, for the same strain rate –i e. curves which have the same colour– at a certain value of the stretch the stress is very similar, as it is expected. Therefore, it can be concluded that the influence of the size is not so relevant.

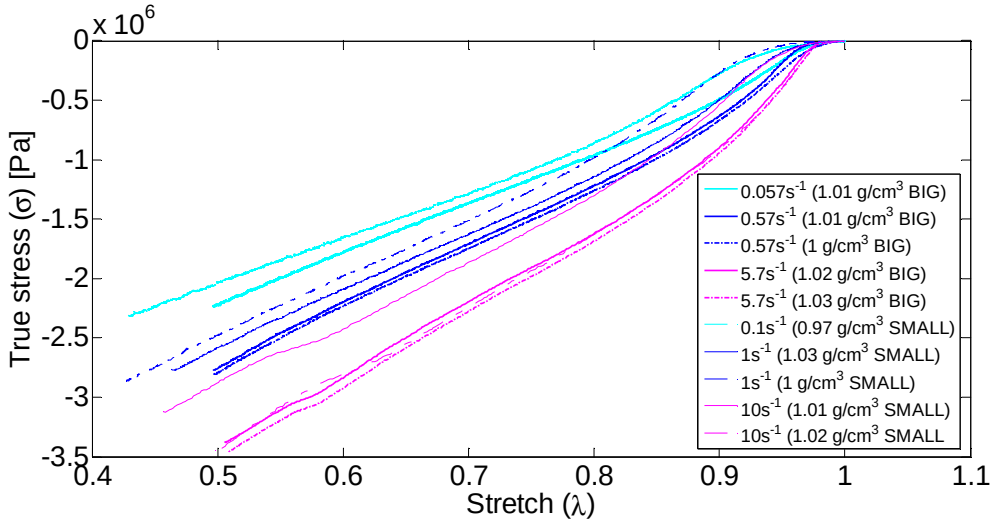

Fig. 3-18 Stress-stretch curves for big and small sample sizes for 1 g/cm^3 density at different strain rates (90/10 proportion)

Bigger samples are preferred in the potential application case of this material, as they contain more recycled rubber, and they resemble more the coatings of the barriers.

Next, another comparative plot is shown in Fig. 3-19, where curves corresponding to different densities are compared for the same strain rate (big samples):

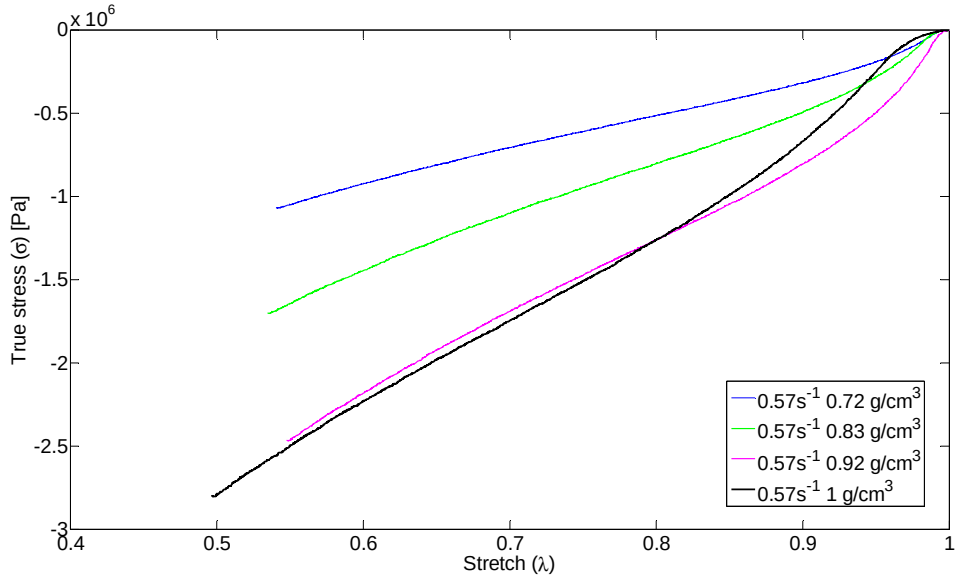

Fig. 3-19 Stress-stretch curves for 0.7, 0.8, 0.9 and 1 g/cm^3 densities at 0.57 s^{-1} strain rate (90/10 proportion, BIG samples)

As it can be seen in Fig. 3-19, a higher density material has got a bigger area below the curve; it would be interesting, therefore, to use a material with higher density as coating in the road barriers, in order to absorb more energy during the impact.

3.5.2 75/25 Proportion

Compression tests corresponding to densities of 0.7 g/cm^3, 0.8 g/cm^3 and 0.9 g/cm^3 are resumed in Table 3-10 and Table 3-11, first for big samples and afterwards for small samples; results corresponding to 1 g/cm^3 density small sample can also be found in Table 3-11.

Table 3-10 Stress-stretch curves for big samples and densities 0.7 , 0.8 and 0.9 g/cm^3 (75/25 blends)

BIG SAMPLES	
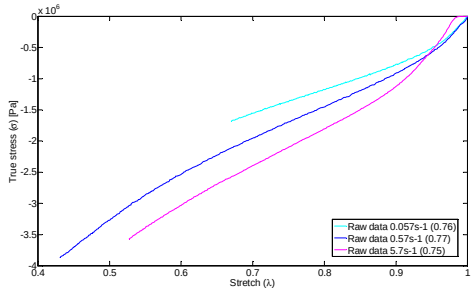 (a)	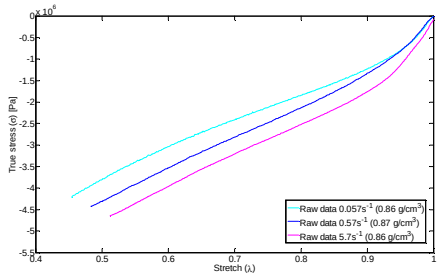 (b)
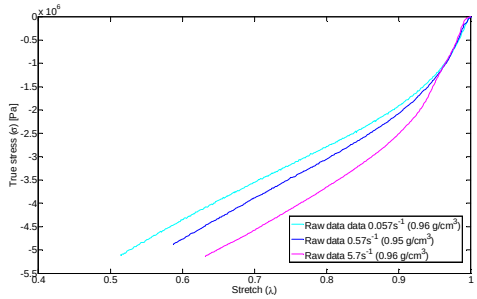 (c)	
It can be appreciated that the strain rates vary progressively. In all cases (all densities) hyper-viscoelastic behavior is exhibited.	

Table 3-11 Stress-stretch curves for small samples and densities 0.7, 0.8, 0.9 and 1 g/cm^3 (75/25 blends)

SMALL SAMPLES	
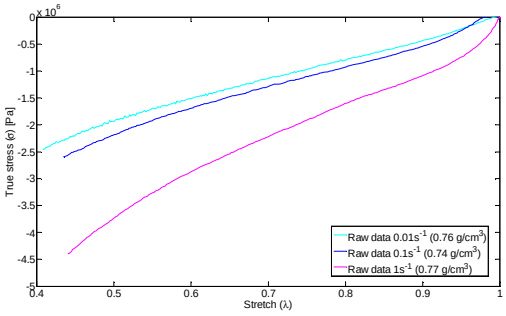 (a)	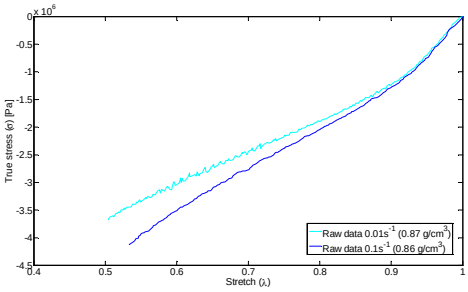 (b)
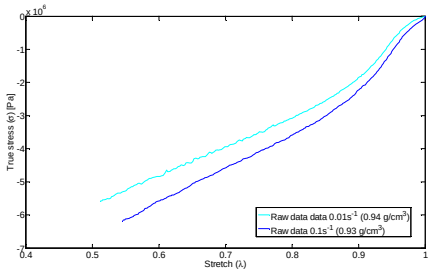 (c)	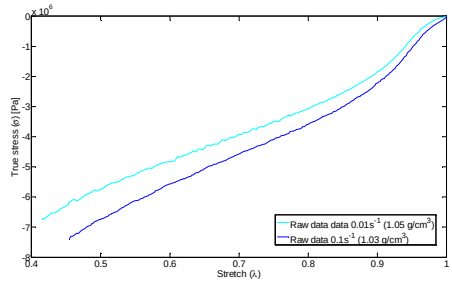 (d)

Next two figures compare samples of 0.9 g/cm^3 densities, Fig. 3-20 with 75/25 and 90/10 proportions, for big samples, and Fig. 3-21 with 60/40, 75/25 and 90/10 proportions, for small samples.

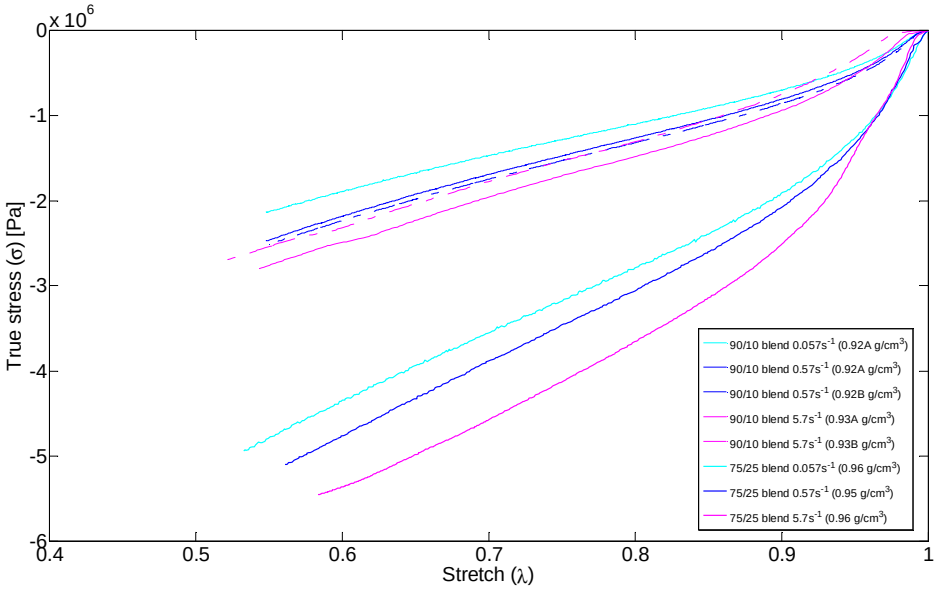

Fig. 3-20 Comparison between BIG samples and 0.9 g/cm^3 density for both blends, 75/25 and 90/10

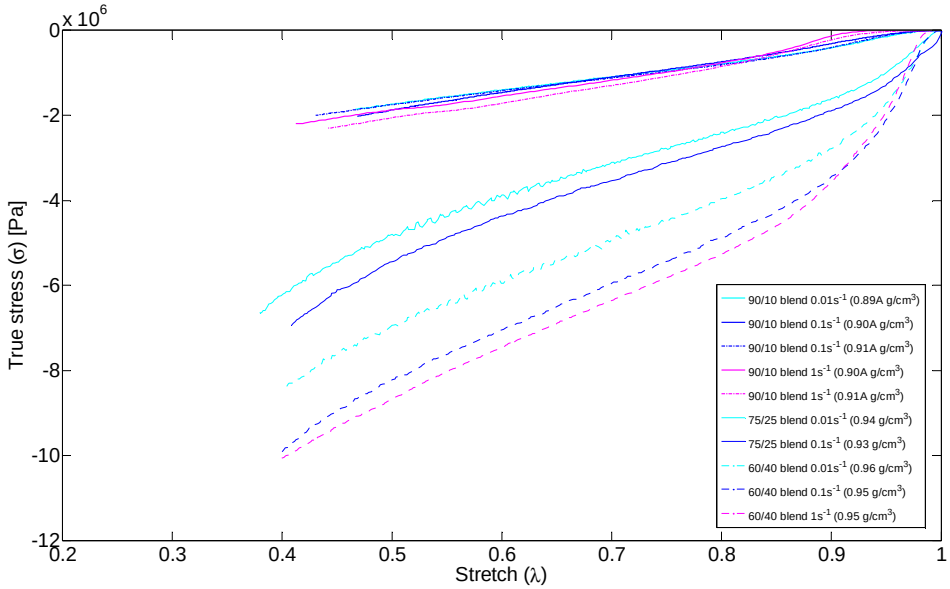

Fig. 3-21 Comparison between SMALL samples and 0.9 g/cm^3 density for blends 60/40, 75/25 and 90/10

It can be appreciated that the stiffness increases with the higher proportion of PE in the blend, being the 60/40 proportion, therefore, the one with the highest stiffness.The stress at a stretch value of 0.5 for the same strain rate is approximately 4 times higher for the blend 60/40 compared to the blend of 90/10, as it is shown in Fig. 3-21. The energy absortion capability increases with the PE proportion of the blend. Neverthelesss, a compromise

solution is considered where as much rubber as possible is recycled, without losing the benefits of the blend in a substantial way; therefore, 90/10 blend is chosen to use as coating in road barrier simulations.

3.5.3 60/40 Proportion

Compression tests corresponding to densities of 0.7 g/cm^3, 0.8 g/cm^3, 0.9 g/cm^3 and 1 g/cm^3 and small samples are introduced in next table (see Annex for further details):

Table 3-12 Stress stretch curves for 0.7 g/cm^3, 0.8 g/cm^3, 0.9 g/cm^3 and 1 g/cm^3 densities and small samples (60/40 blends)

SMALL SAMPLES

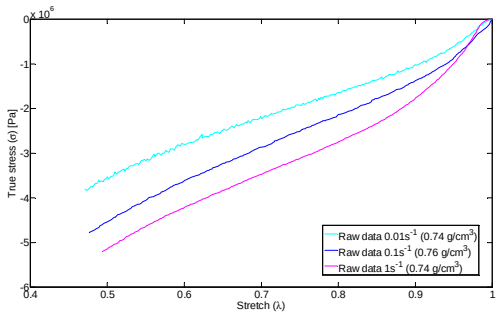

(a)

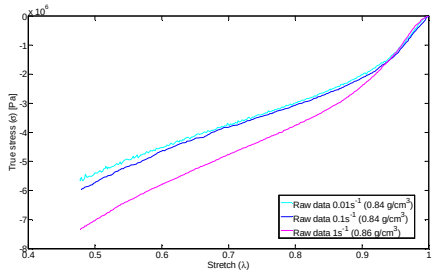

(b)

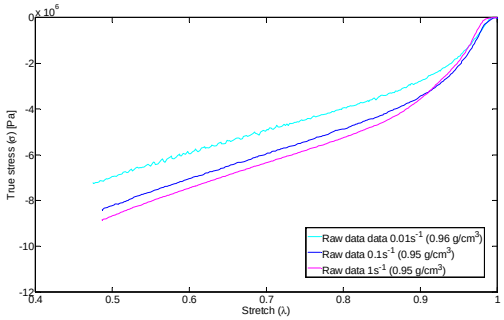

(c)

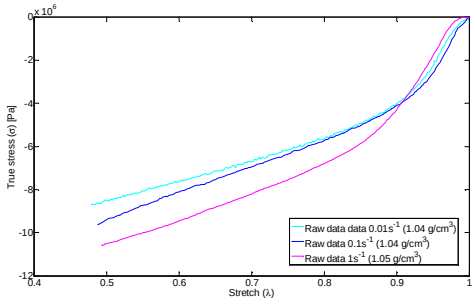

(d)

4.

METHOD TO CORRECT THE HIGH STRAIN RATE CURVES

4.1 INTRODUCTION

System ringing is one of the most important factors affecting the quality of data obtained in high speed dynamic material tests using servo-hydraulic machines. The tests performed at intermediate strain rates, ranging from 1 s^{-1} to 100 s^{-1}, present some experimental difficulties[97]. Commonly, the experimental tests in the mentioned strain ranges are conducted on high speed servo-hydraulic machines[13]. The appearance of vibrations in the strain rate range between 10-60 s^{-1} results critical as these vibrations corrupt the obtained stress-strain responses. This issue is recognized as being a primary obstacle for a proper material characterization in these types of tests. These vibrations, known as system ringing, are caused by the excitation of predominant modes of the testing frame and produce oscillations at one or more natural frequencies[14], corrupting the measured material response (producing distinctive waves in material curves that distort severely the required results).

The negative effects of system ringing have mainly been addressed applying numerical low-pass filtering techniques to measured material curves. However, this standard practice must be applied carefully, since filtering implies an inherent tendency to distort the corrected signals[98]. Several researchers have confirmed this statement through their experiments. Dutton[99] concluded that no filter can satisfactorily smooth the curves without adversely affecting the data and Rehrmann et al.[100] determined that the negative effects

consist in a delay and a phase shift in the filtered signals, as well as a lost of information about the rise in the load at the beginning of the test. Zhu et al.[14] noted the importance of correctly identifying the cutoff frequency of the filter and, in the same line, Larour[101] showed that different corrected signals are obtained depending on the selected cutoff frequency, pointing out that the final result depends on this subjective selection. Xia et al.[12] noted that the accuracy of the filtering process is highly dependent on the choice of the filtering algorithm, and Bardenheier et al.[102] obtained different smoothed solutions depending on the applied filtering algorithm.

Due to the mentioned limitations, it has been recommended to reduce the oscillations by other means before applying filtering algorithms to raw experimental data[103]. This correction requires a previous knowledge of the factors that originate the ringing vibrations and, for this purpose, it is necessary to model the dynamic response of the servo-hydraulic machine. Xiao[97] was the first author to use a mathematical model to quantitatively describe system ringing in dynamic tests. She used a basic single degree of freedom (SDOF) model to predict amplitudes, frequencies and decaying rates of vibrations and described the influence of the loading rate and the natural frequency on the magnitude of ringing. This SDOF model has been used extensively as reference in subsequent works. However, some of these researches have reported discrepancies between experimental and analytical results, attributing the errors to the fact that the vibratory response is dominated by multiple frequencies[14,104,105]. Therefore, the dynamic testing system is more complicated than the SDOF model presented by Xiao. Zhu et al.[14] presented a more elaborated study, detecting the predominant modes and frequencies through a modal analysis and determining the importance of these modes in the vibratory response. Again, the effects of these predominant modes were analyzed by using SDOF models, considering each resonant frequency individually. They recognized that the SDOF model cannot duplicate the actual vibration characteristics and concluded that a multiple degree of freedom (MDOF) model would produce a better estimate of the vibrations.

In line with this last idea, in this chapter a detailed dynamic model of a high-speed servo hydraulic machine is presented, where multiple vibration modes are considered. The model is based on modal parameters, i.e. mode shapes, natural frequencies and damping factors; obtained through an experimental modal analysis (EMA) performed in the machine and is able to simulate its vibratory response. Time domain simulations have been conducted to predict the input-output behavior of the machine when testing rubber, considering as input

the sudden impact of the actuator against the specimen and taking as output the response on the location of the piezoelectric load cell. The frequency content of the simulated force signals has detected the important frequencies involved in the process and a comparison with the frequency content of the experimentally measured force signals in real rubber tests has demonstrated the effectiveness of the analytical predictions. After this validity check, the model has been used in a subsequent step where simulated force undulations have been subtracted from experimentally measured load cell force signals. The resulting force signals are much smoother than the originally measured ones and a final filtering step completes the correction process. Two factors guarantee the successful application of this last filtering step. First, the knowledge of the frequency content of vibrations allows an accurate identification of the cutoff frequency, which is a condition for a correct filter design[14]. Second, the small undulations of the data to be filtered make it possible to get final curves with negligible distortion. Therefore, after correcting the data, final material curves that represent precisely the real high speed force vs. time behavior are obtained.

4.1.1 High speed rubber characterization

Among the compression tests described in Chapter 3, those covering actuator velocities of 4 m/s, that is, those with higher test speeds produce ringing vibrations, contaminating load cell measurements. Fig. 4-1 shows the compression force vs. time measurement of the load cell and the displacement vs. time measurement of the magnetostrictive sensor corresponding to a test conducted at 4 m/s in a recycled rubber specimen with 60/40 proportion.

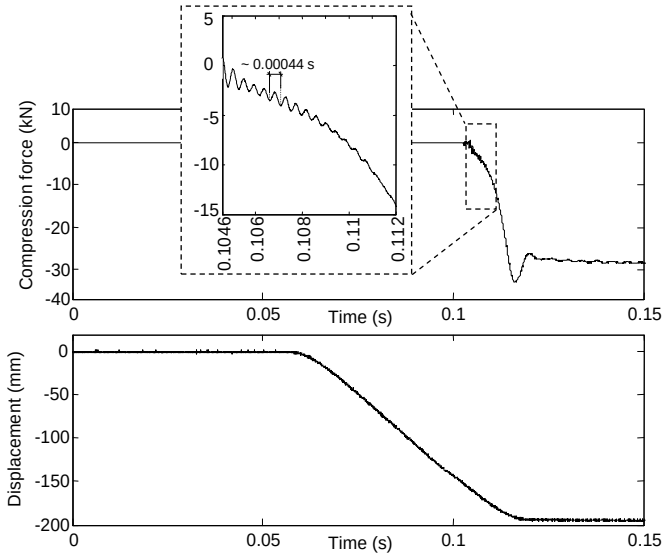

Fig. 4-1 Compression force vs. time and displacement vs. time measurements.

Such a force vs. time curve is not suitable for material characterization due to the presence of unwanted undulations during the loading process (approximately between 0.1046 s and 0.112 s in the test shown in Fig. 4-1). To gain knowledge about the nature and origin of these vibrations, a two-step procedure has been followed. First, an initial estimation of the predominant frequency has been done calculating the inverse of the time elapsed between two peaks (see Fig. 4-1): $f_{estim} \approx 1/0.00044 = 2272.7\ \text{Hz}$. Second, a more precise calculation has been developed extracting the frequency content of the force signal via Fast Fourier Transform (FFT). For optimal results, this transformation requires an input signal with zero mean value to avoid unwanted low frequency components that would tend to misrepresent the frequency content plot shown later in Fig. 4-2. Hence, a high pass filter has been applied. The cutoff frequency has been settled at 1000 Hz, preserving the vibration frequency estimated in the previous step. The distortion added by the filtering algorithm is not crucial in this stage because the aim is not to get a corrected signal, but to eliminate unnecessary information, which is correctly done by the filter. Fig. 4-2 presents the FFT graph, where a high contribution at a specific frequency is appreciated, together with a lower contribution at a lower frequency. A closer inspection shows that the main frequency is around 2320 Hz, which adjusts the previous estimation. The second frequency is around 1920 Hz.

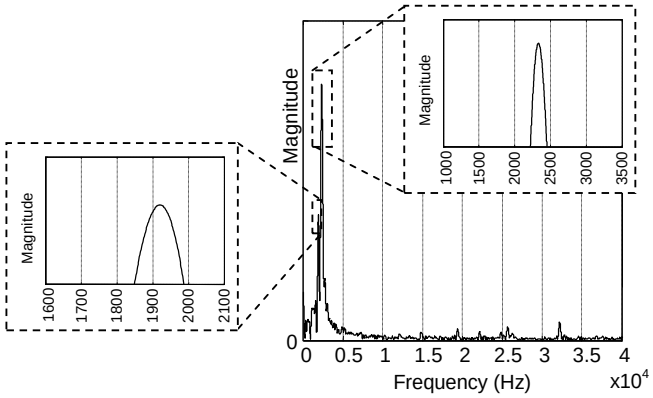

Fig. 4-2 FFT of the measured force signal.

4.1.2 Experimental Modal Analysis

In order to determine the dynamic characteristics of the testing system and create a model that predicts the behavior observed in Fig. 4-2, an EMA has been conducted based on the geometry shown in Fig. 4-3. An instrumented hammer has been used as exciter in two different locations and directions (depicted as "Excitation" in Fig. 4-3) with the idea of exciting effectively different mode shapes. For each input, responses have been measured at the 28 points shown in the same figure. Triaxial accelerometers have been used for this purpose. The frequency range of measurements has been established between 0 Hz and 4000 Hz, covering widely the predominant frequencies excited in operation according to Fig. 4-2. Therefore, two sets of acceleration/force frequency response functions (FRF´s) corresponding to 84 degrees of freedom (dof´s) have been acquired. From these FRF´s, system modal parameters have been extracted using a polyreference least squares complex frequency estimator. 19 mode shapes have been obtained in the frequency range of interest, together with the corresponding natural frequencies and damping factors.

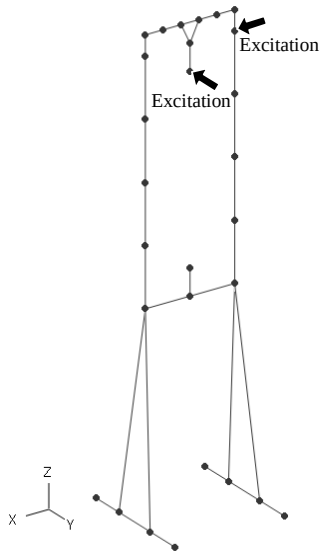

Fig. 4-3 Geometry of the EMA.

4.2 DYNAMIC MODEL OF THE MACHINE

Considering the general equation of motion governing the system in Fig. 4-3, which dynamic behavior can be obtained by the set of second order differential equations[106]:

$$M\ddot{z}(t) + C\dot{z}(t) + K z(t) = L_u f(t) \tag{4.1}$$

Where:

- M, C and K are the mass, damping and stiffness matrices, respectively.
- $z(t)$ is the displacement vector of the system dof´s and $\dot{z}(t)$ and $\ddot{z}(t)$ are its time derivatives.
- Vector $f(t)$ defines the forces acting on the structure and L_u is their influence matrix, indicating the way the input forces act on the structure.

Formulation of a mathematic expression for the energy dissipation is very difficult, as this dissipation is produced by many causes, as hysteretic internal friction, dry and viscous frictions, damping elements, etc. Traditionally simplified models are used; in this work one of the most extended models is considered, viscous damping (dissipative forces are proportional to the velocities).

Eq. (4.1) is described in physical coordinates and results from the EMA of section 4.1.2 require a formulation described in modal coordinates. A change of variables is done according to:

$$z(t) = \Phi q(t) \tag{4.2}$$

Where $q(t)$ is the vector of modal amplitudes (dimensions 84×1) and matrix Φ contains the mass normalized mode shape vectors in its columns (dimensions 84×19). Substituting into eq.(4.1), left multiplying by Φ^T and using the orthogonality relationships[107], one gets:

$$\ddot{q}(t) + 2\xi\Omega\dot{q}(t) + \Omega^2 q(t) = \Phi^T L_u f(t) \tag{4.3}$$

$\dot{q}(t)$ and $\ddot{q}(t)$ are the time derivatives of $q(t)$ and Ω and ξ are diagonal matrices containing the natural frequencies and damping factors, respectively (dimensions 19×19).

M and K matrices have orthogonality conditions which origin is explained next.

Taking into account the free response of a conservative system, this is, without damping (as a dynamic system study start point):

$$M\ddot{z}(t) + Kz(t) = 0 \tag{4.4}$$

This equation can be used to obtain the natural frequencies and vibration modes of the structure; in the case of linear systems, the dynamic of the machine is completely defined by these parameters. The solution of this equation has this form:

$$z(t) = \psi_i e^{jw_i t} \tag{4.5}$$

w_i is the ith natural frequency of the structure and ψ_i is the associated vibration mode.

Substituting eq.(4.5) into eq.(4.4), an eigenvalue and eigenvector problem is obtained:

$$\begin{aligned} &(K - \lambda_i M)\psi_i = 0 \\ &\lambda_i = w_i^2 \end{aligned} \tag{4.6}$$

M and K matrices are symmetric, M is positive defined (all its eigenvalues are positive) and K is positive semi-defined (all its eigenvalues are no negative). Taking this into account, each eigenvalue in previous equation is real and no negative. As this equation defines only the vibration mode but not its amplitude, it results possible to scale it.

The number of natural frequencies and vibration modes is equal to the degrees of freedom of the structure, N (in this case, N=84). The complete solution of the system with no damping usually comes by two matrixes NxN:

$$\Omega^2 = \begin{bmatrix} w_1^2 & 0 & \dots & 0 \\ 0 & w_2^2 & \dots & 0 \\ \vdots & \vdots & \ddots & \vdots \\ 0 & 0 & \dots & w_N^2 \end{bmatrix} \tag{4.7}$$

$$\psi = [\psi_1, \psi_2, \dots, \psi_N] \tag{4.8}$$

These natural frequencies show the frequencies at which the system tends to vibrate and the vibration modes have the property of defining a coordinate transformation that simultaneously orthogonalizes mass and stiffness matrix. This is:

$$\psi_j^T K \psi_i = 0 \tag{4.9}$$

$$\psi_j^T M \psi_i = 0 \tag{4.10}$$

Where ψ_j and ψ_i are two different vibration modes. These orthogonality conditions can be expressed in matrix notation as follows:

$$\psi^T K \psi = k_r \tag{4.11}$$

$$\psi^T M \psi = m_r \tag{4.12}$$

k_r is the diagonal matrix of modal stiffness and m_r is the diagonal matrix of modal mass.

The relationship between these two matrices is:

$$k_r = \Omega^2 m_r \tag{4.13}$$

Matrix ψ is subjected to an arbitrary scale factor, so k_r and m_r are not unique. It is common to use the scale or normalization to unity modal mass. In this case, the matrix of vibration modes is written as ϕ and it has the next properties:

$$\phi^T K \phi = \Omega^2 \tag{4.14}$$

$$\phi^T M \phi = I \tag{4.15}$$

Where I is the unity matrix.

If eq. (4.2) is introduced in eq. (4.1):

$$M\phi\{\ddot{q}(t)\} + C\phi\{\dot{q}(t)\} + K\phi q(t) = L_u f(t) \tag{4.16}$$

Pre multipliying eq.(4.16) by ϕ^T and taking into account these orthogonality conditions:

$$I\ddot{q}(t) + \phi^T C \phi \dot{q}(t) + \Omega^2 q(t) = \phi^T L_u f(t) \tag{4.17}$$

It has to be considered the way of calculation of matrix **C**, as the analytic procedure is often difficult to apply. When data extracted from modal analysis is used, modal damping procedure is applied.

This way, modal damping for each mode is considered as a fraction of the critical damping ξ_i and defined as:

$$\phi^T C \phi = diag(2 \cdot \xi_i \cdot w_i) \tag{4.18}$$

And eq. (4.17) is converted into a set of N uncoupled equations as eq.(4.3); each equation describes the behavior of a vibration mode.

Where:

$$\xi = \begin{bmatrix} \xi_1 & 0 & \dots & 0 \\ 0 & \xi_2 & \dots & 0 \\ \vdots & \vdots & \ddots & \vdots \\ 0 & 0 & \dots & \xi_N \end{bmatrix} \tag{4.19}$$

The values ξ_i for each mode are obtained experimentally.

The eq. (4.3) is defined completely on modal parameters, extracted from the EMA in section 4.1.2.

State-space representation provides a convenient way to analyze the response of the systems to input forces; in this representation a linear time invariant system is described as

a set of first order differential equations. Eq. (4.20) and (4.21) describe the general form of this development:

$$\dot{x}(t) = Ax(t) + Bu(t) \tag{4.20}$$

$$y(t) = Cx(t) + Du(t) \tag{4.21}$$

Eq. (4.20) is the state equation: describes the internal dynamic of the system, and eq. (4.21) is the output equation.

Where:

- A, B, C and D are state-space real matrices, independent of time, that express the system dynamics,

- $u(t)$ is the system input vector (equal to $f(t)$),

- $x(t)$ is the state vector and $\dot{x}(t)$ its derivative, and

- $y(t)$ is the system output vector.

A, B, C and D matrices depend on the selection of the state vector; therefore, different state space representations are possible for the same system inputs and outputs. In order to define the state-space matrices in modal domain, a proper definition of the state vector is[108]:

$$x(t) = \begin{bmatrix} \Omega q(t) \\ \dot{q}(t) \end{bmatrix} \tag{4.22}$$

Applying this definition in eq.(4.3), **A** and **B** matrices are:

$$A = \begin{bmatrix} 0 & \Omega \\ -\Omega & -2\xi\Omega \end{bmatrix} \qquad B = \begin{bmatrix} 0 \\ \Phi^T L_u \end{bmatrix} \tag{4.23}$$

C and D matrices depend on the required outputs, so the model can be used to simulate displacements, velocities and accelerations of the selected dof´s.

The objective of the state space formulation is to obtain the displacements, velocities and accelerations of the different degrees of freedom as output. Depending on which term is wanted, the output equation can be read as:

Displacements:

In case of displacements, output equation is: $\{y(t)\} = \left[L_y\right]^T \{z(t)\}$

$$\{y(t)\} = \left[L_y\right]^T [\phi]\{\eta(t)\} = [\phi]_y [\Omega]^{-1} \{z(t)\} = Cz + Df \tag{4.24}$$

Velocities:

In case of velocities, output equation is: $\{y(t)\} = \left[L_y\right]^T \{\dot{z}(t)\}$

Accelerations:

In case of accelerations, output equation is: $\{y(t)\} = \left[L_y\right]^T \{\ddot{z}(t)\}$

$$y = \left(-[\phi]_y [\Omega] - 2[\phi]_y [\xi][\Omega]\right) z + [\phi]_y \mu^{-1} [\phi]_u^T \{f(t)\} = Cz + Df \tag{4.25}$$

Once the model has been developed, it is important to check its accuracy. The next section describes the verifications conducted in the frame of this work.

4.3 VERIFICATION OF THE MODEL

One common check to validate mathematical models is to compare simulated and measured FRF´s. Subsection 4.3.1 describes this verification. Additionally, a high speed compression test on rubber has been simulated in time domain to predict the frequency content of vibrations, comparing the result to that obtained experimentally. This is summarized in subsection 4.3.2.

4.3.1 Comparison of FRF´s

Experimental accelerance FRF´s, available from the modal analysis described in subsection 4.1.2, can be reproduced with the state-space model. These calculations require a proper definition of **C** and **D** matrices to get accelerations, as follows[108]:

$$C = \left[L_y^T \Phi \Omega \quad -2L_y^T \Phi \xi \Omega\right] \qquad D = L_y^T \Phi \Phi^T L_u \tag{4.26}$$

being L_y the influence matrix of the required outputs.

Fig. 4-4 compares the FRF´s between output dof *j* and input dof *i*. The output dof has been selected in the position and direction where the impact between the upper rod and the specimen is produced, with the idea of detecting the modes transmitted through the load path of the machine.

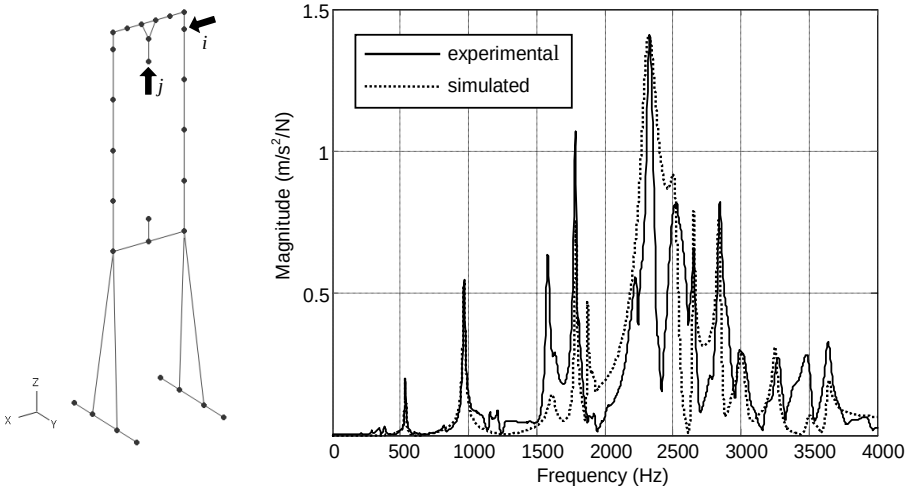

Fig. 4-4 Experimental and simulated accelerance FRF´s between output dof *j* and input dof *i*.

This figure shows that the state-space modal model reflects correctly the system dynamic behavior. It is interesting to note that the peak with highest amplitude is produced around 2320 Hz, the same frequency detected in subsection 4.1.2.

4.3.2 Time domain simulations

The compression impact on the rubber specimen is comparable to a suddenly applied impulse load. This mathematical idealization, adopted widely in previous research works[14,97], provides a convenient way to simulate the time evolution of machine response, since impulsive inputs are easily programmable.

Simulink platform from Matlab software has been used to perform these simulations. In the state-space model, the impulse load has been simulated acting in the two "Input" dof´s shown in Fig. 4-5 through a proper definition of L_u vector. Although two forces are introduced in the system, they are of equal magnitude because they represent the self-

equilibrating forces acting in the piston rod and the upper rod during the impact, thus only one column of $\mathbf{L_u}$ is necessary.

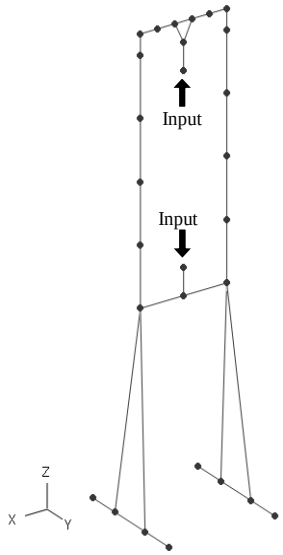

Fig. 4-5 Input dof´s for time domain simulations.

One important issue when working with an impulse load is the adequate estimation of its magnitude. Next section discusses the strategy adopted in this work to determine the impulsive load value.

4.3.2.1. Estimation of impulse magnitude

An impulse is defined as the time integral of the force $\int f(t)dt$ and describes a force of very large magnitude that acts in a very short time interval. Ideally, the time interval approaches zero and the force tends to become infinite, but with a time integral that is finite. In a time-domain simulation environment it is not possible to apply an infinite force and neither is it possible to define a zero time interval so, in practice, a load f is applied over a discrete amount of time Δt. This situation is described in Fig. 4-6.

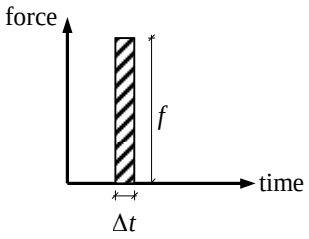

Fig. 4-6 Impulsive force of magnitude *f* with time duration of Δ*t*.

Therefore, the estimation process consists of determining an *f* value that, acting in a Δ*t* time interval, provides a response that reflects the real machine behavior.

The responses selected for this purpose were the accelerations of various control points, where accelerometers had been placed during the test of Fig. 4-1. The simulated accelerations were obtained using the state space model with an appropriate definition of L_y vector. Rubber specimen has been considered very flexible compared to the machine, so no additional stiffness corresponding to this material has been added in the model. Thus, after defining Δ*t*, the value of *f* has been modified iteratively until a correct match between simulated and measured responses has been obtained.

Once a proper magnitude of the impulsive load has been estimated, the next step in the model verification process is to predict the force measured by the load cell in order to determine the degree of precision of the simulations.

4.3.2.2. Simulation of the force measured by the load cell

Fig. 4-7 presents a picture of the piezoelectric load cell, which is located in the upper rod. The force measured by this cell can be estimated following a modeling procedure where the cell is characterized as a spring element. In fact, assuming that the displacements of the ends of the spring are calculated (points *1* and *2* in Fig. 4-7), the force in the load cell (F_{LC}) can be obtained multiplying its stiffness (K_{LC}) by the change in length of the spring ($x_2 - x_1$).

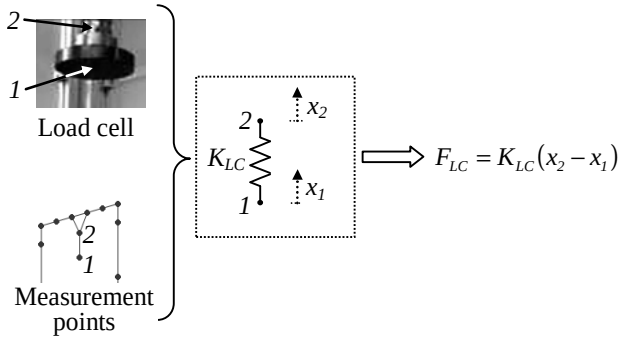

Fig. 4-7 Mathematical idealization of the load cell.

The variables x_1 and x_2 can be calculated from the modal model (the measurement points corresponding to points *1* and *2* are shown in the same Fig. 4-7). C and D matrices must be adapted to give displacements as outputs, as follows[108]:

$$C = \left[L_y^T \Phi \Omega^{-1} \quad 0 \right] \qquad D = 0 \tag{4.27}$$

Therefore, the impulse magnitude obtained in subsection 4.3.2.1. has been applied as input and axial displacements of points *2* and *1* were estimated through the model. The difference between these displacements has been multiplied by K_{LC}, which has been obtained from the manufacturer´s catalog[96]. The resulting temporal signal of the simulated force is shown in Fig. 4-8, together with the FFT of this signal.

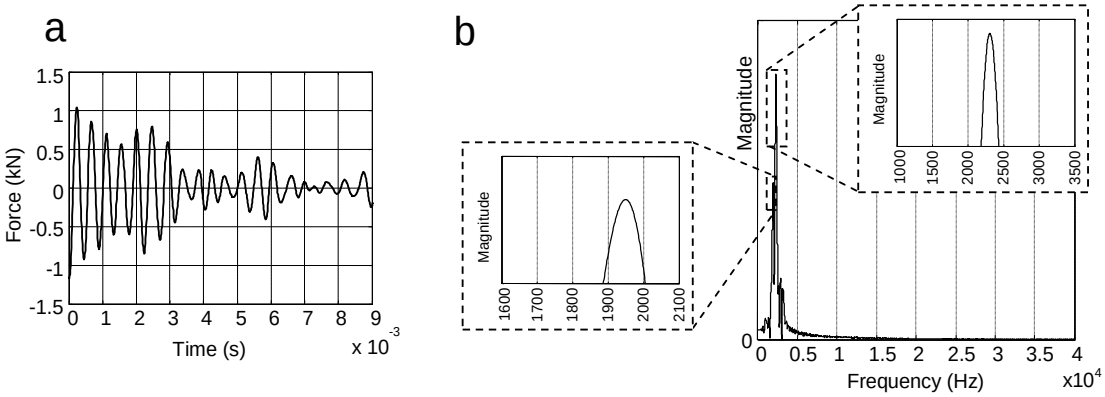

Fig. 4-8 (a) Time evolution and (b) FFT of the simulated load cell force signal.

A clear similarity is observed between the frequency content of the measured load cell force signal (Fig. 4-2) and the simulated one (Fig. 4-8b).

Hence, the model validation process certified the accuracy of the simulations, meaning that the model is suitable for a further force signal correction stage.

4.4 CORRECTION OF THE FORCE MEASURED BY THE LOAD CELL

The force signal predicted by the model in Fig. 4-8a estimates the transient oscillatory component measured by the load cell due to the excitation of machine resonances during the material test shown in Fig. 4-1. Therefore, this oscillatory part can be removed subtracting the simulated response from the measured signal[109].

This idea must be applied with care to avoid any phase shift between the two signals. In fact, time axes of Fig. 4-1 and Fig. 4-8a are independent and accurate correlation requires careful determination of coincident time instants. This objective has been achieved overlapping both signals in the same plot and translating the simulated response until a proper match in the time instants of the peaks has been obtained. This procedure is explained in Fig. 4-9.

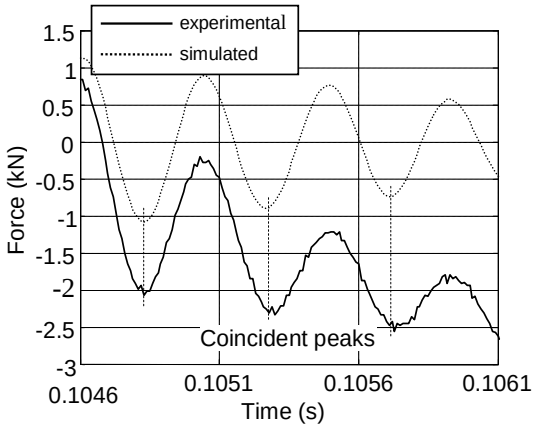

Fig. 4-9 Comparison of experimental and simulated force signals for a proper time correlation after translating the simulated response.

The simulated signal of Fig. 4-9 is now ready to be subtracted from the experimental signal. This operation produced the curve shown in Fig. 4-10.

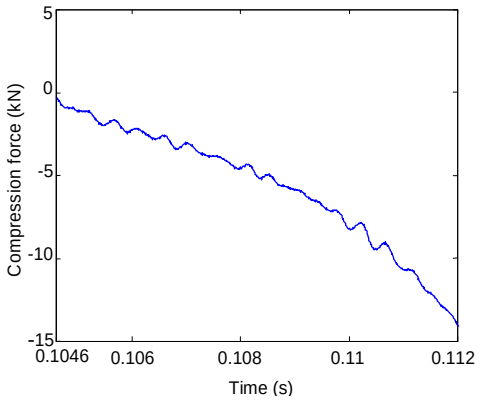

Fig. 4-10 Load cell force signal after subtracting simulated oscillations.

The oscillations, although not completely eliminated, have been reduced considerably. Indeed, compared to the raw curve in Fig. 4-1, a clear reduction in peak amplitudes can be appreciated.

The new signal is more suitable for filter application than the original measurement, as pointed out in the introduction section. Therefore, the signal of Fig. 4-10 has been passes through a low pass filter with a cutoff frequency of 1600 Hz. This cutoff frequency has been selected to effectively filter the oscillation frequencies shown in Fig. 4-8. The resulting curve is shown in Fig. 4-11.

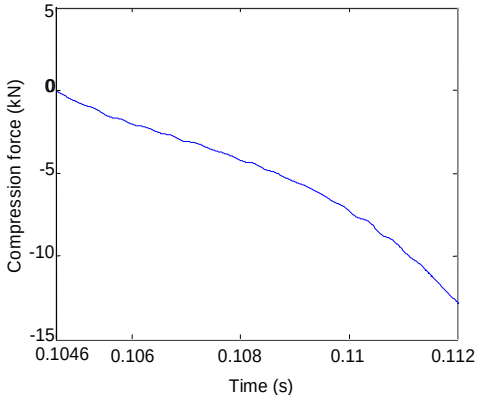

Fig. 4-11 Final force signal after filtering.

This final result shows a smooth behavior where the oscillatory response has been eliminated. Thus, the dynamic contribution of the machine has been removed and the curve reflects the real behavior of the tested material, meaning that the signal is suitable for a further analysis in the field of material characterization at high speeds.

Finally,

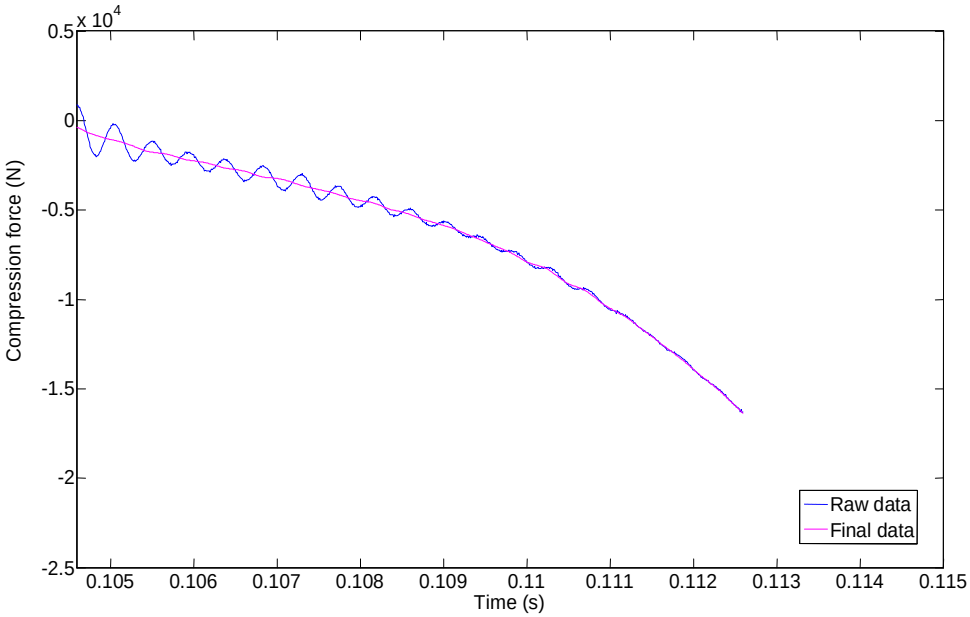

Fig. **4-12** shows both load cell force signal after subtracting simulated oscillations and fnal force signal after filtering.

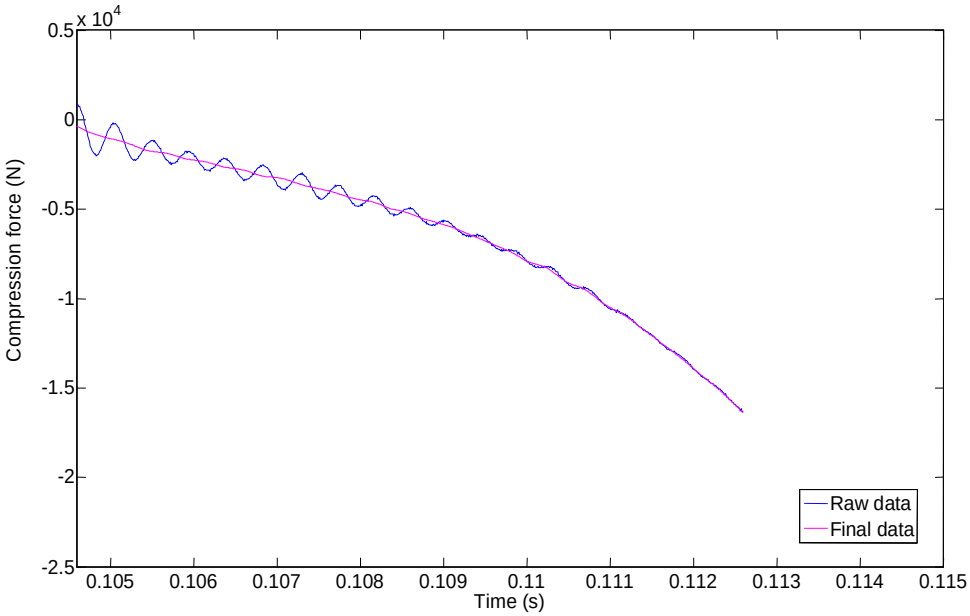

Fig. 4-12 Load cell force signal after subtracting simulated oscillations (raw data) vs. Final force signal after filtering (final data)

4.5 APPLICATION TO OTHER MATERIAL DENSITIES

As previously stated, the density of the studied material curve is 0.75 g/cm^3, for the proportion 60/40. This methodology has been applied to other material densities, namely 0.84, 0.93 and 1.04 g/cm^3. The following figures show initial force versus time curves together with force signals after subtracting oscillations and after filtering for these densities.

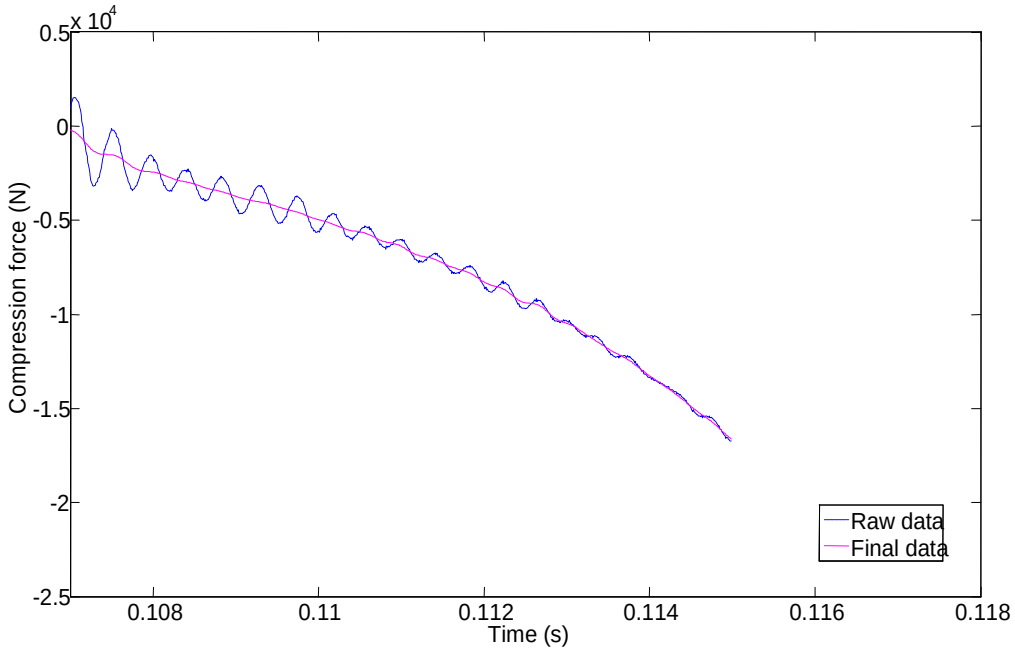

Fig. 4-13 0.84 g/cm^3 density raw and final force signals.

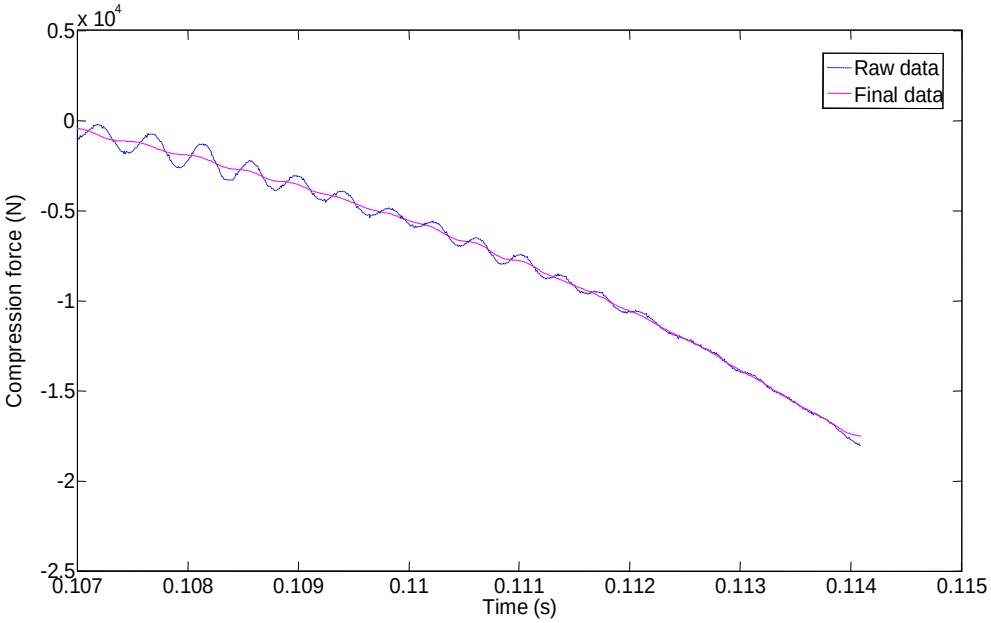

Fig. 4-14 0.93 g/cm^3 density raw and final force signals.

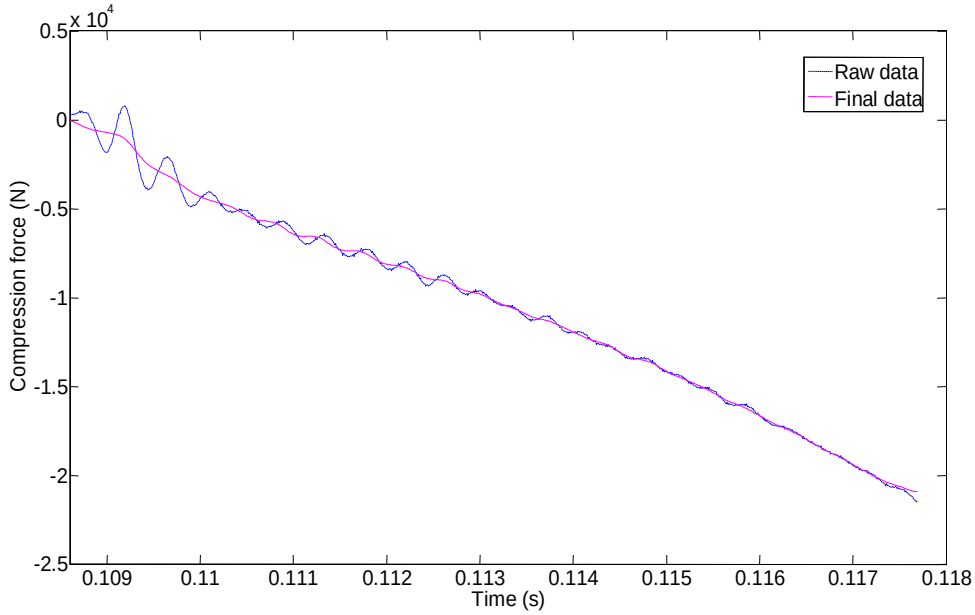

Fig. 4-15 1.04 g/cm^3 density raw and final force signals.

Next, same methodology is applied to the other proportions of materials, that is, 75/25 proportion and 90/10 proportion, and their corresponding densities.

<u>75/25 proportion</u>:

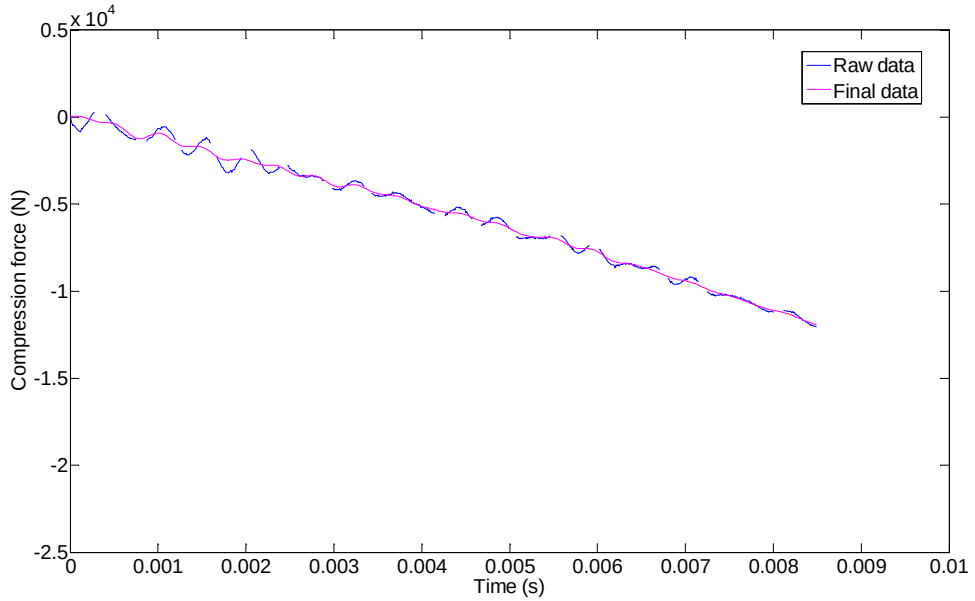

Fig. 4-16 0.77 g/cm^3 density raw and final force signals (BIG sample).

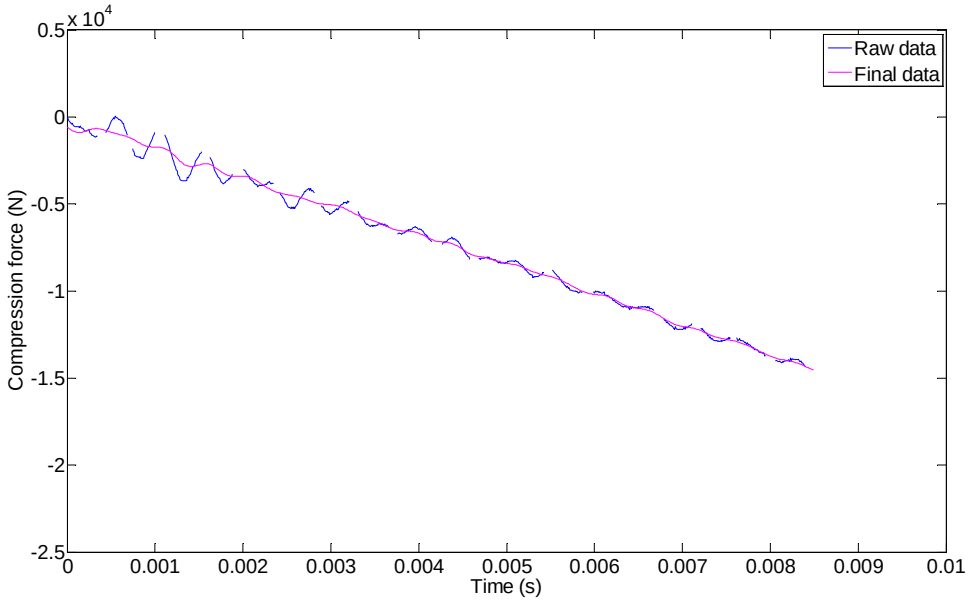

Fig. 4-17 0.85 g/cm^3 density raw and final force signals (BIG sample).

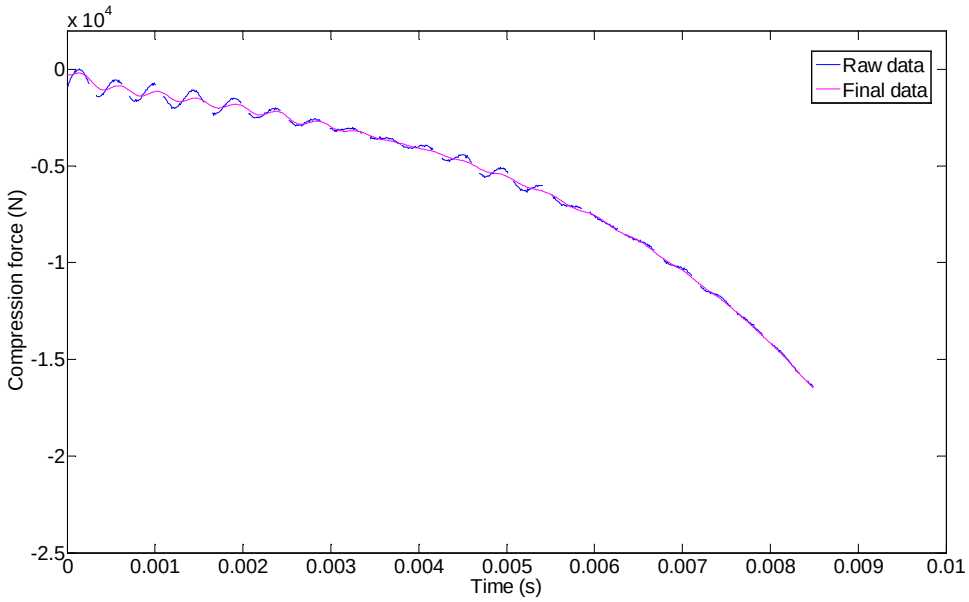

Fig. 4-18 0.73 g/cm^3 density raw and final force signals (SMALL sample).

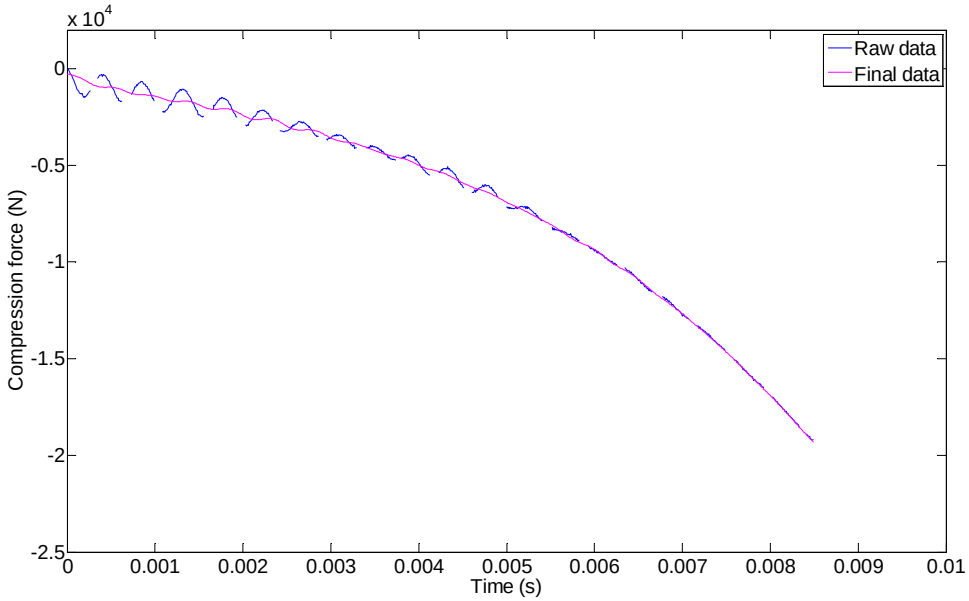

Fig. 4-19 0.83 g/cm³ density raw and final force signals (SMALL sample).

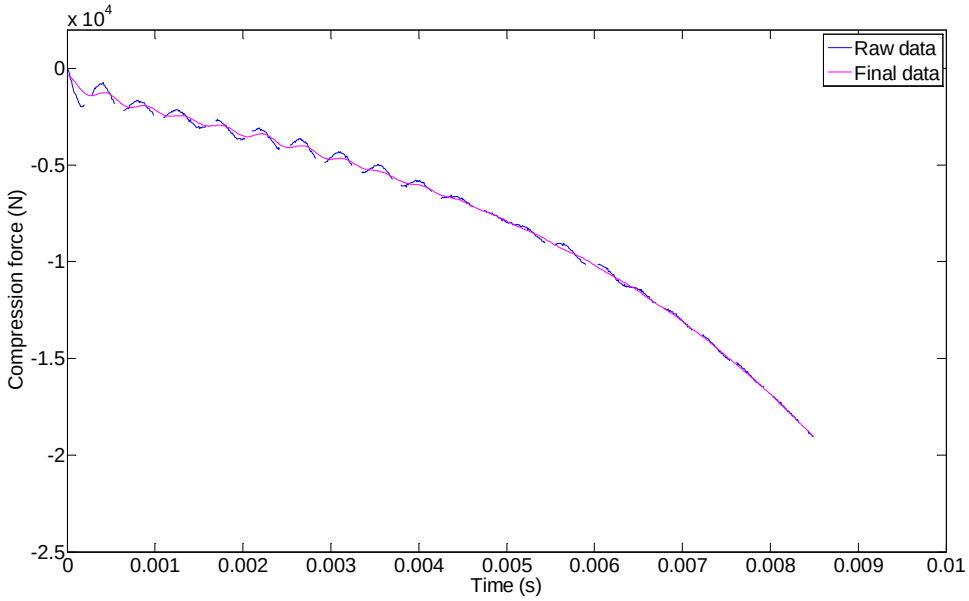

Fig. 4-20 0.93 g/cm³ density raw and final force signals (SMALL sample).

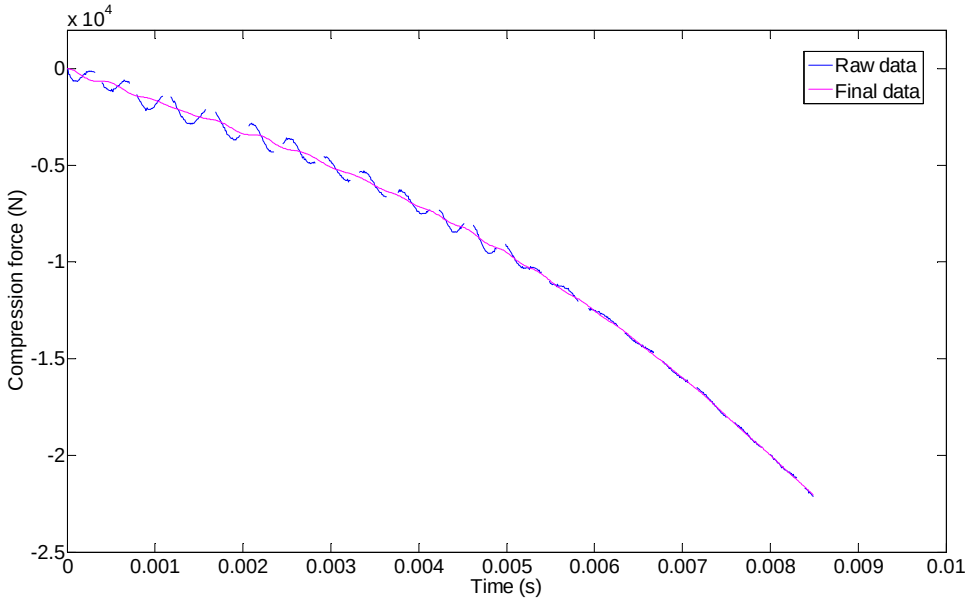

Fig. 4-21 1.07 g/cm^3 density raw and final force signals (SMALL sample).

<u>90/10 proportion</u>:

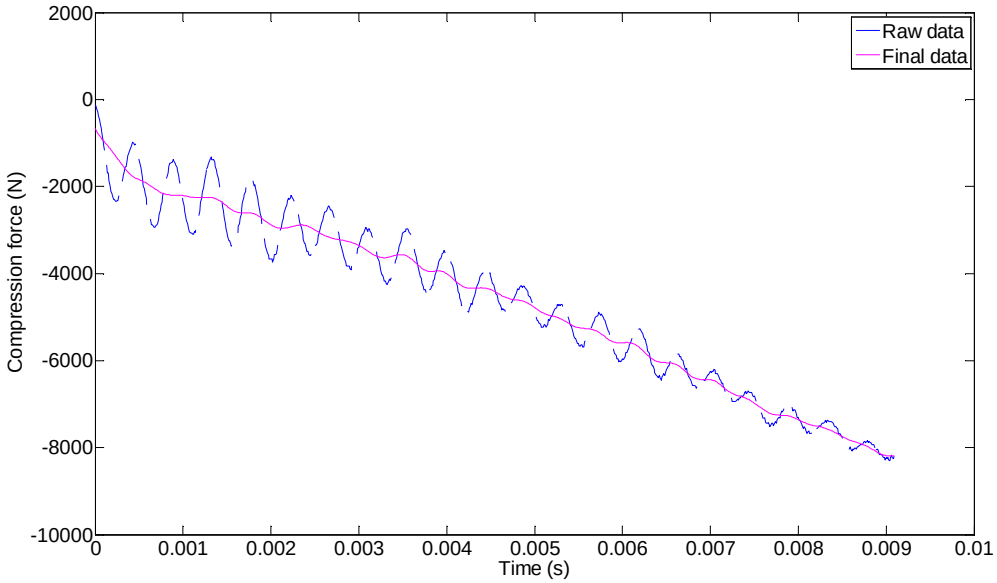

Fig. 4-22 0.73 g/cm^3 density raw and final force signals (BIG sample).

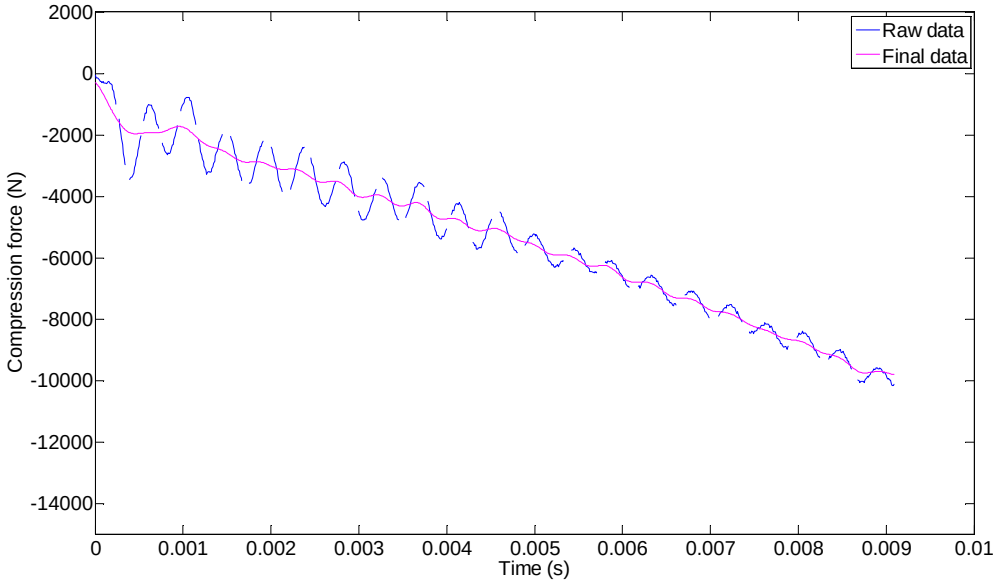

Fig. 4-23 0.83 g/cm³ density raw and final force signals (BIG sample).

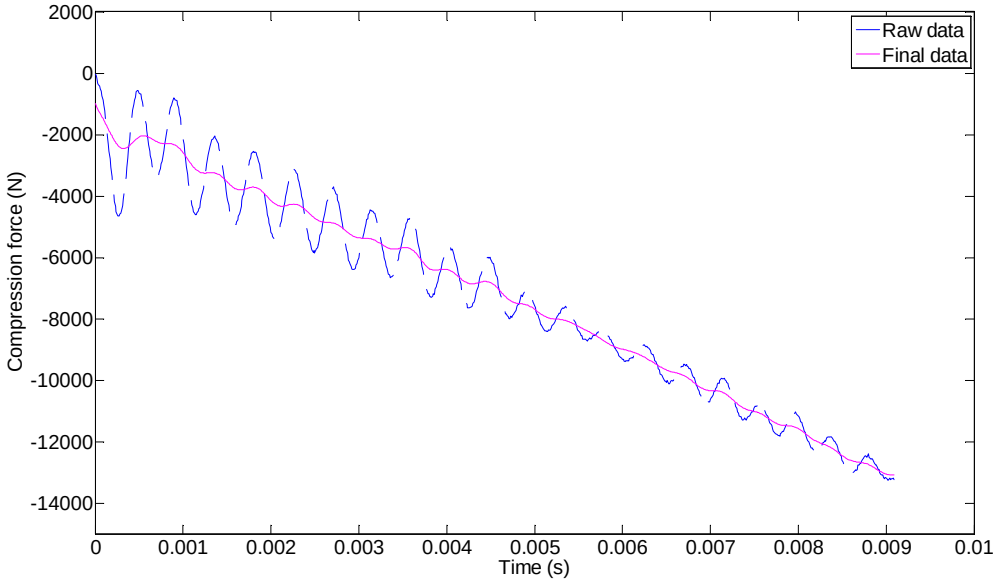

Fig. 4-24 0.93 g/cm³ density raw and final force signals (BIG sample).

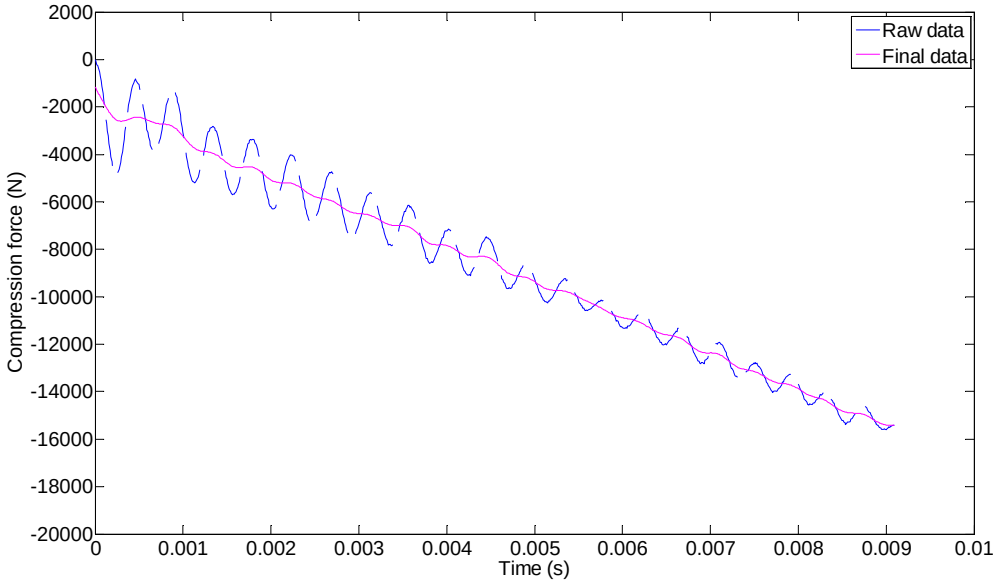

Fig. 4-25 1.02 g/cm^3 density raw and final force signals (BIG sample).

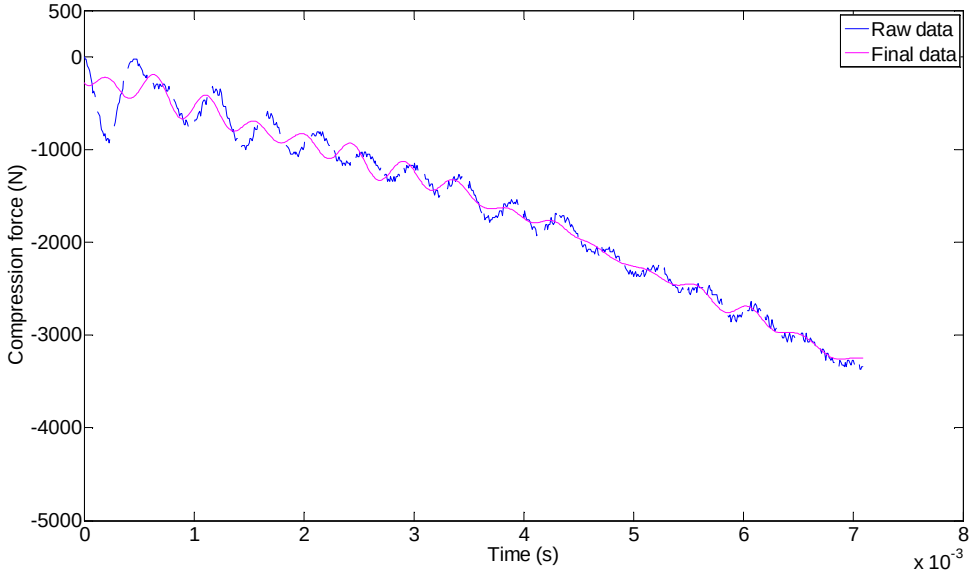

Fig. 4-26 0.82 g/cm^3 density raw and final force signals (SMALL sample).

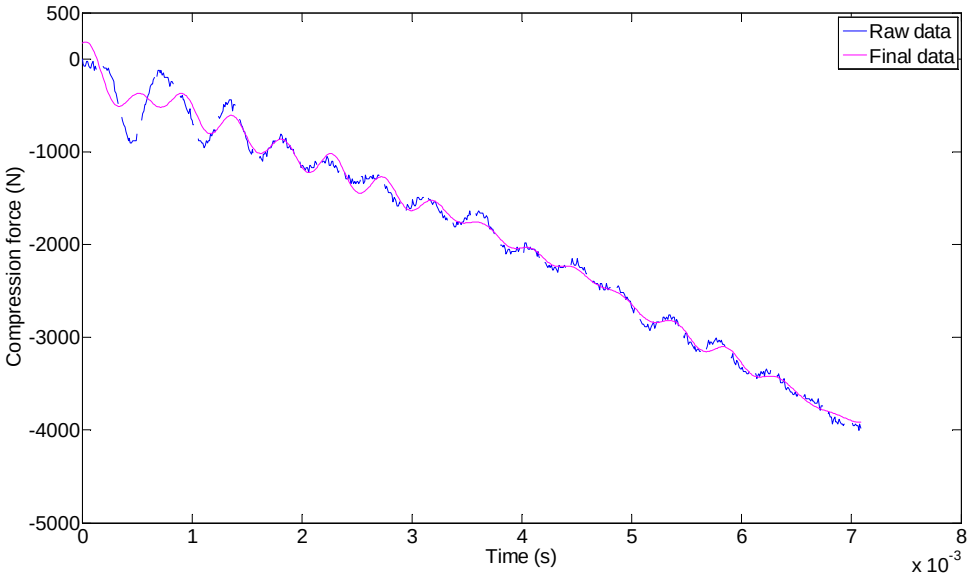

Fig. 4-27 0.92 g/cm^3 density raw and final force signals (SMALL sample).

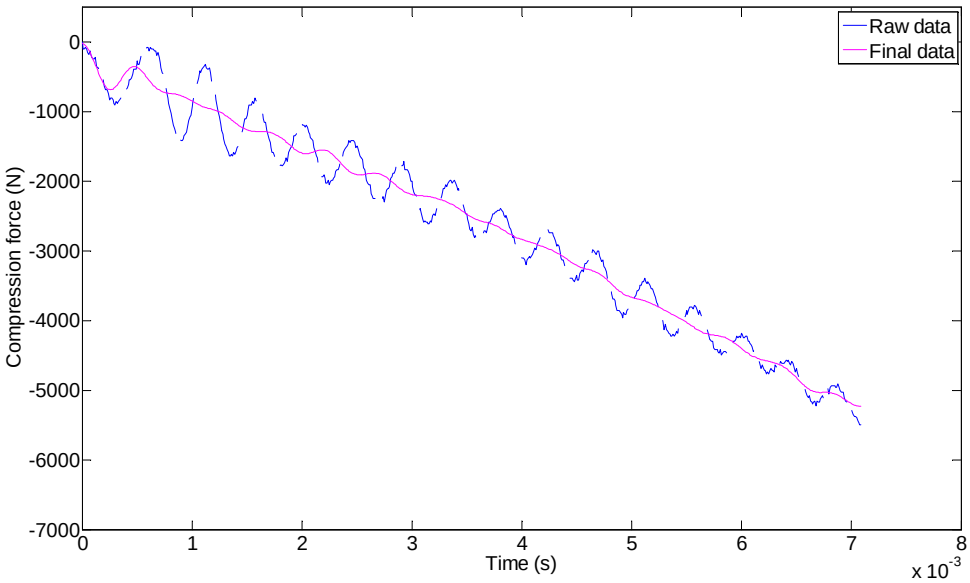

Fig. 4-28 0.99 g/cm^3 density raw and final force signals (SMALL sample).

4.6 DISCUSSION

This new procedure to eliminate ringing undulations from high speed material characterization tests in servo-hydraulic machines has evidenced to be effective. The distinctive key feature of the method is the description of the dynamic properties of the testing system by means of a modal model that considers the predominant vibration modes in the input-output behavior of the machine. This is an unexplored research area, as previous works in recent literature have considered simple one degree of freedom models, leading to errors when comparing simulated and experimental results.

The developed model is able to simulate the transient component of the force measured by the load cell when the material under test is excited impulsively. This component is subtracted from the experimental data reducing vibration amplitudes substantially, so a material curve suitable for a further filtering approach is obtained.

Therefore, the main contribution of this chapter is the development of a machine model that makes it possible to minimize ringing oscillations before data filtering, making this filtering step more effective compared to a direct application to the original test record.

5. CONSTITUTIVE EQUATION FOR THE MATERIAL

5.1 INTRODUCTION

As described in Chapter 3, samples of three blends of recycled rubber and LLDPE have been performed and high strain rate compression tests have been done over them. Experimental results have been corrected for the highest strain rate case in Chapter 4. In this chapter a consititutive equation that explains the behavior of this blend is selected and developed, i.e. Yang's model, presented in section 2.4. The six parameters of the model are adjusted; the first three hyperelastic parameters are fitted by least squares fitting strategy, while an optimization algorithm is applied to adjust the three viscoelastic parameters. This algorithm, called Particle Swarm Optimization (PSO), is explained in detail; it has been selected due to its simplicity, robustness and rapid convergence. It requires the adjustment of only a few parameters and is able to reach a global optimum even if the function to optimize is highly nonlinear[110]. It has been successfully applied in Control Engineering or Computer Science[111,112] and even in some areas of Material Science[113,114].

The algorithm is applied to 90/10 blends, in particular to big samples, for the strain rates 0.057, 0.57 and 5.7 s^{-1}. Thereafter, the Yang's model has been applied to the highest strain rate, that is, 57 s^{-1} and resulting theoretical curves are compared to the corrected curves derived from Chapter 4.

The chapter is organized as follows. First of all, Yang's model is developed in section 5.2. Particle Swarm (PSO) algorithm is introduced afterwards in section 5.3. Next, obtained results are shown in section 5.4. Finally, and due to the difficulty during the fitting process a theoretical study of the parameters is performed in order to obtain more information about the parameters, in section 5.5. The chapter ends with a brief discussion.

5.2 CHOICE OF THE YANG MODEL

Selected visco-hyperelastic constitutive model for this work is proposed by Yang et al.[66], as previously stated in Chapter 2. The model has been chosen because it describes with accuracy the behavior of rubber-like materials in a wide range of strain rates; the researchers' community has studied it fairly in detail[69, 81, 115-118]. First of all it is developed in 3D and thereafter it is applied to uniaxial compression case.

5.2.1 Presentation of the Yang model

The proposed material model consists of a combination of constitutive relationships with a hyperelastic component in parallel with a viscoelastic component. Concerning the hyperelastic part, Rivlin's form truncated to a series with three parameters is found to be adequate to describe this hyperelastic part of the material. Referring to the viscoelastic part, it is composed by K-BKZ model with Yang's modification, leading up to the Maxwell generalized model. It describes three-dimensional visco-hyperelastic large deformation behavior of incompressible rubber-like materials under high strain rates. The total stress is the sum of both components:

$$\sigma = \sigma^e + \sigma^v \tag{5.1}$$

Where σ^e characterizes the quasistatic hyperelastic properties and σ^v is the strain rate and strain history dependent response of the material. This model can be rheologically represented as an equilibrium spring parallel to a Maxwell element, that consists of an intermediate spring followed by a viscous damper[7], as shown in Fig. 5-1:

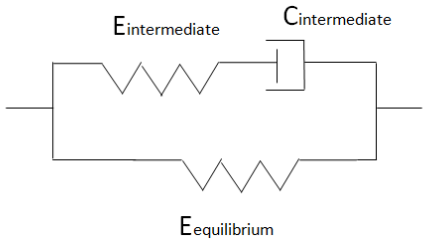

Fig. 5-1 Rheological model of the hyper-viscoelastic model

Both springs in the model are hyperelastic. The viscous damper allows the stress (or the force, at the end) in the intermediate spring to vary with the strain rate.

- When this strain rate is very slow, the damper is not activated and the deformation is governed only by the equilibrium spring;

- When the strain rate is very high, the damper has no time enough to deform and it is as a "rod", so the intermediate spring approaches its maximum value.

Between these two values for the strain rate, the material behaves rate dependent and it is explained by a visco-hyperelastic constitutive law.

The relationship between the Cauchy stress tensor and the left Cauchy-Green strain tensor for a hyperelastic material (see the Annex B for further details) is:

$$\sigma^e = 2\left(\frac{\partial \psi}{\partial I_1} + I_1 \frac{\partial \psi}{\partial I_2}\right) b - 2\frac{\partial \psi}{\partial I_2} b^2 - pI \tag{5.2}$$

Taking into account that the tests are in compression (high strain rate compression tests), last term is "$-pI$". And according to eq. (2.14), Rivlin's form with 3 parameters is:

$$\psi = C_{10}(I_1 - 3) + C_{01}(I_2 - 3) + C_{11}(I_1 - 3)(I_2 - 3) \tag{5.3}$$

Consider uniaxial loading of an incompressible and isotropic specimen. The principal stretches are $\lambda_1 = \lambda = 1 + \varepsilon_{11}$, in the loading direction (being ε_{11} the principal strain in the same direction) and, consequently, $\lambda_2 = \lambda_3 = \lambda^{-1/2}$. Therefore, in eq. (5.2):

$$\sigma_{11}^e = 2\frac{\partial \psi}{\partial I_1}\lambda^2 + 2\frac{\partial \psi}{\partial I_2}(I_1\lambda^2 - \lambda^4) - P \tag{5.4}$$

$$\sigma_{22}^{e} = 0 = \sigma_{33}^{e} \tag{5.5}$$

ψ is defined in eq. (5.3). Replacing:

$$\begin{aligned}\sigma_{11}^{e} &= 2\left[C_{10} + C_{11}\left(I_2 - 3\right)\right]\lambda^2 + 2\left[C_{01} + C_{11}\left(I_1 - 3\right)\right]\left(I_1\lambda^2 - \lambda^4\right) - P = \\ &= 2\lambda^2 C_{10} + 4\lambda C_{01} + C_{11}\left[2\lambda^2\left(I_2 - 3\right) + 4\lambda\left(I_1 - 3\right)\right] - P\end{aligned} \tag{5.6}$$

To extract P from this expression $\sigma_{22}^{e} = 0$ is used.

$$P = 2\lambda^{-1}C_{10} + 2\lambda^{-1}\left(I_2 - 3\right)C_{11} + 2\left(I_1\lambda^{-1} - \lambda^{-2}\right)C_{01} + 2\left(I_1 - 3\right)\left(I_1\lambda^{-1} - \lambda^{-2}\right)C_{11} \tag{5.7}$$

If eq. (5.7) is introduced in eq. (5.6), the final expression for the quasistatic stress is:

$$\sigma_{11}^{e} = 2(\lambda^2 - \lambda^{-1})C_{10} + 2(\lambda - \lambda^{-2})C_{01} + 6(\lambda^3 - \lambda^2 - \lambda + \lambda^{-1} + \lambda^{-2} - \lambda^{-3})C_{11} \tag{5.8}$$

Where C_{10}, C_{01} and C_{11} are parameters determined via one dimensional tests. Stretch and stress data from quasi static tests have been taken into account to be fitted to eq. (5.8). Here least square fitting is used with the objective of minimizing the relative error in the stress.

Regarding the viscoelastic properties, eq.(2.41) is taken as reference for the three dimensional case. Here, the matrix functional $\Omega_{\tau=-\infty}^{t}\left\{C(\tau)\right\}$ describes the effect of the strain history on the stress. As it is difficult to obtain, some approximations have been done by Lockett[84] and Yang et al.[66,67]. For hyperelastic materials as stress for the intermediate spring they have considered[7]:

$$\sigma^{v} = F\frac{\partial \psi}{\partial E}F^{T} \tag{5.9}$$

This $\frac{\partial \psi}{\partial E} = S$ can be assumed as:

$$\frac{\partial \psi}{\partial E} = \int_{-\infty}^{t} \frac{\partial u}{\partial E}(I_1, I_2, I_3, t-\tau)d\tau \tag{5.10}$$

The kernel function $u\left(I_1, I_2, I_3, t-\tau\right)$ can be expressed as a multiplicative function with a part depending on the deformation and another part depending on time:

$$u\left(I_1, I_2, I_3, t-\tau\right) = U(I_1, I_2, I_3) \cdot m(t-\tau) \tag{5.11}$$

Here $m(t-\tau)$ is a memory function, a relaxation function decreasing with t; in general, it is considered as an exponential series called Prony series:

$$m(t-\tau) = \sum_{i=1}^{N} m_i \cdot \exp\left(-\frac{t-\tau}{\theta_i}\right) \tag{5.12}$$

Where:

- m_i are weighting factors complying $\sum_{i=1}^{N} m_i = 1$

- θ_i are relaxation times.

By introducing eq. (5.10) into eq.(5.9), one reaches:

$$\sigma^v = F(t) \cdot \int_{-\infty}^{t} \left(\frac{\partial U}{\partial E}\left(I_1, I_2, I_3\right) \cdot m(t-\tau) \right) d\tau \cdot F^T(t) \tag{5.13}$$

Yang's contribution to this model comes from the definition of U as follows:

$$U\left(I_1, I_2, I_3\right) = \phi\left(I_1, I_2, I_3\right) \cdot \dot{E}(\lambda) \tag{5.14}$$

Where the function ϕ is defined as:

$$\phi(I_1, I_2) = C_2 + C_3(I_2 - 3) \tag{5.15}$$

The effect of strain history on stress has been considered assuming only one relaxation time constant (N = 1) in eq. (5.12). This assumption is in accordance with Yang et al.[66], and meets the objective of formulating a material model which minimizes the number of required parameters without significantly compromising correlation with experimental data. Yang et al. performed a study of the range of strain rates which can be described by the generalized Maxwell model in their research work and they concluded that the relationship between stress and strain rate associated with the dashpot is assumed to be proportional to the n^{th} root of the strain rate. Thus, such a model could be used to get a larger range of strain-rates.

The resultant viscoelastic uniaxial response is given by:

$$\sigma_{11}^{v} = \lambda^2 \int_0^t \dot{\lambda}[C_2 + C_3(I_2(\tau) - 3)] \exp\left(-\frac{t-\tau}{C_4}\right) \dot{\lambda} d\tau + \\ + \frac{1}{2}\lambda^{-1} \int_0^t \dot{\lambda}^{-2}[C_2 + C_3(I_2(\tau) - 3)] \exp\left(-\frac{t-\tau}{C_4}\right) \dot{\lambda} d\tau \tag{5.16}$$

Where I_2 is the second deformation invariant,

$$I_2 = \frac{1}{2}\left[I_1^2 - \mathrm{tr}(B^2)\right] = \lambda^{-2} + 2\lambda \tag{5.17}$$

And B is the left Cauchy-Green deformation tensor, defined by:

$$b = \begin{bmatrix} \lambda^2 & 0 & 0 \\ 0 & \lambda^{-1} & 0 \\ 0 & 0 & \lambda^{-1} \end{bmatrix} \tag{5.18}$$

The standard least squares approximation is difficult to implement in the viscoelastic part; the difficulty lies in the determination of the convolution integral[120]. The algorithm defined here is based on nonlinear multi-fitting procedures, as Doman[119] stated and it is relatively easy to implement; in the present study it has been done in Matlab.

The three viscoelastic parameters (C_2, C_3 and C_4) involved in eq. (5.16) have been adjusted following the PSO approach. The development of the fitting algorithm is described in the following section.

The viscoelastic behavior described by this formulation is analogous to the generalized Maxwell model, which considers a viscous damper and an elastic spring connected in series. The strain dependent spring non-linear modulus $E = C_2 + C_3(I_2 - 3)$, and dashpot viscosity $\eta = E \cdot C_4$ define the relaxation time constant of the model C_4.

The complete constitutive equation results as the sum of eq. (5.8) and eq.(5.16):

$$\sigma_{11} = 2(\lambda^2 - \lambda^{-1})C_{10} + 2(\lambda - \lambda^{-2})C_{01} + 6(\lambda^3 - \lambda^2 - \lambda + \lambda^{-1} + \lambda^{-2} - \lambda^{-3})C_{11} + \\ + \lambda^2 \int_0^t \dot{\lambda}[C_2 + C_3(I_2(\tau) - 3)] \exp\left(-\frac{t-\tau}{C_4}\right) \dot{\lambda} d\tau + \\ + \frac{1}{2}\lambda^{-1} \int_0^t \dot{\lambda}^{-2}[C_2 + C_3(I_2(\tau) - 3)] \exp\left(-\frac{t-\tau}{C_4}\right) \dot{\lambda} d\tau \tag{5.19}$$

5.3 FITTING STRATEGY

The parameters C_{10}, C_{01} and C_{11} are determined by least square fitting as stated in the previous section. The three viscoelastic parameters (C_2, C_3 and C_4), on the other hand, have been adjusted following the PSO algorithm. The development of the fitting algorithm is described now, for 90/10 blend and big samples.

5.3.1 The PSO method

5.2.1.1 Background of the algorithm

PSO is a stochastic optimization technique based on the movement and intelligence of swarms. It has been developed in 1995 by James Kennedy and Russell Eberhart, with the aim of optimizing continuous nonlinear functions. The method has its origin in two main methodologies: on the one hand, artificial life in general and bird flocking and fish schooling in particular; and on the other hand, evolutionary computation, and linked to genetic algorithms. It is not computationally expensive, nor in memory requirements, neither in time consuming[110].

In a PSO the objective is to achieve the minimum value of a given cost function. Usually, this kind of algorithm ensures that its value is improved along the iterations. So the objective can be defined as follows:

$$Cost = f(\vec{p}) \tag{5.20}$$

$$\vec{p} = (p_1, p_2, \ldots, p_n) \tag{5.21}$$

$$\vec{p}_{optim} = Argmin_{\vec{p}} f(\vec{p}) \tag{5.22}$$

The parameters introduced in the equations are defined in Table 5-1.

The proposed optimization algorithm defines N particles constituting a swarm moving around in the search space and each k particle has its own position vector $\vec{p}_k$. The components of the positions of the particles are the parameters to be fitted. So each particle has a $c(\vec{p}_k)$ cost associated to its position. The optimization of the cost function is achieved when the particles move along the parameter space looking for the best solution with the following equations of motion:

$$\overrightarrow{v_k}(t_{n+1}) = w \cdot \overrightarrow{v_k}(t_n) + f_p \cdot r_p \cdot \left(\vec{p}_{k,opt} - \vec{p}_k(t_n)\right) + f_g \cdot r_g \cdot \left(\vec{p}_{globalopt} - \vec{p}_k(t_n)\right) \quad (5.23)$$

$$\vec{p}_k(t_{n+1}) = \vec{p}_k(t_n) + \overrightarrow{v_k}(t_n) \quad (5.24)$$

t_{n+1} and t_n are the actual and the previous iteration times. These two equations are applied several times or iterations.

Concerning the inertia weight coefficient from eq. (5.23), an inertia weight with nonlinear decreasing with concave function has been considered according to Zheng et al.[114], as follows:

$$w = (w_{max} - w_{min})\frac{k^2}{k_{max}^2} + (w_{min} - w_{max})\frac{2k}{k_{max}} + w_{max} \quad (5.25)$$

Where w_{max} and w_{min} are the maximal and minimal inertia weights respectively and k_{max} is the maximal iteration number. A large inertia weight facilitates a global search, while a small inertia weight facilitates a local search[112].

Table 5-1 Parameters of a PSO algorithm

Parameter	Definition	Value or value range
r_p	The attraction strength to the optimal position achieved by the k-th particle	A uniform random value between 0 and 1. This value is calculated at each iteration
r_g	The attraction strength to the global optimal position achieved by all particles	A uniform random value between 0 and 1. This value is calculated at each iteration
f_p	This acceleration coefficient gives more importance to the convergence to each particle optimal position	It is a positive constant value
f_g	This acceleration coefficient gives more importance to the convergence to the global optimal position	It is a positive constant value
w	The inertia of the particles	It is a positive value
$\vec{p}_k(t_n)$	The parameter position of the k^{th} particle at t_n instant	It is initialized into a possible parameter range region in a stochastic way
$\overrightarrow{v_k}(t_n)$	The parameter velocity of the k^{th} particle at t_n instant	It is initialized into small random values
$\vec{p}_{k,optim}$	The best/optimum parameter position of the k^{th} particle	It is initialized into the initial positions of particles
$\vec{p}_{globalopt}$	The best/optimum parameter position of all particles	It is initialized into the best positions of all particles

The classical definition of the determination coefficient R^2 has been applied to measure the accuracy of the fitting algorithm to the experimental data; based on this, the global error GE is defined by the next relation,

$$GE = \frac{\sum_{i=0}^{M-1}\left[\hat{\sigma}_n\left(i\Delta t, C_2, C_3, C_4\right) - \sigma_n(i\Delta t)\right]^2}{\sum_{i=0}^{M-1}\left[\overline{\sigma}_n - \sigma_n(i\Delta t)\right]^2} \tag{5.26}$$

Where M is the number of data points involved in the fitting, Δt is the time step, σ_n is the experimental value of stress at each stretch point, $\hat{\sigma}_n$ is the calculated stress via the constitutive equation and $\overline{\sigma}_n$ is the average of the experimental stress. As the estimated values approach the experimental values, GE approaches 0. The extension of previous equation for multiple curves gives:

$$GE_{total} = \sum GE_N \tag{5.27}$$

Where *N* is the number of curves to be fitted, i.e. the curves corresponding to different strain rates. The coefficient of determination for the simultaneous fitting of several curves has been obtained by subtracting GE_{total} from the number of curves and then dividing by the number of curves[122]. The optimization problem to solve is the minimization of error; this is, to minimize the objective function ($1\text{-}R^2$) towards zero by varying the input parameters:

$$Error = \left(1 - R^2\right) = \frac{GE_{total}}{N} \tag{5.28}$$

The basic optimization sequence is as follows:

1. Given stretch, time and the material constants, determine the stress values $\hat{\sigma}_n$. The initial values of C2, C3 and C4 are taken from the literature. Mean experimental stress is also calculated for all tests at each strain-rate ($\overline{\sigma}_n$). Set the maximum number of iterations.

2. Calculate the objective function by means of eq. (5.28).

3. Using the material constants from previous iterations and comparing the current and previous values of the objective function, predict the new coefficients which will minimize the objective function.

In other words, if the current cost function of each particle, $c(\vec{p}_k)$, is better than the particle's best position, $\vec{p}_{k,opt}$, this cost function will replace $\vec{p}_{k,opt}$ and the current position replaces the particles' best position.

Particles best position, $\vec{p}_{k,opt}$, is compared to all the particles best position, $\vec{p}_{globalopt}$. If the current $\vec{p}_{k,opt}$ is better than $\vec{p}_{globalopt}$, then it replaces the global best position and the current position replaces the particles' best position.

4. Repeat until the maximum number of iterations is reached.

Each particle has its best solution (fitness) at each iteration called personal best, **pbest**; and the best solution of all the particles at each iteration is called the global best, **gbest**. These two values are shown in the flow chart in the Fig. 5-2:

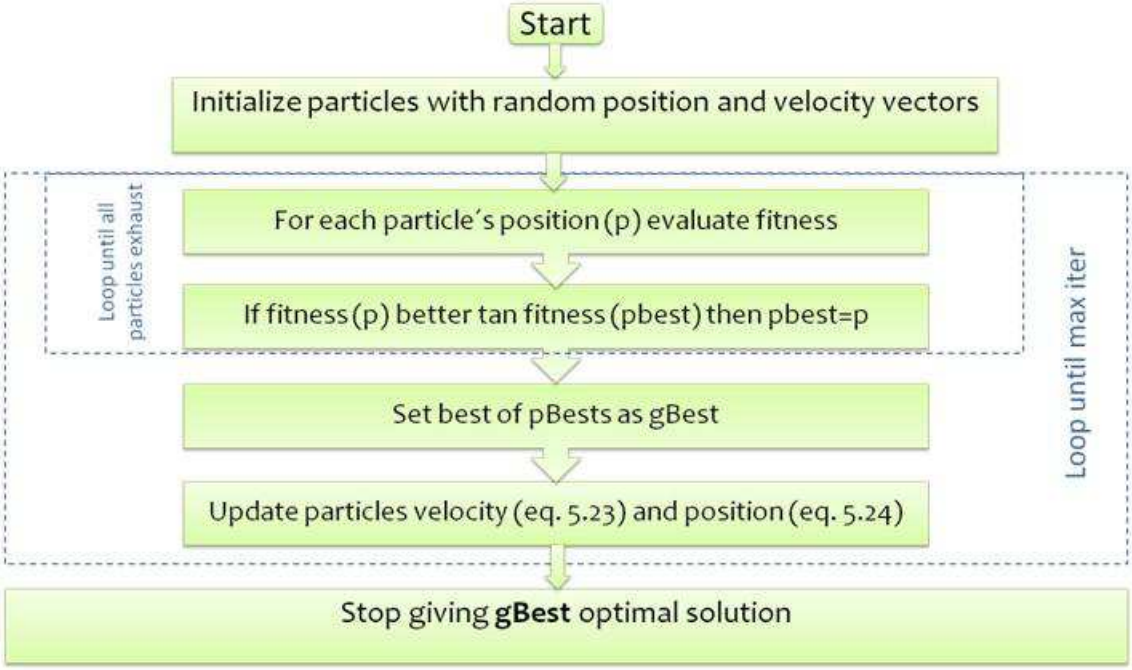

Fig. 5-2 Flow chart of the PSO algorithm

5.2.1.2. Advantages of the algorithm

One of the main advantages of this algorithm is that there are almost no restrictions over the cost function. Even though it is true that the results of this technique are sensitive to

the initial parameter estimations, the solution is continuously improving (it is always better than in the previous iteration); this is not so with the gradient descent algorithm.

All particles in PSO are kept as members of the population through the course of the run. Values calculated in previous iterations are reused in a more direct way than with genetic algorithms.

5.3.2 Application of the PSO to Yang's model (hyperelastic with least squares)

The hyperelastic parameters C_{10}, C_{01} and C_{11} of the proposed model have been fitted to the experimental data by means of a least-squares approximation; this way the relative error in the nominal stress has been minimized. The experimental data corresponding to the slowest strain rate ($0.057s^{-1}$), the one considered as quasistatic, has been used. It has been assumed that the material is fully incompressible to obtain these hyperelastic parameters.

Hence, the relative error that has to be minimized is given in eq. (5.29):

$$relative\_error = \sum_{i=1}^{N} \left(\frac{\sigma_i^{theoretical} - \sigma_i^{experimental}}{\sigma_i^{experimental}} \right)^2 \tag{5.29}$$

Where $\sigma_i^{theoretical}$ corresponds to the theoretical stress from eq. (5.8) and $\sigma_i^{experimental}$ is referred to the experimentally measured stress.

With regard to the viscoelastic parameters, values appearing in the literature for rubber-like materials[66] have been taken as initial guesses for the parameters C_2, C_3 and C_4. These parameters have been fitted by previously explained nonlinear multi-fitting PSO algorithm, being the components of the position vectors of the particles. According to the analogy of the proposed model with the generalized Maxwell model, described in section 5.2, C_2, C_3 and C_4 must necessarily be positive to provide a positive value for E. These requirements give physical sense to the model.

5.4 RESULTS

5.4.1 Strain rates 0.057, 0.57 and 5.7 s^{-1} (all except the highest one)

5.3.2.1. Application of the PSO to Yang's model. Obtaining model parameters

PSO has been applied to the blend proportion of 90/10, and big samples. Next, the obtention of the parameters is divided in hyperelastic and viscoelastic subsections, as the first ones are obtained by means of least squares and PSO is only applied to the viscoelastic ones[123].

a) Hyperelastic parameters

The hyperelastic coefficients corresponding to a blend of 90/10 proportion and 0.9 g/cm^3 density are shown in Table 5-2, along with the coefficient of determination R^2 for the curve fittings. The experimental curves corresponding to the slowest strain rate, that is, strain rate 0.057 s^{-1}, are considered here, as the quasi-static ones.

Table 5-2 Hyperelastic coefficients and coefficient of determination

	C_{01} (Mpa)	C_{10} (Mpa)	C_{11} (Mpa)	R^2
0.92A_0.057	-1,56	2,8	0,24	0,9946
0.93A_0.057	-1,52	2,7	0,23	0,9927

Fig. 5-3 shows the experimental and estimated stress-stretch curves for density 0.9 g/cm^3, where it is possible to appreciate the non-linear elastic material response and the good correspondence of the proposed model's hyperelastic part with the experimental data. These results show that the deviations of the predicted curves from the experimental ones are lower than 1%.

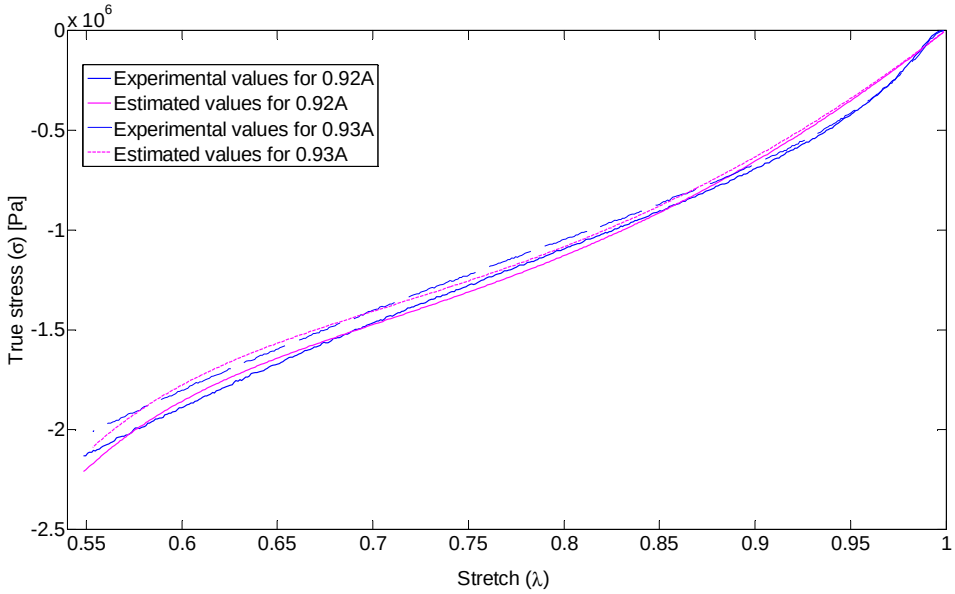

Fig. 5-3 Quasistatic stress-stretch curves vs. hyperelastic component of the theoretical model for 0.9 g/cm^3 density

Regarding the tests for the other densities, the comparison between the model and the quasistatic experimental results are shown in Fig. 5-4, Fig. 5-5 and Fig. 5-6:

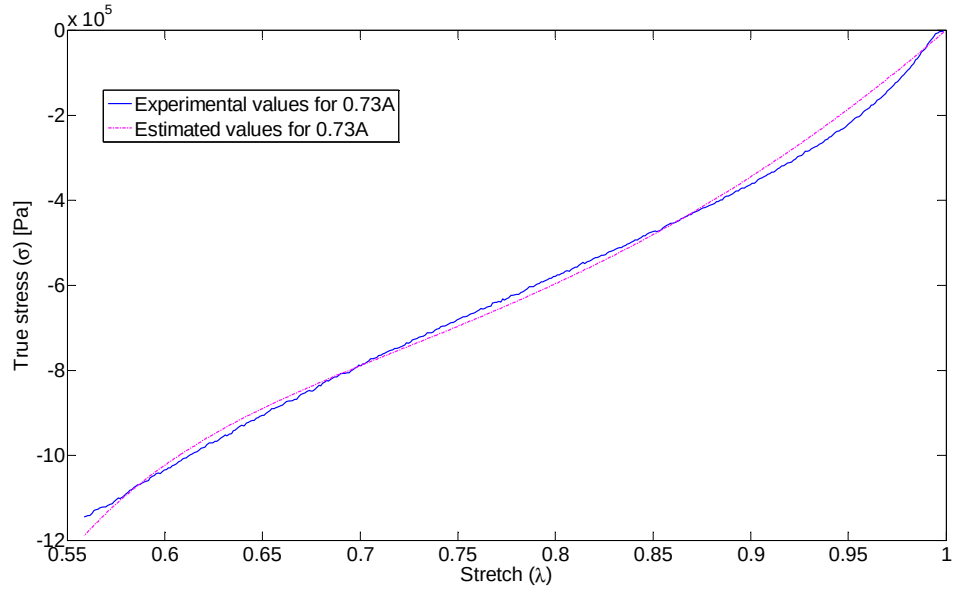

Fig. 5-4 Quasistatic stress-stretch curves vs. hyperelastic component of the theoretical model for 0.7 g/cm^3 density

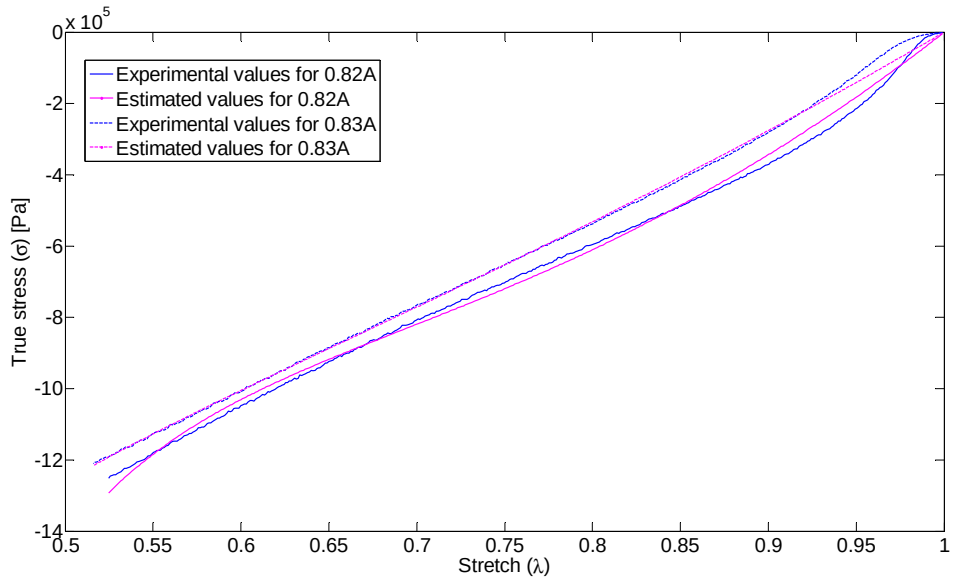

Fig. 5-5 Quasistatic stress-stretch curves vs. hyperelastic component of the theoretical model for 0.8 g/cm^3 density

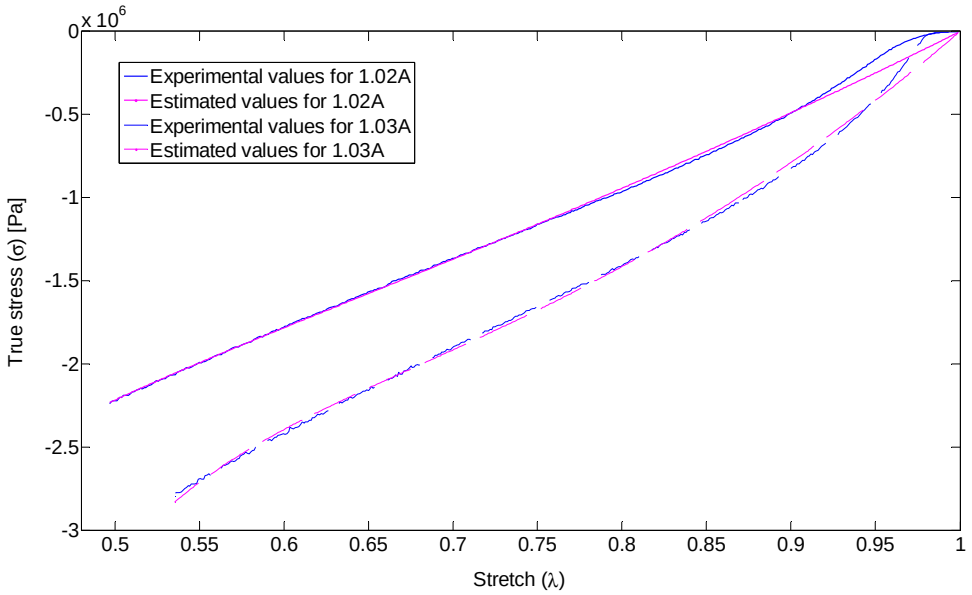

Fig. 5-6 Quasistatic stress-stretch curves vs. hyperelastic component of the theoretical model for 1 g/cm^3 density

b) Viscoelastic parameters

Fig. 5-7 represents the searching space, i.e., the rank of possible values for the three parameters for the 0.9 g/cm^3 density, where the different points at each iteration are shown. These points are triads composed of different values of C_2, C_3 and C_4, as explained in Section 5.3.1. At the beginning of the iterative process the searching space is wide. For subsequent iterations this space becomes narrower, the cost function reduces its value and most points converge towards the optimal position of the triad.

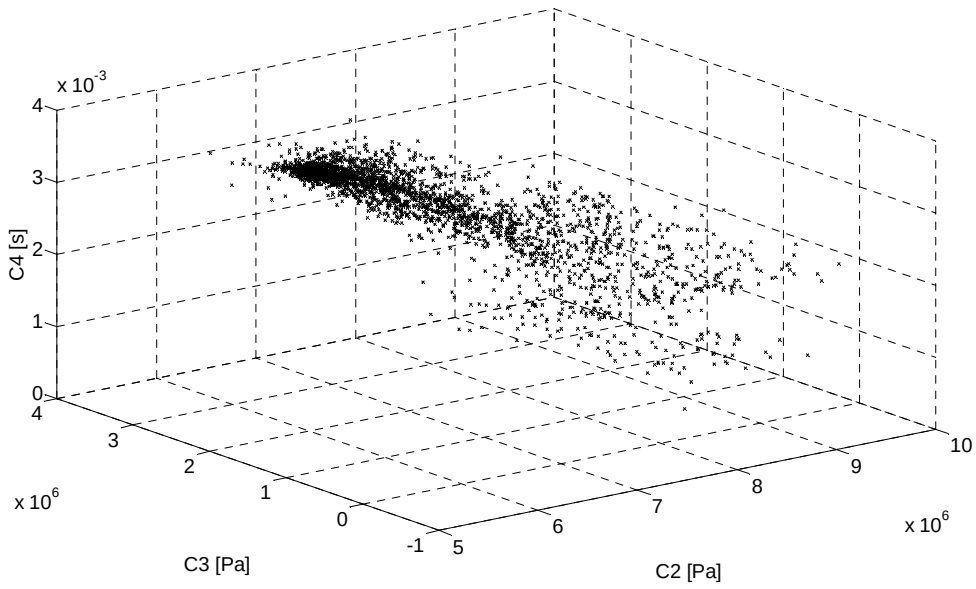

Fig. 5-7 Different values for the viscoelastic parameters along the PSO until it converges to the optimal trio (case of 0.9 g/cm^3)

Fig. 5-8, Fig. 5-9 and Fig. 5-10 show the (1-R^2) cost-function or error along the iterations of the algorithm compared to the parameters C_2, C_3 and C_4 (case of 0.9 g/cm^3). It can be observed how the values of the cost-function decrease at each iteration in the search space as the parameters reach their optimum value; that is, the points that are dispersed in the beginning, converge to a point along the iterations. This point in each graph is the optimal value of the corresponding parameter, as can be seen in Table 5-3. The values obtained for R^2 are also shown in Table 5-3.

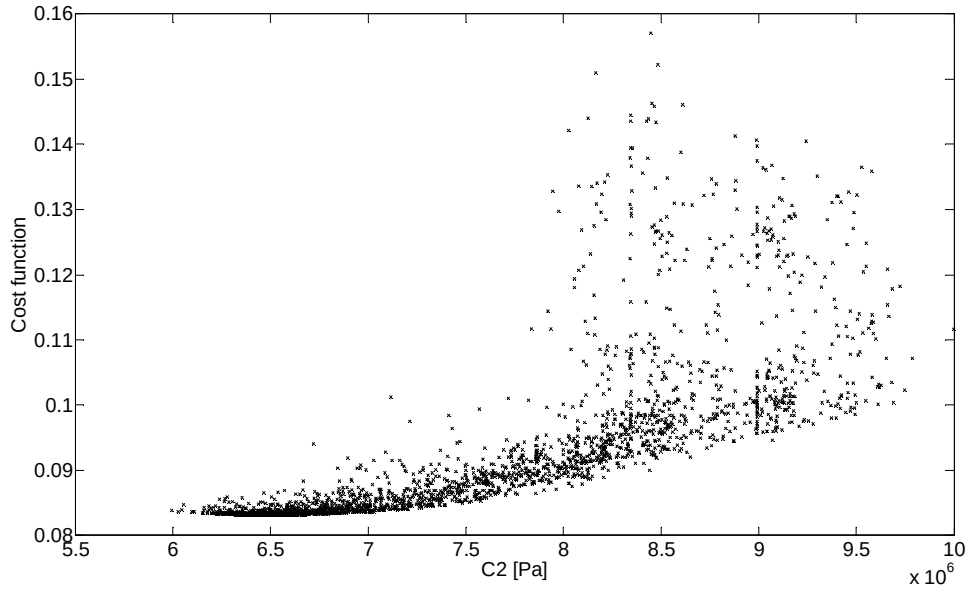

Fig. 5-8 Cost function ($1-R^2$) vs. C_2

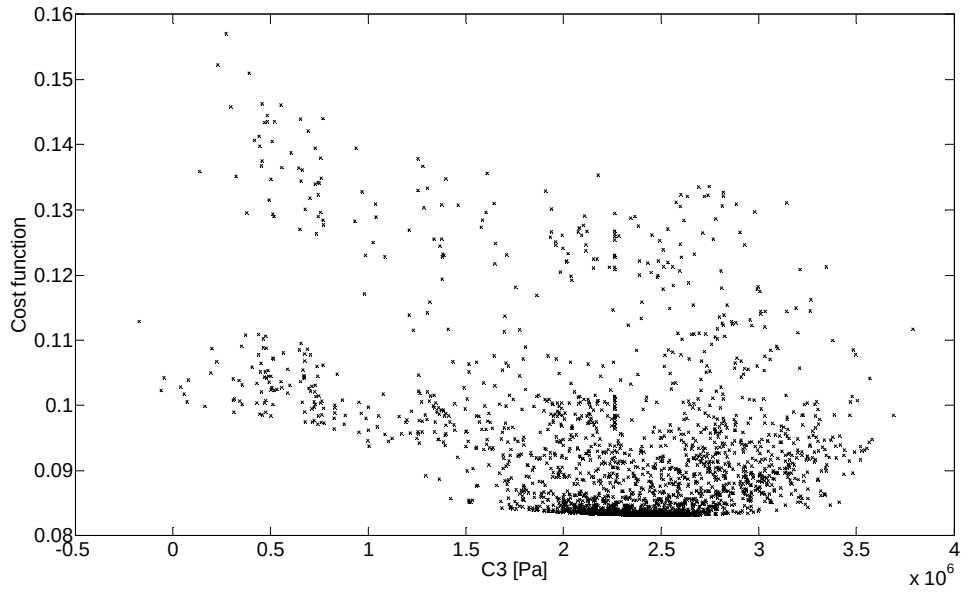

Fig. 5-9 Cost function ($1-R^2$) vs. C_3

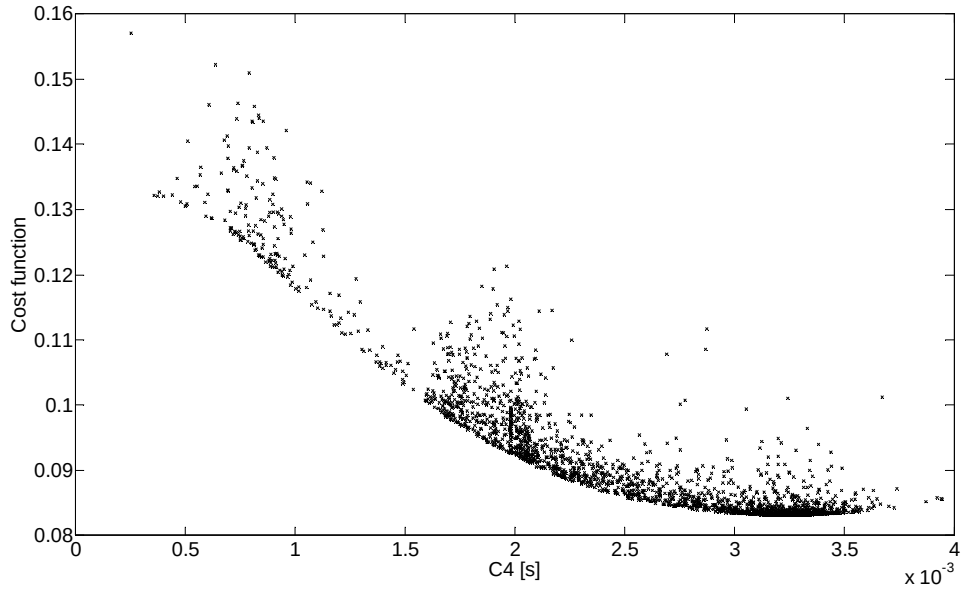

Fig. 5-10 Cost function ($1-R^2$) vs. C_4

Table 5-3 Values for viscoelastic parameters and R^2 for different curves (case of 0.9 g/cm^3)

Parameter	Value
C2 [Pa]	6,5117E+06
C3 [Pa]	2,5077E+06
C4 [s]	3,2202E-03
Cost function	0,08317
R2_0,57 (a)	0,9954
R2_0,57 (b)	0,9905
R2_5,7 (a)	0,9701
R2_5,7 (b)	0,9608

The comparison between theoretical curves and test data is shown in Fig. 5-11; it shows experimental data for strain rates 0.57s^{-1} and 5.7s^{-1}, compared to the proposed model.

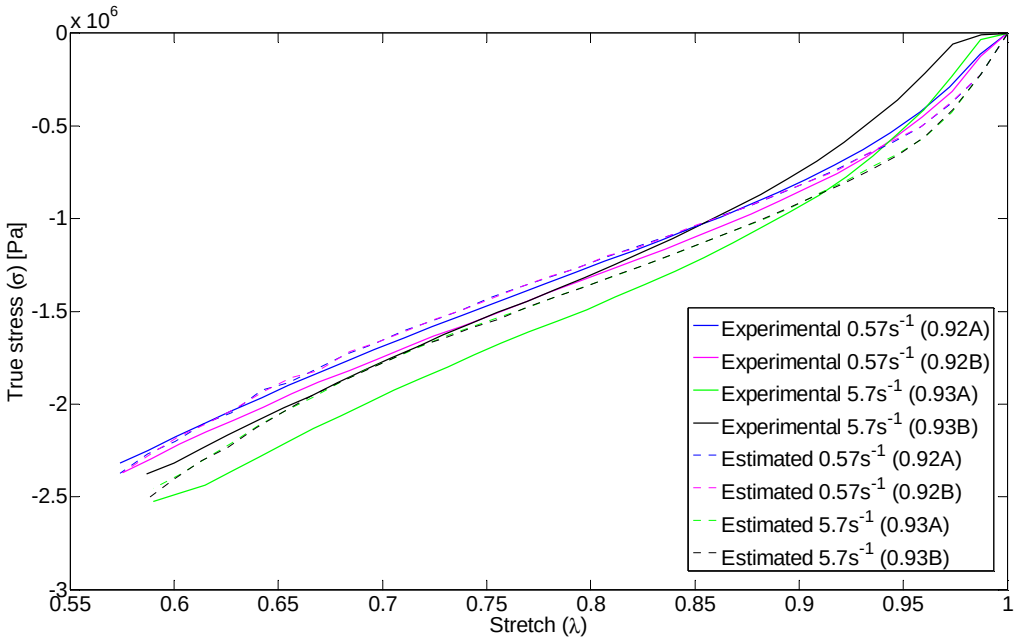

Fig. 5-11 Comparison between the experimental data and the theoretical curves for 0.9 g/cm^3

It can be appreciated that the stretch range between 1 and 0.9 encompasses the test phase during which the initial gaps of the specimen are closing, during the first stages of the experimental data; this first part of the test is therefore omitted when considering model adjustment to the test data. Consequently, the model fits quite well with its homologous experimental data; the deviations of the predicted curves from the experimental ones are around 10% in the worst section.

As far as the PSO optimization algorithm is concerned, even though it is true that the results of this technique are sensitive to the initial parameter guesses, it converges adequately towards final results that show good correlation to their experimental counterpart.

Finally, the comparison between theoretical curves and test data corresponding to densities of 0.7 g·cm^{-3}, 0.8 g·cm^{-3} and 1 g·cm^{-3} are graphically introduced below in Fig. 5-12, Fig. 5-13 and Fig. 5-14:

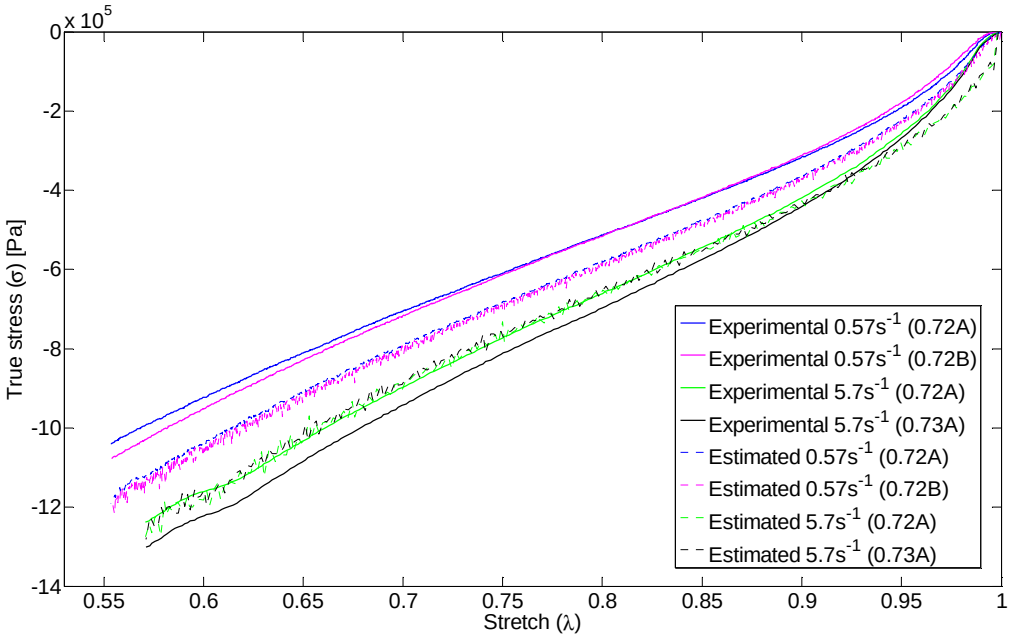

Fig. 5-12 Comparison between the experimental data and the theoretical curves for 0.7 g/cm³

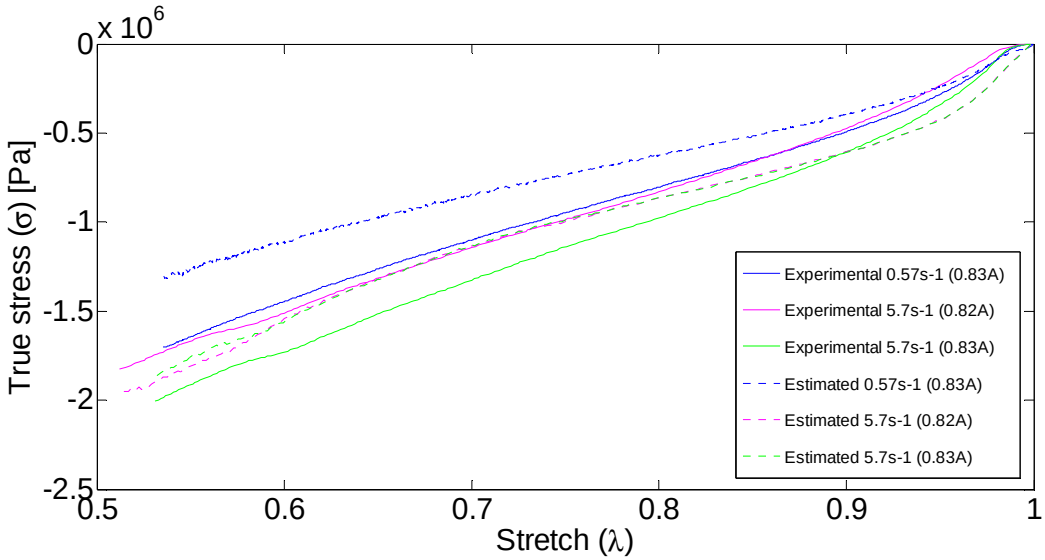

Fig. 5-13 Comparison between the experimental data and the theoretical curves for 0.8 g/cm³

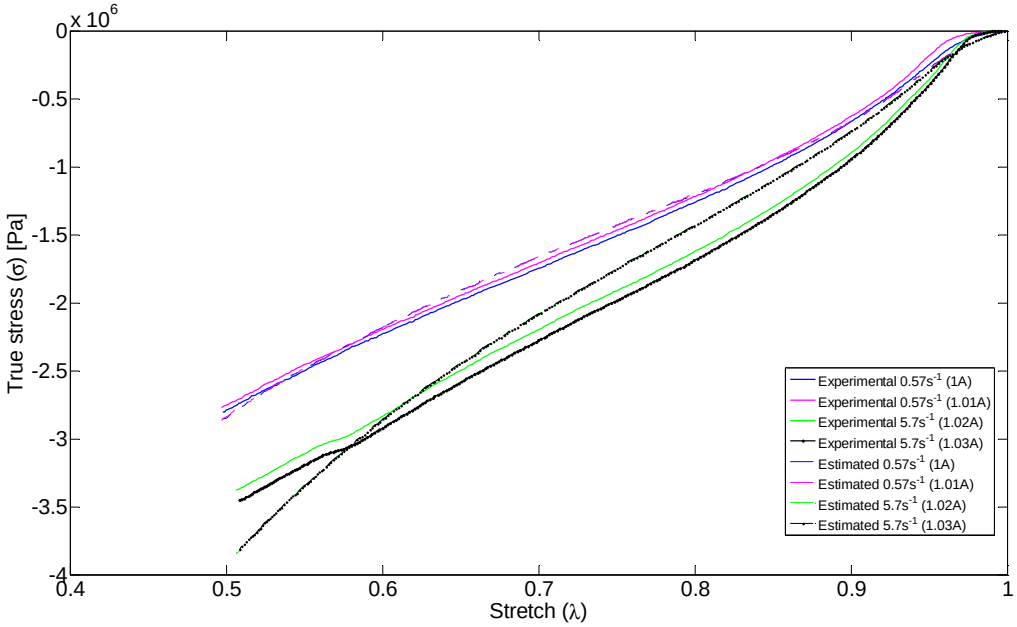

Fig. 5-14 Comparison between the experimental data and the theoretical curves for 1 g/cm^3

5.4.2 57 s^{-1} strain rate (highest one)

5.3.3.1. Application of the Yang's model to the corrected curves. Viscoelastic parameters obtained from the PSO

PSO algorithm has been applied to the corrected highest strain rates, to the blend 90/10 (and the big samples), that is, previously obtained parameters have been used in the theoretical model applied to high strain rate. The comparison between experimental data with the Yang's model predicted data for the different densities is shown next in Fig. 5-15, Fig. 5-16, Fig. 5-17 and Fig. 5-18. Stress-stretch curves predicted by the model show that it is well-suited for the description of visco-hyperelastic behavior of this blend, even at the highest strain rate.

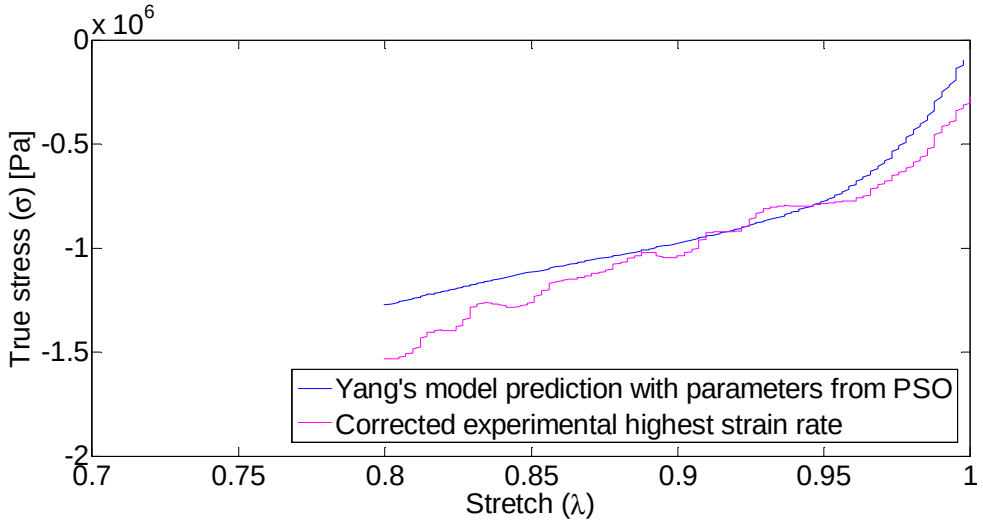

Fig. 5-15 Application of Yang's model to the highest strain rate with 0.7 g/cm^3 density

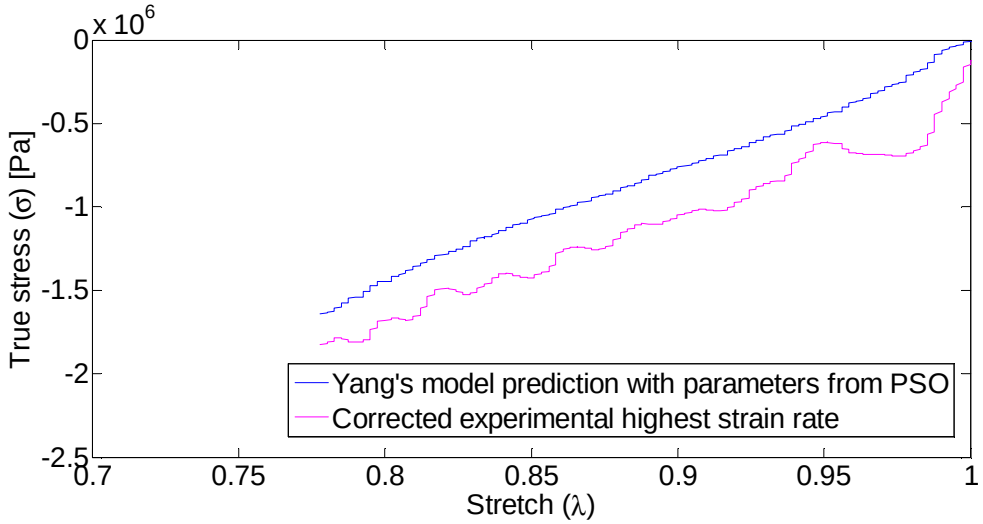

Fig. 5-16 Application of Yang's model to the highest strain rate with 0.8 g/cm^3 density

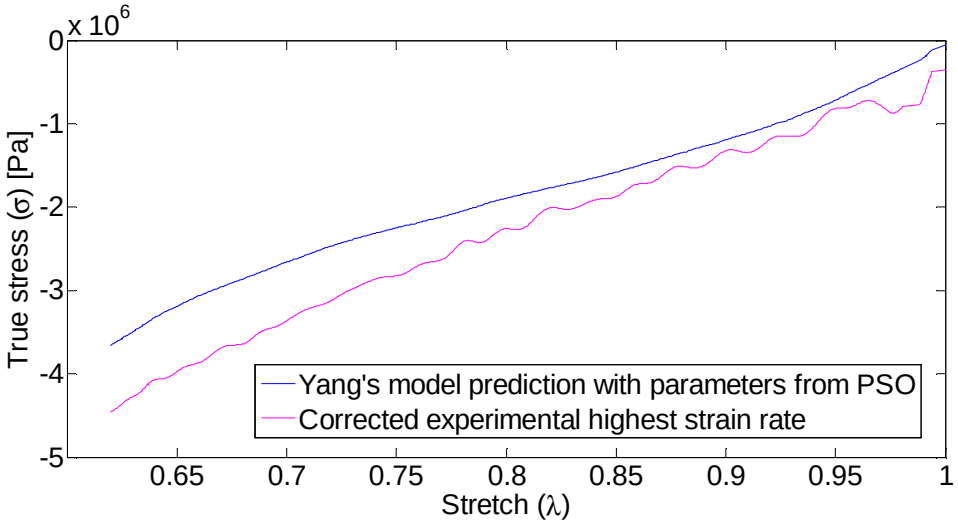

Fig. 5-17 Application of Yang's model to the highest strain rate with 0.9 g/cm^3 density

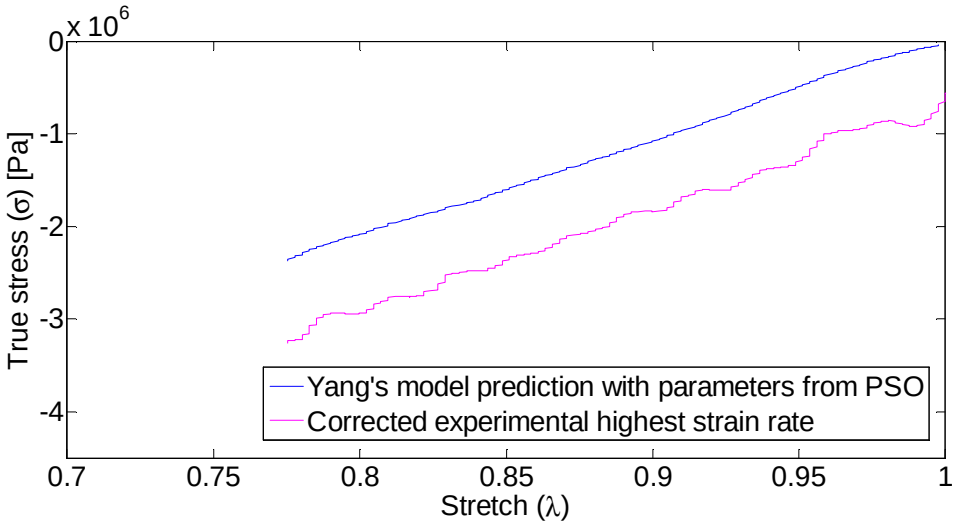

Fig. 5-18 Application of Yang's model to the highest strain rate with 1 g/cm^3 density

5.5 THEORETICAL STUDY OF THE MODEL: INFLUENCE OF EACH PARAMETER

Mean squared error (MSE), J, is considered here as the measure of the average of the squares of the errors that appear when considering the estimated Yang's model $f(p,t)$

instead of the real experimental data σ_{11}, that is, the difference between the estimator and what is estimated.

$$J = \frac{1}{2}\int \left(\sigma_{11} - f(p,t)\right)^2 dt \tag{5.30}$$

Where *p* represents the parameters of the model.

The optimization algorithm defined in Section 5.3 calculates the derivative of J over the parameters $\frac{dJ}{dp}$; therefore, each iteration is calculated as:

$$\hat{p}_{k+1} = \hat{p}_k - \alpha \frac{\partial J}{\partial p} \tag{5.31}$$

Relating eq. (5.30) and eq.(5.31):

$$\begin{aligned} \hat{p}_{k+1} &= \hat{p}_k - \alpha 2 \frac{1}{2}\int \left(\sigma_{11} - f(p,t)\right)\left(-\frac{\partial f}{\partial p}\right)_{dt} dt = \\ &= \hat{p}_k + \alpha \int \left(\sigma_{11} - f(p,t)\right)\frac{\partial f}{\partial p} dt \end{aligned} \tag{5.32}$$

First term inside the integral represents the error $e = \sigma_{11} - f(p,t)$ and the second term, $\frac{\partial f}{\partial p}$, is the sensitive function; in this case, $f(p,t) = \sigma_{Yang}$. This integral represents the scalar product between these two terms:

$$< e, \frac{\partial f}{\partial p} >= \int e \frac{\partial f}{\partial p} dt = \|e\| \left\| \frac{\partial f}{\partial p} \right\| \cos\varphi \tag{5.33}$$

It can be appreciated that the error influences over each iteration, but also the sensitive function does; that is, the algorithm tends to minimize the error value. And the more the parameters influence the function, the more the algorithm takes into account the information that could produce a more accurate estimate.

If eq. (5.19) is considered,

$$\frac{\partial \sigma_{Yang}}{\partial p} = \frac{\partial \sigma_{Hyper}}{\partial p} + \frac{\partial \sigma_{Visco}}{\partial p} \tag{5.34}$$

Next, the derivatives over the hyperelastic parameters are done, taking into account that they do not appear in the viscoelastic part of the model:

$$\frac{\partial \sigma_{Yang}}{\partial C_{10}} = \frac{\partial \sigma_{Hyper}}{\partial C_{10}} = 2(\lambda^2 - \lambda^{-1}) \tag{5.35}$$

$$\frac{\partial \sigma_{Yang}}{\partial C_{01}} = \frac{\partial \sigma_{Hyper}}{\partial C_{01}} = 2(\lambda - \lambda^{-2}) \tag{5.36}$$

$$\frac{\partial \sigma_{Yang}}{\partial C_{11}} = \frac{\partial \sigma_{Hyper}}{\partial C_{11}} = 6(\lambda^3 - \lambda^2 - \lambda + \lambda^{-1} + \lambda^{-2} - \lambda^{-3}) \tag{5.37}$$

Concerning the viscoelastic part, which contains two integrals; this can be formulated as follows:

$$\sigma_{Visco} = \lambda^2 s_1 + \frac{1}{2}\lambda^{-1} s_2 \tag{5.38}$$

Where:

$$s_1 = \int_0^t \lambda[C_2 + C_3(I_2 - 3)]e^{-\frac{t-\tau}{C_4}}\dot{\lambda}d\tau \tag{5.39}$$

$$s_2 = \int_0^t \lambda^{-2}[C_2 + C_3(I_2 - 3)]e^{-\frac{t-\tau}{C_4}}\dot{\lambda}d\tau \tag{5.40}$$

Taking into account Laplace Transform and doing the time derivatives of s_1 and s_2,

$$\dot{s}_1 = -\frac{1}{c_4}s_1 + g_1 \tag{5.41}$$

$$\dot{s}_2 = -\frac{1}{c_4}s_2 + g_2 \tag{5.42}$$

Where:

$$g_1 = \lambda[C_2 + C_3(I_2 - 3)]\dot{\lambda} \tag{5.43}$$

$$g_2 = \lambda^{-2}[C_2 + C_3(I_2 - 3)]\dot{\lambda} \tag{5.44}$$

The derivatives over the viscoelastic parameters are done as follows, taking into account that they do not appear in the hyperelastic part of the model:

$$\frac{\partial \sigma_{Visco}}{\partial p} = \lambda^2 \frac{\partial s_1}{\partial p} + \frac{1}{2}\lambda^{-1}\frac{\partial s_2}{\partial p} \tag{5.45}$$

$$\frac{d}{dt}\left(\frac{\partial s_1}{\partial p}\right) = -\frac{1}{c_4}\frac{\partial s_1}{\partial p} + \frac{\partial g_1}{\partial p} \tag{5.46}$$

$$\frac{d}{dt}\left(\frac{\partial s_2}{\partial p}\right) = -\frac{1}{c_4}\frac{\partial s_2}{\partial p} + \frac{\partial g_2}{\partial p} \tag{5.47}$$

Particularizing for C_2, C_3 and C_4:

$$\frac{\partial \sigma_{Yang}}{\partial C_2} = \frac{\partial \sigma_{Visco}}{\partial C_2} = \lambda^2 \frac{\partial s_1}{\partial C_2} + \frac{1}{2}\lambda^{-1}\frac{\partial s_2}{\partial C_2} \tag{5.48}$$

$$\frac{d}{dt}\left(\frac{\partial s_1}{\partial C_2}\right) = -\frac{1}{c_4}\frac{\partial s_1}{\partial C_2} + \frac{\partial g_1}{\partial C_2} \tag{5.49}$$

$$\frac{d}{dt}\left(\frac{\partial s_2}{\partial C_2}\right) = -\frac{1}{c_4}\frac{\partial s_2}{\partial C_2} + \frac{\partial g_2}{\partial C_2} \tag{5.50}$$

Where $\frac{\partial s_1}{\partial C_2}$ and $\frac{\partial s_2}{\partial C_2}$ are obtained from eq.(5.49) and eq.(5.50). Solving them numerically:

$$\frac{\partial s_1(k)}{\partial C_2} = \frac{\partial s_1(k-1)}{\partial C_2} + \Delta t\left(-\frac{1}{c_4}\frac{\partial s_1(k-1)}{\partial C_2} + \frac{\partial g_1}{\partial C_2}\right) = \frac{\partial s_1(k-1)}{\partial C_2}\left(1 - \frac{\Delta t}{c_4}\right) + \Delta t(\lambda\dot{\lambda}) \tag{5.51}$$

$$\frac{\partial s_2(k)}{\partial C_2} = \frac{\partial s_2(k-1)}{\partial C_2} + \Delta t\left(-\frac{1}{c_4}\frac{\partial s_1(k-1)}{\partial C_2} + \frac{\partial g_2}{\partial C_2}\right) = \frac{\partial s_2(k-1)}{\partial C_2}\left(1 - \frac{\Delta t}{c_4}\right) + \Delta t(\lambda^{-2}\dot{\lambda}) \tag{5.52}$$

Following the same procedure for the other parameters:

$$\frac{\partial \sigma_{Yang}}{\partial C_3} = \frac{\partial \sigma_{Visco}}{\partial C_3} = \lambda^2 \frac{\partial s_1}{\partial C_3} + \frac{1}{2}\lambda^{-1}\frac{\partial s_2}{\partial C_3} \tag{5.53}$$

$$\frac{d}{dt}\left(\frac{\partial s_1}{\partial C_3}\right) = -\frac{1}{c_4}\frac{\partial s_1}{\partial C_3} + \frac{\partial g_1}{\partial C_3} \tag{5.54}$$

$$\frac{d}{dt}\left(\frac{\partial s_2}{\partial C_3}\right) = -\frac{1}{c_4}\frac{\partial s_2}{\partial C_3} + \frac{\partial g_2}{\partial C_3} \tag{5.55}$$

$$\frac{\partial s_1(k)}{\partial C_3}=\frac{\partial s_1(k-1)}{\partial C_3}+\Delta t\left(-\frac{1}{c_4}\frac{\partial s_1(k-1)}{\partial C_3}+\frac{\partial g_1}{\partial C_3}\right)=\frac{\partial s_1(k-1)}{\partial C_3}\left(1-\frac{\Delta t}{c_4}\right)+ \\ +\Delta t(\lambda\dot{\lambda})(I_2-3) \tag{5.56}$$

$$\frac{\partial s_2(k)}{\partial C_3}=\frac{\partial s_2(k-1)}{\partial C_3}+\Delta t\left(-\frac{1}{c_4}\frac{\partial s_2(k-1)}{\partial C_3}+\frac{\partial g_2}{\partial C_3}\right)=\frac{\partial s_2(k-1)}{\partial C_3}\left(1-\frac{\Delta t}{c_4}\right)+ \\ +\Delta t(\lambda^{-2}\dot{\lambda})(I_2-3) \tag{5.57}$$

$$\frac{\partial \sigma_{Yang}}{\partial C_4}=\frac{\partial \sigma_{Visco}}{\partial C_4}=\lambda^2\frac{\partial s_1}{\partial C_4}+\frac{1}{2}\lambda^{-1}\frac{\partial s_2}{\partial C_4} \tag{5.58}$$

$$\frac{d}{dt}\left(\frac{\partial s_1}{\partial C_4}\right)=-\frac{1}{c_4}\frac{\partial s_1}{\partial C_4}+\frac{\partial g_1}{\partial C_4} \tag{5.59}$$

$$\frac{d}{dt}\left(\frac{\partial s_2}{\partial C_4}\right)=-\frac{1}{c_4}\frac{\partial s_2}{\partial C_4}+\frac{\partial g_2}{\partial C_4} \tag{5.60}$$

$$\frac{\partial s_1(k)}{\partial C_4}=\frac{\partial s_1(k-1)}{\partial C_4}+\Delta t\left(-\frac{1}{c_4}\frac{\partial s_1(k-1)}{\partial C_4}+\frac{\partial g_1}{\partial C_4}\right)=\frac{\partial s_1(k-1)}{\partial C_4}\left(1-\frac{\Delta t}{c_4}\right)+ \\ +\frac{1}{C_4^{\,2}}\int_o^t \lambda\left[C_2+C_3(I_2-3)\right]e^{-\frac{t-\tau}{C_4}}\dot{\lambda}d\tau \tag{5.61}$$

$$\frac{\partial s_2(k)}{\partial C_4}=\frac{\partial s_2(k-1)}{\partial C_4}+\Delta t\left(-\frac{1}{c_4}\frac{\partial s_2(k-1)}{\partial C_4}+\frac{\partial g_2}{\partial C_4}\right)=\frac{\partial s_2(k-1)}{\partial C_4}\left(1-\frac{\Delta t}{c_4}\right)+ \\ +\frac{1}{C_4^{\,2}}\int_o^t \lambda^{-2}\left[C_2+C_3(I_2-3)\right]e^{-\frac{t-\tau}{C_4}}\dot{\lambda}d\tau \tag{5.62}$$

These equations are introduced in Matlab and solved numerically. Next, time vs $\frac{\partial \sigma_{Yang}}{\partial p}$ relations are plotted for the six parameters in Fig. 5-19, Fig. 5-20, Fig. 5-21, Fig. 5-22, Fig. 5-23 and Fig. 5-24.

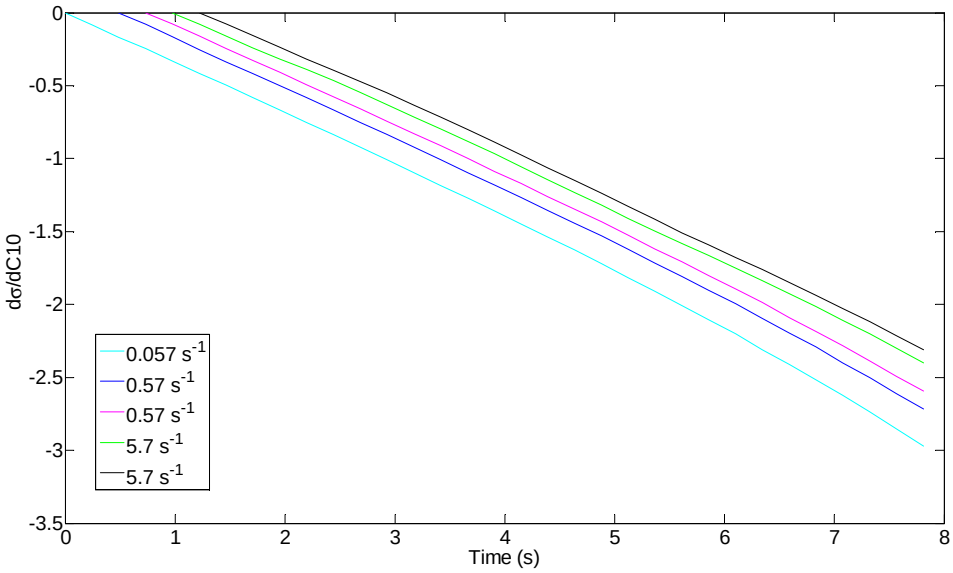

Fig. 5-19 Sensitivity of the different tests over C10 hyperelastic parameter

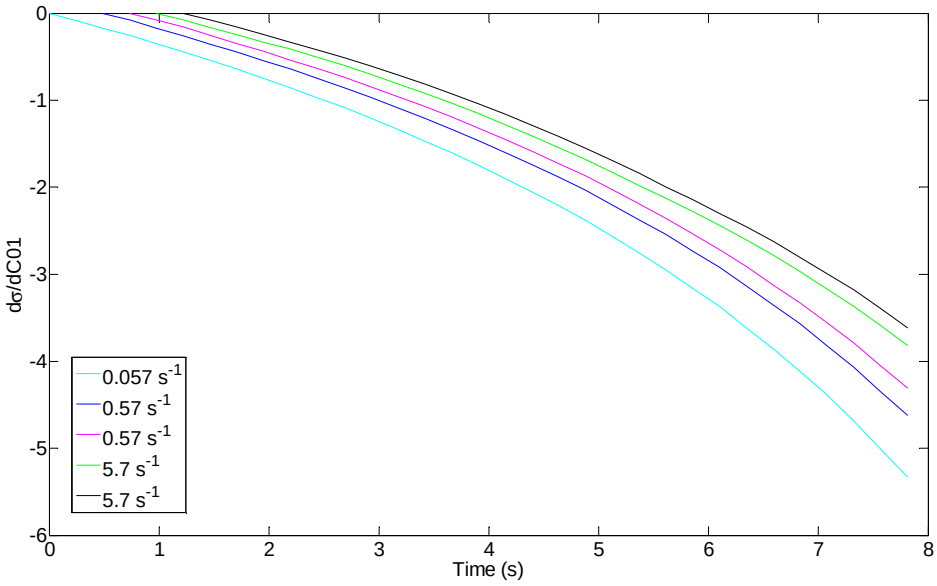

Fig. 5-20 Sensitivity of the different tests over C01 hyperelastic parameter

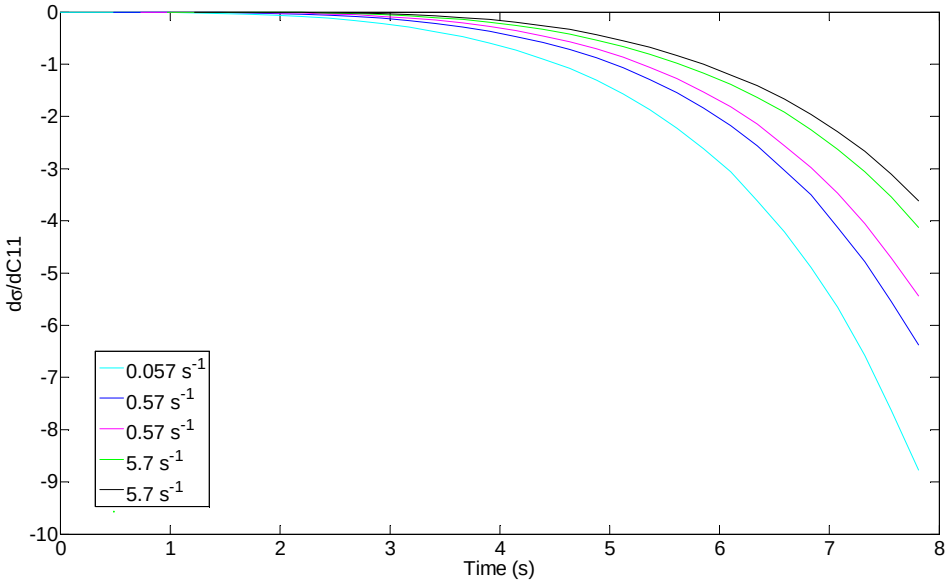

Fig. 5-21 Sensitivity of the different tests over C11 hyperelastic parameter

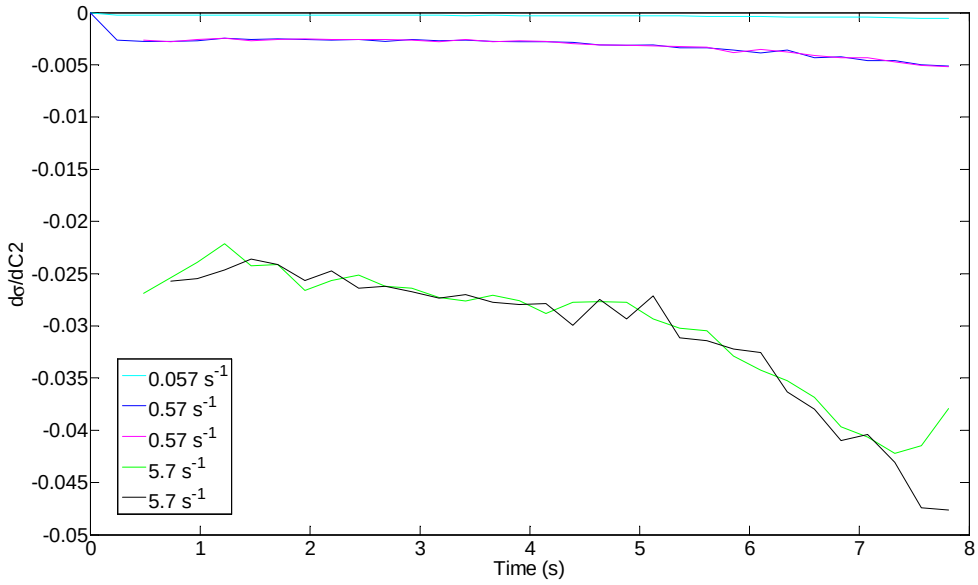

Fig. 5-22 Sensitivity of the different tests over C2 viscoelastic parameter

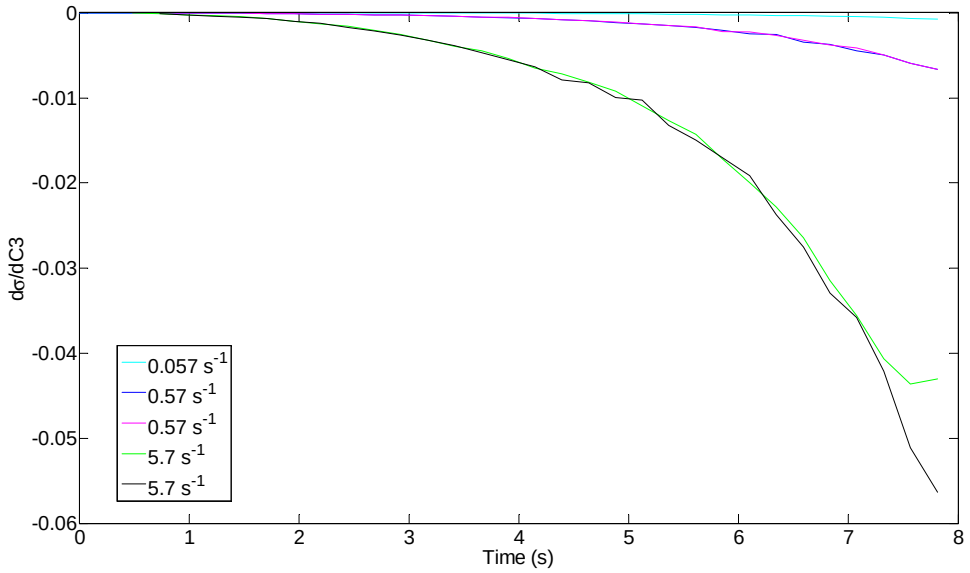

Fig. 5-23 Sensitivity of the different tests over C3 viscoelastic parameter

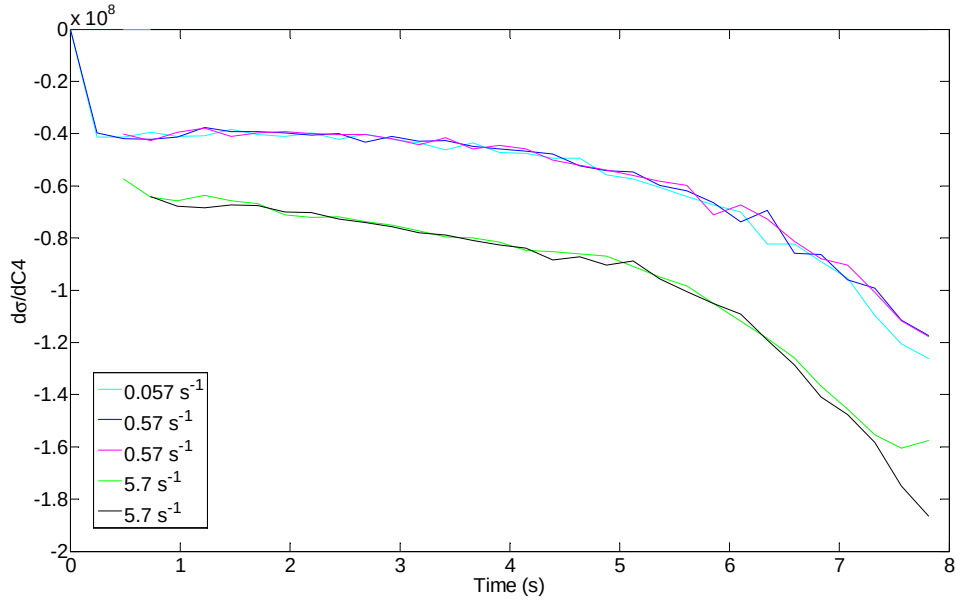

Fig. 5-24 Sensitivity of the different tests over C4 viscoelastic parameter

The sensitivity of the Cauchy stress regarding the three hyperelastic parameters can be observed in Fig. 5-19, Fig. 5-20 and Fig. 5-21. The data corresponding to the tests at different strain rates has been used. The maximum value for $\frac{\partial \sigma_{Yang}}{\partial C_{10}}$ corresponds to a value of -3

(adimensional) at 8 s approximately, taking into account the slowest strain rate curve data, i.e., precisely the data used to adjust the hyperelastic parameters. If $\frac{\partial \sigma_{Yang}}{\partial C_{01}}$ versus time is observed, this maximum value ascends to -5.5 at 8 s, and in the case of the third hyperelastic parameter, $\frac{\partial \sigma_{Yang}}{\partial C_{11}}$, this maximum value rises up to -9 at 8 s. This demonstrates the similar significance of the three hyperelastic parameters between them, being the influence of C11 a little bit higher that the other two; however, they have the same order of magnitude influence.

If Fig. 5-22, Fig. 5-23 and Fig. 5-24 are considered next, the influence of the viscoelastic parameters can be considered. While $\frac{\partial \sigma_{Yang}}{\partial C_{2}}$ and $\frac{\partial \sigma_{Yang}}{\partial C_{3}}$ are two orders of magnitude smaller than the sensibility on the hyperelastic parameters, $\frac{\partial \sigma_{Yang}}{\partial C_{4}}$ is seven orders of magnitude higher than the sensitivity on the hyperelastic parameters. This study shows the small influence of the parameters C10, C01, C11, C2 and C3 facing C4.

5.6 DISCUSSION

Yang's model has been selected to explain the behavior of the material. The parameters of the model have been adjusted for a 90/10 blend and 0.9 g/cm3 density, considering big samples. The first three hyperelastic parameters have been adjusted by means of least squares fitting technique. The results show that the differences between the predicted curves and the experimental data are lower that 1%. The determination of the viscoelastic parameters has been performed through a nonlinear multifitting procedure based on PSO, as the least-squares algorithm has been cumbersome to implement and does not always converge to the optimal solution. In this case, the deviations of the predicted curves from the experimental data are about 10% in the worst section.

The algorithm shows its robustness and ability to reach the global minimum of this non-linear function, because it is based on an intelligent approach with multiple versions of the

optimization problem known as particles. This approach enables us to go beyond local minimum solutions of the optimization problem. Furthermore, the algorithm does not impose any important mathematical limitation to the optimization fitting function. It has shown to be a good optimization method, simple, versatile and consisting of few parameters that accelerate to the optimal solution.

The measured R_2 value has been 0.99, which indicates that the proposed model corresponds well with its experimental counterpart. The constitutive model predicts correctly the material behavior over a rank of strain rates between $0.057s^{-1}$ and $5.7s^{-1}$ and deformations up to 45%. It should be noted that at higher strains rates, the nonlinear effects become more pronounced, and consequently, they become more difficult to describe with the reduced number of terms considered in this model. The PSO algorithm has demonstrated to be an efficient optimization method in the area covered in this work.

A theoretical study of the parameters has been performed to gain knowledge on the influence of these parameters on the model, as the results of the PSO are sensitive to the initial parameter guesses. The study sheds light on the fact that care must be taken when selecting the C_4 viscoelastic parameter, as its influence over the model is seven orders of magnitude higher than the rest of the parameters of the model.

6.

METHODOLOGY FOR THE CREATION OF THE MATERIAL SUBROUTINE

6.1 INTRODUCTION

The methodology to implement the previously proposed Yang's model in the Finite Element software Ansys, with its solver for explicit analysis LS Dyna, is introduced in this chapter. It is reminded the potential application of this material as coating in road barriers, and threfore, it is aimed to simulate impacts. Firstly, simulations of compression tests that will last a very short time over a material with large deformations and non-linear behavior are wanted to carry out; that is the reason to perform an explicit analysis.

Even though the blend of recycled rubber and LLDPE is nearly incompressible, it has to be taken into account the compressibility dependant component on the constitutive equation, in order to be able to implement in the FE code. Based on the expression for the Cauchy stress calculated from Yang's model in section 6.2, the compressibility component has been added. Also a different solving methodology for the viscoelastic part of the model has been considered; Midpoint Method has been applied as shown in section 6.2. Consequently, the PSO algorithm is applied to this equation to recalculate the new parameters, following this solving methodology.

6.2 OBTENTION OF THE NEW PARAMETERS BY PSO

Rubber like materials deform at almost constant volume, they are assumed incompressible. That is why I_3 in eq.(1.17) is equal to unity. In reality, rubbers have a finite compressibility, which being small, does not result negligible in all circumstances. As the objective is to implement the material model in a FE code, in this chapter the deformation gradient is separated in two parts, an isochoric part (distortional part) and a volumetric part (dilatational part):

$$F = \left(J^{1/3} I\right)\overline{F} = J^{1/3}\overline{F} \tag{6.1}$$

And therefore:

$$C = \left(J^{2/3} I\right)\overline{C} = J^{2/3}\overline{C} \tag{6.2}$$

$$\overline{I}_1 = J^{-2/3} I_1 \tag{6.3}$$

$$\overline{I}_2 = J^{-4/3} I_2 \tag{6.4}$$

Where:

$$\det\overline{F} = \overline{\lambda}_1\overline{\lambda}_2\overline{\lambda}_3 = 1 \tag{6.5}$$

$$\det\overline{C} = 1 \tag{6.6}$$

Where $\overline{\lambda}_a = J^{(-1/3)}\lambda_a, a = 1, 2, 3$. Taking into account that $\frac{\partial I_3}{\partial C} = I_3 C^{-1}$ and $I_3 = \det b = J^2$:

$$\frac{\partial J^2}{\partial C} = J^2 C^{-1} \tag{6.7}$$

And by means of the chain rule:

$$\frac{\partial J}{\partial C} = \frac{J}{2} C^{-1} \tag{6.8}$$

$$\frac{\partial J^{-2/3}}{\partial C} = -\frac{1}{3} J^{-2/3} C^{-1} \tag{6.9}$$

The strain energy can be also separated into two terms, by adding a term reproducing the free energy associated purely with the change of volume to the previous free energy, the one of the network deformation:

$$\psi(C) = \psi_{vol}(J) + \psi_{isoc}(\bar{C}) \tag{6.10}$$

Different strain energies are defined in the literature. The volumetric part depends on the compressibility coefficient K. The criteria of Petiteau[40] has been considered here, who selects that proposed by Simo[77] (one of the simplest one). It is reminded that the aim here is to use it to model an almost incompressible material; therefore, K is selected with a high value compared to the hyperelastic parameters.

$$\psi_{vol}(J) = U(J) = \frac{K}{2}(J-1)^2 \, LnJ \tag{6.11}$$

Next expression is used for the calculation of the volumetric part of the stress, as is stated in eq. (1.49) from Annex B:

$$\sigma_{hyper\_vol} = \frac{\partial \psi_{vol}}{\partial J} I = \left(K(J-1)LnJ + \frac{K}{2}(J-1)^2 \frac{1}{J} \right) I \tag{6.12}$$

Referring to the isochoric part of the strain energy, it can be approximated by one of the strain energies already collected in Chapter 2, $\psi_{isoc}(\bar{C}) = \bar{\psi}$. Therefore, this part can be obtained from the eq. (1.49) from the Annex B:

$$\sigma_{hyper\_isoc} = 2J^{-1} dev\left[\left(\frac{\partial \psi_{isoc}}{\partial \bar{I}_1} + \bar{I}_1 \frac{\partial \psi_{isoc}}{\partial \bar{I}_2} \right) \bar{b} - \frac{\partial \psi_{isoc}}{\partial \bar{I}_2} \bar{b}^2 \right] \tag{6.13}$$

Considering eq. (5.3), one gets: $\psi_{isoc} = C_{10}(\bar{I}_1 - 3) + C_{01}(\bar{I}_2 - 3) + C_{11}(\bar{I}_1 - 3)(\bar{I}_2 - 3)$.

From eq.(6.13):

$$\sigma_{hyper\_isoc} = 2J^{-1} dev\left[\left[C_{10} + C_{11}(\bar{I}_2 - 3) + \bar{I}_1 \left(C_{01} + C_{11}(\bar{I}_1 - 3) \right) \right] \bar{b} - \left(C_{01} + C_{11}(\bar{I}_1 - 3) \right) \bar{b}^2 \right] \tag{6.14}$$

Taking into account that $\det(F) = \lambda_1 \lambda_2 \lambda_3 = J$ and that in uniaxial compression $\lambda_2 = \lambda_3$, F can be formulated as:

$$F=\begin{pmatrix}\lambda & 0 & 0\\ 0 & \left(\frac{J}{\lambda}\right)^{1/2} & 0\\ 0 & 0 & \left(\frac{J}{\lambda}\right)^{1/2}\end{pmatrix} \tag{6.15}$$

Taking into account eq. (6.1), next expression is obtained for $\overline{b}$:

$$\begin{aligned}\overline{b}=(\overline{FF}^{T})=J^{-1/3}&\begin{pmatrix}\lambda & 0 & 0\\ 0 & \left(\frac{J}{\lambda}\right)^{1/2} & 0\\ 0 & 0 & \left(\frac{J}{\lambda}\right)^{1/2}\end{pmatrix}J^{-1/3}\begin{pmatrix}\lambda & 0 & 0\\ 0 & \left(\frac{J}{\lambda}\right)^{1/2} & 0\\ 0 & 0 & \left(\frac{J}{\lambda}\right)^{1/2}\end{pmatrix}=\\ =J^{-2/3}&\begin{pmatrix}\lambda^{2} & 0 & 0\\ 0 & \frac{J}{\lambda} & 0\\ 0 & 0 & \frac{J}{\lambda}\end{pmatrix}=\begin{pmatrix}J^{-2/3}\lambda^{2} & 0 & 0\\ 0 & \frac{J^{1/3}}{\lambda} & 0\\ 0 & 0 & \frac{J^{1/3}}{\lambda}\end{pmatrix}\end{aligned} \tag{6.16}$$

Concerning the viscoelastic part of Yang's model, and considering the numerical integration of the response as next step, same approach as Petiteau[40] is followed here:

$$\overline{\sigma}_{visco}=\frac{1}{J}dev\left[\overline{F}_{n}\overline{H}_{n}\overline{F}_{n}^{T}\right] \tag{6.17}$$

This $\overline{\sigma}_{visco}$ corresponds to an instant of time n. According to Yang's model in eq. (5.13)-(5.16) here $\overline{H}_{n}$ can be considered as:

$$\overline{H}_{n}=\int_{-\infty}^{t}[C_{2}+C_{3}(\overline{I}_{2}(\tau)-3)]\exp\left(-\frac{t-\tau}{C_{4}}\right)\dot{\overline{E}}d\tau \tag{6.18}$$

If this expression is separated in two parts:

$$\bar{H}_n = \int_{-\infty}^{t_{n-1}} [C_2 + C_3(\bar{I}_2(\tau) - 3)] \exp\left(-\frac{t_n - t_{n-1}}{C_4}\right) \exp\left(-\frac{t_{n-1} - \tau}{C_4}\right) \dot{\bar{E}} d\tau + \\ + \int_{t_{n-1}}^{t_n} [C_2 + C_3(\bar{I}_2(\tau) - 3)] \exp\left(-\frac{t_n - \tau}{C_4}\right) \dot{\bar{E}} d\tau \tag{6.19}$$

And taking into account that $\Delta t = t_n - t_{n-1}$:

$$\bar{H}_n = \exp\left(-\frac{\Delta t}{C_4}\right) \bar{H}_{n-1} + \int_{t_{n-1}}^{t_n} [C_2 + C_3(\bar{I}_2(\tau) - 3)] \exp\left(-\frac{t_n - \tau}{C_4}\right) \dot{\bar{E}} d\tau \tag{6.20}$$

Next, Midpoint Method is applied, which is an approximation of 1st order, where τ is approximated by $\frac{t_n + t_{n-1}}{2}$:

$$\bar{H}_n = \exp\left(-\frac{\Delta t}{C_4}\right) \bar{H}_{n-1} + \exp\left(-\frac{\Delta t}{2C_4}\right) \left[C_2 + C_3 \left(\bar{I}_2 \left(\frac{t_n + t_{n-1}}{2} \right) - 3 \right) \right] \int_{t_{n-1}}^{t_n} \dot{\bar{E}} d\tau \tag{6.21}$$

Finally, replacing $E = \frac{1}{2}(C - I)$:

$$\bar{H}_n = \exp\left(-\frac{\Delta t}{C_4}\right) \bar{H}_{n-1} + \exp\left(-\frac{\Delta t}{2C_4}\right) \left[C_2 + C_3 \left(\bar{I}_2 \left(\frac{t_n + t_{n-1}}{2} \right) - 3 \right) \right] \frac{1}{2} (\bar{C}_n - \bar{C}_{n-1}) \tag{6.22}$$

Apart from the six material parameters $C_{10}, C_{01}, C_{11}, C_2, C_3, C_4$ the volume ratio J is also unknown; as its value is around $J = 1$ it is considered this as an approximation to apply the PSO and calculate the parameter first of all. It has been taken into account a 90/10 blend and 0.9 g/cm^3 density, big sample, as in Chapter 5.

Hyperelastic parameters C_{10}, C_{01}, C_{11} are obtained by Mean Squared Error procedure. Their values can be found in Table 6-1; if they are compared with the ones obtained previously in Table 5-2 it can be appreciated that they are very similar, as expected. The values here are a little bit higher, but not significantly. Fig. 6-1 shows the stress-stretch curves for both experimental data and the result estimated by the model.

Table 6-1 Values for the hyperelastic parameters for a 90/10 blend and 0.9 g/cm^3 density, when compressibility is included and Midpoint Method is applied

Parameter	Value
C_{10} [MPa]	3.08
C_{01} [MPa]	-1.47
C_{11} [MPa]	0.22

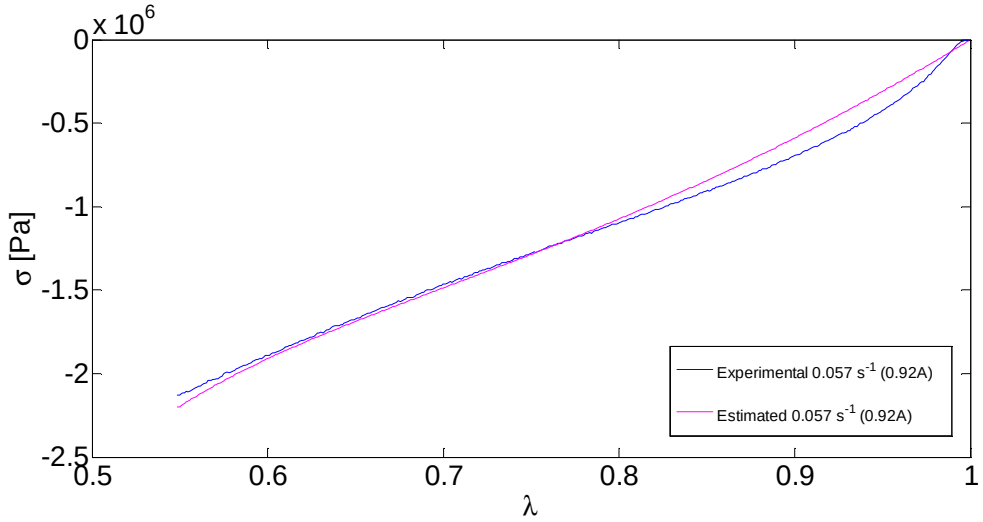

Fig. 6-1 Quasistatic stress-stretch curves vs. hyperelastic component of the theoretic model for 0.9 g/cm^3 density when compressibility is included and Midpoint Method is applied

Concerning viscoelastic parameters, PSO has been applied; different values of the viscoelastic parameters along the algorithm until the optimal trio are reached, as shown in Fig. 6-2. The values of this optimal trio are summarized in Table 6-2.

Table 6-2 Values for the viscoelastic parameters for a 90/10 blend and 0.9 g/cm^3 density, when compressibility is included and Midpoint Method is applied

Parameter	Value
C_2 [MPa]	12.29
C_3 [MPa]	1.03
C_4 [s]	0.0056

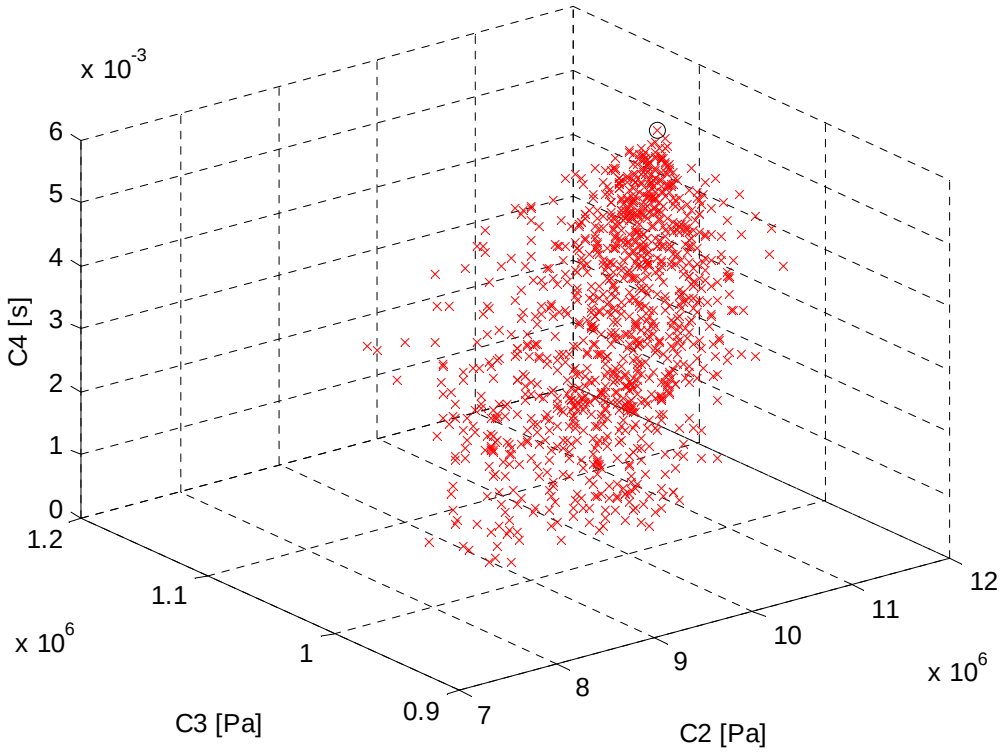

Fig. 6-2 Different values for the viscoelastic parameters along the PSO until it converges to the optimal trio (case of 0.9 g/cm³) when compressibility is included and Midpoint Method is applied

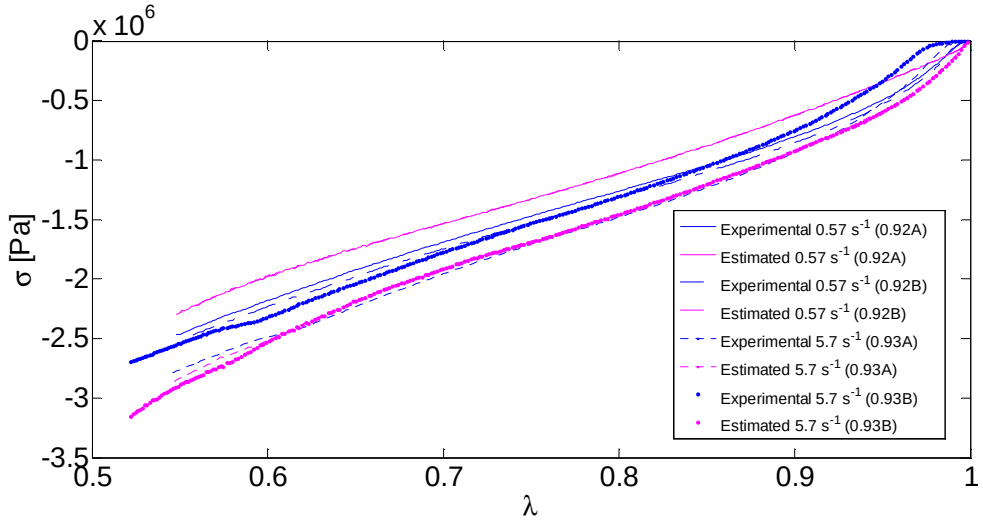

Fig. 6-3 Comparison between the experimental data and the theoretical curves for a 90/10 blend and 0.9 g/cm³ density when compressibility is included and Midpoint Method is applied

Fig. 6-3 shows the stretch-stress curves both for the experimental data and the estimated curves for a 90/10 blend and 0.9 g/cm^3 density, big samples.

6.3 ALGORITHM FOR THE MATERIAL SUBROUTINE TO OBTAIN THE CONSTITUTIVE RESPONSE

Once the six parameters of the model are recalculated, the methodology to implement this material constitutive equation in the FE code is introduced next. This is based on the algorithm proposed by Petiteau[40], but applied to Yang's model. The steps are summarized below:

- ✓ At a t_n time instant and the corresponding stretch λ_n, next information is taken into account from previous instant: $\overline{C}_{n-1}$ and $\overline{H}_{n-1}$ (both needed for eq.(6.22)).
- ✓ F_n, $J=\det(F_n)$ and $\overline{F}_n = J^{-1/3}F_n$ are calculated.
- ✓ $\overline{b}_n = \overline{F}_n\overline{F}_n^T$ Left Cauchy-Green deformation tensor's isochoric part is calculated, in order to use in the eq.(6.13) together with its invariants $\overline{I}_1 = tr(\overline{b}_n)$ and $\overline{I}_2 = \frac{1}{2}\left[\overline{I}_1^2 - tr(\overline{b}_n^2)\right]$
- ✓ Hyperelastic stress part is calculated, as sum of the isochoric part from eq. (6.14) after introducing Rivlin's form in the strain energy expression and the volumetric/spheric part from eq.(6.12).
- ✓ Viscoelastic stress part is calculated next replacing eq.(6.22) into eq.(6.17).
- ✓ $\overline{C}_{n-1}$ and $\overline{H}_{n-1}$ values are updated, saving $\overline{C}_n$ and $\overline{H}_n$ inside them.
- ✓ Finally total Cauchy stress is calculated by:

$$\sigma_n = \left(\sigma_n^{hyper\_vol} + \overline{\sigma}_n^{hyper\_isoc}\right) + \overline{\sigma}_n^{visco} \tag{6.23}$$

It has to be noted that here J is an unknown, that is, the equations depend on J. Therefore, it results necessary to solve $\sigma_{22} = \sigma_{22\_hyper} + \sigma_{22\_visco} = 0$ equation (or in the same manner $\sigma_{33} = 0$) to get the value of J at each time instant. This algorithm has been implemented in Matlab first. The results obtained, again for a 90/10 blend with 0.9 g/cm^3 density,

considering big samples, are shown next in Fig. 6-4. As it can be appreciated, the results obtained from the subroutine are in good agreement with their experimental counterparts.

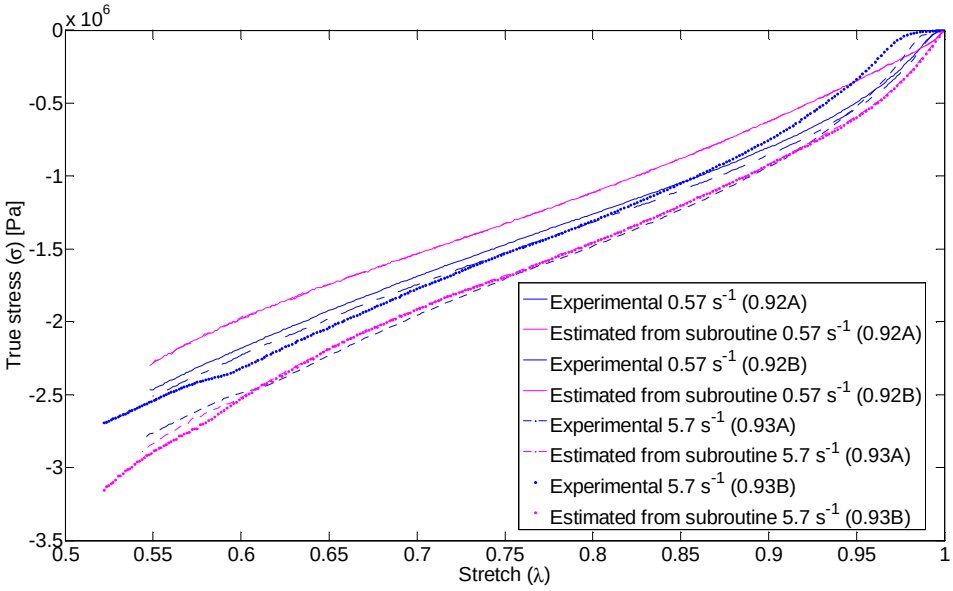

Fig. 6-4 Comparison between the experimental data and the theoretical curves obtained from the algorithm for a 90/10 blend and 0.9 g/cm^3 density

6.4 DISCUSSION

The methodology to implement Yang's constitutive equation for the blend presented in this work is explained in this chapter. Regarding the potential use of the material as coating in road barrier, explicit analysis is considered the best option to perform in Ansys FE code. Therefore, LS Dyna solver is beared in mind. It also has to be accounted for the use of compressibility in the constitutive equation as FE simulations require this condition. Hence, it has presented the model including the compressibility, and PSO has been applied to this equation, in order to recalculate the parameters and to obtain the best values of them to this implementation.

Thereafter the algorithm of the material subroutine is presented and implemented in Matlab, with these new values of the parameters. The results show that the model is in good agreement with its experimental counterpart. Next step consists of the introduction of the Matlab code in LS Dyna, the simulation of the compression tests and to adjust the FE model to the experimental data. This way, it will be possible to model the road barriers in LS Dyna, considering this as a future research line.

7.
CONCLUSIONS AND FUTURE CONSIDERATIONS

Three blends of recycled rubber from used tires and Linear Low Density Polyethylene as adhesive have been manufactured, with different proportions of each material and a constant proportion of TiO_2 as colorant on all of them. These proportions are called 90/10, 75/25 and 60/40, where the second term denotes the percentage of LLDPE, and the first one comprehends 3% of TiO_2 and the rest of recycled rubber. The potential application for this material is as coating in road barriers in order to restrain motorcyclists in crash impacts. This use is included into impacts; hence the mechanical characterization of the blend has encompassed high strain rate compression tests.

A visco-hyperelastic constitutive equation well known in the literature has been chosen to characterize the material, i.e. Yang's model. This model has Rivlin's form with three parameters as hyperelastic part and a viscoelastic part with another three parameters based on K-BKZ model, with an aportation done by Yang et al. The hyperelastic part has been adjusted by the least-squares fitting technique. Concerning the parameters of the viscoelastic part, based on convolution integral, resulted very difficult to adjust. Particle Swarm Optimization (PSO) algorithm has been selected to obtain the values of these parameters. The PSO algorithm has shown to be a good optimization method, simple, versatile, and consisting of few parameters that accelerate to the optimal solution even if the function to optimize is highly nonlinear. Considering that the main objective to attain

with this blend is to recycle as much rubber as possible, in principle the 90/10 blend has been selected between the three studied. A compromise solution has been aimed, recognizing that the other blends would be better in energy absortion capability, but also that they have higher stiffness, and the interest here resides in the need of recycling to greatest extend. Thus, the parameters of the model have been adjusted for a 90/10 blend and a density of 0.9 g/cm^3.

Four different densities have been studied, at four different speeds, between 0.004 and 4 m/s; this speed is limited due to security reasons of the machine. At the highest speed the material curves exhibited distinctive ondulations, usually called as "ringing" in the specialized literature. This data can not be used in its original form as it is distorted. Therefore, Experimental Modal Analysis (EMA) has shown to be essential to study in detail the dynamic characteristics of the servo hydraulic machine. From this analysis it has been concluded that predominant modes of the testing machine have been excited during the tests and this has affected the experimental data. Thus, a multiple degree of freedom machine model has been developed based on modal parameters, i.e., natural frequencies, mode shapes and damping factors obtained from the EMA. This mathematical model has shown which modes have affected mainly the system ringing. It has been excited by an impulse load that simulates adequately the frequency content of the measured load cell force signal. Thereby, the oscillatory part of the simulated response has been subtracted from the measured force signal. Thereafter, as the new signal had a clear reduction of the waves, it resulted suitable for applying a low pass filter with a cutoff frequency of 1600 Hz. That way the final data resulted treatable with an obvious reduction of the oscillations.

The methodology to implement the previously proposed Yang's model in the Finite Element software Ansys, with its solver for explicit analysis LS Dyna, has been introduced next. This constitutive equation is not implemented in this software yet and consequently, a material user subroutine has been developed first in Matlab. It is aimed to perform simulations of compression tests that will last a very short time over a material with large deformations and non-linear behavior; that is the reason to perform an explicit analysis. The algorithm to implement the material subroutine is explained in this work; the process of introducing the subroutine in the FE code is a future work to be carried out based on the work done in this thesis.

FUTURE LINES OF INVESTIGATION:

The main aspects to consider in future work can be resumed as:

- One possible future line consists of the improvement of the correction of the force measured by the load cell. This work has been "handmade" and it would be interesting to develop a kind of automatization of the process of locating coincident time instants when both signals, the experimental and the simulated, are overlapped in the same plot with the aim of obtaining coincident peaks.

- In this work experimental tests have been performed at constant speed. If the speed is variable instead of constant, this will give more information to the experimental data. Therefore, the influence of the parameters on the model will be higher and this way it will be easier to control the error produced when identifying them. This is an open door to study this subject more in depth.

- It has been observed that the Yang's model is especially sensitive to one of its viscoelastic parameters, C_4, by means of the study of the parameters. With the information extracted from this analysis, it can be argued that it would be appropriate to fit firstly this parameter and then the rest; this would lead to more precise results of the fitting, although the error commited in this work is already less that the 10-15% approximately.

- Continue with the simulations of high strain rate compression tests in LS Dyna, in order to obtain a model validated with the experimental results. Thereafter, a FE model of a road barrier with its coating of the interested blend would be created and simulations of crashes of a dummy against it would be performed. First, at speeds similar to those of the experimental ones, and then, at speeds stated in the standards. Once an adequate model is obtained, a prototype would be created and real tests would be carried on it. As the experimental approach is expensive and time-consuming, the use of this predictive model shortens these expenses.

- Another possible research line is connected to the improvement of the parameters identification algorithm. There is substantial literature around the PSO with the aim

of tuning it: adaptative algorithms, the use of the good results or not instead of iteration numer in order to stop the algorithm, etc.

- The viscoelastic response of the model may require additional analysis, which could help to identify easier the viscoelastic parameters. If its stationary part is analyzed, an algebraic expression of this viscoelastic response could be proposed. It looks an interesting line to study, as viscoelastic models based on convolution integral seem to be moved away or isolated due to its mathematical complexity.

REFERENCES

1. De SK, Isayev A, Khait K. *Rubber recycling. boca raton, FL: CRC press, taylor & francis group.* 2005.

2. Myhre M, MacKillop DA. Rubber recycling. *Rubber Chemistry and Technology*. 2002;75(3):429-474.

3. Rajeev R, De S. Thermoplastic elastomers based on waste rubber and plastics. *Rubber chemistry and technology*. 2004;77(3):569-578.

4. Stevenson K, Stallwood B, Hart AG. Tire rubber recycling and bioremediation: A review. *Bioremediation J*. 2008;12(1):1-11.

5. Shim J, Mohr D. Rate dependent finite strain constitutive model of polyurea. *Int J Plast*. 2011;27(6):868-886.

6. Shim J, Mohr D. Rate dependent finite strain constitutive model of polyurea. *Int J Plast*. 2011;27(6):868-886. doi: http://dx.doi.org/10.1016/j.ijplas.2010.10.001.

7. Anani Y, Alizadeh Y. Visco-hyperelastic constitutive law for modeling of foam's behavior. *Mater Des*. 2011;32(5):2940-2948. doi: http://dx.doi.org/10.1016/j.matdes.2010.11.010.

8. FUNG Y. Stress, strain, growth, and remodeling of living organisms. *Z Angew Math Phys*. 1995;46:S469-S482.

9. Gil-Negrete N. *On the modeling and dynamic stiffness prediction of rubber isolators.* [Universidad de Navarra]. ; 2004 [Ph.D. thesis].

10. FEMA (The Federation of European Motorcyclist Associations). A project to develop recommendations to road traffic authorities for reducing injuries to motorcyclist in collision with crash barriers. *Final Report of the Motorcyclist & Crash Barriers Project*. 2000.

11. Haugou G, Markiewicz E, Fabis J. On the use of the non direct tensile loading on a classical split hopkinson bar apparatus dedicated to sheet metal specimen characterisation. *Int J Impact Eng*. 2006;32(5):778-798. doi: http://dx.doi.org/10.1016/j.ijimpeng.2005.07.015.

12. Xia Y, Zhu J, Zhou Q. Verification of a multiple-machine program for material testing from quasi-static to high strain-rate. *Int J Impact Eng*. 2015;86:284-294. doi: http://dx.doi.org/10.1016/j.ijimpeng.2015.07.010.

13. Petiteau J, Othman R, Guégan P, Le Sourne H, Verron E. Dynamic uniaxial extension of elastomers at constant true strain rate. *Polym Test*. 2013;32(2):394-401. doi: http://dx.doi.org/10.1016/j.polymertesting.2012.10.007.

14. Zhu D, Rajan S, Mobasher B, Peled A, Mignolet M. Modal analysis of a servo-hydraulic high speed machine and its application to dynamic tensile testing at an intermediate strain rate. *Exp Mech*. 2011;51(8):1347-1363. doi: http://dx.doi.org/10.1007/s11340-010-9443-2.

15. Roche N. *Comportement vibro-acoustique de matériaux et structures à base de poudrettes de pneumatiques recyclés*. 2010.

16. Navarro FJ, Partal P, Martínez-Boza FJ, Gallegos C. Novel recycled polyethylene/ground tire rubber/bitumen blends for use in roofing applications: Thermo-mechanical properties. *Polym Test*. 2010;29(5):588-595.

17. Amari T, Themelis NJ, Wernick IK. Resource recovery from used rubber tires. *Resour Policy*. 1999;25(3):179-188.

18. Sonnier R, Leroy E, Clerc L, Bergeret A, Lopez-Cuesta J. Polyethylene/ground tyre rubber blends: Influence of particle morphology and oxidation on mechanical properties. *Polym Test*. 2007;26(2):274-281.

19. Rocha MCG, Leyva ME, Oliveira MGd. Thermoplastic elastomers blends based on linear low density polyethylene, ethylene-1-octene copolymers and ground rubber tire. *Polímeros*. 2014;24(1):23-29.

20. Kumar CR, Fuhrmann I, Karger-Kocsis J. LDPE-based thermoplastic elastomers containing ground tire rubber with and without dynamic curing. *Polym Degrad Stab*. 2002;76(1):137-144.

21. Scaffaro R, Dintcheva NT, Nocilla MA, La Mantia FP. Formulation, characterization and optimization of the processing condition of blends of recycled polyethylene and ground tyre rubber: Mechanical and rheological analysis. *Polym Degrad Stab*. 2005;90(2):281-287. doi: 10.1016/j.polymdegradstab.2005.03.022.

22. Fainleib A, Grigoryeva O, Starostenko O, Danilenko I, Bardash L. Reactive compatibilization of recycled low density polyethylene/butadiene rubber blends during dynamic vulcanization. . 2003;202(1):117-126.

23. Sonnier R, Leroy E, Clerc L, Bergeret A, Lopez-Cuesta J. Compatibilisation of polyethylene/ground tyre rubber blends by γ irradiation. *Polym Degrad Stab*. 2006;91(10):2375-2379.

24. Grigoryeva O, Fainleib A, Tolstov A, Starostenko O, Lievana E, Karger-Kocsis J. Thermoplastic elastomers based on recycled high-density polyethylene, ethylene–propylene–diene monomer rubber, and ground tire rubber. *J Appl Polym Sci*. 2005;95(3):659-671.

25. de Sousa, Fabiula Danielli Bastos, Gouveia JR, de Camargo Filho, Pedro Mário Franco, et al. Blends of ground tire rubber devulcanized by microwaves/HDPE-part B: Influence of clay addition. *Polímeros*. 2015;25(4):382-391.

26. Ausias G, Thuillier S, Omnes B, Wiessner S, Pilvin P. Micro-mechanical model of TPE made of polypropylene and rubber waste. *Polymer*. 2007;48(11):3367-3376.

27. Guo B, Cao Y, Jia D, Qiu Q. Thermoplastic elastomers derived from scrap rubber powder/LLDPE blend with LLDPE-graft-(epoxidized natural rubber) dual compatibilizer. *Macromolecular Materials and Engineering*. 2004;289(4):360-367.

28. Naskar AK, Bhowmick AK, De S. Thermoplastic elastomeric composition based on ground rubber tire. *Polymer Engineering & Science*. 2001;41(6):1087-1098.

29. Scaffaro R, Dintcheva NT, Nocilla M, La Mantia F. Formulation, characterization and optimization of the processing condition of blends of recycled polyethylene and ground tyre rubber: Mechanical and rheological analysis. *Polym Degrad Stab*. 2005;90(2):281-287.

30. Zhu J, Zhang X, Liang M, Lu C. Enhancement of processability and foamability of ground tire rubber powder and LDPE blends through solid state shear milling. *Journal of Polymer Research*. 2011;18(4):533-539.

31. Mészáros L, Fejős M, Bárány T. Mechanical properties of recycled LDPE/EVA/ground tyre rubber blends: Effects of EVA content and postirradiation. *J Appl Polym Sci*. 2012;125(1):512-519.

32. Parenteau T, Bertevas E, Ausias G, Stocek R, Grohens Y, Pilvin P. Characterisation and micromechanical modelling of the elasto-viscoplastic behavior of thermoplastic elastomers. *Mech Mater*. 2014;71:114-125.

33. Drozdov A. Constitutive equations for the nonlinear viscoelastic and viscoplastic behavior of thermoplastic elastomers. *Int J Eng Sci*. 2006;44(3):205-226.

34. Drozdov A, Christiansen J. Thermo-viscoplasticity of carbon black-reinforced thermoplastic elastomers. *Int J Solids Structures*. 2009;46(11):2298-2308.

35. Austrell P. *Modeling of elasticity and damping for filled elastomers.* [Lund University]. ; 1997 [Ph.D. thesis].

36. Pouriayevali H, Guo YB, Shim VPW. A constitutive description of elastomer behaviour at high strain rates – A strain-dependent relaxation time approach. *Int J Impact Eng*. 2012;47(0):71-78. doi: http://dx.doi.org/10.1016/j.ijimpeng.2012.04.001.

37. Pouriayevali H, Arabnejad S, Guo YB, Shim VPW. A constitutive description of the rate-sensitive response of semi-crystalline polymers. *Int J Impact Eng*. 2013;62:35-47. doi: 10.1016/j.ijimpeng.2013.05.002.

38. Ciambella J, Paolone A, Vidoli S. A comparison of nonlinear integral-based viscoelastic models through compression tests on filled rubber. *Mech Mater*. 2010;42(10):932-944. doi: http://dx.doi.org/10.1016/j.mechmat.2010.07.007.

39. Ogden R, Saccomandi G, Sgura I. Fitting hyperelastic models to experimental data. *Comput Mech*. 2004;34(6):484-502.

40. Petiteau J. *Experimental characterization and modelling of the behaviour of elastomers under fast dynamic loading. application to suspension mounts.* Ecole Centrale de Nantes (ECN) (ECN) (ECN) (ECN); 2012.

41. Banks HT, Hu S, Kenz ZR. A brief review of elasticity and viscoelasticity for solids. *Advances in Applied Mathematics and Mechanics*. 2011;3(01):1-51.

42. Holzapfel GA. *Nonlinear solid mechanics.* Vol 24. Wiley Chichester; 2000.

43. Treloar LRG. *The physics of rubber elasticity.* Oxford University Press, USA; 1975.

44. Arruda EM, Boyce MC. A three-dimensional constitutive model for the large stretch behavior of rubber elastic materials. *Journal of the Mechanics and Physics of Solids*. 1993;41(2):389-412. doi: http://dx.doi.org/10.1016/0022-5096(93)90013-6.

45. Mooney M. A theory of large elastic deformation. *J Appl Phys*. 1940;11(9):582-592.

46. Rivlin R. The elasticity of rubber. *Rubber Chemistry and Technology*. 1992;65(3):51-66.

47. Yeoh O. Characterization of elastic properties of carbon-black-filled rubber vulcanizates. *Rubber chemistry and technology*. 1990;63(5):792-805.

48. Gent A. A new constitutive relation for rubber. *Rubber chemistry and technology*. 1996;69(1):59-61.

49. Marckmann G, Verron E. Comparison of hyperelastic models for rubber-like materials. *Rubber chemistry and technology*. 2006;79(5):835-858.

50. Steinmann P, Hossain M, Possart G. Hyperelastic models for rubber-like materials: Consistent tangent operators and suitability for treloar's data. *Arch Appl Mech*. 2012;82(9):1183-1217. http://dx.doi.org/10.1007/s00419-012-0610-z. doi: 10.1007/s00419-012-0610-z.

51. Verron E. *Contribution expérimentale et numérique aux procédés de moulage par soufflage et de thermoformage.* Ecole Centrale de Nantes; Université de Nantes; 1997.

52. Rivlin RS, Saunders D. Large elastic deformations of isotropic materials. VII. experiments on the deformation of rubber. *Philosophical Transactions of the Royal Society of London A: Mathematical, Physical and Engineering Sciences*. 1951;243(865):251-288.

53. Gent AN, Thomas AG. Forms for the stored (strain) energy function for vulcanized rubber. *Journal of Polymer Science*. 1958;28(118):625-628. doi: 10.1002/pol.1958.1202811814.

54. Beda T, Gacem H, Chevalier Y, Mbarga P. Domain of validity and fit of gent-thomas and flory-erman rubber models to data. *Parameters*. 2008;1:K2.

55. Carmichael A, Holdaway H. Phenomenological elastomechanical behavior of rubbers over wide ranges of strain. *J Appl Phys*. 1961;32(2):159-166.

56. Valanis K, Landel R. The Strain-Energy function of a hyperelastic material in terms of the extension ratios. *J Appl Phys*. 1967;38(7):2997-3002.

57. Ogden R, Saccomandi G, Sgura I. Fitting hyperelastic models to experimental data. *Comput Mech*. 2004;34(6):484-502.

58. Blatz P, Sharda SC, Tschoegl N. Strain energy function for rubberlike materials based on a generalized measure of strain. *Transactions of the Society of Rheology*. 1974;18(1):145-161.

59. Yeoh O, Fleming P. A new attempt to reconcile the statistical and phenomenological theories of rubber elasticity. *Journal of Polymer Science-B-Polymer Physics Edition*. 1997;35(12):1919-1932.

60. Shariff M. Strain energy function for filled and unfilled rubberlike material. *Rubber chemistry and technology*. 2000;73(1):1-18.

61. Pucci E, Saccomandi G. Some remarks about a simple history dependent nonlinear viscoelastic model. *Mech Res Commun*. 2015;68:70-76.

62. Fatt MSH, Bekar I. High-speed testing and material modeling of unfilled styrene butadiene vulcanizates at impact rates. *J Mater Sci*. 2004;39(23):6885-6899. http://dx.doi.org/10.1023/B:JMSC.0000047530.86758.b9. doi: 10.1023/B:JMSC.0000047530.86758.b9.

63. Wineman A. Nonlinear viscoelastic solids—a review. *Mathematics and Mechanics of Solids*. 2009;14(3):300-366.

64. Drapaca C, Sivaloganathan S, Tenti G. Nonlinear constitutive laws in viscoelasticity. *Mathematics and Mechanics of Solids*. 2007;12(5):475-501.

65. Park S. Analytical modeling of viscoelastic dampers for structural and vibration control. *Int J Solids Structures*. 2001;38(44):8065-8092.

66. Yang L, Shim V, Lim C. A visco-hyperelastic approach to modelling the constitutive behaviour of rubber. *Int J Impact Eng*. 2000;24(6):545-560.

67. Yang L, Shim V. A visco-hyperelastic constitutive description of elastomeric foam. *Int J Impact Eng*. 2004;30(8):1099-1110.

68. Shim V, Yang L, Lim C, Law P. A visco-hyperelastic constitutive model to characterize both tensile and compressive behavior of rubber. *J Appl Polym Sci*. 2004;92(1):523-531.

69. Hoo Fatt MS, Xin Ouyang. Integral-based constitutive equation for rubber at high strain rates. *Int J Solids Structures*. 2007;44(20):6491-506. doi: 10.1016/j.ijsolstr.2007.02.038.

70. Ward I, Pinnock P. The mechanical properties of solid polymers. *British Journal of Applied Physics*. 1966;17(1):3.

71. Christensen R. A nonlinear theory of viscoelasticity for application to elastomers. *Journal of Applied Mechanics*. 1980;47(4):762-768.

72. Khajehsaeid H, Arghavani J, Naghdabadi R, Sohrabpour S. A visco-hyperelastic constitutive model for rubber-like materials: A rate-dependent relaxation time scheme. *Int J Eng Sci*. 2014;79:44-58. doi: 10.1016/j.ijengsci.2014.03.001.

73. Bergström J. *Large strain time-dependent behavior of elastomeric materials.* [Massachusetts Institute of Technology]. ; 1999.

74. Bergström J, Boyce M. Constitutive modeling of the time-dependent and cyclic loading of elastomers and application to soft biological tissues. *Mech Mater*. 2001;33(9):523-530.

75. Jongmin Shim, Mohr D. Rate dependent finite strain constitutive model of polyurea. *Int J Plast*. 2011;27(6):868; 868-886; 886. doi: 10.1016/j.ijplas.2010.10.001.

76. Shim J, Mohr D. Punch indentation of polyurea at different loading velocities: Experiments and numerical simulations. *Mech Mater*. 2011;43(7):349-360.

77. Simo J. On a fully three-dimensional finite-strain viscoelastic damage model: Formulation and computational aspects. *Comput Methods Appl Mech Eng*. 1987;60(2):153-173.

78. Drozdov AD. A constitutive model for nonlinear viscoelastic media. *Int J Solids Structures*. 1997;34(21):2685-2707.

79. Green AE, Rivlin RS. The mechanics of non-linear materials with memory. *Archive for Rational Mechanics and Analysis*. 1957;1(1):1-21.

80. Coleman BD, Noll W. The thermodynamics of elastic materials with heat conduction and viscosity. *Archive for Rational Mechanics and Analysis*. 1963;13(1):167-178.

81. Pouriayevali H, Guo Y, Shim V. A visco-hyperelastic constitutive description of elastomer behaviour at high strain rates. *Procedia Engineering*. 2011;10:2274-2279.

82. Drozdov AD, Dorfmann A. Finite viscoelasticity of filled rubber: Experiments and numerical simulation. *Arch Appl Mech*. 2003;72(9):651-672.

83. Bergström J, Boyce M. Large strain time-dependent behavior of filled elastomers. *Mech Mater*. 2000;32(11):627-644.

84. Lockett FJ. *Nonlinear viscoelastic solids.* Academic Press; 1972.

85. Bernstein B, Kearsley E, Zapas L. A study of stress relaxation with finite strain. *J Rheol*. 1963;7:391.

86. Kaye A. *Non-Newtonian flow in incompressible fluids*. 1962.

87. Tanner RI. From A to (BK)Z in constitutive relations. *The Society of Rheology*. 1988.

88. Chang W, Bloch R, Tschoegl N. On the theory of the viscoelastic behavior of soft polymers in moderately large deformations. *Rheologica Acta*. 1976;15(7-8):367-378.

89. Fung Y, Skalak R. *Biomechanics: Mechanical properties of living tissues*. 1981.

90. Morman Jr K. An adaptation of finite linear viscoelasticity theory for rubber-like viscoelasticity by use of a generalized strain measure. *Rheologica acta*. 1988;27(1):3-14.

91. AENOR. Standard on the evaluation of performance of the protection systems for motorcyclists on safety barriers and parapets - part 1: Terminology and test procedures. *UNE 135900-1:2008*. 2008.

92. AENOR. Standard on the evaluation of performance of the protection systems for motorcyclists on safety barriers and parapets - part 2: Performance clasess and aceptance criteria. *UNE 135900-2:2008*. 2008.

93. Mullins L. Softening of rubber by deformation. *Rubber Chemistry and Technology*. 1969;42(1):339-362.

94. UNE-ISO 4664-1. UNE-ISO 4664-1. rubber, vulcalized or thermoplastic. determination of dynamic properties. part 1: General guidance. *UNE-ISO 4664-1*. 2011.

95. Sierakowski R. Strain rate effects in composites. *Appl Mech Rev*. 1997;50:741-761.

96. Kistler. Quartz force links, manufacturer's catalog. . 2010.

97. Xiao X. Dynamic tensile testing of plastic materials. *Polym Test*. 2008;27(2):164-178. doi: http://dx.doi.org/10.1016/j.polymertesting.2007.09.010.

98. Yang X, Hector Jr L, Wang J. A combined theoretical/experimental approach for reducing ringing artifacts in low dynamic testing with servo-hydraulic load frames. *Exp Mech*. 2014;54(5):775-789. doi: http://dx.doi.org/10.1007/s11340-014-9850-x.

99. Dutton J. *Dynamic tensile properties of thin sheet materials.* Research Report 303; 2005.

100. Rehrmann T, Kopp R. Recent enhancements to determine flow stress data in high speed compression tests. . 2004;1st International Conference in High Speed Forming:71-80.

101. Larour P. *Strain rate sensitivity of automotive sheet steels: Influence of plastic strain, strain rate, temperature, microstructure, bake hardening and pre-strain.* [Doctoral Thesis: RWTH Aachen, Germany]. Lehrstuhl und Institut für Eisenhüttenkunde; 2010.

102. Bardenheier R, Rogers G. Dynamic impact testing. *Instron Ltd., High Wycombe, UK*. 2003.

103. Eriksen R,Normann Wilken. *High strain rate characterisation of composite materials; high strain rate characterisation of composite materials.* Doctoral Thesis ed. DTU Mechanical Engineering; 2014.

104. Silva FdA, Zhu D, Mobasher B, Soranakom C, Toledo Filho RD. High speed tensile behavior of sisal fiber cement composites. *Materials Science and Engineering: A*. 2010;527(3):544-552. doi: http://dx.doi.org/10.1016/j.msea.2009.08.013.

105. Zhu D, Mobasher B, Rajan S, Peralta P. Characterization of dynamic tensile testing using aluminum alloy 6061-T6 at intermediate strain rates. *J Eng Mech*. 2011;137(10):669-679.

106. Pneumont A. Vibration control of active structures. . 1997.

107. Ewins D. Modal testing: Theory, practice and application (mechanical engineering research studies: Engineering dynamics series). . 2003.

108. Preumont A. *Vibration control of active structures: An introduction.* Springer Science & Business Media; 2002.

109. Uriarte I, Garitaonandia I, Guraya T, Arriaga A. Suppression of ringing oscillations from high speed rubber compression curves through a detailed modal characterization of servo-hydraulic machines. *Polym Test*. 2017;60:365-373.

110. Kennedy J, Eberhart R. *Particle swarm optimization.* Proceedings of IEEE International Conference on Neural Network: ; 1995, p.1945-1948:1948.

111. Poli R. Analysis of the publications on the applications of particle swarm optimisation. *Journal of Artificial Evolution and Applications*. 2008;2008:1-10.

112. Shi Y, Eberhart RC. Fuzzy adaptive particle swarm optimization. . 2001;1:101-106.

113. Cao YQ, Deng ZX, Li J, Liu HJ. Multi-parameter optimization algorithm of frequency-dependent model for viscoelastic damping material. *Advanced Materials Research*. 2010;129-131:416-420. doi: 10.4028/www.scientific.net/AMR.129-131.416.

114. Zheng X, Lin G, Wang J, Zhang Y. *Parameter identification of nonlinear viscoelastic-plastic constitutive equation of soybean and cottonseed based on particles swarm optimization.* Proceedings of IEEE International Workshop on Knowledge Discovery and Data Mining: ; 2008, p.101-106:552.

115. Khajehsaeid H, Arghavani J, Naghdabadi R, Sohrabpour S. A visco-hyperelastic constitutive model for rubber-like materials: A rate-dependent relaxation time scheme. *Int J Eng Sci*. 2014;79:44-58.

116. Moravec F, Holeček M. Microstructure-dependent nonlinear viscoelasticity due to extracellular flow within cellular structures. *Int J Solids Structures*. 2010;47(14):1876-1887.

117. Kraaij G, Zadpoor AA, Tuijthof GJ, Dankelman J, Nelissen RG, Valstar ER. Mechanical properties of human bone–implant interface tissue in aseptically loose hip implants. *Journal of the mechanical behavior of biomedical materials*. 2014;38:59-68.

118. Hao D, Li D, Liao Y. A finite viscoelastic constitutive model for filled rubber-like materials. *Int J Solids Structures*. 2015;64:232-245.

119. Doman D, Cronin D, Salisbury C. Characterization of polyurethane rubber at high deformation rates. *Exp Mech*. 2006;46(3):367-376.

120. Beda T, Casimir J, Atcholi K, Chevalier Y. Loaded rubber-like materials subjected to small-amplitude vibrations. *Chinese Journal of Polymer Science*. 2014;32(5):620-632.

121. Cao YQ, Deng ZX, Li J, Liu HJ. Multi-parameter optimization algorithm of frequency-dependent model for viscoelastic damping material. *Materials and Manufacturing Technology, Pts 1 and 2*. 2010;129-131:416-420. doi: 10.4028/www.scientific.net/AMR.129-131.416.

122. Salisbury C. *On the deformation mechanics of hyperelastic porous materials.* [University of Waterloo]. ; 2011 [Ph.D. thesis].

123. Uriarte I, Zulueta E, Guraya T, Arsuaga M, Garitaonandia I, Arriaga A. CHARACTERIZATION OF RECYCLED RUBBER USING PARTICLE SWARM OPTIMIZATION TECHNIQUES. *Rubber Chemistry and Technology*. 2015;88(3):343-358. http://dx.doi.org/10.5254/rct.15.85916. doi: 10.5254/rct.15.85916.

ANNEX A

A.1. EXPERIMENTAL CURVES FOR BLENDS 75/25 AND 60/40 (SUMMARIZED IN CHAPTER 3).

75/25 BLEND

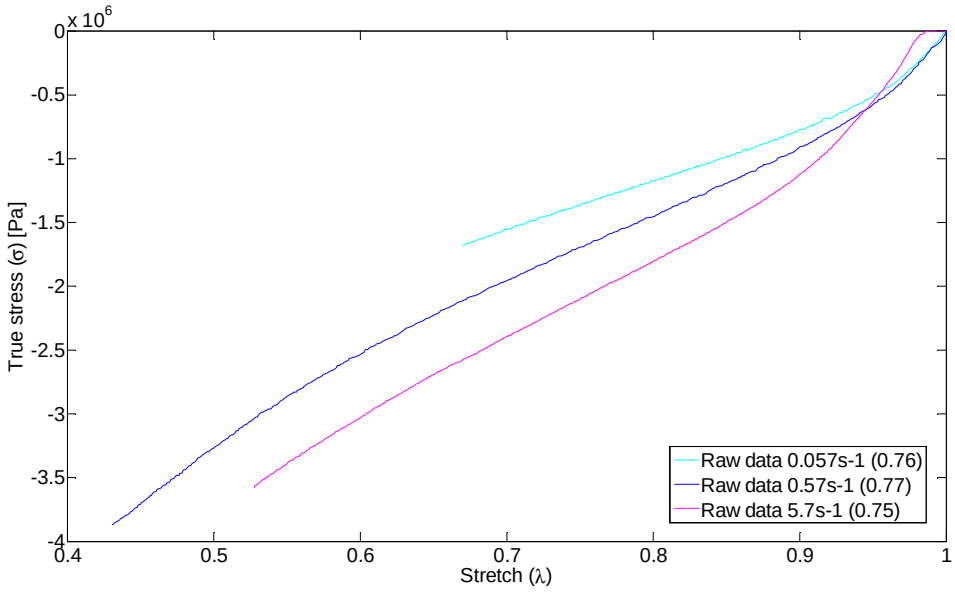

Fig. A - 1 Stress-stretch curves for density 0.7 g/cm^3 at different strain rates (BIG samples, 75/25 proportion).

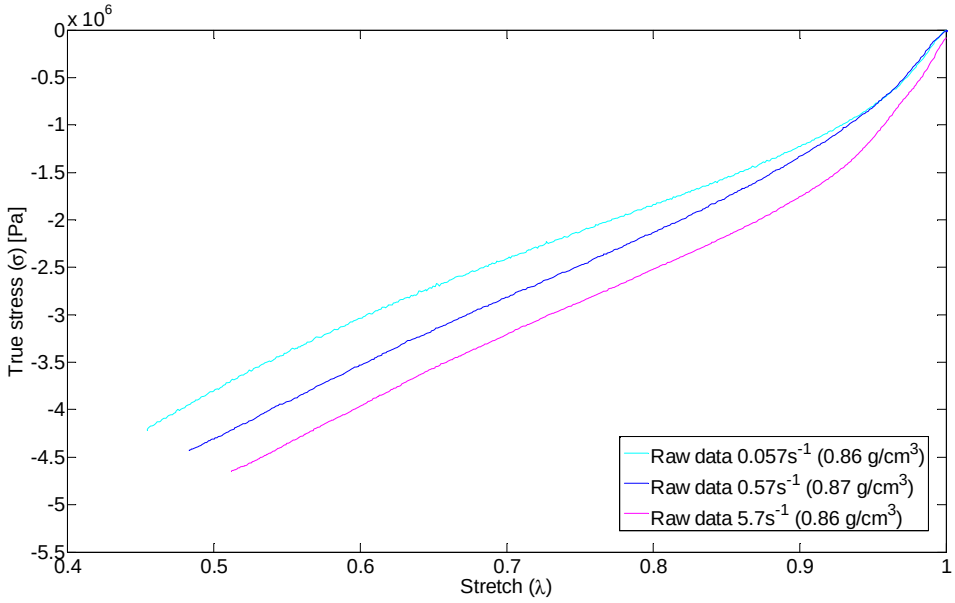

Fig. A - 2 Stress-stretch curves for density 0.8 g/cm³ at different strain rates (BIG samples, 75/25 proportion).

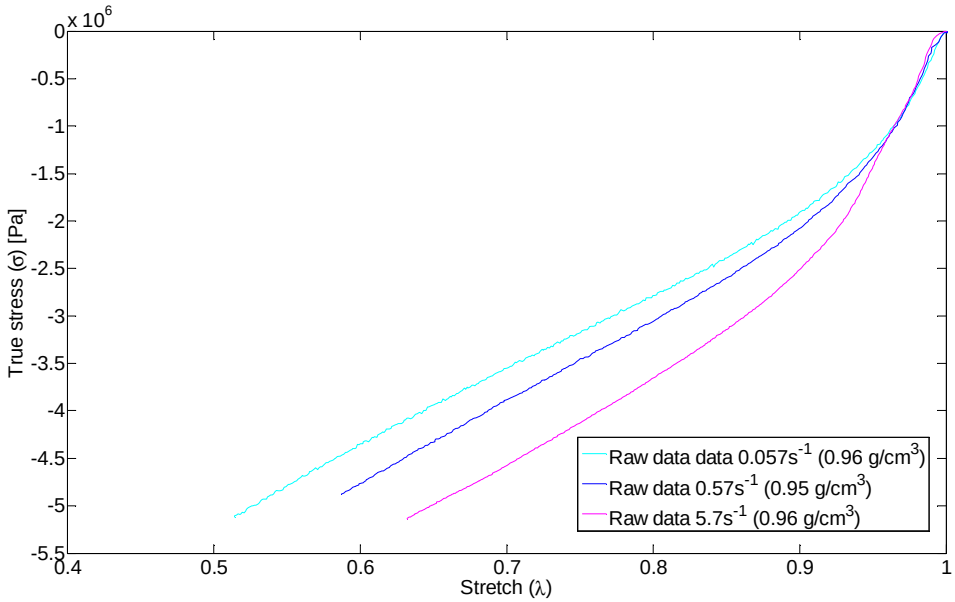

Fig. A - 3 Stress-stretch curves for density 0.9 g/cm³ at different strain rates (BIG samples, 75/25 proportion).

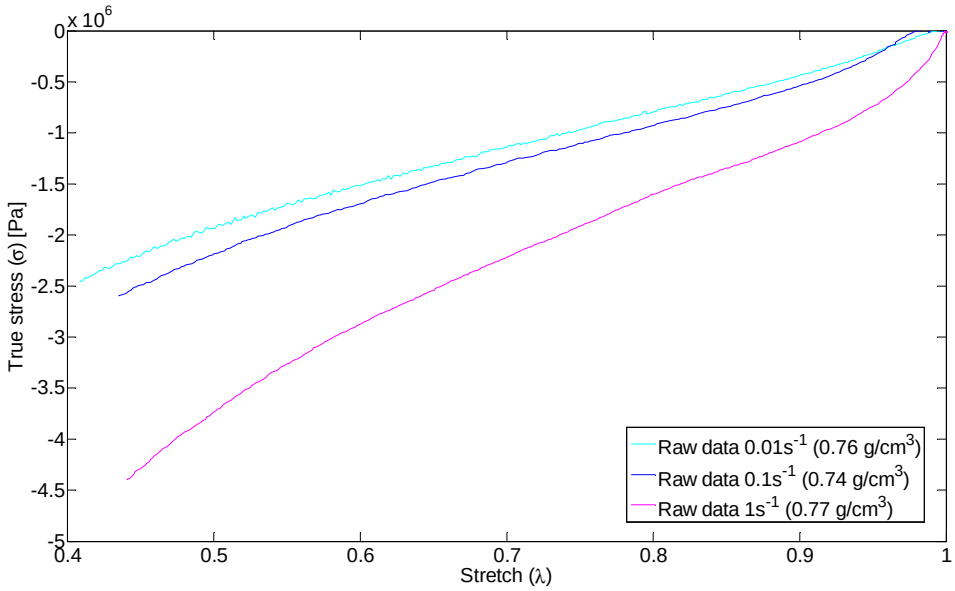

Fig. A - 4 Stress-stretch curves for density 0.7 g/cm³ at different strain rates (SMALL samples, 75/25 proportion).

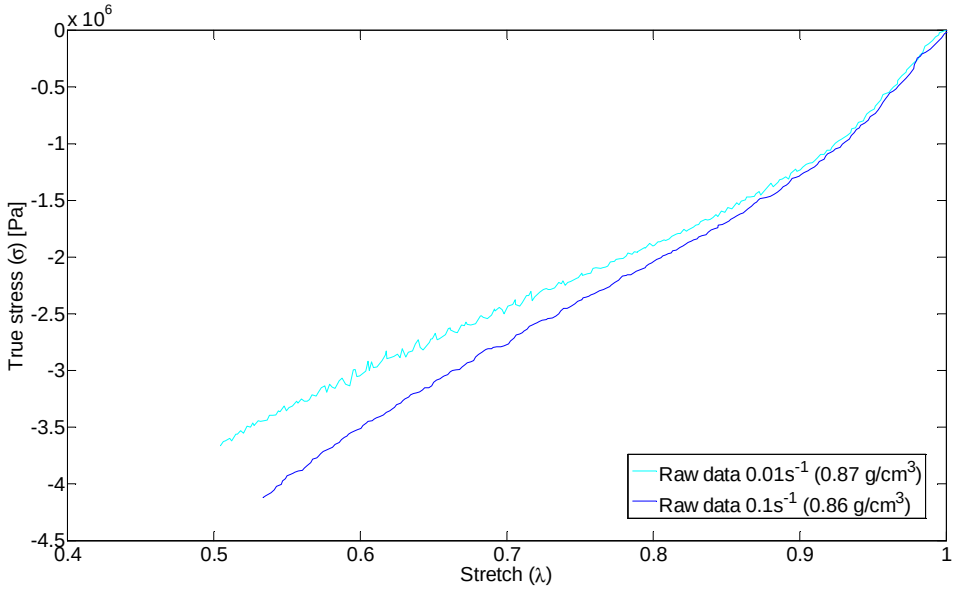

Fig. A - 5 Stress-stretch curves for density 0.8 g/cm³ at different strain rates (SMALL samples, 75/25 proportion).

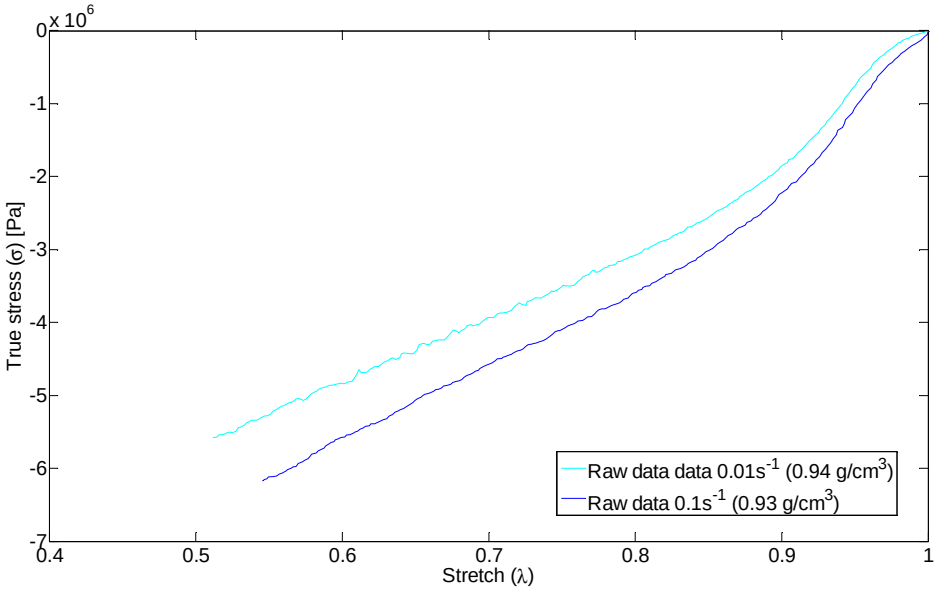

Fig. A - 6 Stress-stretch curves for density 0.9 g/cm³ at different strain rates (SMALL samples, 75/25 proportion).

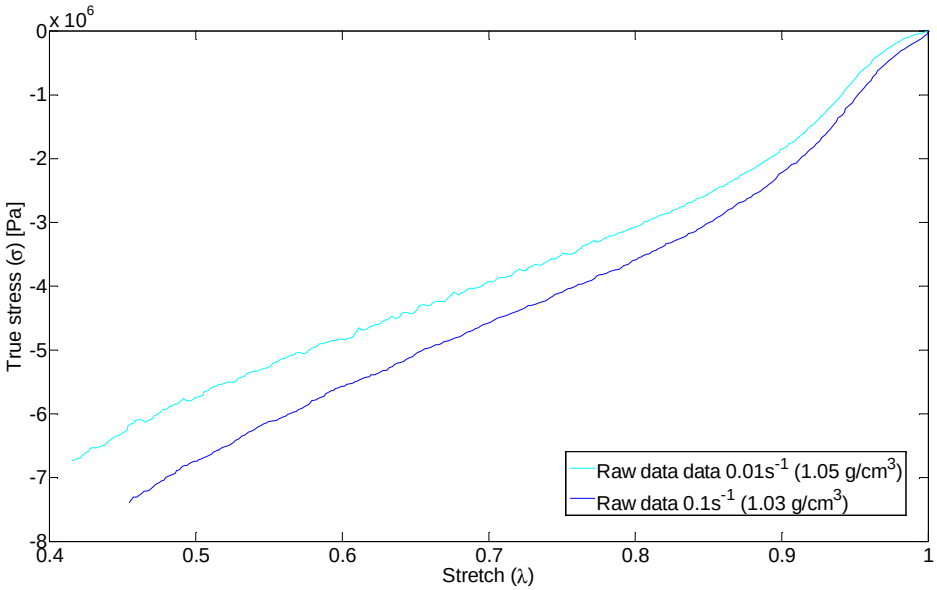

Fig. A - 7 Stress-stretch curves for density 1 g/cm³ at different strain rates (SMALL samples, 75/25 proportion).

60/40 BLEND

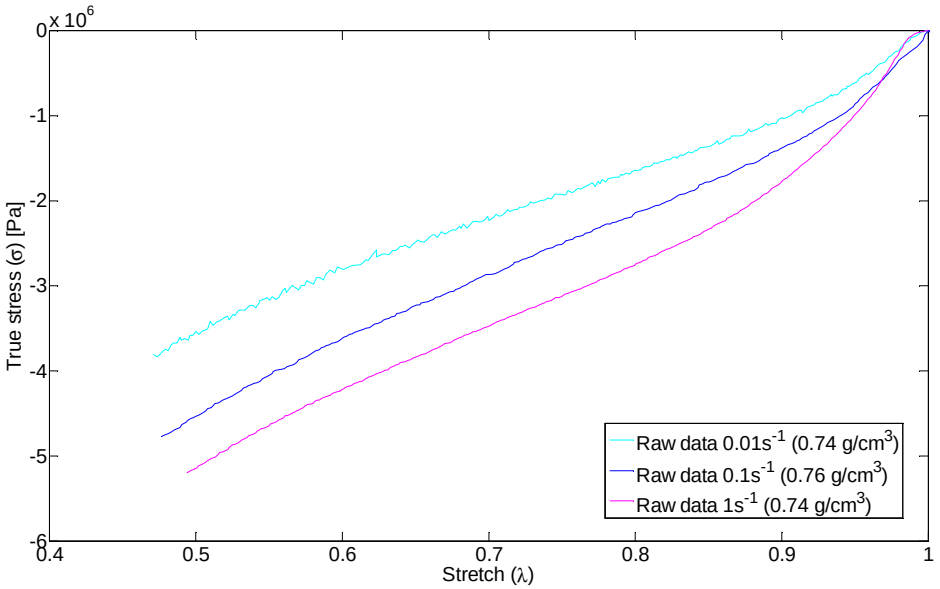

Fig. A - 8 Stress-stretch curves for density 0.7 g/cm3 at different strain rates (SMALL samples, 60/40 proportion).

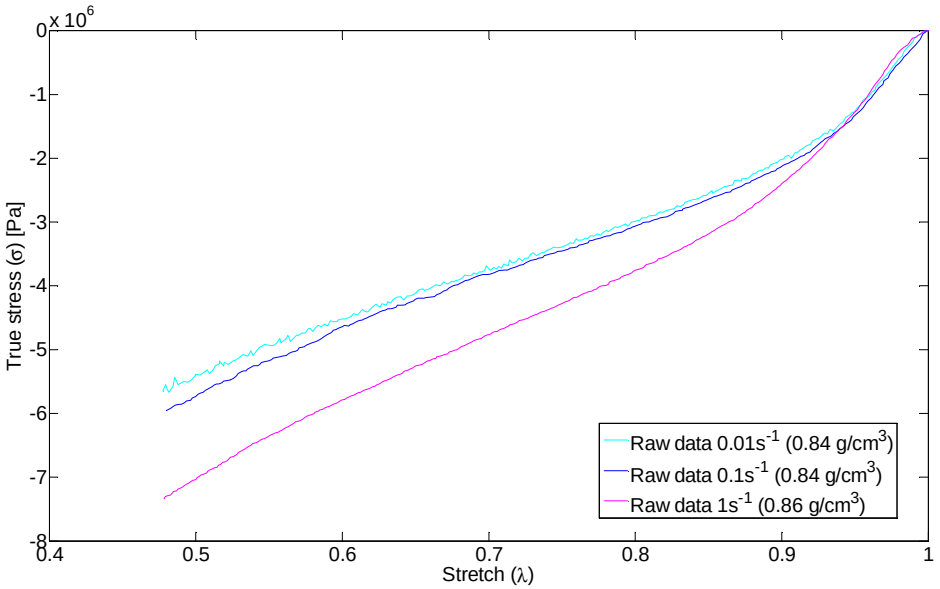

Fig. A - 9 Stress-stretch curves for density 0.8 g/cm^3 at different strain rates (SMALL samples, 60/40 proportion).

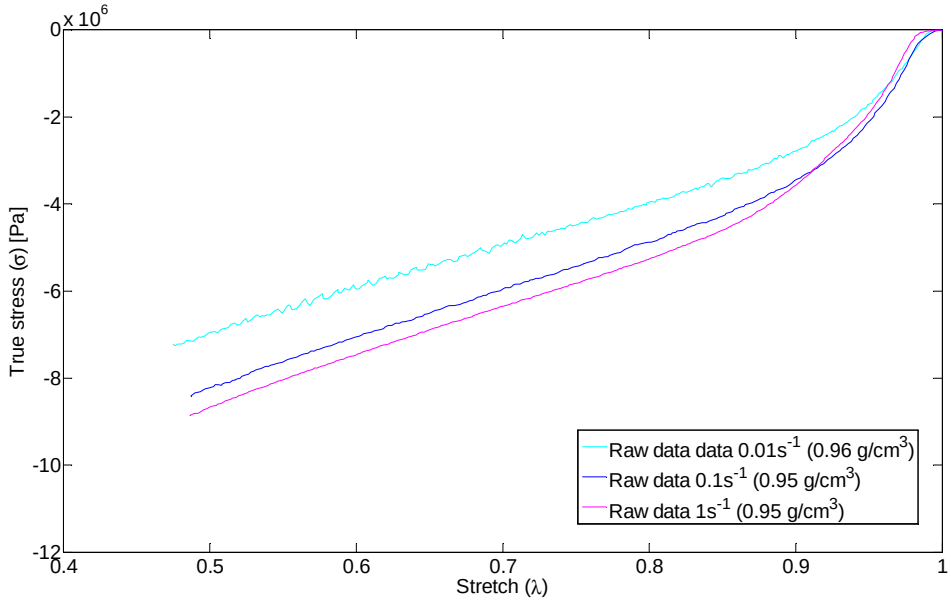

Fig. A - 10 Stress-stretch curves for density 0.9 g/cm³ at different strain rates (SMALL samples, 60/40 proportion).

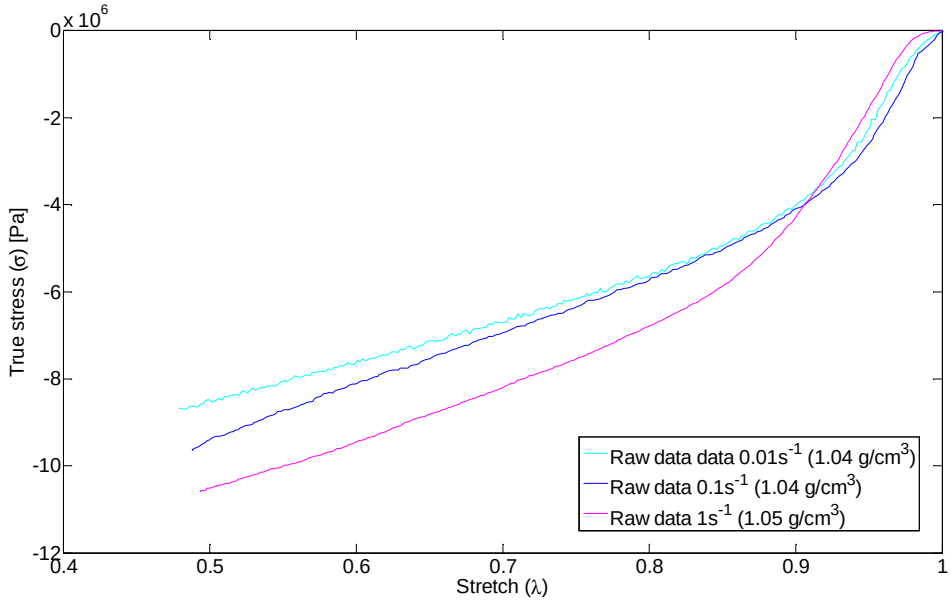

Fig. A - 11 Stress-stretch curves for density 1 g/cm³ at different strain rates (SMALL samples, 60/40 proportion).

ANNEX B

B.1. SOME REMARKS ON OBJECTIVITY, ISOTROPY AND INCOMPRESSIBILITY CHARACTERISTICS OF HYPERELASTIC MATERIALS

The **strain-energy function** is assumed to be **objective** (invariant to the change of the observer), that is, after a translation and a rotation of the **hyperelastic** material the amount of stored energy remains unchanged. If x^* is the position of a point in the space after a translation and a rotation of the point x from the reference configuration, they are related by the expression:

$$x^* = c(t) + Q(t)x \tag{1.1}$$

$$t^* = t + \alpha \tag{1.2}$$

Where the vector c(t) describes de rigid body translation; and the tensor Q –proper orthogonal tensor, det(Q)=1 – describes a rigid body rotation.

$$\begin{aligned} F(X,t) &= \frac{\partial x(X,t)}{\partial X} \\ F^*(X,t^*) &= \frac{\partial x^*(X,t^*)}{\partial X} \end{aligned} \tag{1.3}$$

$$F^* = \frac{\partial x^*}{\partial X} = Q\frac{\partial x}{\partial X} = QF \tag{1.4}$$

$$\psi(F) = \psi\left(F^*\right) = \psi(QF) \tag{1.5}$$

As any proper orthogonal tensor Q is valid in previous expression, if the transpose of the rotation tensor is considered, $Q = R^T$,

$$\psi(F) = \psi(QF) = \psi\left(R^T F\right) = \psi\left(R^T RU\right) = \psi(U) \tag{1.6}$$

Here, it can be concluded that $\boldsymbol{\psi}$ only depends on the **stretching part of F** (it is independent of the rotational part R). As $C = F^T F = U^T R^T RU = U^2$ ($R^T R = 1$ and $U^T = U$) and $E = \frac{U^2 - I}{2}$, $\boldsymbol{\psi}$ can be expressed as a function of these:

$$\psi(F) = \psi(C) = \psi(E) \tag{1.7}$$

If the derivative of the strain energy function is done, it is obtained the next expression:

$$\begin{aligned} \dot{\psi} &= \mathrm{tr}\left[\left(\frac{\partial \psi(F)}{\partial F}\right)^T \dot{F}\right] = \mathrm{tr}\left[\left(\frac{\partial \psi(C)}{\partial C}\right)^T \dot{C}\right] = \mathrm{tr}\left[\left(\frac{\partial \psi(C)}{\partial C}\right)^T \left(\dot{F}^T F + F^T \dot{F}\right)\right] = \\ &= 2\,\mathrm{tr}\left(\frac{\partial \psi(C)}{\partial C} F^T \dot{F}\right) \end{aligned} \tag{1.8}$$

From here it can be obtained:

$$\left(\frac{\partial \psi(F)}{\partial F}\right)^T = 2\frac{\partial \psi(C)}{\partial C} F^T \tag{1.9}$$

And taking into account that $PF^T = FP^T$, the Cauchy stress is:

$$\sigma = J^{-1} F \left(\frac{\partial \psi(F)}{\partial F}\right)^T = 2J^{-1} F \frac{\partial \psi(C)}{\partial C} F^T \tag{1.10}$$

The first Piola Kirchhoff stress tensor:

$$P = \left(\frac{\partial \psi(F)}{\partial F}\right) = 2F \frac{\partial \psi(C)}{\partial C} \tag{1.11}$$

The second Piola Kirchhoff stress tensor:

$$S = F^{-1} P = 2\frac{\partial \psi(C)}{\partial C} = \frac{\partial \psi(E)}{\partial E} \tag{1.12}$$

As $2E = C - I$.

If the material is **isotropic**, this is, if the response of the material is the same in all directions, and a superimposed rigid body motion is considered on the reference configuration of a material, being:

$$X^* = c(t) + Q(t)X \tag{1.13}$$

Where $F^* = \frac{\partial x}{\partial X^*}$.

$$F = \frac{\partial x}{\partial X} = \frac{\partial x}{\partial X^*} Q = F^* Q \rightarrow F^* = FQ^T \tag{1.14}$$

A hyperelastic material is isotropic if:

$$\psi(F) = \psi(F^*) = \psi(FQ^T) \tag{1.15}$$

Taking into account that $\psi(F) = \psi(C)$ if the material is hyperelastic, $\psi(C) = \psi(C^*) = \psi(F^{*T}F^*) = \psi(QF^TFQ^T) = \psi(QCQ^T)$.

If this expression holds for all symmetric tensors C and orthogonal tensors Q, $\psi(C)$ is an invariant of C (invariant under rotation), so it can be expressed in terms of the principal invariants of C.

$$\psi(C) = \psi[I_1(C), I_2(C), I_3(C)] = \psi[I_1(b), I_2(b), I_3(b)] \tag{1.16}$$

$$\begin{aligned} I_1(C) &= tr(C) \\ I_2(C) &= \frac{1}{2}\left[(tr(C))^2 - tr(C^2)\right] \\ I_3(C) &= \det(C) \end{aligned} \tag{1.17}$$

Remembering that $S = F^{-1}P = 2\frac{\partial \psi(C)}{\partial C}$ and differentiating $\psi(C)$:

$$\frac{\partial \psi(C)}{\partial C} = \frac{\partial \psi}{\partial I_1}\frac{\partial I_1}{\partial C} + \frac{\partial \psi}{\partial I_2}\frac{\partial I_2}{\partial C} + \frac{\partial \psi}{\partial I_3}\frac{\partial I_3}{\partial C} \tag{1.18}$$

$$\frac{\partial I_1}{\partial C}=\frac{\partial trC}{\partial C}=\frac{\partial (I:C)}{\partial C}=I$$
$$\frac{\partial I_2}{\partial C}=\frac{1}{2}\left(2(trC)I-\frac{\partial tr(C^2)}{\partial C}\right)=I_1 I-C \tag{1.19}$$
$$\frac{\partial I_3}{\partial C}=I_3 C^{-1}$$

$$S=2\frac{\partial \psi(C)}{\partial C}=2\left[\frac{\partial \psi}{\partial I_1}I+\frac{\partial \psi}{\partial I_2}(I_1 I-C)+\frac{\partial \psi}{\partial I_3}I_3 C^{-1}\right] \tag{1.20}$$

$$S=2\left[\left(\frac{\partial \psi}{\partial I_1}+I_1\frac{\partial \psi}{\partial I_2}\right)I-\frac{\partial \psi}{\partial I_2}C+I_3\frac{\partial \psi}{\partial I_3}C^{-1}\right] \tag{1.21}$$

$$\sigma=J^{-1}FSF^T \tag{1.22}$$

Taking into account that:

$$FIF^T=FF^T=b$$
$$FCF^T=\left(FF^T\right)^2=b^2 \tag{1.23}$$
$$FC^{-1}F^T=FF^{-1}F^{-T}F^T=I$$

Following expression is obtained:

$$\sigma=2J^{-1}\left[\left(\frac{\partial \psi}{\partial I_1}+I_1\frac{\partial \psi}{\partial I_2}\right)b-\frac{\partial \psi}{\partial I_2}b^2+I_3\frac{\partial \psi}{\partial I_3}I\right] \tag{1.24}$$

Remembering eq. (5.88) from Holzapfel[42], $b^2=I_1 b-I_2 I+I_3 b^{-1}$, and replacing it in previous equation:

$$\begin{aligned}\sigma&=2J^{-1}\left[\left(\frac{\partial \psi}{\partial I_1}+I_1\frac{\partial \psi}{\partial I_2}\right)b-\frac{\partial \psi}{\partial I_2}\left(I_1 b-I_2 I+I_3 b^{-1}\right)+I_3\frac{\partial \psi}{\partial I_3}I\right]=\\&=2J^{-1}\left[\left(I_2\frac{\partial \psi}{\partial I_2}+I_3\frac{\partial \psi}{\partial I_3}\right)I+\left(\frac{\partial \psi}{\partial I_1}\right)b-I_3\frac{\partial \psi}{\partial I_2}b^{-1}\right]\end{aligned} \tag{1.25}$$

In the case of **incompressible** materials, the related constraint is $J=1$, and the strain energy function is defined as:

$$\psi=\psi(F)-p(J-1) \tag{1.26}$$

With p as Lagrange multiplier. It can be determined from the boundary conditions and equilibrium equations, as hydrostatic pressure.

Differentiating this equation with respect to F and taking into account that $\frac{\partial J}{\partial F} = JF^{-T}$,

$$P = \frac{\partial \psi(F)}{\partial F} - pF^{-T} \tag{1.27}$$

If previous equation is multiplied by F^{-1} from the left-hand side:

$$S = F^{-1}\frac{\partial \psi(F)}{\partial F} - pC^{-1} = F^{-1}2F\frac{\partial \psi(C)}{\partial C} - pC^{-1} = 2\frac{\partial \psi(C)}{\partial C} - pC^{-1} \tag{1.28}$$

If eq.(1.27) is multiplied by F^T from the right-hand side:

$$\sigma = \frac{\partial \psi(F)}{\partial F}F^T - pI \tag{1.29}$$

As for the incompressible case the invariant $I_3 = \det C = \det b = 1$, the strain energy function may be expressed in terms of I_1 and I_2:

$$\psi(C) = \psi\left[I_1(C), I_2(C)\right] - \frac{1}{2}p(I_3 - 1) = \psi\left[I_1(b), I_2(b)\right] - \frac{1}{2}p(I_3 - 1) \tag{1.30}$$

Where $\frac{p}{2}$ is a Lagrange multiplier.

Taking into account that $S = 2\frac{\partial \psi(C)}{\partial C}$, if $\psi\left(I_1(C), I_2(C)\right)$ is derived:

$$\frac{\partial \psi(C)}{\partial C} = \frac{\partial \psi(I_1, I_2)}{\partial C} - \frac{\partial \frac{1}{2}p(I_3 - 1)}{\partial C} = I\frac{\partial \psi}{\partial I_1} + (I_1 I - C)\frac{\partial \psi}{\partial I_2} - \frac{1}{2}pI_3 C^{-1} \tag{1.31}$$

$$S = 2I\frac{\partial \psi}{\partial I_1} + 2(I_1 I - C)\frac{\partial \psi}{\partial I_2} - 2\frac{1}{2}pI_3 C^{-1} = 2\left(\frac{\partial \psi}{\partial I_1} + I_1\frac{\partial \psi}{\partial I_2}\right)I - 2\frac{\partial \psi}{\partial I_2}C - pC^{-1} \tag{1.32}$$

Taking into account eq. (1.23) and the relationship between Cauchy stress and second Piola-Kirchhoff stress next expression is obtained:

$$\sigma = 2(\frac{\partial \psi}{\partial I_1} + I_1 \frac{\partial \psi}{\partial I_2})b - 2\frac{\partial \psi}{\partial I_2} b^2 - pI \tag{1.33}$$

Which is the **expression used by Yang et al.** for a hyperelastic, isotropic, incompressible material showm in eq.(5.2).

The strain energy can be also separated, as stated in eq. (6.10). Keeping in mind eq.(1.20):

$$S = 2\frac{\partial \psi_{isoc}}{\partial C} + 2\frac{\partial \psi_{vol}}{\partial J}\frac{\partial J}{\partial C} \tag{1.34}$$

From $\frac{\partial J}{\partial C} = \frac{J}{2}C^{-1}$:

$$S = 2\frac{\partial \psi_{isoc}}{\partial C} + J\frac{\partial \psi_{vol}}{\partial J}C^{-1} \tag{1.35}$$

In the isotropic case, $\psi_{isoc} = \psi_{isoc}(\overline{I}_1, \overline{I}_2)$; differentiating it:

$$\frac{\partial \psi_{isoc}}{\partial C} = \frac{\partial \psi_{isoc}}{\partial \overline{I}_1}\frac{\partial \overline{I}_1}{\partial C} + \frac{\partial \psi_{isoc}}{\partial \overline{I}_2}\frac{\partial \overline{I}_2}{\partial C} \tag{1.36}$$

Next, eq.(6.3) and eq.(6.4) are introduced in (1.36), and with

$$\frac{\partial I_1}{\partial C} = \frac{\partial trC}{\partial C} = \frac{\partial (I:C)}{\partial C} = I \tag{1.37}$$

$$\frac{\partial I_2}{\partial C} = \frac{1}{2}\left(2(trC)I - \frac{\partial tr(C^2)}{\partial C} \right) = I_1 I - C \tag{1.38}$$

Differentiating $\overline{I}_1$ and $\overline{I}_2$ over C:

$$\frac{\partial \overline{I}_1}{\partial C} = \frac{\partial J^{-2/3}}{\partial C} I_1 + J^{-2/3}\frac{\partial I_1}{\partial C} = -\frac{1}{3}J^{-2/3}C^{-1}I_1 + J^{-2/3}I \tag{1.39}$$

$$\frac{\partial \overline{I}_2}{\partial C} = \frac{\partial J^{-4/3}}{\partial C} I_2 + J^{-4/3}\frac{\partial I_2}{\partial C} = -\frac{2}{3}J^{-4/3}C^{-1}I_2 + J^{-4/3}(I_1 I - C) \tag{1.40}$$

Therefore:

$$S = 2\frac{\partial \psi_{isoc}}{\partial \bar{I}_1}\frac{\partial \bar{I}_1}{\partial C} + 2\frac{\partial \psi_{isoc}}{\partial \bar{I}_2}\frac{\partial \bar{I}_2}{\partial C} + J\frac{\partial \psi_{vol}}{\partial J}C^{-1} =$$
$$= 2\frac{\partial \psi_{isoc}}{\partial \bar{I}_1}\left(-\frac{1}{3}J^{-2/3}C^{-1}I_1 + J^{-2/3}I\right) + 2\frac{\partial \psi_{isoc}}{\partial \bar{I}_2}\left(-\frac{2}{3}J^{-4/3}C^{-1}I_2 + J^{-4/3}(I_1 I - C)\right) + J\frac{\partial \psi_{vol}}{\partial J}C^{-1} = \quad (1.41)$$
$$= 2J^{-2/3}\left[\frac{\partial \psi_{isoc}}{\partial \bar{I}_1}\left(I - \frac{1}{3}C^{-1}I_1\right) + J^{-2/3}\frac{\partial \psi_{isoc}}{\partial \bar{I}_2}\left(I_1 I - C - \frac{2}{3}C^{-1}I_2\right)\right] + J\frac{\partial \psi_{vol}}{\partial J}C^{-1}$$

This expression may be written as:

$$S = 2J^{-2/3}DEV\left[\frac{\partial \psi_{isoc}}{\partial \bar{I}_1}I - J^{-2/3}\frac{\partial \psi_{isoc}}{\partial \bar{I}_2}C^{-2}\right] + J\frac{\partial \psi_{vol}}{\partial J}C^{-1} \quad (1.42)$$

With $DEV(\bullet) = (\bullet) - \frac{1}{3}[(\bullet):C]C^{-1}$ as the deviatoric operator over the material configuration.

Remembering eq.(1.21), one gets next expression:

$$S_{deviatoric} = 2\left(\frac{\partial \psi_{isoc}}{\partial \bar{I}_1} + \bar{I}_1\frac{\partial \psi_{isoc}}{\partial \bar{I}_2}\right)I - 2\frac{\partial \psi_{isoc}}{\partial \bar{I}_2}\bar{C} \quad (1.43)$$

And the Cauchy stress becomes ($\sigma = J^{-1}FSF^T$):

$$\sigma = 2J^{-2/3}J^{-1}\left[\frac{\partial \psi_{isoc}}{\partial \bar{I}_1}F\left(I - \frac{1}{3}C^{-1}I_1\right)F^T + J^{-2/3}\frac{\partial \psi_{isoc}}{\partial \bar{I}_2}F\left(I_1 I - C - \frac{2}{3}C^{-1}I_2\right)F^T\right] + J\frac{\partial \psi_{vol}}{\partial J}FC^{-1}F^T \quad (1.44)$$

And considering eq. (1.23) again:

$$\sigma = 2J^{-1}\left[J^{-2/3}\frac{\partial \psi_{isoc}}{\partial \bar{I}_1}\left(b - \frac{1}{3}I_1 I\right) + J^{-4/3}\frac{\partial \psi_{isoc}}{\partial \bar{I}_2}\left(I_1 b - b^2 - \frac{2}{3}I_2 I\right)\right] + \frac{\partial \psi_{vol}}{\partial J}I \quad (1.45)$$

Remembering that $\bar{b} = J^{-2/3}b$ and $\bar{b}^2 = \bar{I}_1\bar{b} - \bar{I}_2 I + \bar{b}^{-1}$ next expression is obtained:

$$\bar{b}^{-1} = -\bar{I}_1\bar{b} + \bar{I}_2 I + \bar{b}^2 \quad (1.46)$$

And therefore:

$$\sigma = 2J^{-1}\left[\frac{\partial \psi_{isoc}}{\partial \bar{I}_1}\left(\bar{b} - \frac{1}{3}\bar{I}_1 I\right) - \frac{\partial \psi_{isoc}}{\partial \bar{I}_2}\left(\bar{b}^{-1} - \frac{1}{3}\bar{I}_2 I\right)\right] + \frac{\partial \psi_{vol}}{\partial J}I \quad (1.47)$$

This expression may be written as:

$$\sigma = 2J^{-1} dev\left[\frac{\partial \psi_{isoc}}{\partial \bar{I}_1} \bar{b} - \frac{\partial \psi_{isoc}}{\partial \bar{I}_2} \bar{b}^{-1} \right] + \frac{\partial \psi_{vol}}{\partial J} I \tag{1.48}$$

With $dev(\bullet) = (\bullet) - \frac{1}{3} tr(\bullet) I$ as the deviatoric operator over the spatial configuration.

Considering eq. (1.46) once more, if it is introduced into eq.(1.48):

$$\begin{aligned}
&\sigma = 2J^{-1} dev\left[\frac{\partial \psi_{isoc}}{\partial \bar{I}_1} \bar{b} - \frac{\partial \psi_{isoc}}{\partial \bar{I}_2} \left(-\bar{I}_1 \bar{b} + \bar{I}_2 I + \bar{b}^2 \right) \right] + \frac{\partial \psi_{vol}}{\partial J} I = \\
&= 2J^{-1} dev\left[\left(\frac{\partial \psi_{isoc}}{\partial \bar{I}_1} + \bar{I}_1 \frac{\partial \psi_{isoc}}{\partial \bar{I}_2} \right) \bar{b} - \frac{\partial \psi_{isoc}}{\partial \bar{I}_2} \left(-\bar{I}_2 I - \bar{b}^2 \right) \right] + \frac{\partial \psi_{vol}}{\partial J} I = \\
&= 2J^{-1} dev\left[\left(\frac{\partial \psi_{isoc}}{\partial \bar{I}_1} + \bar{I}_1 \frac{\partial \psi_{isoc}}{\partial \bar{I}_2} \right) \bar{b} - \frac{\partial \psi_{isoc}}{\partial \bar{I}_2} \bar{b}^2 \right] + \frac{\partial \psi_{vol}}{\partial J} I
\end{aligned} \tag{1.49}$$